THE FRICTION STIR WELDING OF OXIDE DISPERSION STRENGTHENED FERRITIC ALLOYS

Thesis submitted in accordance with the requirements of the
University of Liverpool for the degree of
Doctor in Philosophy

By

Kiriakos Moustoukas

September 2016

PREFACE

This dissertation is submitted for the degree of Doctor of Philosophy at the University of Liverpool. The work undertaken and described herein was carried out under the supervision of Professor Gordon J Tatlock in the School of Engineering and Material Science, at the Centre for Materials and Structures, University of Liverpool, between October 2012 and September 2016.

This work is original except where acknowledgement and references are made to the previous work. Neither this nor any substantially similar dissertation has been or is being submitted for a degree, diploma or any other qualification at any other university.

Part of this work has been presented in the following publication:

G. J. Tatlock, K. Dawson, T. Boegelein, K. Moustoukas, and A. R. Jones, *High Resolution microstructural studies of the evolution of nano-scale, yttrium-rich oxides in ODS steels subjected to ball milling, selective laser melting or friction stir welding.* **ARRMA 2016, Advances in Refractory and Reactive Metals and Alloys Conference, Mumbai, India January 2016**

Oral presentations of research carried out:

I. *The friction stir welding of oxide dispersion strengthened ferritic alloys.*

National Student Conference in Metallic Materials, University of Sheffield June 2014

II. *The friction stir welding of oxide dispersion strengthened ferritic alloys.*

2nd Odisseus Workshop, Department of Materials, University of Oxford March 2015

Poster presentation of research carried out:

The European Congress and Exhibition on Advance Materials and Processes EUROMAT, Warsaw, Poland September 2015.

Kiriakos Moustoukas

September 2016

ACKNOWLEDGMENTS

First and foremost I would like to express my sincere gratitude to my primary supervisor, Professor Gordon J. Tatlock for the opportunity that has been presented to me, the support, the guidance, the patience and the encouragement throughout the duration of this work.

I would also like to thank my secondary supervisor Professor Yuyuan Zhao for many useful discussions and valuable input.

I would like to express my sincere thanks to Dr Karl E. Dawson for the preparation of FIB samples, TEM microscopy, and for sharing his knowledge on so many aspects of the work undertaken.

I would like to thank Dr Thomas Boegelein for all his help and useful discussions during my time at the University of Liverpool.

I would like to express my thanks to The Welding Institute (TWI) and in particular Mr Stephen Cater and Mr Chris Stunhope for the provision of Friction Stir welds and their help and guidance.

I would like to thank Dr Sebastien N Dryepondt at Oak Ridge National Laboratories (ORNL) for the mechanical testing of samples.

I would like to express my gratitude to Mr David Atkinson for all his help and advice in the sample preparation and optical microscopy laboratories.

A special thanks to all at the Nanoinvestigation Centre at Liverpool (NiCaL), Dr Simon Romani, Dr Tobias Heil, Dr Kerry Adams, Mr Alan Titbury and Lynn Alan.

I would like to express my sincere thanks to Margaret Robinshaw for all her help and advice.

I would like to express my sincere gratitude to all my staff at The Village Chef for allowing me the time to pursue my studies at the University of Liverpool.

A special thanks to my colleagues Keith Arnold and Mark Duffield for all the support and encouragement and for sharing this amazing experience with me.

Finally I would like to express my deepest gratitude to my family. To my parents Takis and Christoulla thank you for all your love and support over the years.

To all my children Yeoryia, Christophora Nikolaos and Dimitris, thank you for all your encouragement, support and love you have given me over the years.

To my adorable grandchildren Panayiotis, Thanos and Theo, thank you for the smiles and joy that you bring in my life.

To my wife, Panayiota thank you for all your love support encouragement and all the patience and understanding that you have shown me always.

ABSTRACT

FeCrAl ferritic alloys are highly oxidation and corrosion resistant alloys but have limited creep strength at high temperatures. The incorporation of a stable rare earth oxide such as yttrium oxide in a FeCrAl alloy increases the in service temperature of the alloy up to 1100^0C. Oxide Dispersion Strengthening (ODS) is achieved by the Mechanical Alloying (MA) process where the yttrium oxide is added to the alloy powders, and is forced into solution with the matrix powder. MA is a time consuming and expensive process but it results in high number density of fine nanometer size particles that provide excellent creep resistance at high temperatures. One such alloy is PM2000 alloy made by Plansee™ GmbH

A more cost effective processing route for the inclusion of oxides in the matrix is the Rapid Solidification Powder (RSP) process where the oxide powder is added to the gas atomised powder from the melt of the alloy to form an ODS alloy but with a much lower number density of larger particles. The alloy still has excellent oxidation and corrosion resistance but limited high temperature stressed applications. Kanthal™ APMT is one such alloy that is commercially available.

Conventional joining techniques that produce a melt zone cannot be used to join ODS steels as the nanoparticles tend to agglomerate and slag off to the surface weakening the weld. Friction Stir Welding (FSW) is a relatively new solid state joining technique that preserves the nanoparticle distribution in the matrix. In this work 4 different types of welds of ODS steels, using FSW were studied. The welds were of a combination of either MA produced PM2000 and/or RSP produced APMT alloys.

The FSW of butt configuration as-rolled PM2000 were studied. Fragments of the polycrystalline cubic boron nitride (PCBN) tool were observed in the thermal mechanically affected zone (TMAZ). On the application of post weld heat treatment (PWHT) these fragments were partially broken down due to a phase change in PCBN and TiN grains were observed around the fragment with the surrounding matrix being rich in Ti.

The FSW of as-extruded plates of PM2000 has revealed an area in the TMAZ with an unsuitable grain structure, the grain structure being controlled by the high number of nucleation sites for new grains during recrystallisation.

In both types of weld above, coarsening of the nanoparticle distribution was observed in the TMAZ with extensive agglomeration of the particles observed in the top part of the welds. This was attributed mainly to the flow of the material creating more ‘encounters’ between particles rather than the heat created by the friction of the tool.

The FSW of APMT has revealed that the wormhole type voids observed in the TMAZ, originated from a feature on the tool surface, as the voids were formed in a spiral along the welding direction.

Finally in the dissimilar metal FSW between APMT and as-extruded PM2000, a distinct region of PM2000 was observed in the APMT half of the weld. Diffusion due to concentration differences were observed by Fe, Mo and Cr as expected. However diffusion of Ti from PM2000 towards APMT had resulted in the formation of Ti(C,N) rich particles after the application of PWHT at the prior boundary between APMT and PM2000. The higher C and N concentration in APMT had resulted in diffusion towards the PM2000 and the capture of Ti present in PM2000 in particles before Ti could diffuse out toward the APMT.

CONTENTS

CHAPTER 1

Introduction

CHAPTER 2

Literature Review

CHAPTER 3

Materials and Experimental Technique

CHAPTER 4

Friction Stir Welding of Rolled PM2000

CHAPTER 5

Friction Stir Welding of As-Extruded PM2000

CHAPTER 6

The Friction Stir Welding of Kanthal™ APMT Alloy

CHAPTER 7

Dissimilar Metal Friction Stir Weld between APMT and As-Extruded PM2000

CHAPTER 8

Discussion

CHAPTER 9

Conclusions and Future Work

REFERENCES

LIST OF SYMBOLS

A_d	m^2	Deformed cross sectional area
A_o	m^2	Original cross sectional area
α	m	Lattice parameter
b	m	Burgers vector
C	%	Creep constant
C_i	%Wt	Elemental concentration
$C_{(i)}$	%Wt	Elemental concentration of known standard
C_0	%Wt	Initial concentration
C_s	%Wt	Concentration at the surface
C_x	%Wt	Concentration at x
D	m^2/s	Diffusion coefficient
D_o	m^2/s	Diffusion pre-exponential
d	m	Inter-planar atomic spacing
d_G	m	Mean grain diameter
d_m	m	Moiré fringe spacing
$d_{(hkl)}$	-	Miller indices
e	-	Efficiency factor
F	N/m	Force per unit length
F_{Max}	N/m	Maximum force per unit length
F_p	N	Force acting on a particle
F_v	-	Volume fraction
G	Pa	Shear modulus
H	m	Height
HI	kJ/mm	Heat Input
I_i	no of counts	Signal intensity
$I_{(i)}$	no of counts	Signal intensity of known standard
K	-	Non constant correction factor

k	-	Material constant
L	m	Camera length
M	-	Taylor factor
N_s	m^{-3}	Number of particles per unit area by $2r_m$ wide
N_v	m^{-3}	Number of particles per unit volume
P	Pa	Pressure
P_z	Pa	Pinning pressure
Q	kJ/mol	Activation energy
q_o	W	Average heat input per unit area and time
R	J/m K^{-1}	Universal gas constant
R_t	m	Tool radius
r	m	Radius
r_m	m	Mean particle radius
r_o	m	Initial particle radius
r_p	m	Particle radius
s_r	rev/m	Rotational speed
s_t	mm/m	Transverse speed
T	ºK	Absolute temperature
T_R	ºC	Temperature of Recrystallisation
T_m	ºC	Temperature of Melting
T_q	N/m	Spidle torque
W	m	Width
β	º	Angle
γ	J/m	Boundary energy per unit length
γ_{mp}	J/m	Interfacial energy between matrix and particle per unit length
γ_m	º	Misorientation angle

γ_{GB}	J/m^2	Grain boundary energy
δ	-	Unconstrained misfit
δ_ε	-	Constrained misfit
ε	%	Creep
ε_e	%	Initial creep
θ	°	Scattering angle
λ	m	Electron wavelength
λ_p	m	Interparticle distance
μ	-	Coefficient of friction
v	-	Poisson's ratio
v_β	-	Molar fraction
σ_{GB}	Pa	Grain boundary yield strength contribution
σ_o	Pa	Material constant
σ_{oro}	Pa	Orowan yield strength contribution
σ_y	Pa	Yield strength
τ_p	Pa	Shear stress acting on a particle
ω	rad/s	Angular velocity

ABBREVIATIONS

ASTM	American Society for Testing and Materials
BCC	Base Centred Cubic
BF	Bright Field
BOP	Bead on Plate
DIC	Differential Interference Contrast
EBSD	Electron Back Scatter Diffraction
EELS	Electron Energy Loss Spectroscopy
EDX	Energy Dispersive X-Ray Spectroscopy
FCC	Face Centred Cubic
FEG	Field Effect Gun
FIB	Focused Ion Beam
FSW	Friction Stir Weld
HAADF	High Angle Annular Dark Field
HIP	Hot Isostatic Pressure
HRTEM	High Resolution Transmission Electron Microscopy
HZ	Heat Zone

LPB	Liquid Phase Bonding
MA	Mechanical Alloying
MIG	Metal Inert Gas
ODS	Oxide Dispersion Strengthening
PCA	Process Control Agent
PCBN	Polycrystalline Cubic Boron Nitride
PWHT	Post Weld Heat Treatment
RSP	Rapidly Solidified Powder
RPW	Resistance Pressure Welding
ROI	Region of Interest
SAD	Selected Area Diffraction
SEM	Scanning Electron Microscopy
SED	Secondary Electron Detector
SFE	Stacking Fault Energy
STEM	Scanning Transmission Electron Microscopy
TEM	Transmission Electron Microscopy
TMAZ	Thermal Mechanical Affected Zone
TIG	Tungsten Inert Gas
TWI	The Welding Institute
YAG	Yttrium Aluminium Garnet
YAH	Yttrium Aluminium Hexagonal

YAM Yttrium Aluminium Monoclinic

YAP Yttrium Aluminium Perovskite

CHAPTER 1

Introduction

1.1 High Temperature Applications

Modern power generation faces many challenges. There is a need to generate more power to meet the ever increasing demand for energy, while reducing the level of CO_2 emissions due to environmental constraints. There is a renewed interest in nuclear power generation because of the low CO_2 emissions but there are safety concerns that need to be addressed. Both conventional fired power plants using coal or gas, and nuclear power generation benefit from higher operating temperatures because of increased efficiencies, and in the case for coal and gas power plants, further reductions in CO_2 emissions. In order to realise better efficiencies, components such as heat exchangers need to operate in temperatures in excess of 1100°C and be able to withstand the harsh oxidising and corrosive environments.

1.2 Material Selection

Oxide Dispersion Strengthened (ODS) ferritic steels are candidate materials for such applications. The fine dispersion of stable oxides within the matrix pins down dislocations providing excellent creep resistance at high temperatures. The introduction of the fine oxide dispersoid is achieved through the mechanical alloying (MA) process [1]. Elemental powders are milled together with the oxide powder in an attritor for a number of hours after which the oxide is forced into solution with the matrix powders. The mixed powders are then consolidated to form the alloy. MA produces a fine dispersion of oxide particles with a high number density of nanometre sized particles [2].

PM2000 is one such alloy produced by Plansee GbmH. Production ceased in 2007 and availability was limited. The major drawback of MA process is the high cost of production.

An alternative process route for ODS steels is the rapidly solidified powder metallurgical (RSP) process which involves the atomisation of a melt to form a powder which is then consolidated. Inclusions include carbides, nitrides and oxides of rare earth additions to the melt. One such alloy is Kanthal™ APMT. The RSP process is more cost effective than the MA process but the dispersoid distribution in APMT is inferior to PM2000 with a lower number density of much larger particles. APMT is an ideal material for high temperatures under low loading applications because of its excellent oxidation and corrosion properties [3]

Using a combination of MA produced PM2000 for stressed components and RSP produced APMT for less stressed components minimises costs while ensuring that the use of PM2000 is optimised.

1.3 Joining Techniques

Welding of ODS alloys is problematic as conventional welding techniques involve a melt pool which causes the oxide particles to slag off and float to the surface weakening the weld. A recently developed solid state joining technique called Friction Stir Welding (FSW) has been used to join ODS steels. It uses friction to plasticise and a tool bit to stir the materials to be joined together without melting the alloys. The FSW process retains the dispersoids in the weld which is necessary for creep strength at high temperatures.

1.4 Scope and Structure of the Thesis

Four different types of friction stir welds, using a combination of PM2000 and APMT ODS steels were characterised in this study using a variety of analytical techniques to assess the suitability of the FSW process for the welding of ODS steels. The effects of the FSW process, with or without PWHT, on the microstructure and on the mechanical properties of ODS steels was investigated.

The thesis is presented in 9 Chapters. A brief introduction of the thesis is given in Chapter 1. In Chapter 2 relevant background information with a literature review is

presented. A detailed account of the materials used and of the various analytical techniques, used in this thesis, is given in Chapter 3. In Chapter 4 the FSW of as-rolled PM2000 is presented. The parameters used were refined for the FSW of the as-extruded PM2000 with the results presented in Chapter 5. In Chapter 6 the results from the FSW of several APMT welds are presented. Additional mechanical testing was carried out as there was more material available for analysis. In Chapter 7 the dissimilar metal FSW between APMT and PM2000 was characterised to investigate the possibility of using two different ODS alloys with different properties for components with different stress environments. The results are summarised in Chapter 8 and conclusions and further work are discussed in Chapter 9.

CHAPTER 2

Literature Review

2.1 High Temperature Alloys

The ferritic Fe Cr Al alloy system is the preferred choice for high temperature applications compared to Ni based alloys because of the lower cost, superior strength to weight ratio, higher melting temperature, higher creep resistance, and the lower coefficient of expansion which, under cyclic thermal conditions would give rise to lower thermal stresses. ODS steels have the best combination of high temperature strength and oxidation resistance of any material [4, 5].

The main requirement of a high temperature alloy is to be able to resist oxidation and corrosion. Alloys that form a protective surface oxide layer that is stable and is able to adhere to the surface of the alloy are the main considerations. The oxides of Cr_2O_3 and Al_2O_3 are considered as the most suitable protective oxides as they are slow growing and very stable. In an alloy system with both aluminium and chromium the composition of the alloy will dictate which of the two oxide formers will dominate and will preferentially form Al_2O_3 oxide layer if the aluminium content is at least 5% [6].

Under cyclic temperature conditions and mechanical loading FeCrAl alloys suffer from spallation due to stresses from the oxide growth or the difference in thermal expansion coefficients of the oxide layer and the base metal [7, 8]. In 1937 Pfeil et al. [9] added rare earth elements to a Ni 20Cr alloy and was found to have beneficial effects in terms of adhesion of the oxide layer. This effect is now known as the reactive element effect. Such reactive elements include yttrium, zirconium, hafnium, titanium lanthanum, cerium amongst others.

Sulphur was identified as being detrimental to the scale adhesion [10]. One of the suggested ways in which RE's improve the scale adhesion is by bonding to traces of sulphur present in the alloy, which prevents the segregation of sulphur to the alloy/alloy oxide boundary. Any sulphur present at the boundary increases faceting

of the interface between the alloy and the oxide layer which has a detrimental effect on the lifespan of FeCrAl alloys [10, 11].

In addition RE's suppress the transport of metal ions through the scale from the bulk alloy by segregation to the oxide scale grain boundaries, which decreases the growth rate of the scale by limiting the growth of the oxide layer by the inward oxygen transport [5, 12].

B. A. Pint [13], in 1995 proposed the Dynamic-Segregation theory to explain the RE effect. The RE effect is only observed once the initial transient stage of oxidation is reached where native oxides are formed. Rare earth ions diffuse into the oxide scale, which is formed as a result of the oxygen gradient present from the gas to oxide scale to alloy boundaries. Once at the alloy/scale boundary, the ions diffuse into the scale through the scale grain boundaries outwards up to a critical point. At this point two beneficial effects are observed:

- The RE ions diffuse more slowly than either Cr or Al cations, which in turn limits the inward diffusion of oxygen.
- The parabolic rate constant of oxidation is reduced and the solute-drag effect of the rare earth ions on the scale grain boundaries reduces the growth rate of the scale grains.

RE's such as yttrium cannot be added to a Fe rich melt as the two elements are immiscible.

2.2 Mechanical Alloying

Historical Background

In his quest to develop a Ni based superalloy for gas turbine applications at the International Nickel Company (INCO) John Benjamin [1] realised that the ball milling process used at the time to mix powder alloys was limited by the size of the starting powder particles. Coarse powder particles would not inter-diffuse sufficiently during consolidation. Benjamin realised that a high energy mill was

required to shorten the process time required and to produce homogenised powders by using a mixture of master powders and elemental powders without the need to use lubricants that could contaminate the powders.

In a conventional ball mill, steel balls in a horizontal drum would rotate and by a series of fracture and weld events, mixing of the powder components was achieved. This set up had its limitations because as the drum rotated faster to speed up the process the steel ball would rotate with the drum due to the centrifugal force. A vertical drum was used with an impeller that agitated the steel balls. This setup achieved the required results in a shorter time scale and mechanically alloying process was born [1, 14].

The first use of an inert dopant to improve high temperature mechanical properties was in 1910 by W.D. Coolidge [15] in thoriated tungsten. Benjamin used a mixture of yttria and thorium as dispersoids in a nickel alloy and concluded that yttria was just as effective as a dispersoid but crucially yttria was not radioactive, unlike thoria [2]. Today Y_2O_3 is widely used as the dispersoid in the production of ODS steels.

The Process Steps

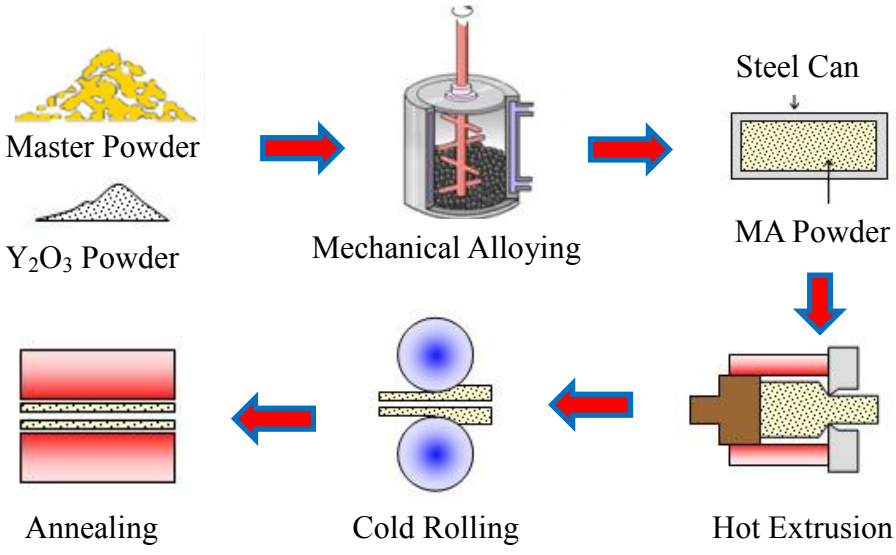

Figure 2.1 *A schematic of the process steps for ODS steels. [16]*

Powders to be milled are combined initially with Y_2O_3 before being introduced in the attritor for mechanical alloying. The milled powder is then degassed under a vacuum, and sealed in a steel can. Consolidation is by extrusion using Hot Isotropic Pressure (HIP) and a combination of either hot or cold rolling and an anneal process to the finished product. Each thermomechanical process will have an impact on the final microstructure so careful consideration is required in the design stage for the different parameters needed to achieve the desired microstructure [17].

The milling process is performed in a vertical stationary drum that is water cooled as illustrated in the schematic in Figure 2.1. A central rotating impeller agitates the steel ball bearings. Powder particles trapped between the steel balls are repeatedly deformed, cold welded, fractured and rewelded as illustrated in the schematic in Figure 2.2a.

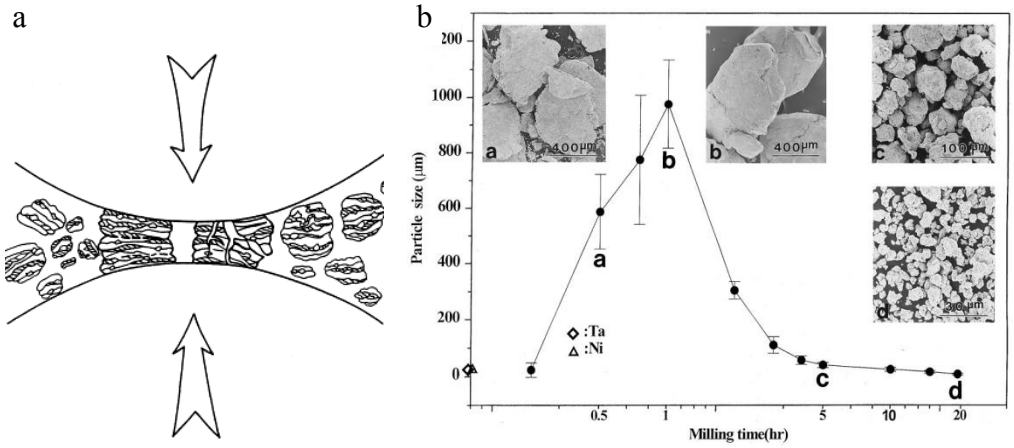

Figure 2.2 a) Schematic of the welding and fragmenting of powder particles trapped between the steel bearings and b) A graph of the average particle size with milling times. SEM images are shown at various stages of milling. Reproduced from [14].

Figure 2.2b shows a graph of the average powder particle size with milling time and SEM images of the particles at the different stages of milling as indicated on the graph [14].

Initially the size of the powder particles increases they are plastically deformed creating new surfaces and are welded together. As the milling time increases the

particles are cold worked and become more brittle and fragment, eventually decreasing in size. Steady state is reached when the powder particles are refined to a narrow size distribution. With the increase in deformation in the powder particles such as dislocations and other crystal defects, and the shorter distances for diffusion due to the lamella microstructure of the powder particles as seen in Figure 2.3 it becomes easier for the elemental powders and the oxide dispersoid to dissolve in the matrix that would otherwise be insoluble.

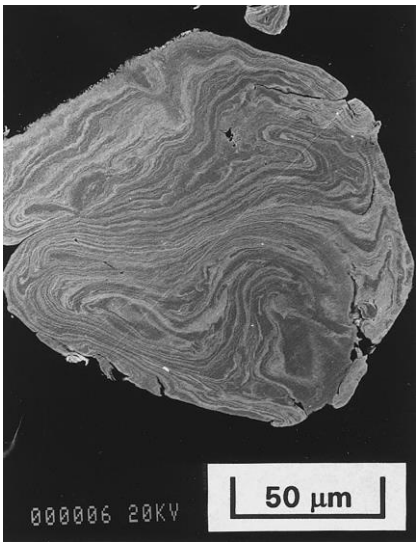

Figure 2.3 *SEM image of a milled powder particle showing the lamellar microstructure of a ductile-ductile component system (Cu Ag)[14].*

Important process parameters such as ball to powder weight ratio processing temperature, milling speed, milling atmosphere and the use of process control agents (PCA) are outside the scope of his thesis and are covered in detail in 'Mechanical Alloying and Milling' by Suryanarayana [14].

X ray diffraction studies on mechanically alloyed powders show that with increasing milling time the dispersoid oxide powder is steadily dissolved into the matrix. Dai et al [18] manually mixed 76%Wt Fe, 9%Wt Cr and 15%Wt Y_2O_3 powders before milling in a high energy planetary ball mill for different times. Figure 2.4a shows an XRD pattern of the as mixed powder, powder milled at 10 hours, 50 hours and 100 hours.

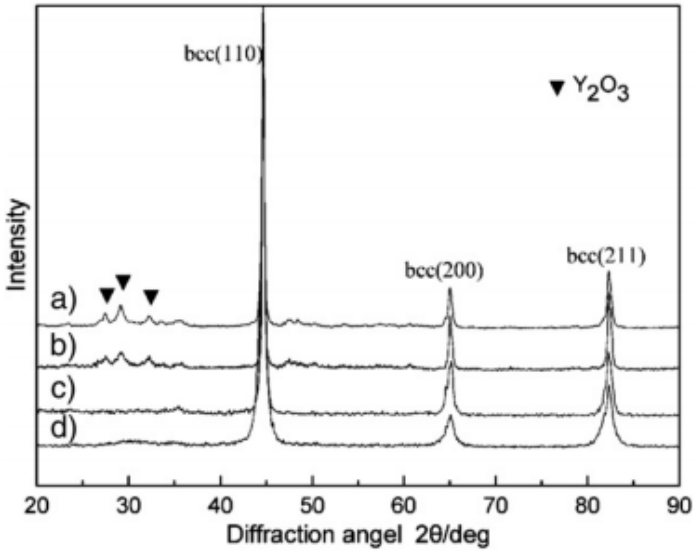

Figure 2.4 *X ray diffraction patterns of a 76%Wt Fe, 9%Wt Cr and 15%Wt Y_2O_3 composition, a) as mixed powder, b) after 10 hours, c) after 50 hours and d) after 100 hours of milling time [18].*

The intensity of Y_2O_3 diffraction peaks is steadily reduced with increased milling time. The broadening of the diffraction peaks is attributed to the smaller grain size of the particles as the milling is progressing and due to distortion of the lattice with time. So in effect the Y_2O_3 had been reduced to very small irregular arrangements of atoms of in the order of about 5nm within the matrix [18].

a

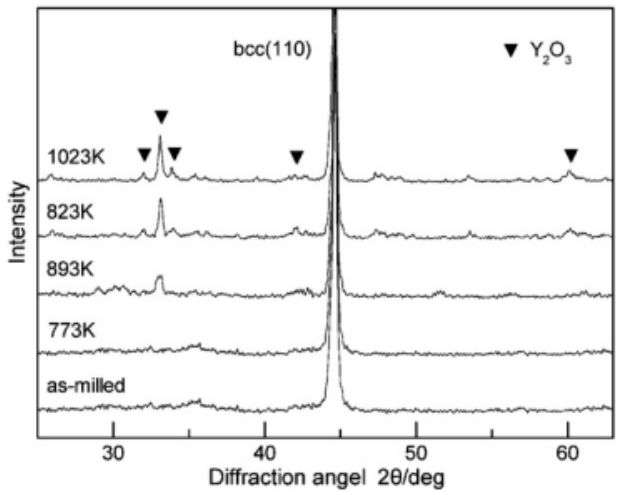

Figure 2.5 *X-ray diffraction patterns of a powder with composition of 76%Wt Fe, 9%Wt Cr and 15%Wt Y_2O_3 showing the increase in the diffraction peaks for Y_2O_3 with increasing annealing temperature [18].*

Dai et al also used X-ray diffraction analysis on a mechanically alloyed powder Fe Cr Y_2O_3 that has been annealed for one hour at different temperatures. The as milled powder was devoid of any peaks that would indicating the presence of Y_2O_3 but as the powder was annealed for 1 hour at temperatures from 500°C, 620°, 650°C and at 750°C progressively stronger diffraction peaks appear indicating the presence Y_2O_3. The higher temperatures have resulted in the growth of the Y_2O_3 particles.

Consolidation Process

A similar effect is observed during the consolidation of the mechanically alloyed powders using hot extrusion or a HIP process after degassing and canning in a steel can.

Dou et al [19] interestingly had studied the effects of the extrusion temperature on the size of the dispersoids in two identical alloy systems at two different extrusion temperatures. The %Wt composition of the alloys was Fe 15.5Cr 4Al 2W 0.1Ti $0.35Y_2O_3$ with alloy No1 extruded at 1050°C and alloy No2 extruded at 1150°C. Both alloys were heat treated after extrusion at 1050°C for 1 hour. The effect of the extrusion temperature on the particle distribution was significant in that alloy No 1 extruded at 1050°C had lower mean diameter particles, 3.21 nm compared to 6.68 nm for alloy No 2, and a higher number density of $9.28 \times 10^{22} m^{-3}$ compared to $1.72 \times 10^{22} m^{-3}$ for alloy No 2. The higher extrusion temperature had coarsened the dispersoid distribution. The link between the temperature of extrusion and number density of the dispersoid particles was reported by Hoelzer et al. [20] as well.

Summary

Mechanical alloying allows the mixing of dispersoids in alloys that would normally be insoluble [21]. Process parameters have an effect on the final powder morphology and need careful consideration. The extrusion temperature has an impact on the number density and the average size of the dispersoids in the matrix. Any additional thermomechanical processing steps after extrusion, such as hot rolling and annealing will have an effect on the particle distribution.

2.3 Gas Atomisation Process

An alternative process to mechanical alloying is the gas atomisation process as illustrated in Figure 2.6. This entails a chamber with the alloy melt that is atomised to produce alloy powder. This powder is essentially quenched as gas atomisation is a rapid cooling process. Inclusions are added to the smelt prior to the gas atomisation process which provide precipitation strengthening such as carbides and nitrides. The gas used is usually argon, nitrogen or helium.

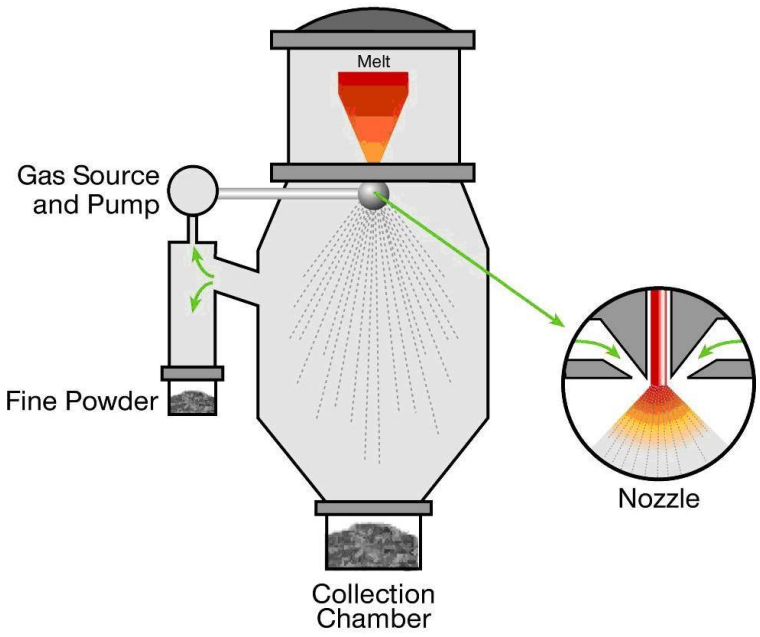

Figure 2.6 *A schematic showing details of the Gas Atomisation process [22].*

The specific details for the manufacture of APMT alloy used in this thesis was obtained from the Patent No US 6,761,751 [23] as details were not available from the manufacturer.

The main point taken from the patent application is that a FeCrAl melt is used with the addition of M, Ti, Y, Hf, Zr, N, and O. The addition of Ti is beneficial as it allows for the formation of Y, Ti oxides which tend to be small in size and therefore provide good strengthening properties but it was found that during the atomisation process, Ti would form nitrides and carbides at the nozzle and cause blockages that

resulted in the interruption of the production for the unblocking of the nozzles [23]. A way round this problem was the addition of up to 0.5% Ta and the reduction of Ti to below 0.1% which was sufficient to resolve the problem of clogging of the nozzles.

The consolidated alloy has therefore a complex particle distribution which includes yttrium oxides, aluminium oxides, yttrium aluminium oxides, carbides and nitrides of hafnium zirconium and tantalum.

To date no literature was available on the characterisation of the particles in APMT.

2.4 Deformation and Recrystallisation

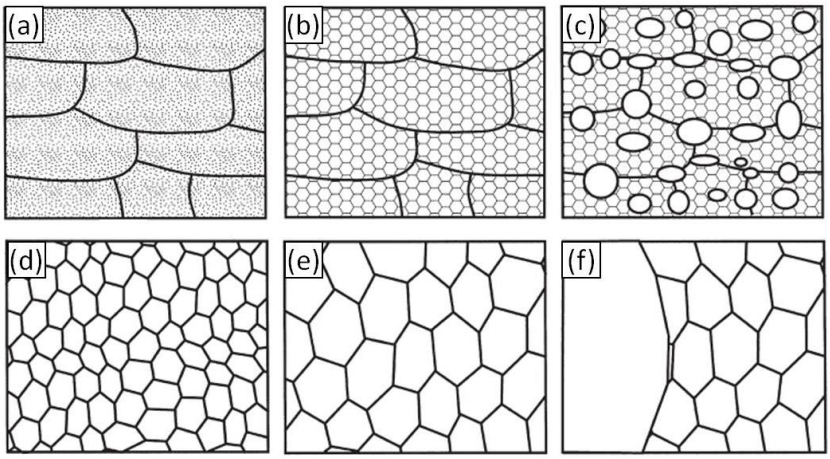

Figure 2.7 *Schematic of a) Deformed state, b) Recovered state, c) Partially Recrystallised, d) Fully Recrystallised e) Grain Growth and f) Abnormal Grain Growth reproduced from Recrystallisation and Related Annealing Phenomena [24].*

The plastic deformation of metals and alloys during processing introduces defects in the microstructure. These defects are in the form of dislocations, point imperfections and interfaces (Figure 2.7a). The application of sufficient heat can result in recovery, partial recrystallisation, full recrystallisation, grain growth and abnormal grain growth or secondary recrystallisation all of which depend on temperature and time, as shown in Figure 2.7 b to f.

The Deformed State

The free energy of a system that is deformed is increased and is thermodynamically unstable. Most of the energy expended to deform the metal is given off as heat but some of the energy used is stored in the metal mainly in the form of strain energy associated with dislocations [24, 25].

There are two types of dislocations. Edge dislocations and screw dislocations. In Figure 2.8, a schematic of the two types of dislocations are shown. In both types of dislocations the end result, in terms of crystal structure, is the same.

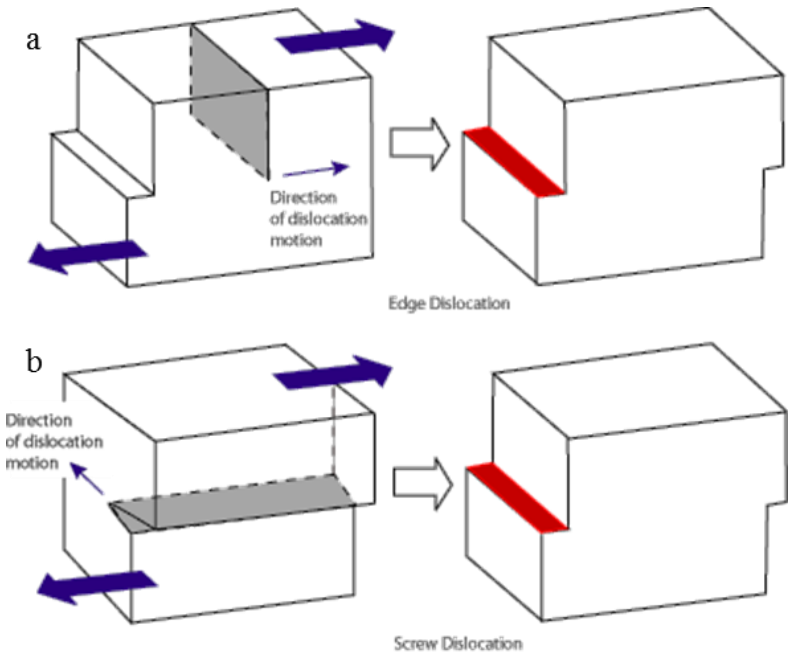

Figure 2.8 *Schematic showing a) an edge dislocation and b) a screw dislocation. Note that the end result is the same in both types of dislocations.[26]*

An edge dislocation is a linear imperfection which is defined by the edge of an extra half plane of atoms as illustrated in Figure 2.9. The edge dislocation line is perpendicular to the plane of atoms illustrated. The magnitude and direction of the dislocation is represented by the Burgess vector b which has the magnitude of a single atomic spacing. With edge dislocations the Burgess vector b is perpendicular to the dislocation line.

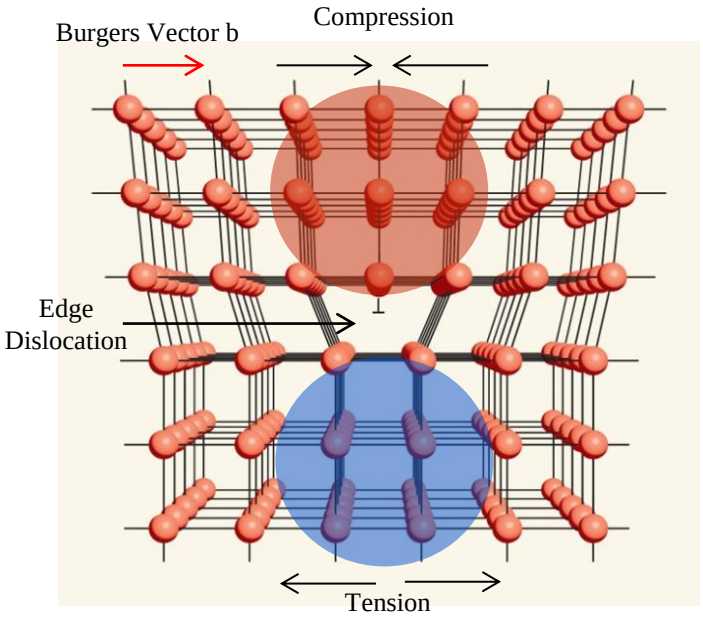

Figure 2.9 *A schematic showing the stress field above and below an edge dislocation. Adapted from [25].*

.

There is a strain field associated with the lattice dislocation as the extra half plane of atoms is causing a compressive field above the dislocation line and a tensile field below the dislocation line as illustrated in Figure 2.9. The amount of distortion decreases as the distance away from the dislocation increases.

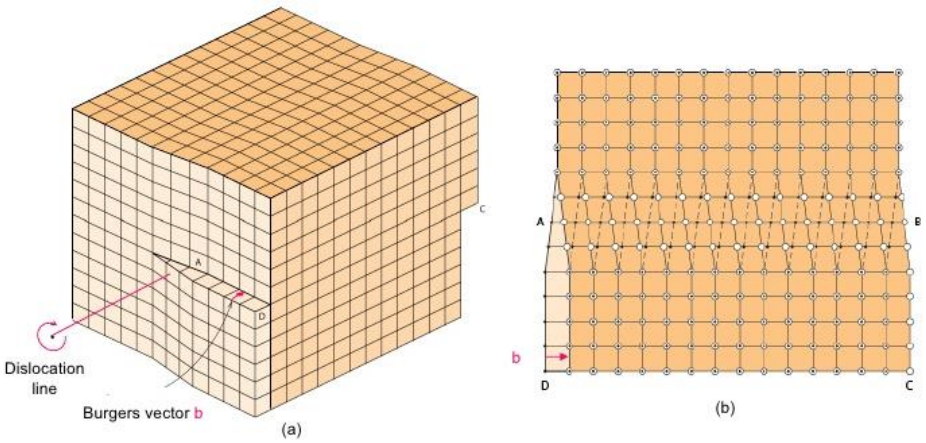

Figure 2.10 *A schematic showing a) a screw dislocation and the burgess vector b, and b) the dislocation line A-B. The dislocation line is parallel to the burgess vector b [25]*

A screw dislocation is caused by shear stress where a part of the lattice is shifted by a single atomic spacing, as illustrated in Figure 2.10a. With screw dislocations the burgess vector b is parallel to the dislocation line A-B shown in Figure 2.10b.

Most dislocations are mixed in nature as illustrated in Figure 2.11 where a dislocation line can have an edge, mixed and screw components to it. Throughout the dislocation line the Burgess vector remains constant at all points along its line [25, 27].

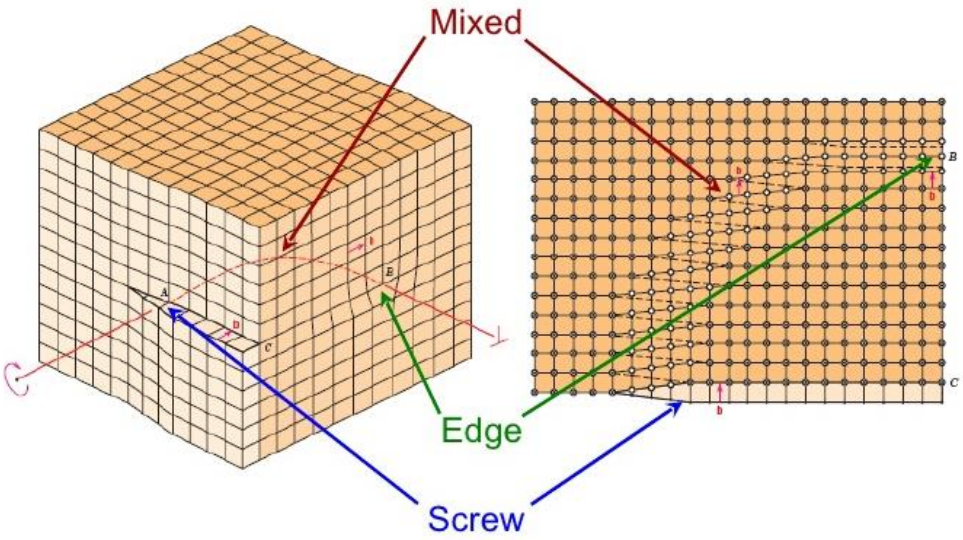

Figure 2.11 *A schematic of a dislocation line with edge, screw and mixed components along the dislocation line [25].*

Dislocation lines occur in preferred, closed pack planes and along close packed directions within the preferred planes. This is known as the slip system. For an FCC crystal dislocations occur along the <110> directions of the {111} planes giving rise to a possible 12 slip systems in total. For BCC crystals there are 3 preferred planes, {110}, {211} and the {321} all with the preferred direction of <111>. This gives rise to a possible 48 slip systems. Despite the fact that BCC crystals have more slip systems than FCC, the BCC crystal structure tend to be more brittle than FCC crystal structure especially at lower temperatures. This is because in FCC crystals, slip occurs more readily due to the close atomic packing of the slip planes. In BCC crystals, slip planes are lower in atomic density and do not slip as readily [28].

The energy of a dislocation line γ per unit length is proportional to the Burgess vector, b squared. Much less energy is required for the formation of dislocations along close packed directions as the magnitude of b is the interatomic spacing of the particular orientation in which a dislocation was formed [25, 27].

Increased deformation increases the dislocation density in a metal. The motion of dislocations becomes harder as the number of dislocations increase. The strain needed to further deform a metal increases. This increases the strength of the metal. This is the strain hardening effect also known as work hardening [25].

With medium to high Stacking Fault Energy (SFE) materials such as ferritic iron, with the application of strain, a number of sub-grain structures develop such as dislocation boundaries, deformation bands and shear bands [25]. With increasing strain the boundaries become more pronounced and the break-up of grains into regions of misorientated lattice arrangements with defined boundaries [29].

Manufacturing processes such as cold rolling and extrusion or HIP processes introduce deformation in the metal and subsequent annealing is needed to improve the ductility of the material.

Recovery

Recovery is the process by which some of the internal energy of a deformed material is relieved and the material is partially restored to its original state due to the enhanced diffusion of atoms at higher temperatures that reduce the number of dislocations. The driving force for recovery is the difference in free energy between the deformed state and the recovered state. Recovery has several stages as illustrated in Figure 2.12

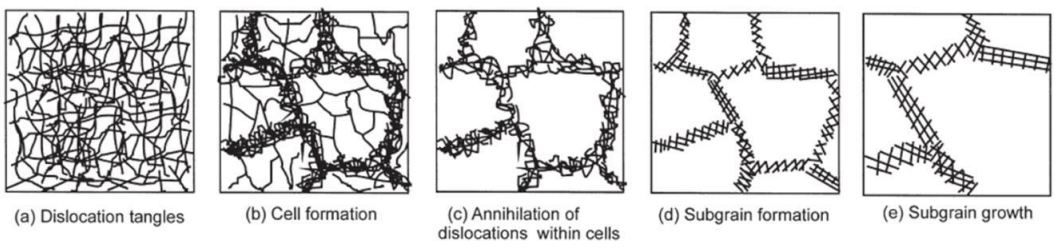

Figure 2.12 *The different stages of recovery of a deformed material [24].*

Recovery is the process that can precede recrystallisation. There is a gradual reduction in dislocation density and the segregation of dislocations to sub grain boundaries as illustrated in Figure 2.12 b-e. This is a gradual process and as sub grains form they can grow to low angle grain boundaries by the alignment of dislocations. The reduction in the free energy due to recovery also reduces the driving force for recrystallisation [24].

Recrystallisation

The onset of recrystallisation, also termed primary recrystallisation, is characterised by the formation of new strain free grains that nucleate within a deformed grain sub boundary that eventually consume all the deformed grain structure resulting in a near strain free grain structure [24, 30].

The recrystallisation temperature T_R is defined as the temperature at which a completely new strain free grain structure is obtained in 1 hour. The recrystallisation temperature is often written in terms of the melting temperature T_m with typical values of between $0.3T_m$ and $0.6T_{m.}$ During recrystallisation the mechanical properties of the pre strained microstructure is gradually restored. The recrystallised microstructure consists of grains with high angle boundaries and with a preferred texture which is different to the texture of the deformed state. The size of the recrystallised grains is being controlled by the number and distribution of nucleation sites.

Grain Growth

Once all of the previously deformed grains have been consumed during the recrystallisation process, strain free grains may continue to grow especially in pure metals. The driving force for grain growth is the reduction in grain boundary energy. Grains grow by the diffusion of atoms across the grain boundary [25]. This process requires the boundaries to be relatively unimpeded by precipitates and second phases as the driving force, which is the removal of grain boundaries, is much lower.

Dynamic Recrystallisation

This is a special case of recrystallisation that is observed when deformation is applied at a high temperature. Dynamic recrystallisation originates from high angle grain boundaries that spread out along the grain boundary until it has been consumed forming a 'necklace' structure as illustrated in Figure 2.13. Grains then grow and eventually a dynamically recrystallised grain structure replaces the previous grain structure [24].

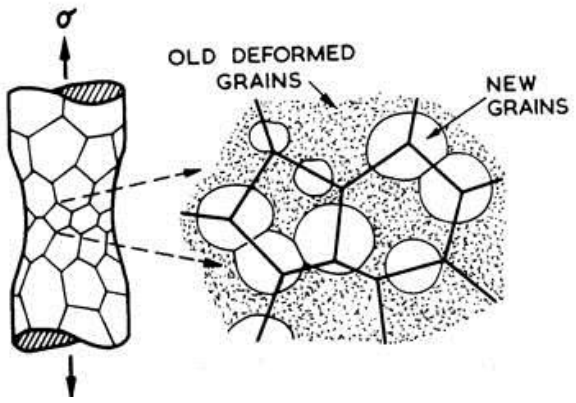

Figure 2.13 *A schematic showing the formation of dynamically recrystallised grains on the deformed grain boundary forming a 'necklace' structure[31].*

As deformation is applied, the dislocation density increases while dynamic recovery reduces the dislocation density. When dislocation density is too high, dynamic recrystallisation initiates. An amount of critical stress is needed for dynamic recrystallisation which corresponds to a maximum amount of energy that can be stored in the material. The onset of dynamic recrystallisation is characterised by the peak in the flow stress i.e. the true stress strain graph. Nucleation and growth of grains is taking place during the application of strain [30, 32, 33].

Secondary Recrystallisation

Also known as abnormal grain growth is the preferential growth of a few grains that grow to a very large size consuming the smaller recrystallised grain structure. This process is not fully understood yet and has been the subject of ongoing research for

many years. The incidence of a recrystallised grain that grows abnormally is about one in a million [30]. In an adaptation of the particle coarsening theory by Lifshitzs and Slyozov [34] and by Wagner [35] known as the LSW theory, to investigate grain growth, Thompson et al. [36] has concluded that in the absence of any other contributions to grain growth other than grain boundary energy, larger grains do not grow at a relative higher rate than their smaller counterparts. In other words the pre-existence of a size advantage does not result in a breakaway large grain size. Indeed a large initial grain relative to the surrounding grains will grow more slowly. Therefore abnormal growth should only occur when normal grain growth is inhibited.

It has been theorised and subsequently confirmed [30, 37, 38] that the source of the secondary recrystallised grains are sub grain structures with a high misorientation angle relative to nearby regions as regions of low angle misorientation do not have the necessary mobility required to form new recrystallised grains. There is a large difference in mobility of 100-1000 times between low angle (2^{o}-5^{o}) and large angle ($>15^{o}$) grain boundaries [24].

These regions include high angle transition bands within grains due different lattice rotations and deformation zones of high misorientation around large particles.

Second phase particles, texture and strain are known to have an inhibitive effect on the abnormal grain growth of materials [24] and as the alloys considered in this work contain high concentrations of precipitates it would seem unlikely that secondary recrystallisation would occur, even though this mechanism is used by some researchers to explain observed microstructures.

2.5 Recrystallisation Behaviour of ODS Steels

The recrystallisation of ODS steels with the fine distribution of second phase particles and with a strong texture induced by the extrusion process and the rolling process has been investigated by many authors [39-44]. The fine grain structure, typical of ODS alloys, the alignment of the particle distribution and any strain

introduced before recrystallisation are factors which influence the recrystallisation behaviour of ODS steels.

Grain Structure

ODS steels recrystallise at a much higher temperature than their non-ODS counterparts. Typically ODS steels will recrystallise at $0.9T_m$. This has been attributed to the sub-micron grain size. Recrystallisation involves the bowing out of grain boundaries as illustrated in Figure 2.14. Due to the smaller grains the grain boundary junctions act as pinning points which restrict the bowing of the grain boundaries increasing the activation energy required for recrystallisation [41, 45].

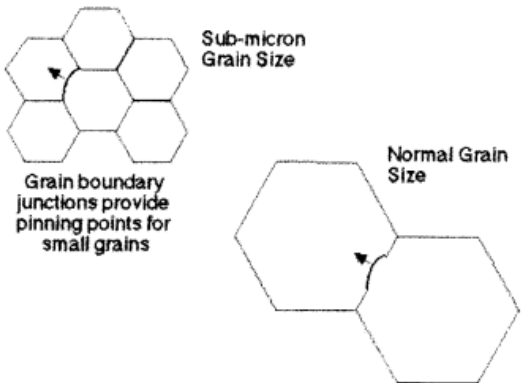

Figure 2.14 *Bulging of grains is restricted by the grain boundary junctions in ODS steels due to the sub-micron grain structure [41].*

Pre-annealing of ODS steels prior to recrystallisation increases the grain size which in turn reduces the pinning effect of the grain boundary junctions therefore reducing the recrystallisation temperature. As the pre-annealing time is increased there is a reduction in the driving force of recrystallisation which increases the recrystallisation temperature required. This produces a minima in the graph of recrystallisation temperature versus the size of the unrecrystallised grains as presented by Sha al. [39] on experiments performed on a nickel ODS steel MA 760 (see Figure 2.15).

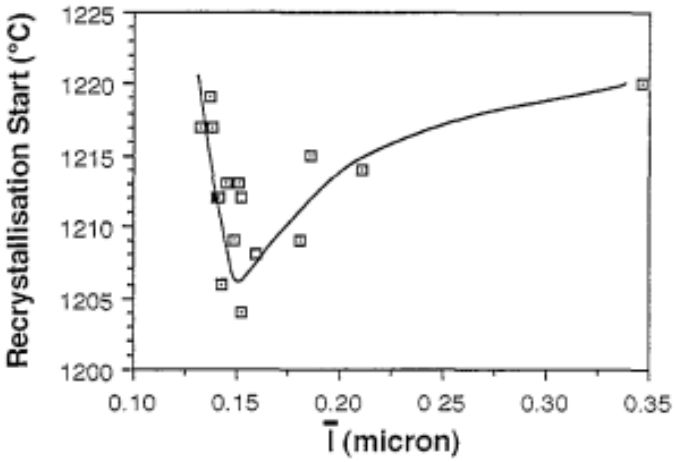

Figure 2.15 *Graph of recrystallisation start temperature versus unrecrystallised grain size for a nickel ODS alloy MA760 [39].*

Particle Alignment

The grain structure of secondary recrystallised ODS steels tend to be columnar. This is attributed to the alignment of the nanoparticles along the extrusion direction. Capdevila et al. [40] concluded that recrystallised grains propagate by a ledge mechanism as illustrated in Figure 2.16. The boundary velocity along the extrusion direction is much faster, as there is less resistance from the particle alignment, which results in the elongation of the recrystallised grains.

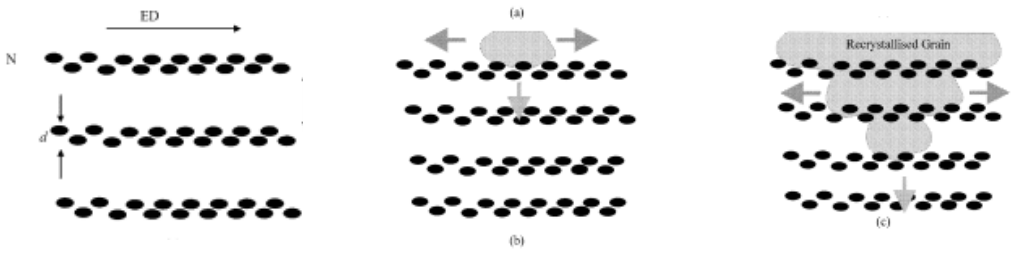

Figure 2.16 *The recrystallised grain boundary propagation through an array of nanoparticles showing the elongation of the grains along the extrusion direction [40].*

Effects of Strain on Recrystallisation

Recrystallisation requires a minimum amount of strain which provides the stored energy that is required for the nucleation event for recrystallisation [24]. In a classic paper by Reggle et al. [46] the recrystallisation temperature of MA956 and MA957 was reduced when the amount of deformation was increased. This is consistent with the increased stored energy increasing the driving force for recrystallisation therefore the nucleation of recrystallisation can occur at lower temperatures.

It is generally accepted that recrystallisation originates from a highly deformed sub-grain region with a high misorientation angle with regards to the surrounding deformed regions as only these regions have the necessary mobility for recrystallisation [30]. The application of a lower, uniform strain results in fewer nucleation sites which upon the onset of recrystallisation, a coarse grain structure is obtained. The application of a high strain process such as cold rolling with a high reduction introduces many nucleation sites which results in a finer recrystallised microstructure. Therefore the size and distribution of the recrystallised grains is determined by the number and distribution of the nucleation sites.

The effects of compressive and tensile strain on bent bars of ODS PM2000 alloy with different degrees of deformation i.e. amount of bending were analysed by Capdevila et al. [44]. Bending introduces varying degrees of both compressive and tensile strain. A central region of unrecrystallised grains was linked to the neutral axis, and with areas above and below undergoing recrystallisation. A variation in the recrystallised grain size was attributed to the amount of strain gradient so that in order to achieve recrystallisation with a large grain structure, the amount of strain has to be fairly uniform and minimised so as to limit the number of nucleation sites.

Recrystallisation and Texture

Texture is a non-random crystallographic alignment of grains with reference to a specified processing direction normally the rolling or extrusion direction. A strong texture denotes a high number of grains orientated in a certain way. The main textures with regards to MA ODS steels are the {001} <110> also known as α fibre and the {111} $<\bar{1}10>$ also known as the γ fibre in crystal orientation distribution

space. The stored energy in an alloy varies with texture and therefore influences the recrystallisation temperature [47].

PM2000 has a strong α fibre component. That means that the plane parallel to the surface of the plate is {001} and the direction <110> of the plane is along the rolling direction [33, 48]. There are also weaker textures observed by Mathon et al. of {111}<1$\bar{2}$1> and {221} <1$\bar{1}$0> which are characteristic of cold rolling texture in bcc materials [49]. After the FSW process the texture is weak with no particular orientation favoured as this region undergoes dynamic recrystallisation.

2.6 Strengthening Mechanisms

Several strengthening techniques are available to enhance the performance of metals and alloys. All the methods employed have an effect on the mobility of dislocations through the matrix which affects the ability of a metal or alloy to plastically deform. Any strengthening used will involve a trade off in terms of ductility as the ability of a metal to plastically deform is reduced [25].

Solid Solution Strengthening

The alloying of pure metals always increases their strength. An impurity atom can be is in a solid solution with a pure metal either in a substitutional site or interstitial site depending on the relative difference in atomic sizes between the impurity atom and the host atom. A substitutional impurity atom creates lattice distortion which restricts dislocation motion. Impurity atoms tend to diffuse and segregate at dislocation sites as they can reduce the overall strain energy of the lattice as illustrated in Figure 2.17.

Interstitial impurity atoms such as carbon and boron tend to be small in atomic size as they occupy the gaps between the larger host atoms. They too restrict dislocation motion and therefore increase the strength of the pure metal. Alloying elements are generally not chosen purely on their solid solution strengthening as other considerations such as oxidation and corrosion resistance will dictate the material chosen but solid solution strengthening is an additional benefit in any case.

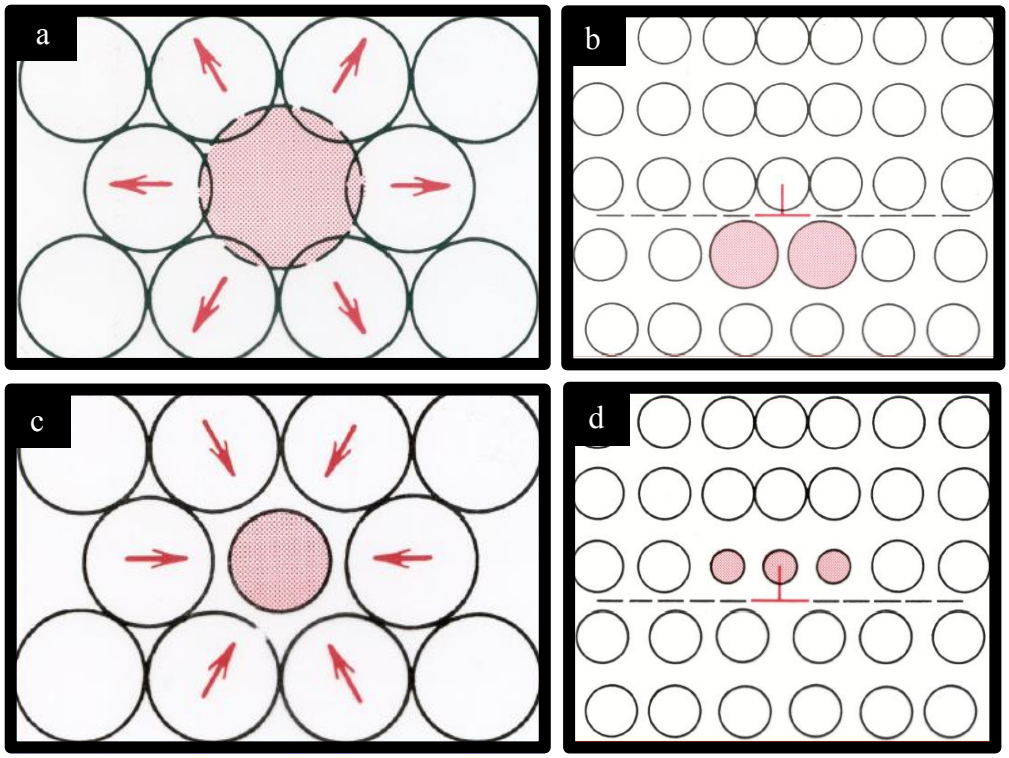

Figure 2.17 *A Schematic of the effect of an impurity atom in a matrix with a) a larger impurity atom in a matrix, b) its position in an edge dislocation, c) a smaller impurity atom in a matrix and d) its position in an edge dislocation [25].*

Grain Size Strengthening

Grains generally have a different orientation to their neighbours and are separated by grain boundaries which act as a barrier to dislocation movement for temperatures up to $T<0.5T_m$. A low angle grain boundary is not very effective in hindering dislocation motion. Dislocations pile up against a high angle grain boundary. The stress concentration at the high angle grain boundary may trigger new dislocations in the adjacent grain [25]. Decreasing the grain size increases the strength of a material. The Hall-Petch relationship describes the yield strength σ_y in terms of the grain size as follows:

$$\sigma_y = \sigma_0 + k{d_G}^{-1/2} \qquad \textit{(Equation 2.1)}$$

where σ_0 and k are material constants and d_G is the mean grain diameter. This relationship has been found to hold for grain sizes up to sub-micron range [50, 51].

At higher temperatures of T >0.5$T_{m,}$ a small grain size actually weakens the material as discussed in the section on Creep Strength (Chapter 2.8).

Strain Hardening

As a material is plastically deformed it becomes harder. The dislocation density of a metal increases with increasing strain due to dislocation multiplication and to new dislocations. This is also known as cold working and is measured in terms of % CW (cold worked) which is defined by:

$$\%CW = (\frac{A_0 - A_d}{A_0}) \times 100 \qquad \textit{(Equation 2.2)}$$

where A_0 is the original cross sectional area and A_d is the cross sectional area after deformation. With rolled plates as the width of the plate is kept constant the thickness of the plate is used instead.

Strain hardening is used along with annealing processes, which increase ductility by way of recovery, to obtain the required balance between strength and ductility characteristics in metals during fabrication [25].

2.7 Second Phase Particles

A distribution of second phase particles in an alloy has an effect on the mechanical properties, on the grain morphology and on the recrystallisation behaviour of the alloy. The fine dispersion of a second phase is chosen so that the strengthening is maintained even at high temperatures. For this reason second phase particles of inert oxides are ideal as they are stable above 2000°C [52]. The main advantage of these oxides is that they do not dissolve back into solution and do not coarsen to the same extent with increased temperatures unlike precipitation hardened alternatives [24].

The increased strengthening from second phase particles is from the pinning effect of the particles to grain boundary movement and to dislocation movement. Both these effects are discussed further.

Second Phase Particles and Grain Boundary Interactions

Figure 2.18 shows a particle pinning a grain boundary. When a boundary approaches an incoherent spherical particle the pinning force is given by [24]:

$$F = 2\pi r_p \gamma_{GB} cos\beta sin\beta \qquad \textit{(Equation 2.3)}$$

where r_p is the particle radius, γ_{GB} is the boundary energy per unit length and β is the angle as indicated in Figure 2.8.

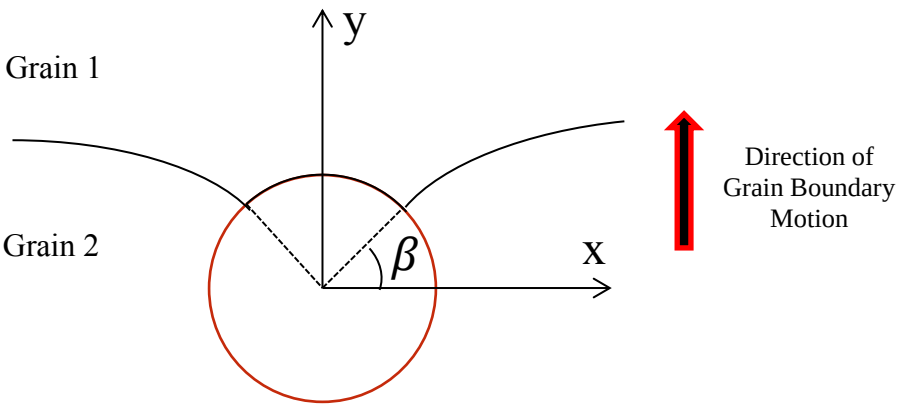

Figure 2.18 *The interaction between a grain boundary and an incoherent spherical particle.*

The maximum pinning force is obtained when $\beta = 45°$ where

$$F_{Max} = \pi r_p \gamma_{GB} \qquad \textit{(Equation 2.4)}$$

In effect a part of boundary is removed by the particle lowering the energy of the system [53, 54]. In the case of a high angle grain boundary moving past a coherent particle more energy is required for the particle to lose coherency which must be provided by the moving grain boundary. The maximum force exerted by the particle on the grain boundary is given by [24]:

$$F_{Max} = 2\pi r_p \gamma_{GB} \qquad \textit{(Equation 2.5)}$$

Where F_{Max} is the maximum force exerted by the particle at a point when it is enveloped by the grain boundary [53]. A full derivation of the equation can be found

on page 111 in *´Recrystallization and Related Annealing Phenomena´[24]* This is twice the force exerted by an incoherent particle.

A coherent particle interacting with a high angle grain boundary results in the loss of coherency with the matrix. The particle may dissolve during the passage of the boundary and precipitate in the new boundary as a coherent particle or it may orientate itself to a coherent orientation [24, 55].

Pinning Force from a Distribution of Particles

For a volume fraction F_v of spherical particles in a random distribution with a mean radius r_m then the number of particles in a unit volume N_v is given by [24]

$$N_v = \frac{3F_v}{4\pi r_m^3} \qquad \textit{(Equation 2.6)}$$

The number of particles interacting with a unit area of grain boundary a distance r_m either side N_s is given by:

$$N_s = 2rN_v = \frac{3\gamma_{GB}F_v}{2\pi r_m^2} \qquad \textit{(Equation 2.7)}$$

The pinning pressure exerted on a unit area of the boundary is given by:

$$P_z = N_s F_{max} \qquad \textit{(Equation 2.8)}$$

Combining Equation 2.4 and 2.7 and assuming all the particles interacting with the grain boundary exert maximum force ($\beta = 45^0$), the pinning pressure P_z known as the Zener pinning force is given by:

$$P_z = \frac{3F_v\gamma_{GB}}{2r_m} \qquad \textit{(Equation 2.9)}$$

This equation holds reasonably well if the grain size is much larger than the interparticle spacing [24].

Second Phase Particles and Dislocation Interactions

When a dislocation encounters an array of particles two possible outcomes are likely. If the particle is coherent and weak the dislocation will shear and pass through the particle and if the particle is incoherent and strong the dislocation will bypass the particle by bowing and then forming an Orowan loop around it.

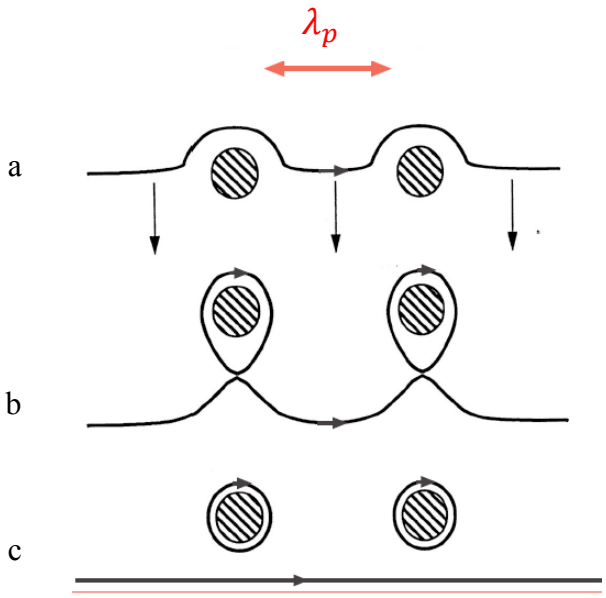

Figure 2.19 *A dislocation moving towards an array of non-deformable particles.*

A schematic of a dislocation approaching an array of non-deformable particles is shown in Figure 2.19. As a dislocation line approaches the bowing of the dislocation line is observed. As the dislocation advances a loop is formed around the particle and the dislocation line is able to move beyond the array of particles. The force exerted by the dislocation line between a pair of particles is given by:

$$F_p = \tau_p b \lambda_p \qquad \textit{(Equation 2.10)}$$

where τ_p is the applied stress, b is the Burgess vector and λ_p is the interparticle spacing.

A dislocation loop around a non-deformable particle will exert a shear force on the particle which is given approximately by:

$$\tau_p = \frac{Gb}{2r} \qquad \textit{(Equation 2.11)}$$

Coarsening of Second Phase Particles

Consider a solution of a small volume fraction second phase particles in a matrix. Second phase particles nucleate at different times which give rise to a size distribution. The concentration of the elements of the second phase at the interface between a large particle and the matrix is lower than the concentration of the elements of the second phase at the interphase between a smaller particle and the matrix. This is known as the Gibbs Thompson effect. This gives rise to a concentration gradient and larger particles will coarsen with time at the expense of smaller particles. This is known as Ostwald Ripening. This is a diffusion led process and as the larger particles coarsen there is a reduction in the free energy of the system as larger particles reduce the overall interfacial energy of the system.

The LSW theory named after Lifshitz, Slyozov and Wagner [34, 35] predicts the coarsening rate of a second phase particle with time which is given by:

$$r_p{}^3 - r_0{}^3 = \frac{8\gamma_{m/p} v^\beta D}{9RT} t \qquad \textit{(Equation 2.12)}$$

where r_p is the radius of the particle after a time t, r_0 is the initial particle radius, $\gamma_{m/p}$ is the interfacial energy between the matrix and the particle, v^β is the mole fraction of the second phase, D is the diffusion coefficient, R is the gas constant and T is the absolute temperature. One of the concepts introduced by the LSW theory is that of particle encounters where if the distance between any two particles is less than their mean diameter then the two particles unite or undergo a diffusion interaction. The volume of the two particles is mostly conserved as some of the second phase may go back into solution.

Particle Coherency

A particle is said to be coherent with the matrix when the lattice arrangement of the atoms of both the particle and the matrix match and are continuous across the

interface. In some cases the lattice spacing of a particle may be strained in order to maintain coherency [56].

In Figure 2.20 the interface between two different crystal lattices are illustrated showing a) a coherent interface, b) a coherent interface with lattice strain, c) a semi coherent interface with a number of misfit dislocations along the interface and d) an incoherent interface which is not energetically favourable.

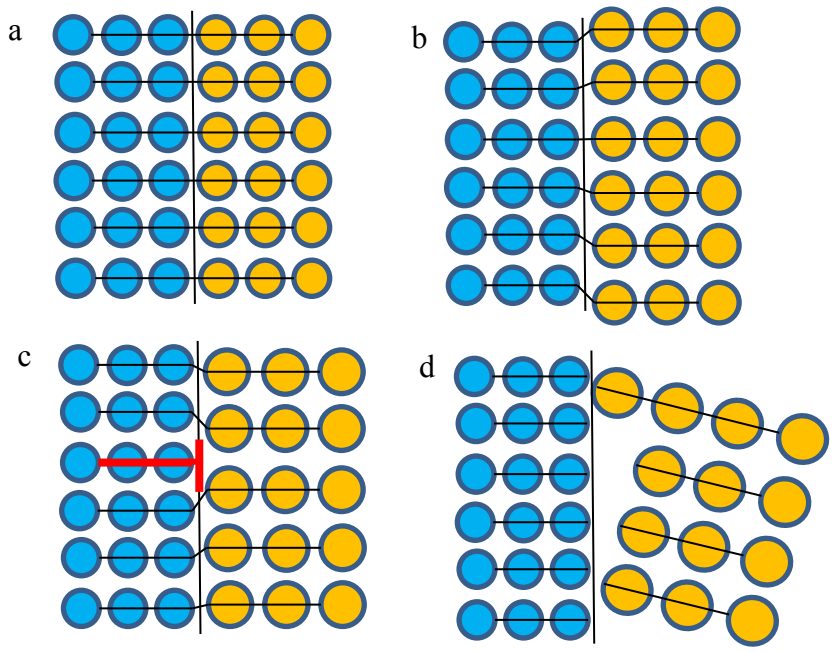

Figure 2.20 *A schematic showing the lattice arrangement of two different crystals with a) a coherent interface, b) coherent interface with lattice strain, c) semi coherent interface with a misfit dislocation and d) an incoherent interface (Author's own illustration).*

In both dispersion strengthened and precipitation strengthened materials small particles tend to be coherent. This is due to the homogeneous precipitation or nucleation of the particles from the solution with the matrix. As the particles coarsen they become semi coherent up to a critical size when coherency is lost [56]. For the case of very small spherical particle in a matrix that is coherent with a lattice strain, there is a strain field around the particle as illustrated in Figure 2.21.

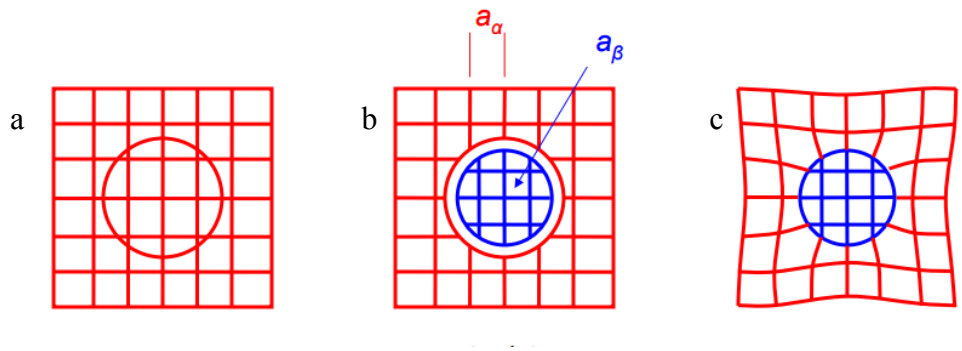

Figure 2.21 *Schematic of a) a coherent particle, b) particle in the matrix with an unconstrained misfit and c) a coherent particle with a constrained misfit [56].*

The lattice of the precipitate distorts so that coherency is maintained. If the lattice parameters of the matrix and the unstrained particle are α_α and α_β respectively then the unconstrained misfit δ is given by:

$$\delta = \frac{\alpha_\beta - \alpha_\alpha}{\alpha_\alpha} \qquad \textit{(Equation 2.13)}$$

The misfit of a coherent particle with a constrained misfit δ_ε is given by:

$$\delta_\varepsilon = \frac{\acute{\alpha}_\beta - \alpha_\alpha}{\alpha_\alpha} \qquad \textit{(Equation 2.14)}$$

where $\acute{\alpha}_\beta$ is the distorted lattice parameter of the particle which is uniform in all directions. In practice δ_ε usually lies between 0.5 δ and δ [56].

A semi coherent particle (Figure 2.22a) which has some lattice planes line up and misfit dislocation can still have a lattice strain field whereas an incoherent particle (Figure 2.22b) in a matrix has little or no lattice strain although if an incoherent particle is the wrong size for the space it occupies then misfit strain can still be present [56].

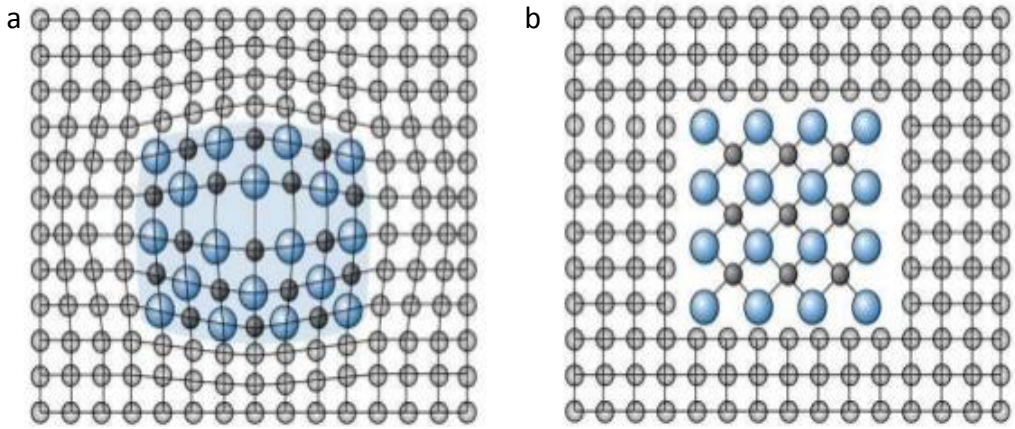

Figure 2.22 *A schematic of a) a semi coherent particle and b) an incoherent particle in a matrix. Image adapted from [57]*

2.8 Y-Al-O Dispersoids in PM2000

PM2000 is a FeCrAl ODS alloy that was commercially produced by Plansee™ using the mechanical alloying process. The yttrium oxide dispersoid in the matrix when consolidated reacts with the aluminium present in the alloy powder to form several types of yttrium aluminium oxides [58, 59]. The phases are listed in Table 2.1.

Table 2.1 *List of the different phases of yttrium aluminium oxide [60].*

Yttrium Aluminium	Acronym	Formula	Crystal Structure
Garnet	YAG	$Y_3Al_5O_{12}$	Cubic
Perovskite	YAP	$YAlO_3$	Orthorhombic
Perovskite	YAP'	$YAlO_3$	Cubic
Monoclinic	YAM	$Y_4Al_2O_9$	Monoclinic
Hexagonal	YAH	$YAlO_3$	Hexagonal

Several researchers have characterised the particles in terms of their particle size their volume fraction and their crystal structures. Klimiankou et al. [58] studied the dispersoids in PM2000 using TEM analysis. Dispersoids were found to be uniformly

distributed throughout the matrix with the majority of the particles of 8-10 nm in diameter. A number of particles were analysed using HRTEM with EDX analysis and EFTEM (Energy Filtered TEM) techniques that revealed the presence of YAG, and YAP and several large inclusions of γ-Al_2O_3. Multiphase particles were also observed with γ-Al_2O_3/Y-Al-O and Ti(C,N) particles as well. No ODS particles containing Ti were observed.

Capdevila et al. [61] reported an average particle size of 19nm. Particles coarsened to 89nm with annealing at a temperature of 1350°C for 3 hours with particles at the grain boundaries coarsening more than the intra granular particles. Once again the finer particles were observed to be YAG, YAP and YAH phase Y Al oxides with coarser particles of α-Al_2O_3 Ti(C,N) observed. No Ti was observed in any ODS particle.

More recently Shen et al. [62] has reported the presence of YAG and YAP phases in PM2000 but found no evidence of YAG, YAM or YAH phases. Also no Ti(C,N) particles were observed. Additional phases observed that were not reported previously were Al-Fe-O type particles, namely $Al_2Fe_2O_6$ (orthorhombic), Al_3FeO_6 (cubic) and $Al_3Ti_5O_{12}$ were identified using TEM studies with SAD patterns.

Clearly there are a number of different particles that have been observed in PM2000 due to the complex reactions that take place during the consolidation process. Different particles will have different coarsening rates which will depend on which of the particles is thermodynamically more stable at any particular set of conditions.

2.9 Creep Strength

Creep strength is the ability of an alloy to resist strain under a constant stress that is applied over time at high temperatures [63]. Different creep mechanisms are involved depending on the homologous temperature, which is expressed in terms of the absolute melting temperature T_m. At low temperatures the mechanism for creep is mainly dislocation glide. As the temperature increases other mechanisms come into play.

The main processes in creep are:

1. The glide of dislocations leading to slip
2. The climb of dislocation leading to sub grain formation
3. The sliding of grain boundaries, and
4. The diffusion of vacancies.

The mechanism that is dominant depends on the temperature and stress applied and several mechanisms can contribute to the total creep [64]. Low temperature creep up to $0.3T_m$ is called logarithmic creep and is given by:

$$\varepsilon = \varepsilon_e + a \ln(1 + bt) \qquad \textit{(Equation 2.14)}$$

Where is ε_e the initial creep, and a , b are constants, and t is time.

Intermediate temperature creep is at temperatures of $0.3T_m < T < 0.5T_m$ and is given by:

$$\varepsilon = \varepsilon_e + ct^n \qquad \textit{(Equation 2.15)}$$

where c is a constant and generally $n \approx 3$. This is called parabolic creep or transient creep.

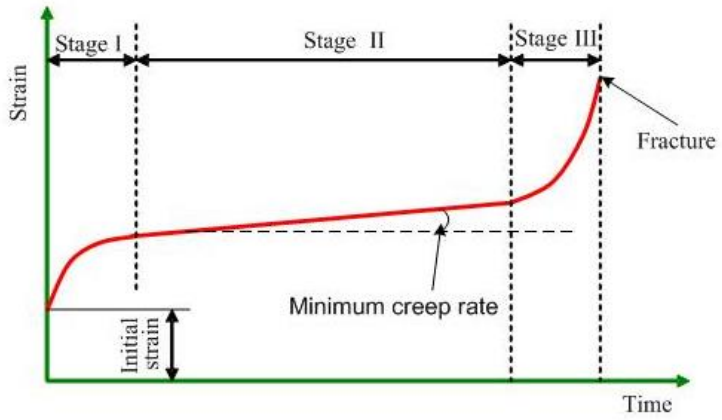

Figure 2.23 *A typical stress time graph showing the 3 stages of creep. Image adapted from [65]*

High temperature creep where $T > 0.5\ T_m$ a typical curve consists of three distinct stages as shown in the graph of stress versus time in Figure 2.23.

1. Primary
2. Secondary or Steady – State
3. Tertiary. This leads to rapture. Requires high T and σ.

Steady state creep rate is given by [63]:

$$\frac{d\varepsilon}{dt} = Cexp(-\frac{Q}{RT}) \qquad \textit{(Equation 2.16)}$$

C = creep constant, and Q (activation energy) depend on the material.

At very high temperatures (T/Tm) diffusion creep is the main mechanism which involves bulk diffusion of vacancies and interstitials through a grain under an applied stress known as Nabarro-Herring creep. As temperature increases ($T > 0.5T_m$) creep rate is given by:

$$\frac{d\varepsilon}{dt} = A\left(\frac{\sigma}{d^2}\right) exp - Q/RT \qquad \textit{(Equation 2.17)}$$

In this equation d_G is the mean diameter of the grains in a given material. At these high temperatures larger grains improve creep strength as creep rate:

$$d\varepsilon/dt \propto 1/{d_G}^2 \qquad \textit{(Equation 2.18)}$$

At lower temperatures (T/T_m) Coble creep is dominant as diffusion along grain boundaries is faster.

A deformation map of the normalised stress over the homologous temperature is useful as it shows the dominant mechanism for a given stress and temperature. One such map is shown in Figure 2.24 for Fe8Cr2WVTa steel [66].

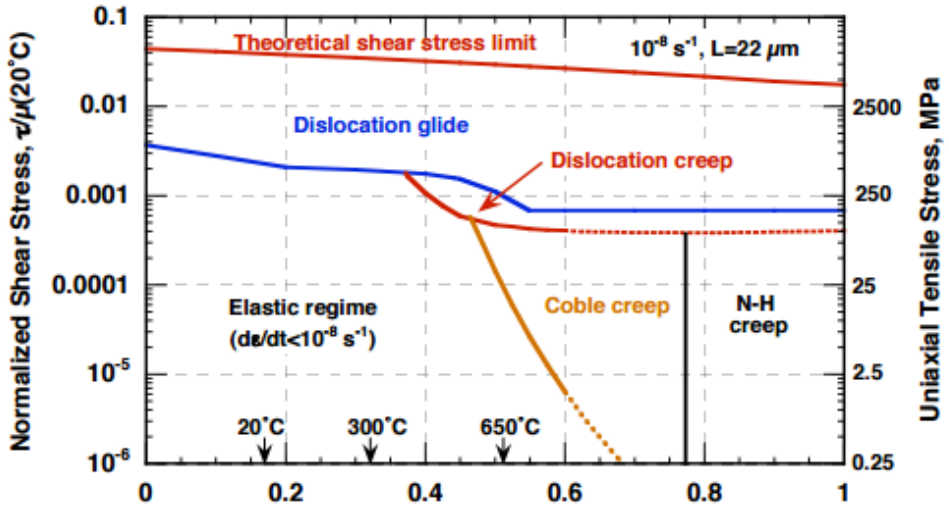

Figure 2.24 *Deformation mechanism map for a Fe8Cr2WVTa steel at a strain rate of $10^{-8}s^{-1}$ [66].*

The formation of large grains in ODS steels is paramount to improve the creep resistance at the high temperatures (high T/Tm), for applications in which ODS steels are being considered. This is reported by some researchers to be secondary recrystallisation (see section 2.4).

2.10 Joining of ODS steels

The joining of ODS steels is a major technological bottleneck to the widespread use of ODS steels [67]. Any welding method that produces a melt pool causes the agglomeration of the nanoparticles and they slag off to the surface. The excessive heat causes oxide coalescence so the dispersoid is no longer effective in pinning dislocations and grain boundaries [68].

Joining techniques such as fusion welding which require a heat source and a filler material are therefore not suitable to be used for the joining of ODS steels. This type of welding includes methods such as Tungsten Inert Gas (TIG) welding and Metal Inert Gas (MIG) welding.

Laser welding has been investigated and compared to TIG welding of PM2000 by Molian et al. [68]. As expected the TIG welding of PM2000 had resulted in the

agglomeration of the dispersoid to the surface leaving the weld zone weaker than the parent region. The laser welding performed better in that the dispersoid was still present in the weld zone but the particle size was in the order of 100nm to 400nm. Extensive coarsening and a degree of agglomeration had increased the particle size substantially in the weld zone.

Solid state joining techniques, by definition, do not use a melt pool which helps in preserving the dispersoid distribution in the weld zone. Such welding techniques include Resistance Pressure Welding (RPW), Diffusion bonding and Transient Liquid-Phase bonding (TLP). Some success was achieved with these joining techniques on ODS steels details of which can be found in references [69-71].

Another solid state joining technique called Friction Stir Welding (FSW) is the subject of this thesis.

2.11 Friction Stir Welding

This relatively new solid state welding technique was invented by Wayne Thomas from The Welding Institute (TWI) in 1991[72].

FSW is a joining technique that uses friction from the rotating shoulder to plasticise, and a tool pin which is plunged into the plates to be joined. The plates are stirred together to form a join. The advantage of FSW is that the nanoparticles present in ODS alloys are left largely intact because melting does not take place at any time during the process.

FSW has been used extensively with aluminium alloys for many years. Due to the success in the FSW of aluminium, focus of attention turned on the FSW of other metals such as titanium magnesium nickel copper and steels. There was also the prospect of dissimilar metal FSW as the process resulted in a minimal amount of mixing between the two dissimilar metals and therefore minimising the solid state reaction between two possibly incompatible metals [73]. The FSW of steels was challenging due to the strength of the material compared to aluminium and was only

possible due to the development of tools sufficiently strong enough to withstand the stresses of welding steels.

The FSW Process

A schematic of the FSW process is illustrated in Figure 2.25a. The two plates to be joined are aligned and clamped into position. The rotating tool is plunged into the plates to be joined for a certain amount of time until the material is plasticised enough for the tool to start moving along the weld line. Once the end of the weld line is reached, the tool still which is still rotating, is slowly withdrawn from the plates. After the plates are left to cool they are removed from the clamps.

The cross section of the weld can be asymmetrical due to the difference of the rotation of the tool either side of the weld as illustrated in Figure 2.25b. The advancing side is the side that both the rotation of the tool is in the same direction as the toll travel line. The retreating side is when the rotation of the tool is in the opposite direction to the tool travel line. Material is sheared away from the advancing side of the weld and redeposited behind the tool as is moves along the weld line.

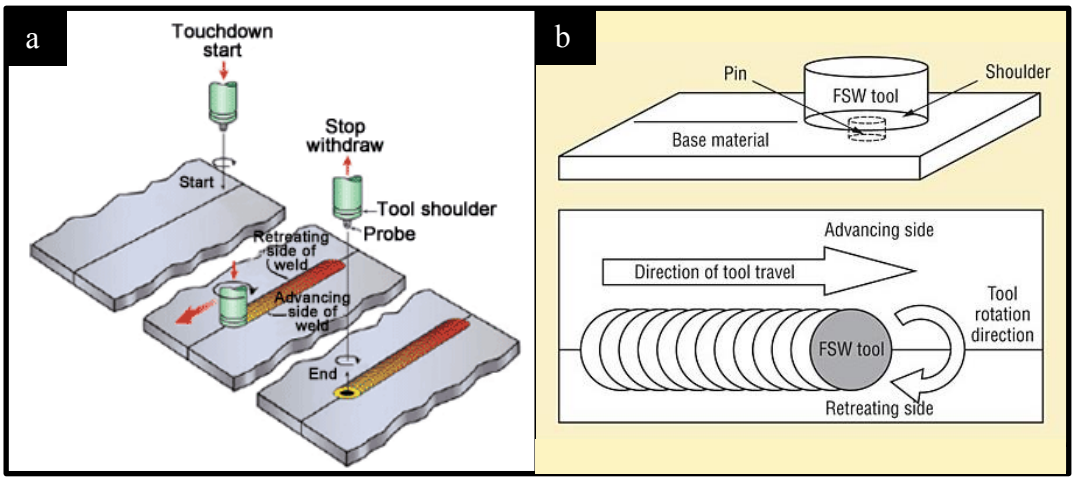

Figure 2.25 *A schematic of a) the FSW process and b) the difference between advancing side and retreating side of the weld.*

Figure 2.26 shows a typical cross section of a FSW with the main regions named. The parent region is the region in the cross section that has not been affected at all from the FSW process. The thermo-mechanically affected zone (TMAZ) is the region that has been mechanically stirred to form the weld. The region next to the TMAZ is the heat affected zone (HAZ) which is the region that has not experienced any stirring but has experienced elevated temperatures, as the friction from the shoulder and the pin from the tool is thermally conducted into the HAZ.

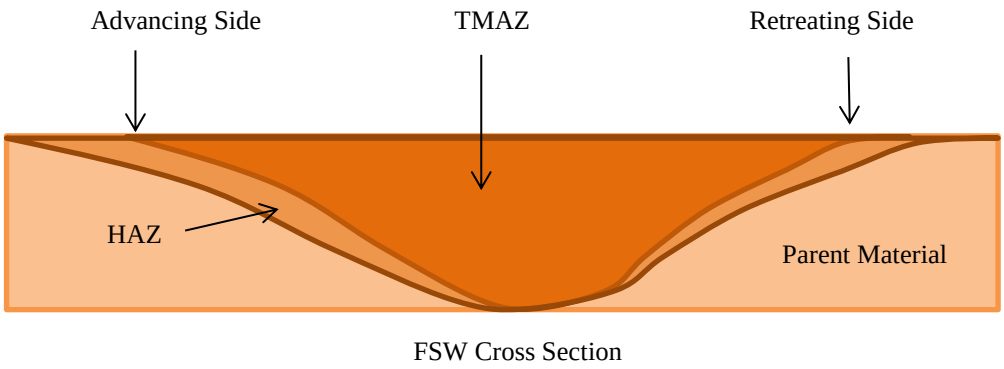

Figure 2.26 *A schematic showing the regions of a cross section of a FSW.*

As a convention in this thesis, the advancing side of the weld is always shown on the left hand side unless otherwise stated.

The FSW Tool

The tool used is a critical component in any FSW process. The FSW of steels was only possible because of the development of tools that were designed to withstand the higher temperatures and strains involved compared to aluminium. When costs and ease of manufacture are taken into account the two main classes of materials that were strong enough to withstand the FSW of steels were high strength ceramics such as boron nitride and some refractory metals such as tungsten. Both materials had their specific limitations with regards to being used for the FSW of steels. PCBN had a tendency to brittle fracture along with high cost and limited processing qualities. Tungsten tended to fracture due to the high ductile brittle transition temperature. This issue was partially resolved by alloying tungsten with rhenium and with the addition of hafnium carbide to enhance wear resistance [74].

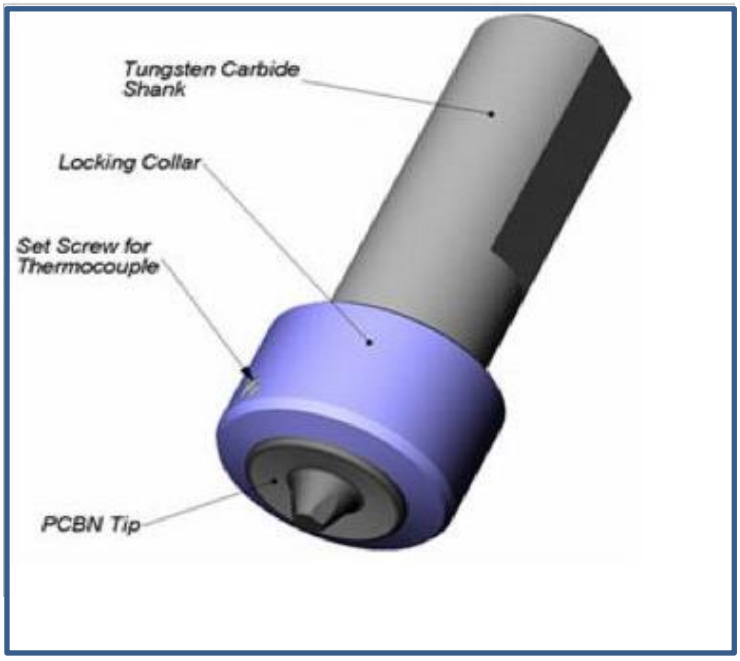

Figure 2.27 *A schematic a typical FSW tool used for the welding of steel [75]*

A hybrid design using PCBN combined with rhenium tungsten (W/Re) binder which uses the wear resistance of the PCBN with the toughness of the W/Re was developed. The amount of binder used with the PCBN depended on the conditions under which the tool was going to be used. The welds studied in this thesis were made using the Q70 tool configuration from MegaStir™ which was made with 70% PCBN and 30% Re/W binder [75].

A typical tool for the FSW of steels as illustrated in Figure 2.27 consists mainly of a shank made of tungsten carbide and locking collar that houses the PCBN/W-Re hybrid tool bit. Groves in the tool bit are designed so that material is stirred as the tool rotates.

Tool Wear

Tool wear is a major concern when performing FSW on ODS ferritic alloys such as PM2000 due to the high cost of tool manufacture. In addition fragments of tool can break up during the FSW process which could have a detrimental effect on the weld.

Wear of the PCBN tool used for the FSW of several steels was reported by Park et al. [76]. Ferritic, duplex and austenitic steels were analysed and traces of both boron and nitrogen were found at the advancing side of the welds. The austenitic steels were found to have higher levels of both boron and nitrogen which was attributed to the higher steady state flow stress of austenitic steels [77].

Process Parameters

The main process parameters in FSW are the rotational speed of the tool, the speed of the tool along the weld line, the down force which keeps the shoulder firmly in contact with the workpiece and the plunge depth which depends on the size of the tool pin.

During FSW heat is generated by the rotation of the tool and the plastic deformation of the workpiece [78, 79]. Increasing the rotational speed of the tool increases the heat generated by the tool in the workpiece. The tool rotation facilitates the removal of material from the advancing side of the weld to the back of the tool. The flow of material has to be sufficient to avoid any voids forming as the tool moves along the weld.

The transverse speed of the tool governs the cooling rate of the workpiece. If the cooling rate is too slow i.e. the transverse speed is slow, excessive heat generation due to the tool rotation as it spends longer at a specific location will have an impact on the nanoparticle distribution in terms of coarsening. If the transverse speed is fast and therefore the cooling rate is fast the formation of voids is likely as the material flow might not be sufficient to fill the gap at the back of the tool as it moves forward.

The down force controls the contact between the tool shoulder and the workpiece. Too much downforce will result in excessive flash to be generated. Not enough downforce will reduce contact of the shoulder and workpiece and therefore reduce friction and the heat generated to plasticise the workpiece [79].

A useful parameter that is an indication of the heat generation in the weld is the Heat Input. This is calculated from the Power divided by the Travel speed and is given by:

$$HI = \frac{2\pi\omega T_q e}{1000 \times s_t} \qquad \textit{(Equation 2.19)}$$

where ω is the rotational speed (rev/min), s_t is the transverse speed (mm/m), T_q is the spindle torque (Nm) and e is the efficiency factor.

The pitch of a weld or the Heat Index is simply the rotational speed divided by the transverse speed and again is an indication of the amount of heat in the weld.

A more detailed approach was calculated by Frigaad et al. [80] which gives the average heat input per unit area and time and is given by:

$$q_0 = \frac{4}{3}\pi^2 \mu P \omega {R_t}^3 \qquad \textit{(Equation 2.20)}$$

Where q_0 is the power, μ is the coefficient of friction, P is the pressure ω is the angular velocity and R_t is the tool shoulder radius.

A more in depth analysis was carried out by Schmidt et al. [81] where the heat generation from the shoulder is added to the heat generation by the tool bit and the tool side. An additional consideration is the sticking or sliding or a combination of both sticking and sliding of the matrix to the rotating shoulder and tool.

The heat transfer during FSW is a complex combination of many factors and most of the work carried out thus far has been on aluminium welds. Transferring the equations to steel FSW would not be a straight forward exercise. For the purposes of this thesis the pitch of the welds provides an illustration of the relative heat input between the different welds that were carried out. This is because all new welds were performed with the same rotational speed of 200rpm.

Defects and Voids in the TMAZ

Wormhole type defects were reported by Crawford et al. [82] in the FSW of AA 6061-T6 type aluminium. Defects were observed in the cross sections of the welds near the base. Four FSW were performed with the same rotational speed of 1500 rpm. The transverse speed was increased from 945mm/m to 1137mm/m to

1353mm/m and to 1607mm/m. The first weld showed no sign of wormhole type defects. As the transverse speed increased so did the size of the defects in the rest of the welds. This was attributed to the lack of material flow behind the tool because of the forward speed of the tool being too high.

Crawford et al. also reported excessive flash of material due to the high rotational speed of the tool.

FSW and Residual Stress

During the FSW process frictional heat is produced which causes the TMAZ to expand. As the region cools down, thermal stresses are created due to the thermal gradient in combination with the mechanical stirring which plastically deforms the TMAZ, as illustrated in Figure 2.28.

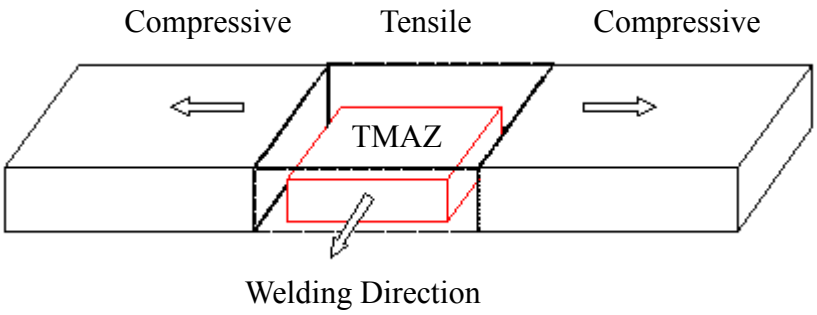

Figure 2.28 *A schematic of the residual stress developed during FSW process. There is a residual tensile stress in the TMAZ as it cools from the heat produced by FSW. Adapted from [83] .*

The residual stress has a characteristic M shape across the TMAZ [48] with the maximum tensile stresses at either side of the TMAZ at the point where the shoulder of the tool ends. The residual stress is measured by the neutron diffraction technique which uses the (110) lattice spacing as a gauge. The residual stress has a longitudinal element which in in the welding direction and along the transverse direction which is across the TMAZ.

2.12 Diffusion in Solids

Diffusion is a process where material is transferred due to atomic motion. The driving force for diffusion is the activity gradient. This is a temperature dependent process in which the coefficient of diffusion D is governed by an Arrhenius type equation [25]:

$$D = D_o \exp[\frac{-Q}{RT}] \qquad \textit{(Equation 2.21)}$$

where D_o is a constant and Q is the activation energy both of which are dependent on the diffusing species for a particular solid where diffusion is taking place. R is the gas constant and T is the absolute temperature.

For a non-steady state diffusion, where the concentration of the diffusing species at a point varies with time is given by [25]:

$$\frac{C_x - C_0}{C_s - C_0} = 1 - (\text{erf})(\frac{x}{2\sqrt{Dt}}) \qquad \textit{(Equation 2.22)}$$

where C_x is the concentration at a distance x after a time t, which applies with the following boundary conditions:

For t=0, $C = C_0$ at $0 \leq x \leq \infty$

For $t > 0$, $C = C_s$ and $C = C_0$ $at\ x = \infty$

Equation 2.22 is an approximation of Fick's second law and the term (erf) is the Gaussian error function. A useful approximation is the distance x where the concentration is midway between C_0 and C_s and is given by [25]

$$x \cong \sqrt{Dt} \qquad \textit{(Equation 2.23)}$$

If diffusion is through interstitial positions the diffusion coefficient is higher reflecting the lower activation energy required. For instance at 500°C the diffusion

coefficient of carbon in α iron is 2.4 x 10^{-12} m^2s^{-1} whereas the self-diffusion coefficient of α iron is 3.0 x 10^{-21} m^2s^{-1}.

2.13 Summary of Literature Review

The fine oxide particle distribution in ODS steels increases the high temperature creep strength of the steels which makes them ideal material candidates for high temperature applications. The main process route for the manufacture of ODS steels is the mechanical alloying process. An alternative process route is the gas atomisation process which results in an alloy with limited high temperature applications but has excellent oxidation and corrosion properties.

Conventional joining techniques cannot be used on ODS steels as the fine oxide particles agglomerate and slag off to the surface. Friction stir welding is a new solid state joining technique in which the fine oxide distribution is left intact.

A large grain microstructure is required for maximum high temperature creep resistance. This is reported to be achieved by minimising the nucleation sites of primary recrystallisation or through secondary recrystallisation where a large grain structure is obtained.

Limited research has been carried out on the friction stir welding of ODS steels. PM2000 has a sub-micron grain structure which is elongated in the rolling or extrusion direction. After friction stir welding, the microstructure in the stir zone consists of mainly equiaxed dynamically recrystallised grains. The stir zone microstructure does not depend of the starting microstructure. The application of a high temperature anneal promotes the formation of a large grain microstructure in the stir zone which is desirable. The amount of residual stress in the stir zone is dependent on the parameters of the friction stir weld process and effects the size of the grain structure after the application of a high temperature anneal.

One of the challenges of friction stir welds carried out on rolled/Sheet PM2000 is the lack of a large grain microstructure of the parent region after the application of a high temperature anneal.

Recent advances in the gas atomisation process have resulted in the manufacture of an ODS type steel APMT at a much lower cost than mechanic alloying. Limited amount of research has been carried out on this type of alloy and no research was found on the friction stir welding of APMT in literature.

Only a handful of researchers have reported on the dissimilar metal welds of ODS steels, using friction stir welding. For future high temperature applications, ODS steels will need the ability to be joined to different types of steels to minimise the cost. A dissimilar metal friction stir weld between two different types of ODS steels is of particular interest.

CHAPTER 3

Materials and Experimental Techniques

3.1 Introduction

In this chapter the composition of the two different types of ODS alloys used for this thesis are listed along with their specific processing routes. A brief outline of the welds analysed is given and the equipment used for the production of the welds is discussed.

Details of the various sample preparation techniques are listed. An explanation of the analytical equipment and any related software used for the examination of the samples is discussed along with the scientific background to each of the equipment used.

3.2 Alloy Composition and Processing Routes.

The two ODS alloys used for this study were PM2000 and APMT and their composition is given in Table 3.1.

Table 3.1 *Nominal chemical composition by wt.% of PM2000 and APMT alloys.*

	Fe	Cr	Al	Mo	Si	Mn	C	Y	Zr	Hf	Ti	Mg	S	N
PM2000	bal	19	5.5	-	-	-	-	0.5(Y_2O_3)	-	-	0.5	-	-	-
APMT	bal	22	5	3	0.7	0.4	0.05	0.1	0.05	0.1	0.02	0.01	0.002	0.05

PM2000

PM2000 is a FeCrAl ODS steel manufactured by Plansee™ GmbH using the mechanical alloying process with the addition of yttrium oxide as the dispersoid.

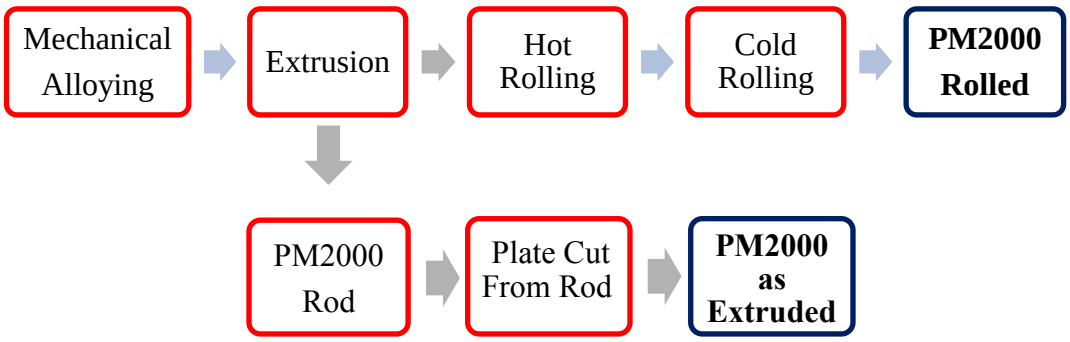

Figure 3.1 *Schematic showing the process steps in the production of PM2000Rolled and As Extruded plates.*

Following extrusion as seen in Figure 3.1, a combination of hot and cold rolling process is used to form PM2000 4 mm plate product. Initial investigation focussed on rolled PM2000 but subsequently for reason that will be revealed later in the thesis plates were cut from as extruded rod PM2000 so as to avoid the rolling process altogether.

The mechanical alloying process is a high energy process and therefore expensive. Production of PM2000 ceased in 2007. The PM2000 used for this research was supplied by Oak Ridge National Laboratory USA.

APMT

Figure 3.2 A schematic showing the different processing steps for the production of APMT alloy

Kanthal™ APMT 5mm plate was purchased directly from the manufacturer. The processing route for APMT is via the rapidly solidified powder (RSP) metallurgy as illustrated in Figure 3.2. It is a gas atomisation process using a FeCrAlMo alloy melt with added inclusions. The powder is then consolidated using a hot isostatic pressing (HIP) and subsequent rolling steps. APMT relies on oxides of Y and Ta as well as

carbides and nitrides of Zr and Hf for dispersion strengthening. APMT is a cost effective alternative for light to moderate stressed components at high temperatures.

3.3 Friction Stir Welding

All friction stir welds were performed at The Welding Institute (TWI) in Rotherham near Sheffield on a gantry style FSW machine, model RM-2, manufactured by Transformation Technologies Inc. (now MTI) of Elkhart, Indiana, USA (Figure 3.1).

The only preparation of the plates required was that they were as straight as possible and that they were the same plate thickness. Plates to be welded were clamped down to the correct position and parameters such as down force, rotational speed, transverse speed and angle of the tool were programmed in to the computer. A printout of the real time welding parameters was produced by the on board computer. All the welds were performed under an argon gas shield to protect against oxidation.

Figure 3.3 *FSW machine model RM-2 used for all the welds at TWI Rotherham UK (Image TWI).*

The three most useful welding configurations with regards to FSW are the bead on plate (BOP) welds, butt welds and lap welds as shown in Figure 3.4. The BOP

configuration is a useful first attempt at finding out the best parameters for a particular type of plate alloy. Several BOP FSW of rolled PM2000 were performed before the start of this research and some idea of parameters and their effect on the welds had been gained already.

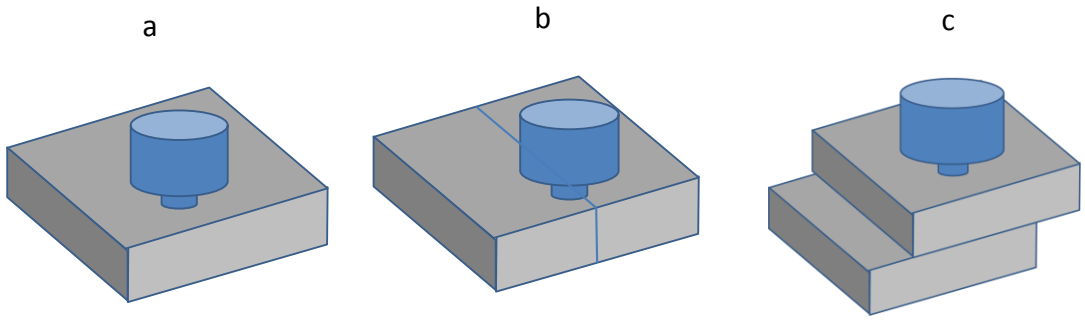

Figure 3.4 *Different FSW configurations. a) Bead on plate (BOP) weld, b) a butt weld and c) a lap weld. (Author's own schematic).*

All new welds produced for this research were butt welds. Once the welds were finished they were allowed to cool down. In some instances the backing plate was attached to the welded plates but they were easily separated. The optical images in Figure 3.5 show the FSW of APMT in progress and the finished weld.

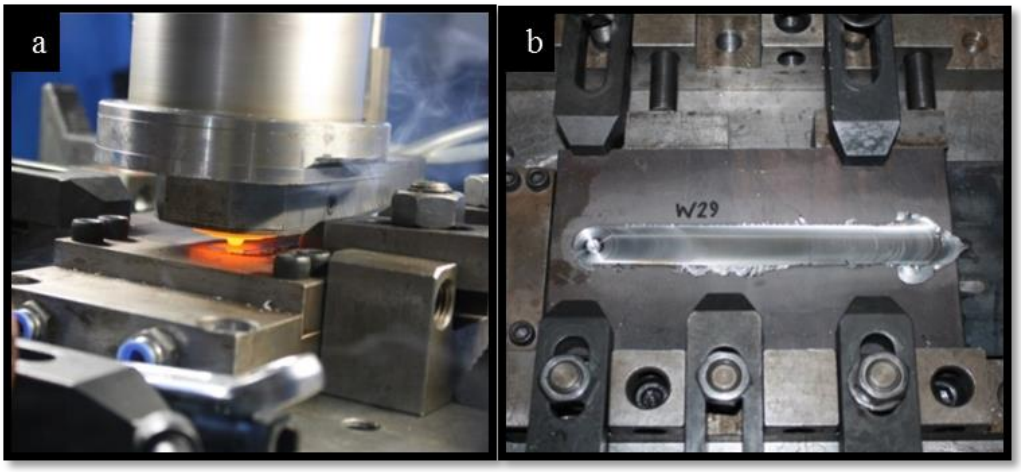

Figure 3.5 *Optical images of a) FSW of APMT in progress and b) the completed weld. (Images taken at TWI Rotherham UK)*

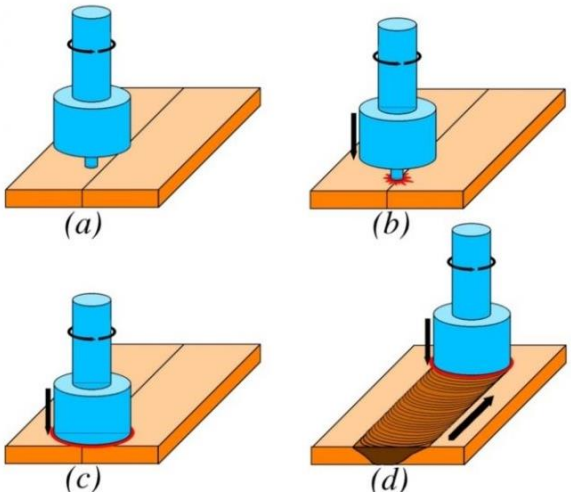

Figure 3.6 *A Schematic showing a) the alignment of the tool, b) the plunging of the tool, c) friction produced by the shoulder of the tool and d) a FSW in progress.[84]*

The schematic in Figure 3.6 illustrates the 4 main steps in the FSW process. Step 1 is to align the two plates at the correct position. Then the plates are clamped down into securely to avoid any movement during processing. Step 2 is the plunging of the tool. During this step some of the material to be welded is displaced and usually forms a flash of material at the beginning of the weld.

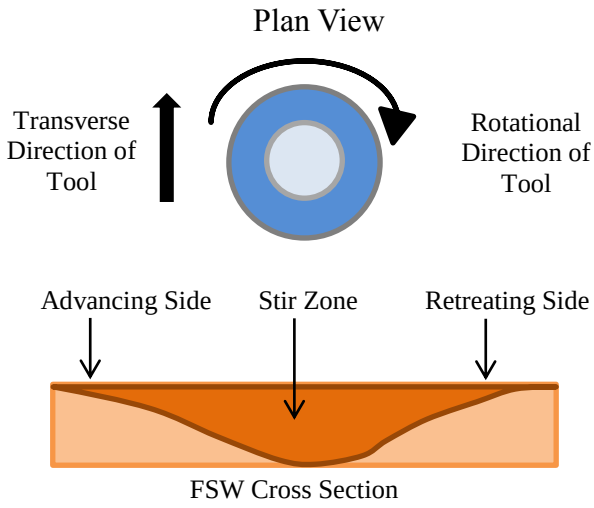

Figure 3.7 *Schematic of the cross section of a FSW showing with the rotation and transverse direction of the tool (Schematic Author's own collection.).*

At this point the tool rotation has to be high enough so that the tool penetrates the plates. Once the shoulder is placed on top of the plates in step 3, friction from the shoulder plasticises the material and becomes pliable enough for the tool to move across the join to form the weld as in step 4.

Once the weld is left to cool it is sectioned for analysis. The schematic in Figure 3.7 illustrates the difference between the advancing and retreating side of the weld. The advancing side is at the point when the rotation of the tool is in the same direction as the direction of the weld and the reversing side is at the point where the rotation of the tool is in the opposite direction to the direction of the weld. In effect material is sheared away from the advancing side and redeposited at the reversing side once the tool has moved on.

Cross sections of the welds were analysed in the as welded condition and in the post weld heat treatment (PWHT) condition. Parent material was taken from as near the weld as possible but far enough so that the FSW process did not affect the characteristics of the material. Using the printout from the on board computer, sections were cut from the region of the weld that has reached steady conditions usually a few centimetres from the start of the weld.

3.4 Heat Treatment

Recrystallisation heat treatment (at 0.9 Tm for 1 hour) was applied to samples in the as-received and post weld heat treated conditions in order to promote recrystallisation. For FeCrAl alloy systems the temperature of 1380°C is used [85]. Cross sections of welds were placed in an alumina boat and into an Elite Thermal Systems Ltd furnace (model no TSH 15/50/450-2216E-2116). Samples were taken out after 1 hour and allowed to cool in air. Samples were then prepared for analysis in the usual manner.

When referring to the as received material the heat treatment will be referred to as HT and for FSW material as PWHT. This is so that a distinction can be made between FSW of as received material with HT and the HT applied post FSW.

3.5 Micro - Indentation Hardness Testing

Hardness of a material is a measure of its resistance to penetration and its localised plastic deformation behaviour [25, 64]. There are several hardness testing techniques and although not very accurate, conversion tables are available between the different techniques for comparisons.

The Vickers hardness technique uses a diamond pyramid to make an indent under a controlled load and for a specified time which can be varied by the operator of the equipment. The diagonals of the indents were measured using the on board microscope and the Vickers Hardness number (HV) is calculated automatically by the micro-indenter using the following formula:

$$HV = (0.1854 \times Load) \div d^2 \quad N/mm^2 \qquad \textit{(Equation 3.1)}$$

Where d is the diagonal of the indents and it is the average between the two diagonals of the pyramid indent.

Vickers hardness measurements were taken using a Matsuzawa Seiki micro-indenter using a loading of 500g and a dwell time of 15 seconds. The loading was chosen so that indents were in the region of 40 microns. Smaller indents would affect the accuracy and would introduce a greater error in the measurement of the diagonals of the indent.

Errors that can affect the accuracy of the measurements were quantified. Using a certified standard with a hardness of Hv 255, 10 readings of the same indent were taken and the error in the actual measurements of the indents was calculated as $\pm$2.5Hv. The error associated with the micro-indenter was measured against the same standard and after 10 different indents the mean hardness number was 252Hv with a standard deviation of 6Hv. Errors were calculated using a 466Hv and 732Hv standards and the HV number was found to be less consistent as the hardness increased.

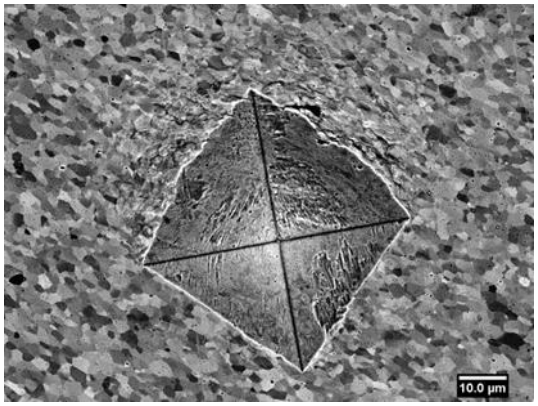

Figure 3.8 *Channelling contrast image of a pyramid indent in PM2000 alloy. (Image from author's own collection)*

As most of the materials tested were in the hardness range of 200Hv to 360Hv, the accuracy of the indenter was calculated at 98% using the 255Hv standard. A channelling contrast image of an indent in PM2000 as seen in Figure 3.8 clearly shows the diagonals of the indent.

3.6 Standard Sample Preparation

The surface of any sample requires polishing so that any features present are easily distinguishable for analysis. Once a sample was cut to a suitable size it was then mounted in a conductive bakelite compound. Mounting of samples helps to protect the edge of the sample and make it easier to handle while polishing. Using a conductive mount also reduces charging when analysing samples in the SEM microscope. Grinding was undertaken using successively finer silicon carbide papers starting with a P180 grit paper up to P4000 grit paper finish. Table 3.2 lists the grit rating of the silicon carbide papers and the median of the size of the silica carbide grains used in the paper. After each successive step the sample was rotated by 90° so that scratches from the previous step were removed and were no longer visible.

Samples to be etched with Kalling's reagent or with 10%HCl in methanol were then polished using a 0.25µm diamond paste on polishing cloth.

Table 3.2 *Classification of SiC paper and the corresponding median grain diameter.*

P grade SiC Paper	Median Grain Diameter (microns)
P180	75
P320	46
P600	26
P1200	15.3
P2500	8
P4000	2.5

For SEM analysis and some optical microscopy a mirror finish using a 40nm colloidal silica suspension was used. Being slightly alkaline (pH9.3) colloidal silica particles are not abrasive but because of a reactive outer layer, the sample is gently chemically etched resulting in a fine finish as shown in the schematic in Figure 3.9. This was used to good effect especially with the dissimilar metal welds.

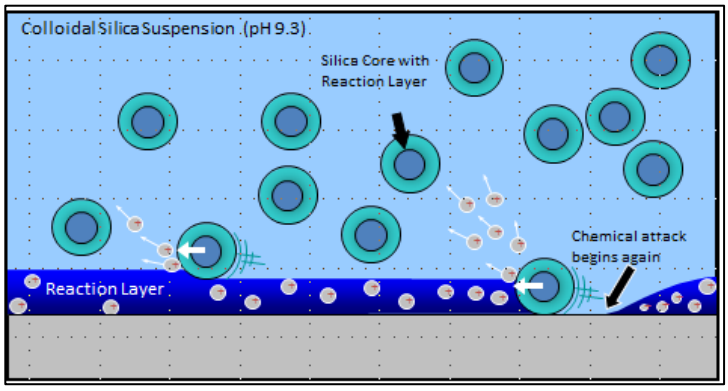

Figure 3.9 *A schematic showing the chemical etching effect of colloidal silica polish on a sample (Image source: Buehler).*

3.7 Chemical Etching

Chemical etching is a technique used to reveal grain boundary and other structural details that can then be studied under an optical microscope. Several etchants were used in this research. Kalling's Reagent which is a solution of 33mlH_2O, 1.5g$CuCl_2$,

33ml methyl alcohol and 33mlHCl was used on weld cross sections as it resulted in very good contrast of the grain structure for low magnification images.

For higher magnification grain structure images a solution of 10%HCl in methanol for 7 minutes in an ultrasonic bath was used as the grain boundaries of the samples were enhanced. In the dissimilar metal FSW between APMT and PM2000 cross sections, final polishing step using colloidal silica was extended to 2 hours instead of the normal 20 minutes. Due to their different etching rates when using acid etchants, PM2000 grain structure was less visible than the APMT grain structure. The slight chemical etching effect of the colloidal silica was useful in that grain boundaries of both were made visible in the optical microscope.

3.8 Optical and Differential Interference Contrast Microscopy

Low magnification images were recorded using a Wild Heerbrugg M8 stereo microscope fitted with a wide angle lens. Optical microscopy was carried out using a Nikon Optiphot 2 microscope and a Leitz Wetzlar Metalloplan microscope.

Differential Interference Contrast (DIC) microscopy uses the interference created when the light beam is split into two and polarised with respect to each other by 90°. The beams are recombined using a prism and any height differences in the sample are enhanced. Samples polished with colloidal silica were ideal for DIC microscopy because of the slight etching of grains that enhanced the contrast of the grain structure. All Images were taken using Lumenera Corporation Camera model Infinity2-2C (colour). Infinity Capture software package was used to process the images taken. Image processing such as scale bars and brightness and contrast adjustments were performed using ImageJ software.

3.9 Scanning Electron Microscopy (SEM)

In an SEM a beam of electrons is scanned across a sample surface and signals emitted are detected to form an image.

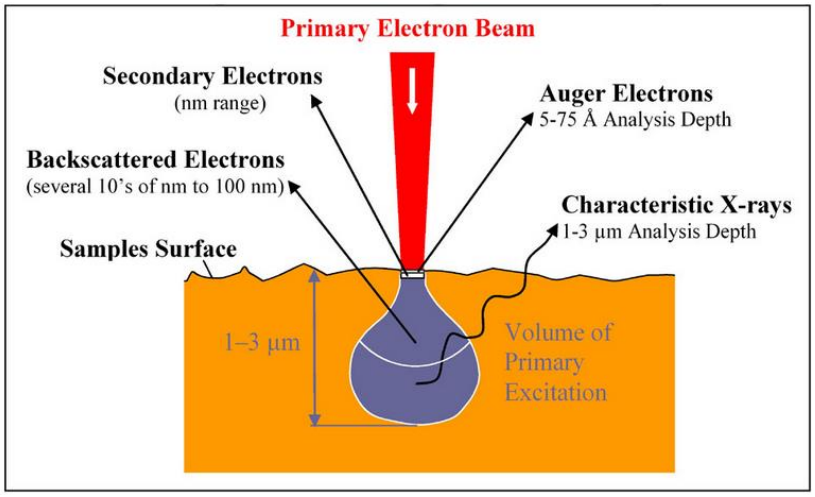

Figure 3.10 *A schematic showing the different types of signal emitted from a sample in an SEM [86]*

Depending on the type of signal and the detector used, detailed information can be obtained about the surface or near surface structure of bulk specimens. A schematic in Figure 3.10 shows the different types of signal emitted from a sample under an electron beam.

The electron source is usually a tungsten filament or for better resolution a Field Emission Gun (FEG) is used. The emitted electrons are then accelerated to a range of energies from 1 keV to 30 keV. The electron beam is then focussed using a series of electromagnetic lenses to form a fine spot of electrons down to a few nano meters in diameter. This beam of electrons is then scanned across a section of the specimen. Depending on the detector used different information can be obtained by detecting the different types of radiation emitted by the sample.

Secondary Electron Detector (SED) is used for imaging the sample using secondary electrons emitted from atoms near the surface of the sample. Secondary electrons are ejected from their shell by the incoming beam of electrons. These low energy electrons (< 50 eV) tend to be easily absorbed by the bulk of the specimen and can only escape the specimen if they originate at the surface or very close to the surface of the specimen. As such, high resolution images of surface details such as inclusions and boundaries are easily imaged in SED mode.

Backscatter Detector is used to form images from electrons reflected back or backscattered by atomic interactions from deeper within the sample.

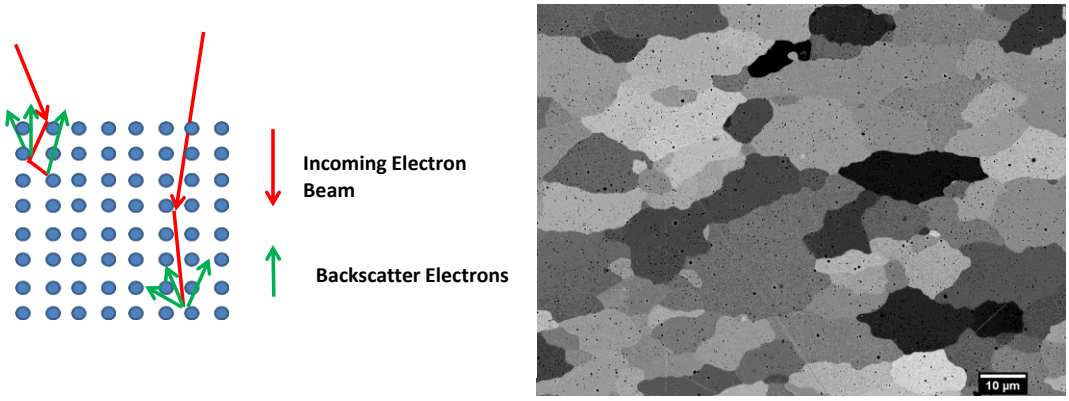

Figure 3.11 *Schematic showing channelling contrast in backscatter mode and an example of a channelling contrast image of the grain structure of PM2000 rolled alloy.in the SEM (Schematic and image from author's own collection).*

In Channelling Contrast imaging backscattered electrons detected are used to form images of the grain structure of the sample. A higher probe current is used to force electrons through the atomic planes of the sample. If the orientation of a grain in the sample is aligned with the electron beam then they are channelled deeper through the sample and more of the resulting backscatter electrons are absorbed. This reduces the amount of signal detected and therefore grains in the sample are revealed due to the difference in signal detected from the different grains in a sample as shown in the illustration in Figure 3.11.

3.10 Energy Dispersive X-Ray Spectroscopy (EDX).

Characteristic X-rays emitted from the bulk of the sample provide information about the elemental composition of the sample. When a sample is illuminated with electrons either in an SEM or a TEM, electrons are ejected from the inner electron shells. An outer shell electron then drops to the inner shell to lower the energy state of the atom, and X-rays are emitted which are characteristic of the two electron energy shells involved from the elements present as shown in Figure 3.12.

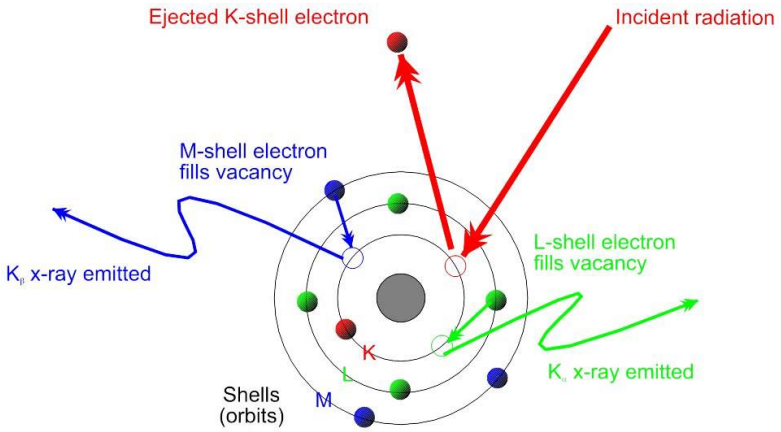

Figure 3.12 *Schematic of the electron energy shells and characteristic X-ray emitted under electron illumination of a sample (image source: Bruker)*

As well as the X-rays emitted from electrons dropping down to fill the lower energy electron shells, interactions between incoming electrons and nuclei of the specimen can produce X-rays with a range of energies that can be detected as well. These are called bremsstrahlung X-rays and are background X-rays seen in EDX plots.

The analysis process is controlled by computer. An incoming X-ray is detected and the energy of the X-ray is assigned to the correct energy channel which is then processed by a multi-channel analyser. This displays the signals received as a histogram or a spectrum. This is a serial process the detector is only able to process one signal at a time and some of the incoming X-rays will not be analysed. Increasing the processing time will reduce the background noise but will also reduce the number of counts and increase the number of signals that are 'binned'. Dead time is the percentage of the signal 'binned' over the total signal and for optimum results a dead time below 40% was maintained in EDX analysis.

Quantitative Analysis

In order to extract useful quantitative analysis from EDX spectra, certain considerations need to be addressed. According to Castaing (Ref 1951), the ratio of concentrations of an element C_i and a known standard $C_{(i)}$ is proportional to the ratio

of their respective signal intensities I_i and $I_{(i)}$ in EDX analysis. The following formula was proposed [87]:

$$\frac{C_i}{C_{(i)}} = [K]\frac{I_i}{I_{(i)}} \qquad \textit{(Equation3.2)}$$

Where K is a non-constant correction factor commonly known as ZAF correction that takes into account the following 3 effects:-

- Z the atomic number
- A the absorption of X rays in the specimen
- F the fluorescence of X rays in the specimen

Several methods can be used to evaluate the corrections and some are incorporated in software packages that analyse EDX spectra. Further details can be found in Williams and Carter [87].

Instruments Used

For this work initially a Joel JSM 6610 was used mainly in SED mode. The main part of the analysis was carried out on a Joel JMS 7001F field emission gun (FE SEM) in both SED and backscatter mode for channelling contrast. In both SEM's detection of X-rays for EDX analysis was with Oxford Instruments X act detectors using INCA software for data analysis.

Using the INCA software controlled EDX analysis, a point or an array of points can be analysed and the time spent on each point can be controlled. Samples were left running overnight so that accurate maps could be produced. Drift control was a useful feature when analysing samples for a long time as at higher magnifications drift was an issue.

The penetration depth and the interaction volume of the electron beam in the sample depend on the beam energy and the material being investigated. Monte Carlo simulations can predict the interaction volume and the penetration depth for a given sample at different microscope parameters.

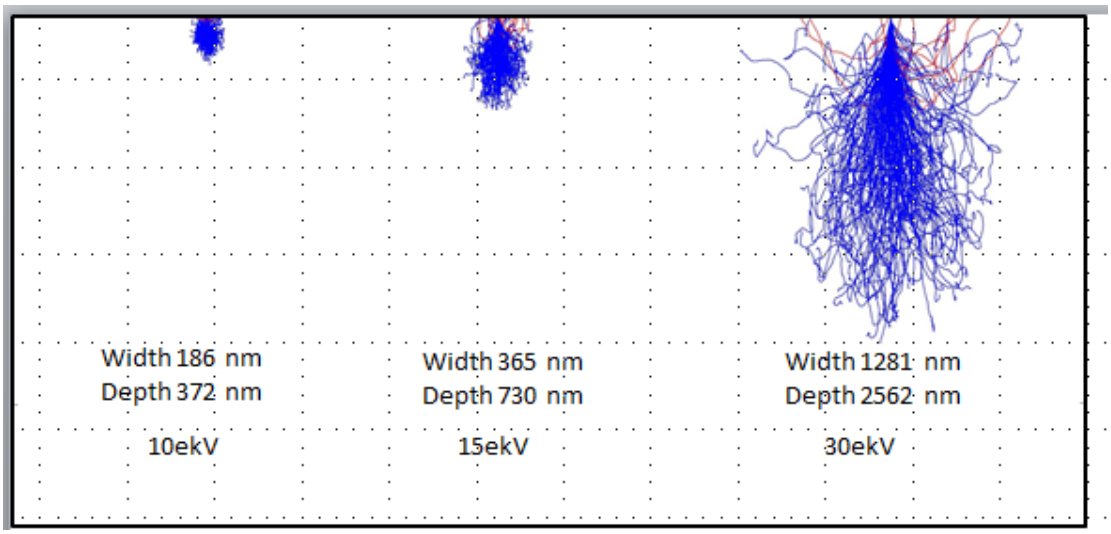

Figure 3.13 *Monte Carlo simulations of penetration depth and interaction volumes for Fe20Cr5Al alloy at 10kV, 15kV and 30kV electron beam energies in an SEM.*

A Monte Carlo simulator software package was used to determine the interaction volume for FeCrAl alloy PM2000 (Fe20Cr5Al) at three different electron beam energies, at10 kV, 15kV and 30kV. The results are presented in Figure 3.13.

In most investigations carried out by SEM the electron beam was set at 15kV as this was sufficient energy for the analysis required in terms of energy of the X-rays for EDX analysis which meant that the spatial resolution of the analysis was maximised.

3.11 TEM Sample Preparation

The principle behind TEM samples is the preparation of thin areas of interest so that they become electron transparent. Thin strips of cross sections of the welds were cut and polished down to 200µm thickness using SiC paper. Using a puncher, a 3mm disc was cut out and glued to a polishing rig. By using a P2500 SiC paper one side was polished until flat and then the glue was dissolved in acetone, the disc was turned over and glued down again. Polishing continued until the disc measured about 50µm in thickness. The thinned disc foils were electro polished using a Struers Tenupol-3 double jet polishing unit. The electrolyte used was a solution of 5% perchloric acid in methanol which was cooled down to -50°C using liquid nitrogen.

A photo sensor was activated once the disc was perforated and the process stopped. A voltage of 20V and a current of 0.05A were used. The foil discs were then immersed in cooled methanol and then ethanol at room temperature. The foil discs were then placed on a hot plate and allowed to dry before placing in a special TEM sample holder.

The TEM sample holder was kept in a desiccator glass jar for storage. TEM samples were analysed soon after they were prepared.

3.12 Focused Ion Beam TEM Sample Preparation

One of the drawbacks of electropolishing is the lack of control with regards to area specific samples. A Focused Ion Beam (FIB) instrument can lift a sample for TEM analysis from a specific site of interest. The lifting process is described in detail by Tomus et al. [88] and Gianuzzi et al. [89]

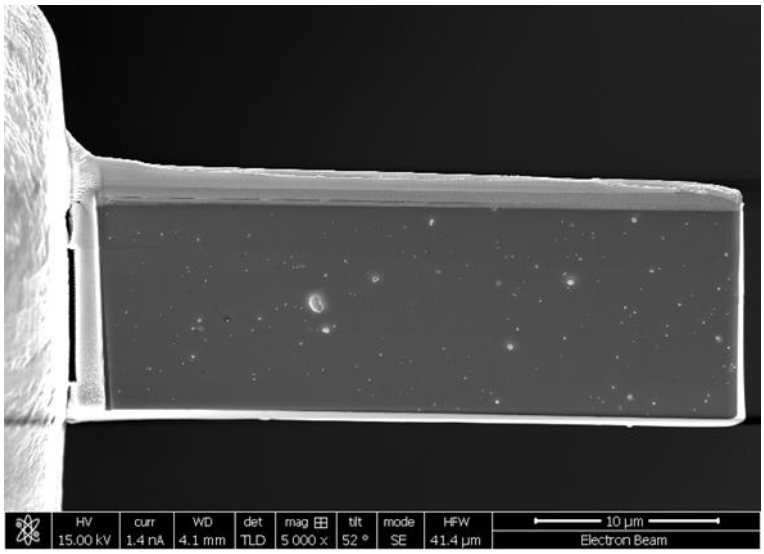

Figure 3.14 *A FIB TEM sample that has been prepared from an ODS steel. (Image: Dr Karl Dawson University of Liverpool)*

The FIB TEM samples were prepared using an FEI Helios 600i dual beam, FIB instrument which was fitted with gas injection sources for the deposition of platinum

and an Omni Probe 100.7 micro-manipulator. A strip of platinum was deposited over the area of interest to protect the sample from redeposited material. Trenches were milled either side using an acceleration voltage of 30kVand a high beam current of 21 to 65nA to facilitate fast material removal. A J cut was made to remove the lamella of material and attached to copper support grid using ion beam deposited platinum. Subsequent thinning to 100nm was carried out using a 30kV Ga ion beam with a reduced current of 80 pA to 2.5nA. A final polish step using a low power (2kV to 8 kV) was applied to remove previous damage layer.

3.13 Carbon Extraction Replicas

Carbon extraction technique enables the study of the precipitates and their distributions to be studied in a TEM without the matrix being present. Cross sections of samples were prepared using SiC paper up to P2500 finish. Samples were suspended in a solution of 10% HCl in methanol in an ultrasonic bath for 7 minutes. This was sufficient time to etch the surface of the sample and reveal precipitates near the surface.

A thin carbon film was deposited using a Quorum Q150T ES vacuum coater using a current of 52 A and an evaporation time of 1.8 minutes. Using a sharp Stanley knife a grid of approx. 1mm x 1mm square scratches were made on the coated surface. This is done to allow subsequent suspension in the 10% HCl in methanol solution to etch below the carbon layer. After careful rinsing with methanol the sample was placed in a beaker with de-ionised water where the carbon film squares were lifted and then collected on to copper grids. The copper grids were left to dry before storage in a TEM sample holder.

3.14 Transmission Electron Microscopy (TEM)

In a TEM a uniform intensity of electrons is used to illuminate a thin electron transparent specimen. In image mode electrons transmitted through the thin specimen are used to form an image. In diffraction mode the diffraction pattern formed at the back focal point is used as the image source.

3.14.1 The Instrument

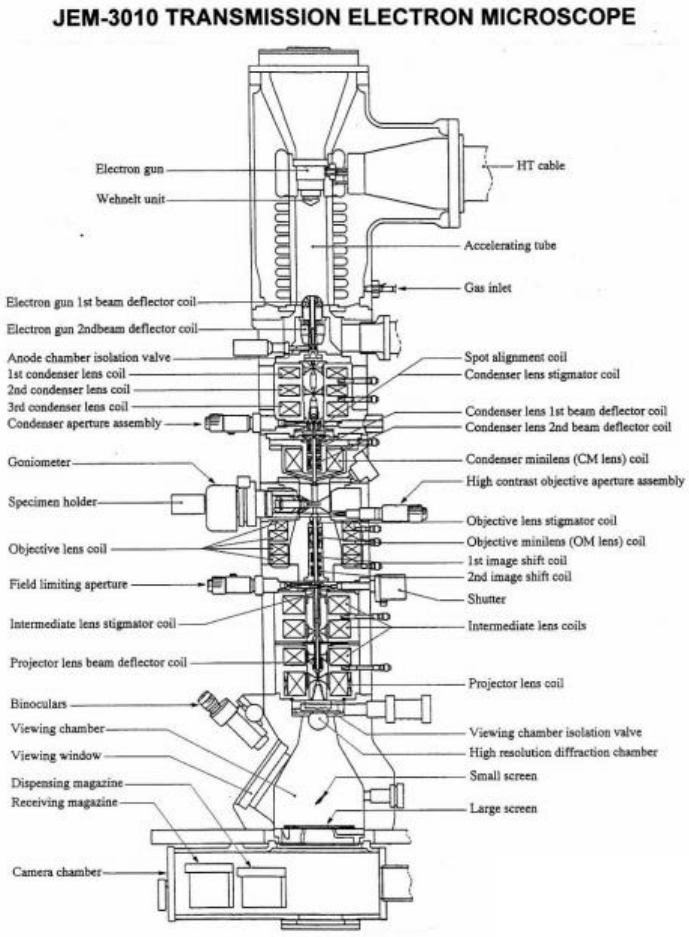

Figure 3.15 *Schematic of the cross section of a JEM 3010 Transmission Electron Microscope [90]*

The main components of a JOEL 3010 TEM, as illustrated in Figure 3.15, are described in more detail.

Electron gun

A thermionic gun which emits electrons when a current is passed through it is used to provide the electron source. They are made mainly tungsten or from lanthanum hexaboride (LaB_6). A negative charge is applied to the filament and the electrons are

accelerated towards an anode. A Wehnelt cap causes the electrons to cross over and at this point becomes the effective electron source.

Condenser Lens

Two or more condenser lenses are used to demagnify the electron source and control the area of illumination on the specimen. This affects the brightness of the image. A condenser aperture controls the convergence angle of the beam.

Objective and Intermediary Lens

The objective lens forms the initial image and depending on the strength of the intermediary lens, an image or a diffraction pattern is then magnified by the projector lenses. The intermediate lens is usually flipped from image mode to diffraction mode by a push of a button. In diffraction mode the intermediary lens is refocused on the back focal plane of the objective lens as opposed to the image plane of the objective lens. (See Figure 3.16)

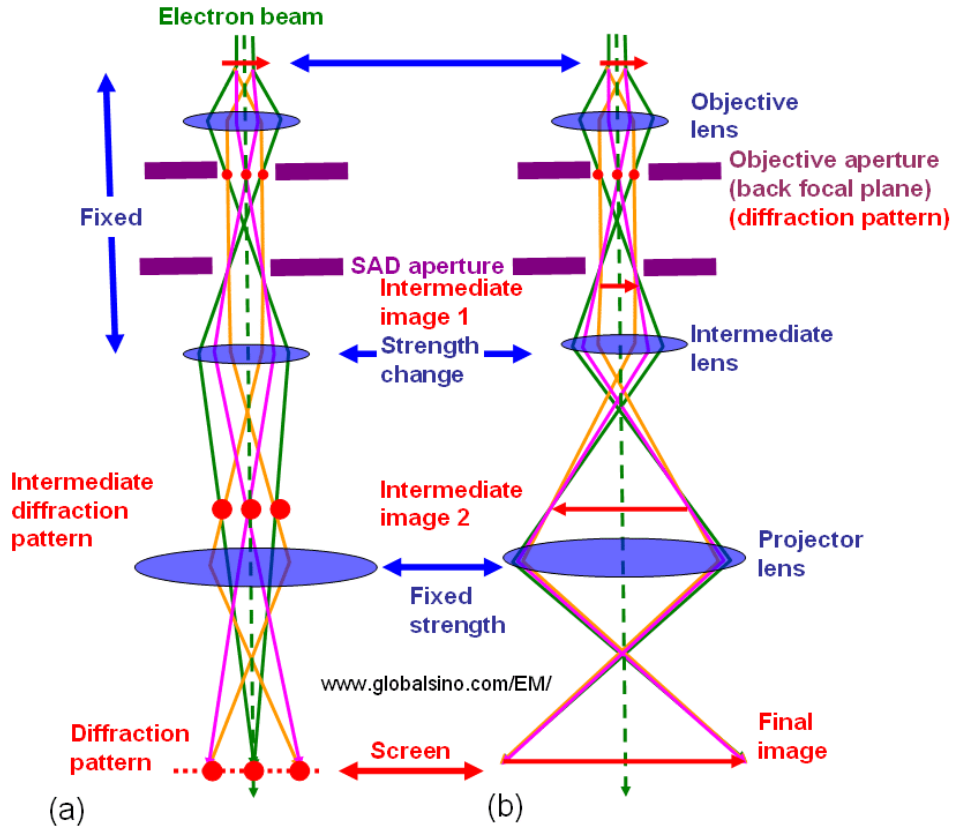

Figure 3.16 *Schematic of ray diagrams for a) diffraction and b) imaging mode in the TEM.) [91].*

Projector lens

Projector lens further magnify the image from the objective and intermediary lens to achieve the required magnification. At lower magnifications not all the lenses need to be used and same of the projector lenses may be switched off.

3.14.2 Imaging

Electrons transmitted through a sample are scattered and a detector in the form of a phosphor screen or a digital camera displays the image. Contrast in the TEM is formed by one of three mechanisms:

1. Mass and/or Thickness Contrast arise from regions of varying thickness and/or differences in atomic number. Electrons are scattered more strongly from thicker regions and from regions of higher atomic number and appear darker in bright field images.
2. Diffraction Contrast is due to the different diffraction intensity as a result of scattering from features such as dislocations grain boundaries and second phase particles.
3. Phase Contrast is due to lattice fringes that are produced from interference between the transmitted and diffracted beam in crystalline specimens. This is typically termed HRTEM (High Resolution TEM) imaging.

Bright Field

A bright field image is formed when an aperture is placed around the main spot of the diffraction pattern. The image information from the direct beam and the very low angle scattered electrons will contribute to the image.

Dark Field

A dark field image is formed when an aperture is placed around a specific spot of a diffraction pattern. Only electrons scattered by the specific orientation will contribute to the image and any features aligned with it will appear bright.

3.14.3 TEM Diffraction Mode

Scattering of electrons in a specimen can provide useful information about crystallographic structure of the specimen examined. Consider an array of atoms in a crystalline specimen. An incident beam is either diffracted by elastic scattering or transmitted through the specimen as illustrated in Figure 3.17. The scattered beams will constructively interfere if the beam scattered from A is in phase with the beam scattered by B.

The difference in the pathway between the two beams must be a whole number of wavelengths for constructive interference which is given by the Bragg equation:

$$2dsin\theta = n\lambda \qquad \textit{(Equation 3.3)}$$

Where d is the atomic inter planar spacing, 2θ is the scattering angle, λ is the electron wavelength and n is an integer.

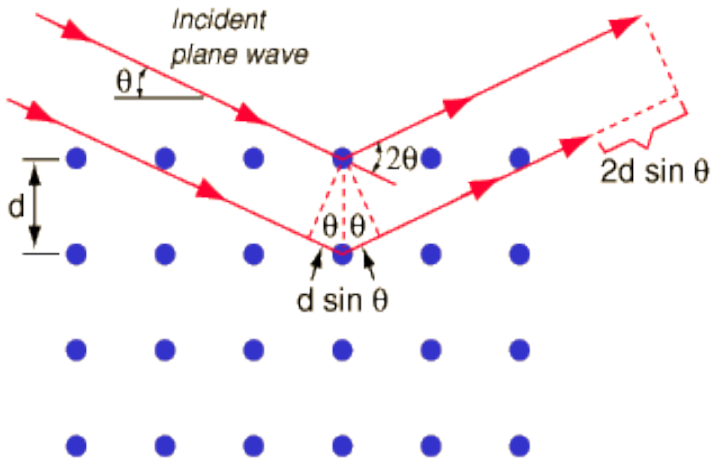

Figure 3.17 *Schematic of electron diffraction by the lattice array of a crystalline specimen [92].*

If we consider 1st order diffraction where $n = 1$ and as the scattering angles involved are so small so that $sin\theta \approx \theta$, then Equation 3.3 becomes:-

$$2\theta = \frac{\lambda}{d} \qquad \textit{(Equation 3.4)}$$

Now consider the ray diagram in Figure 3.18 which illustrates the geometry of the TEM in diffraction mode.

From simple trigonometry and for small scattering angles,

$$\frac{r}{L} = Tan2\theta \approx 2\theta \qquad \textit{(Equation 3.5)}$$

Where L is the camera length and r is the distance of the diffracted spot from the transmitted spot in the diffraction pattern recorded on film.

Combining Equations 3.4 and 3.5

$$\frac{r}{L} = \frac{\lambda}{d} \quad or\ d = \frac{\lambda L}{r} \qquad \textit{(Equation 3.6)}$$

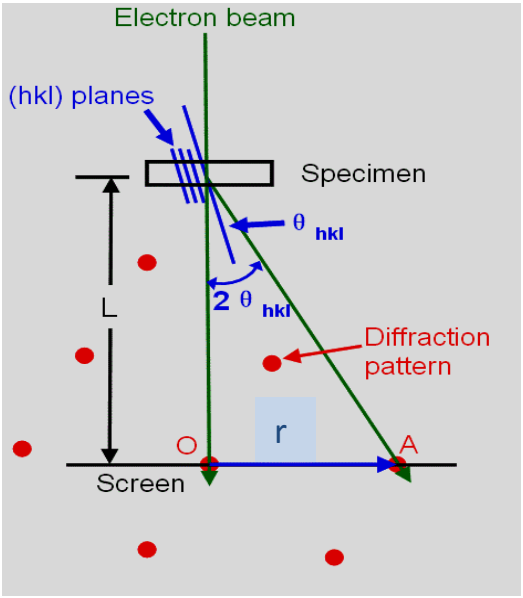

Figure 3.18 *Schematic of the ray diagram in TEM diffraction mode. Image adapted from [91]*

The term λL is called the camera constant as both terms are independent of the specimen. This means that the d spacing of the plane diffracting the incoming

electron beam is inversely proportional to the distance r between the diffracted spot and the transmitted spot in the diffraction pattern.

3.14.4 Selected Area Diffraction

In selected area diffraction an aperture is inserted over a specific region of interest in order to obtain a diffraction pattern from which crystallographic data can be measured as illustrated in Figure 3.19.

The measurements can then be compared to a crystallographic database and in combination with EDX analysis the phase of a particular particle or region of interest can be resolved.

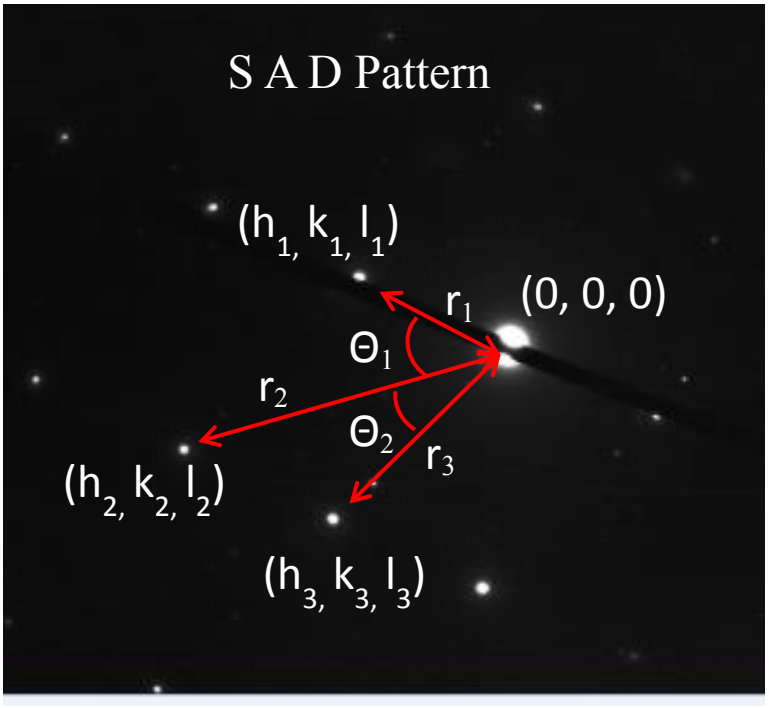

Figure 3.19 *An SAD diffraction pattern. (Image from Author's own collection)*

In a cubic crystalline material, the distance d between atomic planes with miller indices h, k, l, and with a lattice parameter α is given by the equation:

$$d(h,k,l) = \frac{\alpha}{\sqrt{h^2+k^2+l^2}} \qquad \textit{(Equation 3.7)}$$

The distance between the central transmitted spot, which is designated (0, 0, 0), and a diffracted spot is inversely proportional to inter planar spacing (Equation 3.4) and the angle between a pair of spots with the direct beam (0, 0, 0) equates to the angle between the pair of planes. Certain reflections from planar arrangements of atoms are forbidden due to destructive interference. Further details can be obtained from Williams and Carter [87]

The zone axis can be calculated using the Weiss Law equation

$$(h_1,k_1,l_1)x(h_2,k_2,l_2) = [UVW] \qquad \textit{(Equation 3.8)}$$

3.14.5 Convergent Beam Diffraction (CBED)

Obtaining diffraction patterns from very small particles in isolation from nearby particles is not always possible due to the size of the smallest SAD aperture (500nm). An alternative technique is to use convergent beam diffraction CBED.

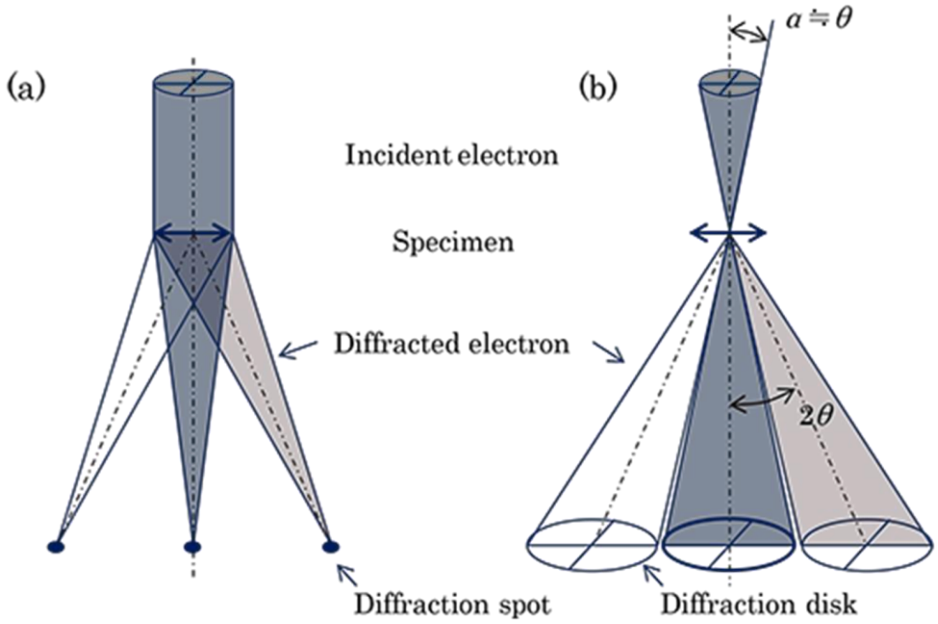

Figure 3.20 *Schematic of a ray diagram of a)SAD pattern and b) CBED diffraction pattern [90] .*

Instead of using a parallel beam to illuminate the specimen so that a diffraction pattern can be obtained, a convergent beam is used and overlapping diffraction discs are observed. By reducing the condenser aperture CBED discs can be separated and the discs are reduced in size by increasing the camera length. They can then be resolved by the same method as SAD patterns. Additional information on the structure of the specimen can be obtained from the patterns inside the disks [87] .

The convergent beam can be as small as a few tens of nm. This is an obvious advantage when examining smaller particles that would otherwise be very difficult to obtain SAD patterns from.

3.14.6 Scanning Transmission Electron Microscopy (STEM)

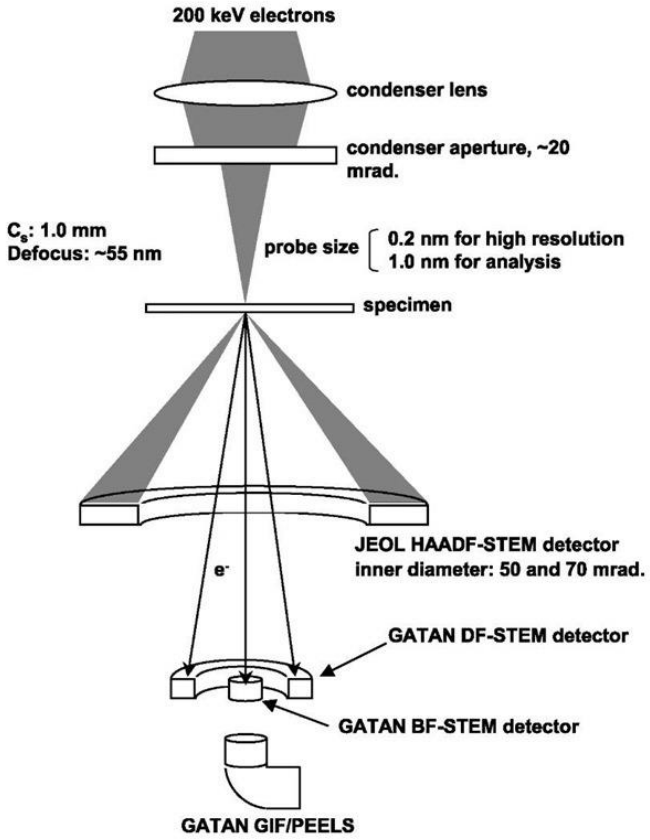

Figure 3.21 *Schematic of a ray diagram and the different detectors in a JEOL JEM2010F Microscope[90]*

Scanning Transmission Electron Microscopy combines the imaging technique of a raster as in an SEM with the transmission electron detection of a TEM. A convergent beam probe of as small as 0.2nm scans the electron transparent sample. In a conventional TEM a regular array of atoms will result in a spot in the diffraction pattern, in the STEM a regular array of atoms will result in diffraction discs as in CBED mode in a conventional TEM. Several detectors as seen in Figure 3.21 are located so that different imaging modes can be utilised.

The BF detector is located on the optic axis and images low angle scattered electrons transmitted. Contrast is observed due to the interference of the triple overlap region between the transmitted and the diffracted discs. An Annular Dark Field (ADF) detector forms an image from electrons scattered over wider angles and a High Angle Annular Dark Field (HAADF) detector forms an image from electrons scattered over greater angles. An Electron Energy Loss Spectroscopy (EELS) detector provides additional information from inelastic scattering events that can provide details of elements present in the sample and their chemical bonding.

3.14.7 EDX analysis in TEM/STEM

EDX analysis in a TEM or STEM uses the same principles as EDX in the SEM instrument but with two main differences. The voltage of the accelerating electrons is much higher in TEM/STEM instruments (up to 300keV) and the interaction volume in a TEM/STEM much less than in a bulk specimen as the TEM specimens are thinned foils of about 100nm thick. These two factors result in better resolution in terms of EDX analysis. Another consideration is the ZAF contribution to the quantitative analysis correction factor K. For thin specimens the X-ray absorption and fluorescence factors may be neglected which simplifies the process of calculating the K factor for EDX analysis in the TEM/STEM [87].

3.14.8 Instruments Used

TEM analysis was carried out using 3 different microscopes. Initial training was given on a Joel 2000FX fitted with a tungsten filament and operating at 200kV.

Images and diffraction patterns were recorded on photographic plates which were developed in a dark room laboratory. EDX analysis was carried out using an EDAX X-ray detector (model PV9757/32ME) and data analysed using EDAX Genesis software.

A Joel 3010 microscope fitted with a LaB_6 filament operating at 300KV was used for high resolution images which were recorded on a digital CCD camera and were processed using Digital Micrograph interface software package.

Diffraction patterns were also recorded on photographic plates. Due to filament failure a tungsten filament was used for a short time but soon another LaB_6 filament was fitted. An Oxford Instruments Link ISIS Pentafet EDX detector was used for elemental analysis and data was processed by ISIS Suite Revision 3.35

Advanced high resolution microscopy was carried out on a JEM 2100F microscope, fitted with an aberration corrector type CEOS GmbH 'CESCOR', and working at 200kV. EDX analysis was carried out using an EDAX optima 60 windowless SDD detector. Data was analysed using EDAX TEAM software. Scanning Transmission Electron Microscopy (STEM) mode was used in addition to (High Resolution) HRTEM imaging mode.

3.14.9 Gold Leaf Calibration

Although some of the regions of interest and some particles were identified using diffraction patterns recorded on film, most of the phase analysis was performed by taking digital HRTEM images and the using the FFT function in Digital Micrograph to reveal d spacing information from lattice fridges.

Calibration of the process was performed using a gold leaf sample on a copper grid as seen in Figure 3.22. A HRTEM image of the sample was taken and a FFT of the image has revealed a pair of spots assigned to the (220) orientation. From crystallographic data the d spacing for the (220) plane is 2.04Å.

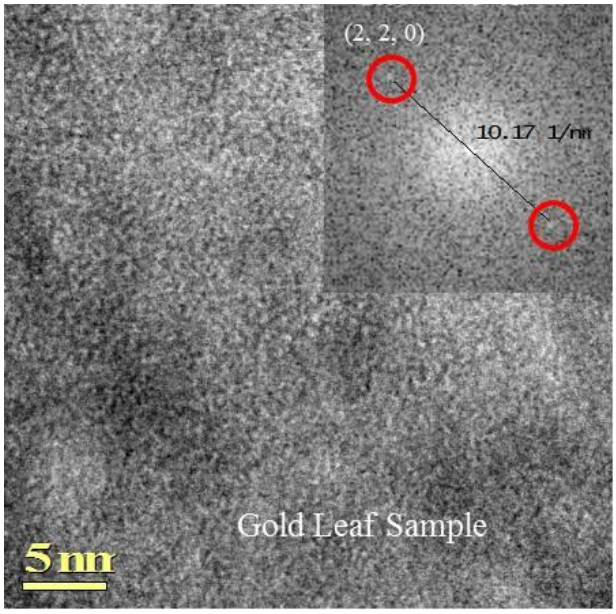

Figure 3.22 *HRTEM image with FFT showing the 2, 2, 0 diffraction spot (insert). Image from author's own collection.*

The calculated d spacing using the FFT image and the d spacing tool from the Digital Micrograph software was calculated to 1.97Å. This gives an error of about 0.07Å. This error margin was taken into consideration when assigning possible d spacing data to FFT spots.

3.15 Electron Backscatter Diffraction (EBSD) Analysis

Electron Backscatter Diffraction technique utilises the backscattered electrons diffracted from a bulk crystalline material when tilted to 70° to the incident electron source in an SEM. Inelastic scattering of a small percentage of electrons with a small loss of energy in effect form a divergent source of electrons that are then diffracted to form cones of electrons that are detected on a phosphor screen and are recorded on a CCD camera for processing as illustrated in Figure 3.23.

Patterns formed are equivalent to kikuchi diffraction observed in TEM. The images are processed to reduce noise and the patterns are resolved by software.

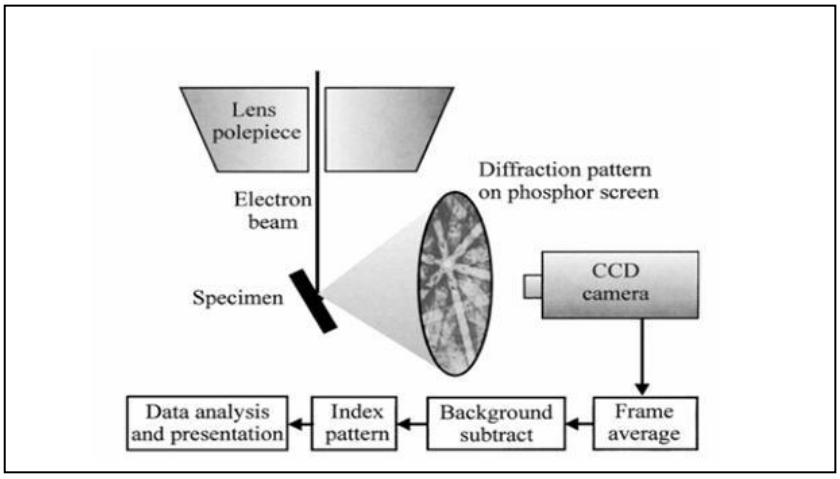

Figure 3.23 *Schematic of EBSD set up in an SEM. Image from Goodhew, Peter J., John Humphreys, and Richard Beanland, Electron microscopy and analysis, CRC Press, 2000.*

A sample is scanned and at each pixel point a pattern is resolved and the data stored. There are different ways in which the data is presented depending on the information that is required. Data can be represented in various formats such as orientation maps grain size analysis, grain boundary maps inverse pole figures and phase maps.

3.16 Particle Phase Identification

An important part of this thesis was the study of the nanoparticles present in both PM2000 and APMT. It was possible to identify phases of the particles observed by using a combination of EDX analysis and crystallographic data obtained from HRTEM images as mentioned in Section 3.13.

Table 3.3 *A list of the different Y Al O phases.*

Yttrium Aluminium	Acronym	Formula	Crystal Structure	Aluminium to Yttrium Ratio (Al:Y)
Garnet	YAG	$Y_3Al_5O_{12}$	Cubic	62.5 : 37.5
Perovskite	YAP	$YAlO_3$	Orthorhombic	50 : 50
Perovskite	YAP’	$YAlO_3$	Cubic	50 : 50
Monoclinic	YAM	$Y_4Al_2O_9$	Monoclinic	33.3 : 66.7
Hexagonal	YAH	$YAlO_3$	Hexagonal	50 : 50

The main particles in PM2000 are yttrium aluminium oxides [58] of which there are several types as listed in Table 3.3**.** By using EDX analysis the ratio of Al and Y signal was calculated from the quantitative analysis data. By comparing the known ratios to the observed ratios it was possible to narrow down the possible options. Since Al is present in the matrix of PM2000, quantitative data was adjusted for this by taking EDX analysis of the matrix nearby a particle and by using the Fe/Al ratio in the matrix the Al % wt. was adjusted accordingly. The Al to Y ratio of the different types of particle is distinct enough that even with the matrix content of Al it was easy to distinguish between the possible ratios. In the case where the ratio was 50:50 the crystallographic data and the diffraction patterns observed was normally sufficient to determine the type of particle observed. There were instances were none of the data was sufficiently definitive and some particles were not identified.

3.17 Particle Size Analysis

The size and distribution of the dispersoids in ODS steels is a key indicator as to the high temperature creep resistance of the alloy. A method of measuring and analysing the data was developed using Pebbles [93] software package.

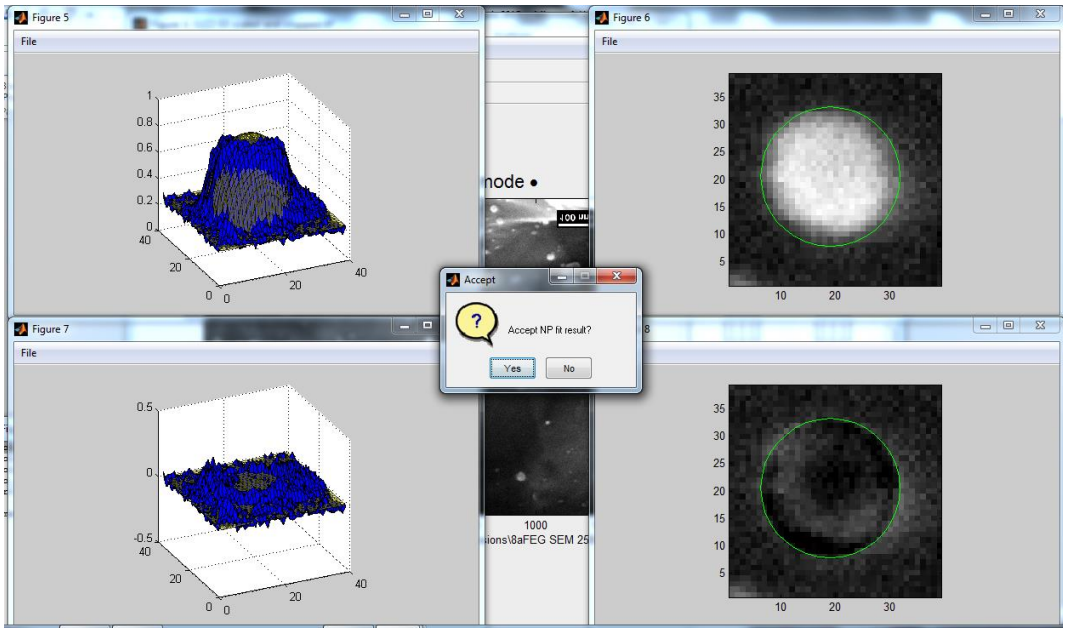

Figure 3.24 *Particle size analysis using 'Pebbles' software and a screen shot of the process [93].*

The software was designed for TEM images but work equally well with SEM images.

Samples were etched for 7 minutes in a solution of 10% HCl in methanol to reveal the nanoparticles in the SEM. Several images were taken in SED mode at different magnifications depending on the size of the particles that were observed. Images were uploaded to the Pebbles software.

A pointer is used to enlarge the image of a particular particle and the software fits the best circle around the particle as shown in the screen shot in Figure 3.24. The number of pixels in view in the enlargement window is controlled by the user. The user is then asked to accept or reject each fit so that the quality of the fit is controlled. Data is then exported and analysed in Excel spreadsheet to produce histograms. After some practice the process was found to be quick and reliable and was used for all the particle size analysis results in this thesis.

CHAPTER 4

Friction Stir Welding of Rolled PM2000

4.1 Introduction

A 4mm thick rolled PM2000 plate was supplied by Oak Ridge National Laboratory USA. The rolled plate was made from as extruded bar which was cut to 12mm thickness and heated to 300°C. The bar was then rolled at successive 5% reduction along the extrusion direction until a 4mm plate thickness was achieved. Finally a heat treatment for 10 minutes at 300°C was followed by a press to flatten the 4mm plate.

The plate was used to perform Friction Stir Welding (FSW) by TWI prior to the commencement of this project. The welds were bead on plate welds (BOP) and were numbered BOP 6, 7, 8, and 9 respectively. Only short end sections of the welds were available for analysis at the beginning of this project as most of the welds were used up by a previous project. A small section of the parent material was retained for characterisation purposes.

The weld parameters were as follows:

Tool down force = 26kN, Transverse speed = 100mm/s,

Rotational speed = 200rpm to 800rpm variable

The tool used was a PCBN W/Re hybrid tool by MegaStir ® with a 3.6mm stepped spiral probe and a 25mm diameter scroll shoulder.

Initially the tool was plunged into the plate at 800 rpm and once the plate was sufficiently plasticised, the rotational speed of the tool was reduced to 200 rpm. Stable conditions are normally achieved after a certain length of weld usually a few cm into the weld but in the case of BOP 7, the region being analysed was at the beginning of the weld and more than likely stable conditions had not been achieved.

The samples were analysed in the as-received condition and in the as-welded condition and in both cases with and without heat treatment at 1380°C.

4.2 Optical Microscopy

The as-received samples were polished to colloidal silica finish for DIC microscopy. The as-welded samples were etched in 10%HCl in methanol solution to reveal macroscopic features.

As-Received Condition

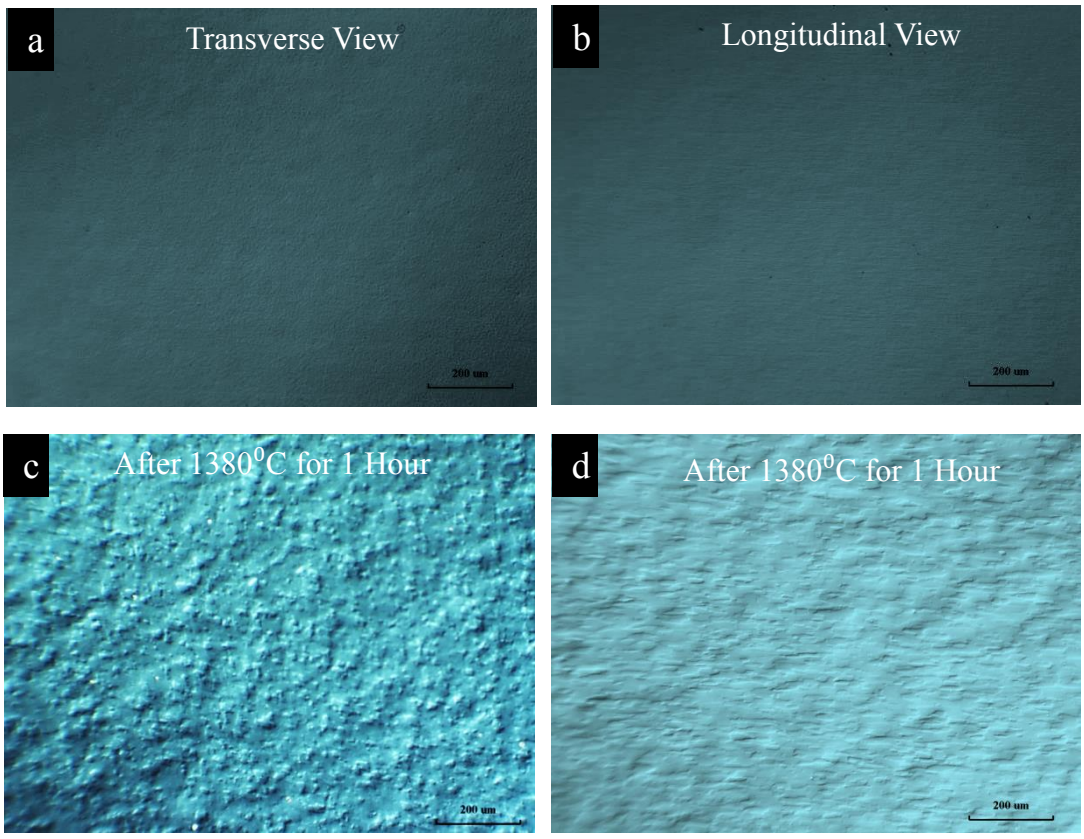

*Figure **4.1** DIC microscopy images of PM2000 rolled plate of, a) transverse view, b) longitudinal view, and after heat treatment at 1380°C for 1 hour of c) transverse view and d) longitudinal view.*

In Figure 4.1 DIC microscopy images show the transverse and longitudinal views of rolled PM2000 plate before and after heat treatment. The scale bars are all at 200

micro metres. The sub-micron grain structure of the as received plate typical of ODS steels is barely visible in the DIC images prior to the heat treatment. A recrystallised grain structure is observed post heat treatment with the equiaxed grain structure in the transverse view increasing in size to several microns and an elongated grain structure in the longitudinal view increasing in size to tens of microns.

As-Welded Condition

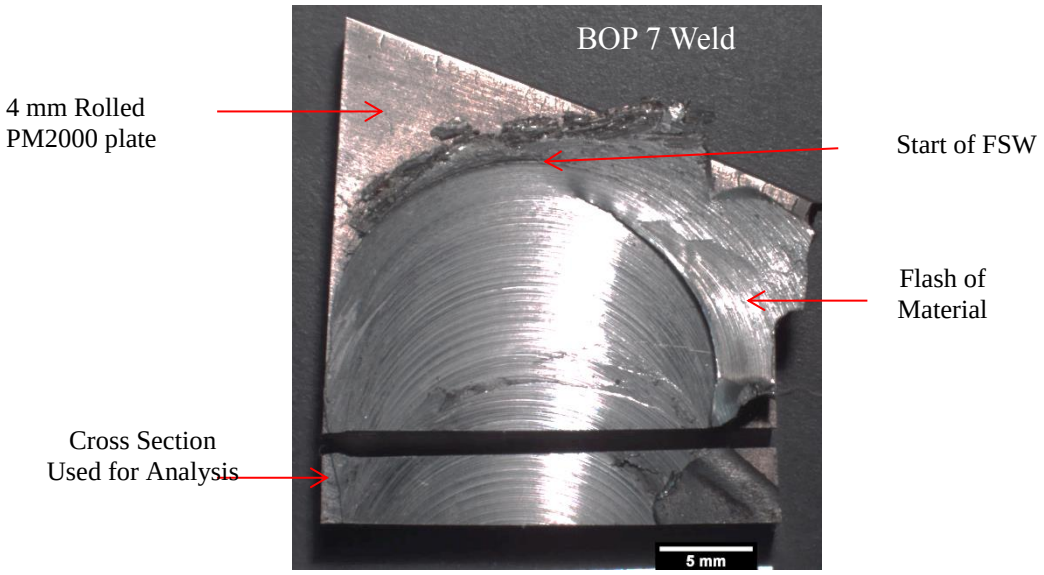

Figure 4.2 *Optical macrograph of BOP 7 with a cross section cut ready for analysis.*

Figure 4.2 shows an optical image of the BOP 7 weld. The weld was performed at an angle to the edge of the plate so that the cross section of the weld would show the longitudinal view of the parent microstructure as shown in the DIC image in Figure 4.1b and 4.1d. Typical of FSW is the concentric markings from the shoulder as it moves along the welding line. Flash of material can be seen which originates from the initial plunge of the tool into the plate.

As can be seen, only small end sections of the welds were available for this initial analysis. In order to try and maintain consistency in the results, most of the characterisation was performed on BOP 7 weld as far as possible but due to the

limited amount of material some aspects of analysis were carried out on other BOP welds as required.

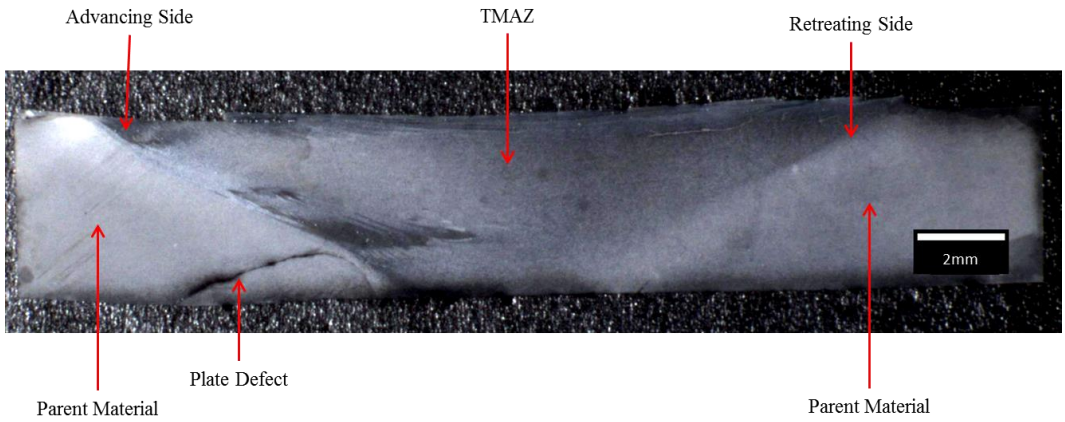

Figure 4.3 *Optical image of transverse view of BOP7 FSW showing the main features of the weld. (Etched with 10%HCl in Methanol)*

The optical image in Figure 4.3 shows the main features of the cross section of the BOP 7 weld. The parent material is the region either side of the weld that has not been thermo-mechanically affected by the weld.

The advancing side boundary is more prominent than the retreating side as this is the region where the material is sheared away from the parent region and then deposited at the retreating side of the weld. The TMAZ is the region where material was stirred to make the join. A good join, without any visible defects, and full penetration throughout the thickness of the sample was achieved by the FSW process. As can be seen in the image in Figure 4.3 there is a large crack near the advancing side of the weld. This was a defect present in the plate before the FSW process but it was quite useful because it acted as a reference point when looking at the weld before and after PWHT.

Post Weld Heat Treated Condition

The cross section of BOP 7 with PWHT is seen in Figure 4.4 with the main regions of the weld indicated with red arrows. An outline of the as-welded TMAZ traced from the as welded optical image in Figure 4.3 is shown for comparison.

The parent material region has recrystallised with grains of several microns in size and the TMAZ region has undergone recrystallisation with a large grain structure (> 0.5cm) probably due to the greatly reduced number of nucleation sites. The grains in the TMAZ are no longer elongated in the rolling direction as the stirring of the tool has evenly redistributed the nanoparticles particles in the TMAZ. The recrystallised grains in the TMAZ appear to have nucleated on the top surface and then grown down towards the base. The grains at the sides of the HAZ also appear to have grown to some extent, causing an elongated grain structure.

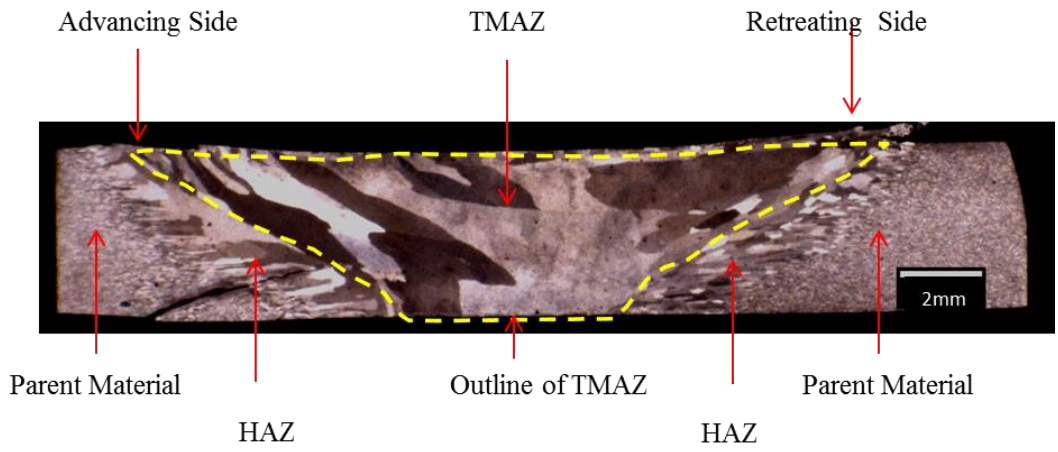

Figure 4.4 *Optical image of the transverse section of BOP7 FSW after the application of PWHT (etched with Kalling's reagent)*

A very large grain has formed in the middle of the TMAZ. At the retreating side of the weld the grain elongation is not as profound as in the advancing side. A close up of the advancing side of BOP 7 is shown in Figure 4.5. The dotted line indicates the boundary between the HAZ and the TMAZ regions of the weld.

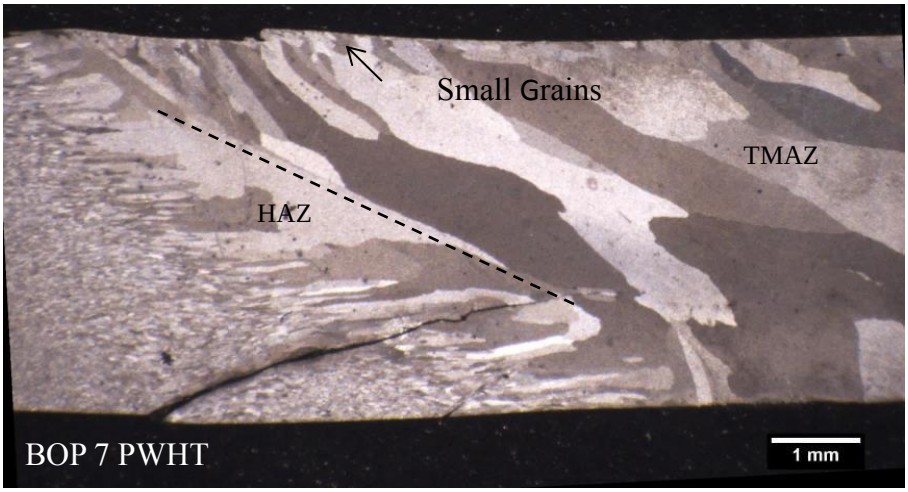

Figure 4.5 *Optical micrograph of the advancing side of BOP7 (etched with Kalling's Reagent)*

The large recrystallised grains in the TMAZ next to the boundary between the HAZ and the TMAZ at the advancing side of the weld are elongated along the material flow from the surface of the weld to the base. Small grains have formed on the surface of the TMAZ.

In the HAZ recrystallised grains have formed right next to the TMAZ but as you move away from the TMAZ the grains are gradually orientated to the near horizontal and are elongated in shape. This region had been affected by heat only as no stirring has taken place in this region yet the grains have recrystallised to fairly large size compared to the parent region, but not as big as the grains in the stir zone.

The shearing of material must create stresses in the surrounding area next to the advancing side but less so at the retreating side. This results in a difference in the number of nucleation sites with a difference in grain size evident between the advancing side and the retreating side. As the nanoparticles have not been stirred, they are still aligned in the rolling direction which results in the elongation of the grains. The heat that was experienced in this region during the FSW process has reduced the driving force for recrystallisation due to a degree of recovery, and probably reduced the pinning effect of the particles due to an element of particle coarsening as well. The net result is that the HAZ has undergone recrystallisation but an elongated grain growth due to the particle alignment.

This region is not distinguishable in the as welded image in Figure 4.3 and therefore was not labelled but as will be shown later in the hardness section the heat experienced in this region has had an effect on its recrystallisation behaviour and its mechanical properties.

A typical feature of FSW of steels is the near vertical grains as seen in Figure 4.5, just inside of the top of the advancing side of the THAZ. The grain morphology appears to follow the flow of material as it is sheared away from the surface and pulled downwards towards the bottom of the weld. This could be possibly due to the alignment of nanoparticles with the material flow along with the alignment and number of nucleation sites for recrystallisation with the formation of the new undeformed recrystallised grains stopping any further transformation. The small grains seen in Figure 4.5 are formed possibly due to the increased number of nucleation sites at the surface of the weld compared to the main body of the weld.

4.3 Hardness Profiles

As-Received Condition

Vickers hardness tests on the rolled PM2000 both in the as received condition and in the heat treated condition were performed in all three directions in order to check for any variation in the hardness number that may be present in the parent material.

Table 4.1 *Vickers hardness of as received and HT rolled PM2000 plate.*

Direction	**No of Indents**	**Average HV**	**Standard Deviation HV**
Plan	19	367	13
Transverse	12	370	12
Longitudinal	11	396	8
Plan HT	10	241	5
Transverse HT	10	227	6
Longitudinal HT	10	230	6

From Table 4.1 the hardness number for the as received material is much higher than the hardness number for the heat treated material with a difference of over 140 HV. Hot and cold rolling processes introduce deformation in the plate such as dislocations and additional grain boundaries which have the effect of increasing the hardness number. Heat treatment has the effect of lowering the hardness number as dislocations are reduced due to the high temperature applied, by way of recrystallisation and the increase in grain size which decreases the hardness due to the Hall Petch relationship.

Also from Table 4.1 there is a higher hardness number for the as-received longitudinal sample by about 26HV compared to the other directions. This is unexpected as the transverse direction has the smallest grain structure and due to the Hall-Petch relationship the hardness number should have been slightly higher for the transverse direction rather than the longitudinal direction. The hardness numbers are homogeneous in the 3 directions after the application of heat treatment.

As detailed records of the thermomechanical processing, that the as-rolled sample was subjected to, were not available but a possible explanation could be texture related.

As-Welded Condition

Hardness tests were performed on the cross section of the weld with 25 indents across three lines at 1.5mm, 2.5mm, and 3.5mm below the surface of the weld as shown in Figure 4.6. The depth varied across the top surface of the weld due to some of the material being displaced at the point where the shoulder made contact with the sample. The depth of the indents was measured at the parent material at either side of the weld and was set so that a clear line of indents could be made right across the sample.

In Figure 4.6 a graph of the hardness values across the weld at different depths of the sample is shown with an optical image of the transverse cross section of the weld. The array of indents is roughly indicated with dashed colour coded lines. Also indicated on the graph is the corresponding position of the TMAZ for each of the line of indents.

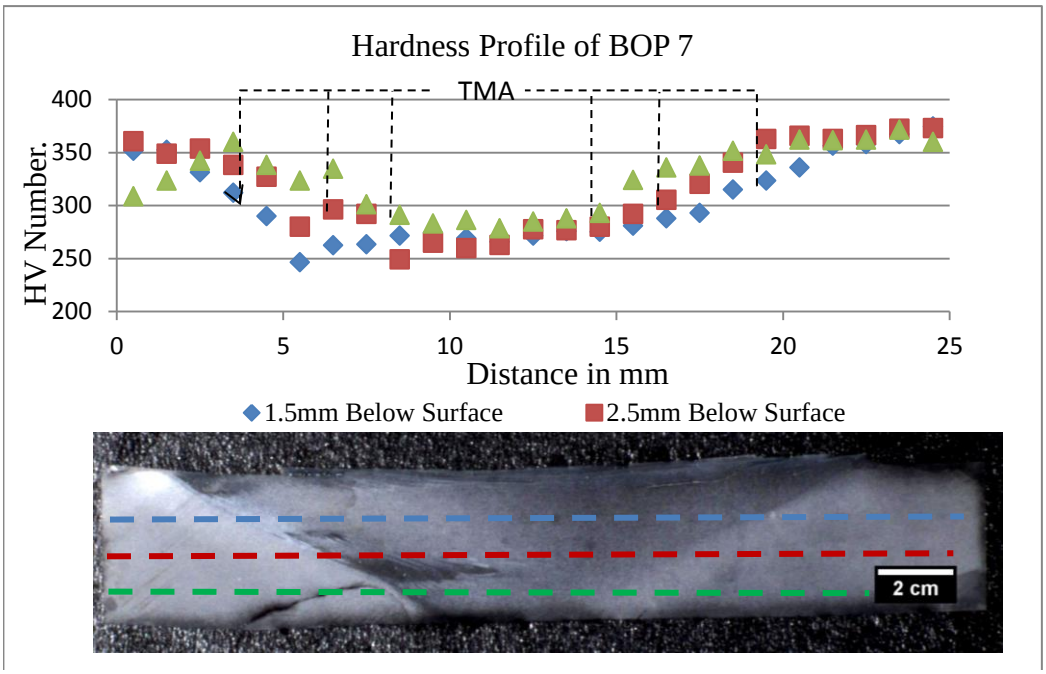

Figure 4.6 *Graph of hardness numbers of the transverse cross section of BOP 7 weld at depths of 1.5 mm, 2.5 mm and 3.5 mm with the corresponding image of the weld.*

As the indents enter the HAZ from the advancing side of the weld, the hardness value starts to decrease and continues to do so well into the TMAZ but then gradually starts to recover and once outside of the TMAZ and into the HAZ on the retreating side of the weld, the HV value recovers to near the parent material level.

It can be seen from the graph in Figure 4.6 that the hardness value from the advancing side towards the TMAZ starts to decrease at a point which corresponds to a distance of about 2 to 3 mm before the start of the TMAZ.

This region of the weld is the HAZ where only heat from the FSW process has affected this region. This region is not obvious when looking at the optical image in Figure 4.6 but the hardness profile clearly shows that the hardness value has been affected by the heat that this region has experienced. The FSW process has altered the microstructure of the TMAZ and the HAZ and this was evident not only in the hardness values but also in the recrystallisation behaviour of the sample. The sharpest contrast in the hardness is at the advancing side of the TMAZ.

Post Weld Heat Treated Condition

Hardness tests were carried out on the cross section of BOP 7 after the application of PWHT as shown in Figure 4.7. After 26 readings at 1.5 mm below the surface of the weld it was obvious that the hardness has changed from the as welded BOP 7 and that it no longer depended on the region of the weld as the readings were fairly homogeneous throughout the sample.

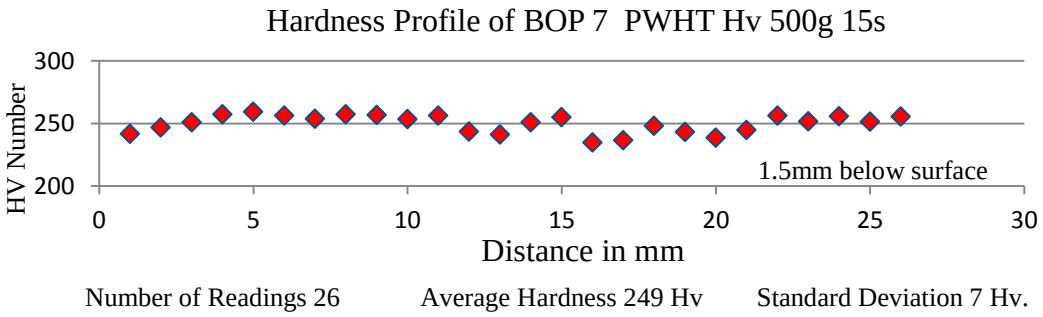

Figure 4.7 *Hardness profile of BOP 7 PWHT with 26 readings at 1.5mm below surface*

The application of PWHT has again reduced the number of dislocations and grain boundaries in the whole sample, due to atomic diffusion and recrystallisation, and therefore the hardness number has reduced accordingly.

4.4 Scanning Electron Microscopy

As-Received Condition

Channelling contrast images of as received PM2000 before and after the application of PWHT in the transverse and longitudinal views are shown in Figure 4.8. The images confirm the observations from the optical images in Figure 4.1 where the fine sub-micron flattened equiaxed grain structure in the transverse direction and an elongated grain structure seen in the longitudinal direction, i.e. along the extrusion and rolling direction, of the as received rolled PM2000 plate is typical of ODS steels [41].

After the application of the PWHT the grain size has increased but the grain structure is still elongated along the extrusion and rolling direction. The grain structure can best be described as a flattened cigar shape with an elliptical cross section of approximately 10µm high, 30µm wide and about 100µm long which gives a grain aspect ratio of about 3:1. The grains have undergone recrystallisation and the overall shape of the grains has not altered but the dimensions of the grains are much increased from the sub-micron grain structure of the as received material.

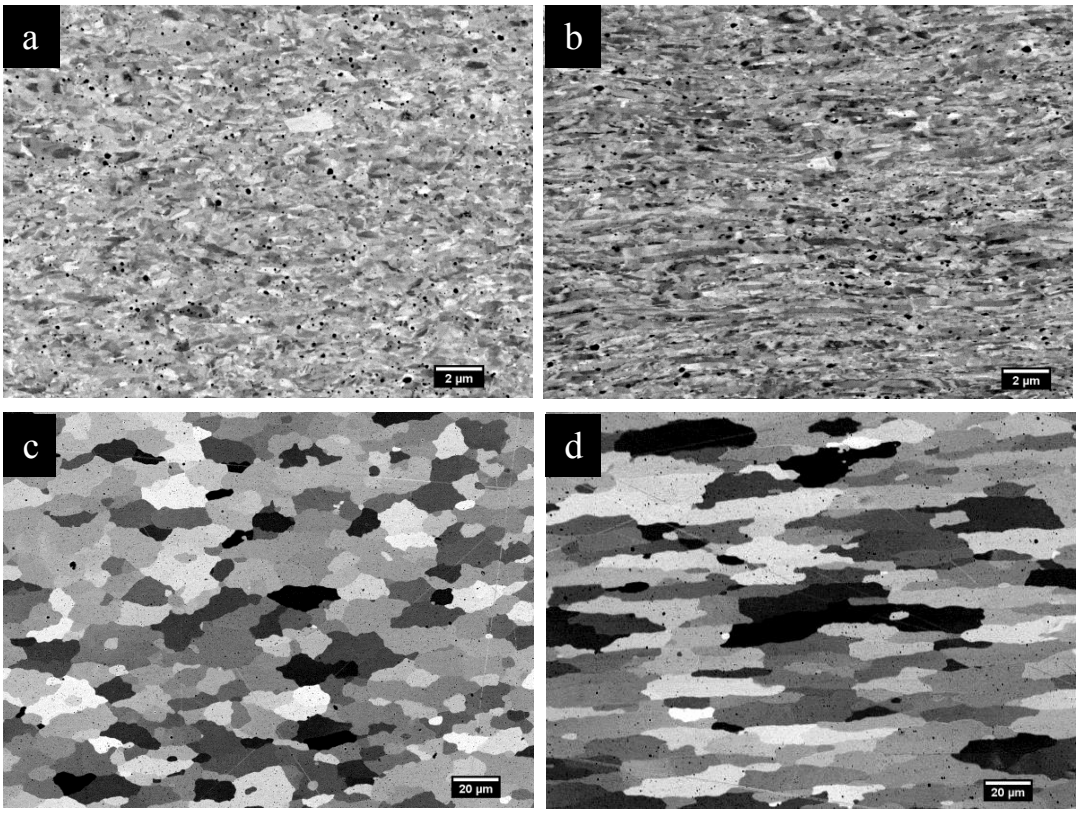

Figure 4.8 *Channelling contrast images of as received 4mm PM2000 rolled plate of a) transverse, and b) the longitudinal views, and after heat treatment at 1380°C for 1 hour of c) transverse and d) longitudinal views.*

As-Welded Condition

The as-welded BOP 7 sample was examined in backscatter mode and the channelling contrast images are presented in Figure 4.9. The sub-micron grain structure of the parent material has been altered to a coarser equiaxed grain structure of several micro meters in size in the TMAZ.

The combination of the deformation due to the rotation of the tool, which had provided the critical stress required, and the elevated temperature due to the frictional heat produced by the shoulder and the tool, had resulted in the dynamic recrystallisation of the TMAZ.

From the advancing side images of the cross section shown in Figure 4.9a and c, the outline of the TMAZ is visible as the transition of the two different grain structures is well defined.

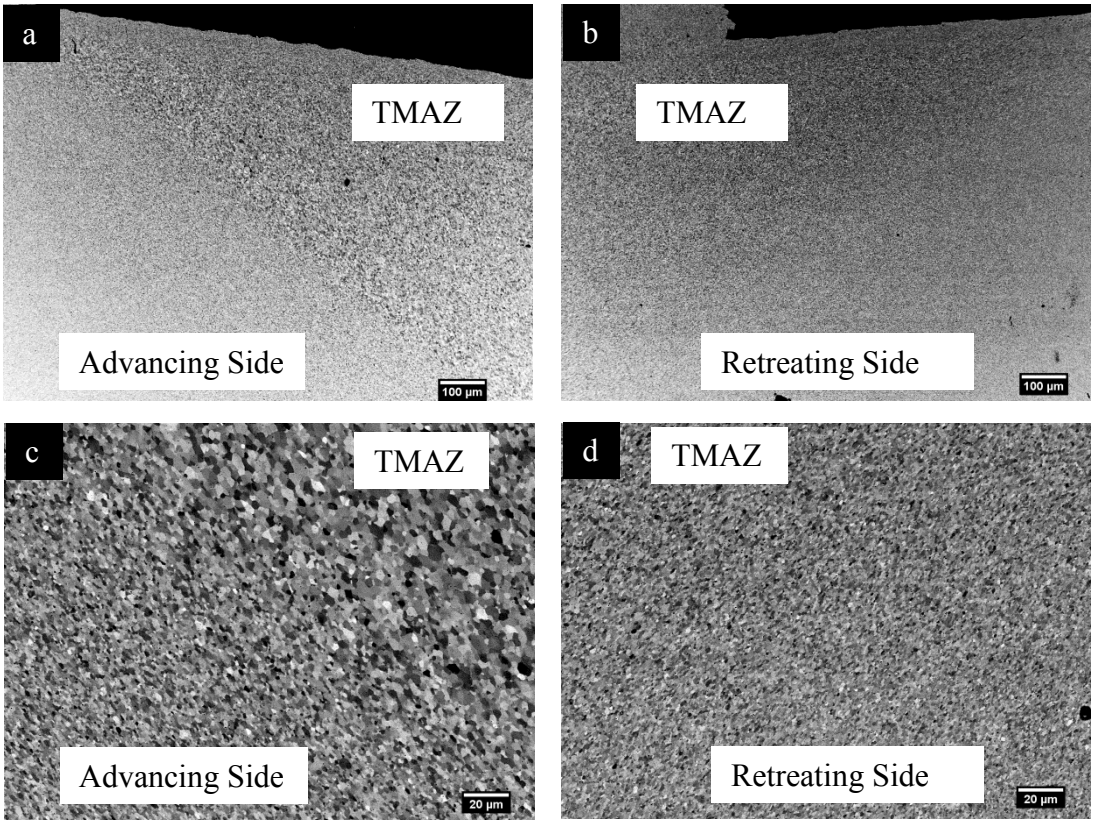

Figure 4.9 *Channelling contrast images of a) and c) advancing side and b) and d) retreating side of BOP 7 as welded.*

Scanning across from the parent material, the grain size is increasing as you approach the TMAZ. This confirms the pre-anneal effect of the heat generated by the FSW process in the HAZ where the stored energy has decreased by the reduction in the grain boundary energy [94].

In the retreating side images of the cross section of the sample there is a much more gradual transition from the TMAZ to the parent material grain structure. The change of the microstructure in the TMAZ is indicative of the fact that the alignment of the nanoparticles is no longer along the rolling direction but because of the stirring of the FSW tool the nanoparticles are more uniformly distributed in the TMAZ and the subsequent grain structure reflects this new arrangement of nanoparticles. The microstructural changes seen in the images are in agreement with the hardness profile measurements taken across the sample where the biggest change in the hardness number corresponds to the biggest change in grain size.

There is a sharper decrease in hardness number from the parent material to the TMAZ at the advancing side and then a gradual recovery of the hardness number from the TMAZ into the parent material in the retreating side of the weld.

Post Weld Heat Treated Condition

Channelling contrast images of the FSW BOP 7 with PWHT are shown in Figure 4.10. The grain structure in the TMAZ is made up of large grains typical of recrystallisation (although some researchers attribute this to secondary recrystallisation) as seen in the previous optical image in Figure 4.4 The advancing side of the weld, as seen in Figure 4.10 a line of discontinuity of the grain morphology can be seen between the HAZ and the TMAZ. This is not present in the retreating side of the weld. This line corresponds to the boundary of the TMAZ and the HAZ which is more pronounced at the advancing side of the weld.

As you move from the parent material to the HAZ-TMAZ boundary on the advancing side, the grain structure is one of increasing in size but still elongated in shape due to the particle alignment. The parent region has recrystallised with the application of PWHT with an increased grain size.

The HAZ has recrystallised with a near horizontal grain orientation with the size of the grains increasing and the aspect ratio of the grains decreasing as you approach the TMAZ boundary.

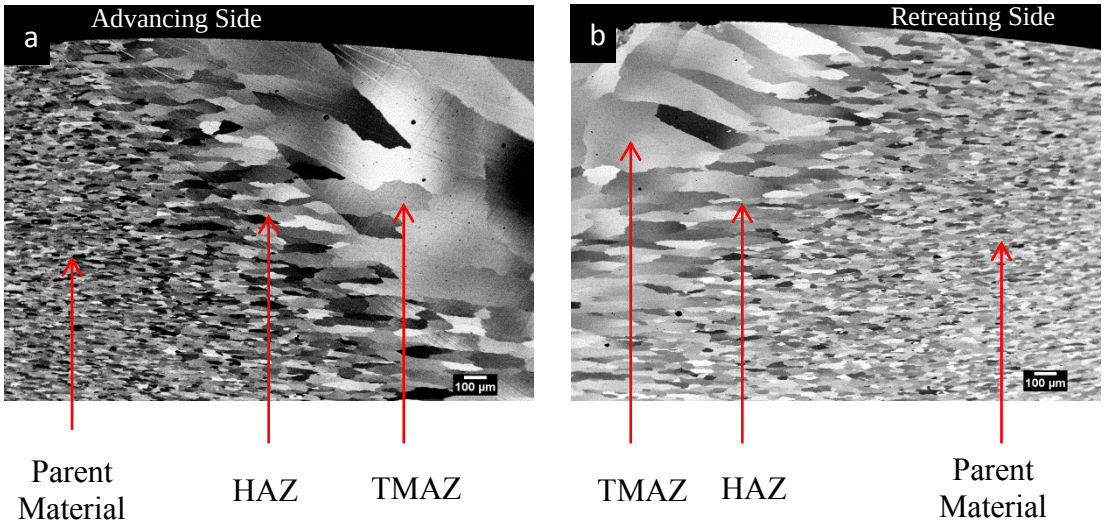

Figure 4.10 *Channelling contrast images of BOP 7 with PWHT showing a) advancing side and b) retreating side of the cross section of the weld.*

The HAZ has recrystallised with a near horizontal grain orientation with the size of the grains increasing and the aspect ratio of the grains decreasing as you approach the TMAZ boundary.

The frictional heat from the tool of the FSW process prior to the PWHT, on this region has resulted in an increased grain size, probably due to recovery reducing the driving force, which varied with the distance away from the TMAZ. The sub-micron grain structure due to its small size restricts grain boundary bulging, [41]. The increase in grain size means that the restriction in grain boundary bulging is reduced. As this effect decreases with increasing distance away from the source of the heat i.e. the TMAZ, so does the grain size which is decreasing as you approach the parent region as can be seen in Figure 4.10

On the retreating side of the weld a similar effect is observed but the grain size difference is not as well defined as in the advancing side. You can still distinguish the TMAZ and the HAZ but the boundary is not as clear as in the advancing side.

4.5 Particle Size Analysis

All the samples were etched in 10% HCl solution in methanol in an ultrasound bath for 7 minutes. The samples were then analysed in the SEM in SED mode. The magnification of the images used depended on the size and number of particles in the image. Pebbles software was used to measure the diameter of the particles and the data was exported to Excel for analysis.

As-Received Condition

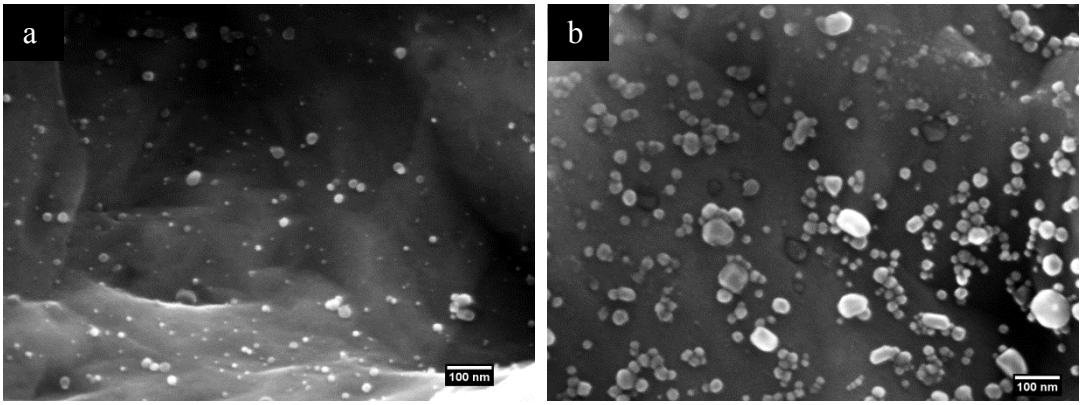

Figure 4.11 *SEM images of etched samples of rolled PM2000 a) as received and b) heat treated.*

Two samples of plan section, as received rolled PM2000 were used for this analysis. One of the samples was heat treated at 1380°C for 1 hour.

As can be seen from the SEM images in Figures 4.11, the particle size distribution has altered with the application of heat treatment. The particle size analysis results are shown in Figure 4.12. Particles in the as-received condition have an average size of 11nm with a standard deviation of 8nm. After the application of heat treatment the average particle size has increased to 27nm and with a standard deviation of 11nm.

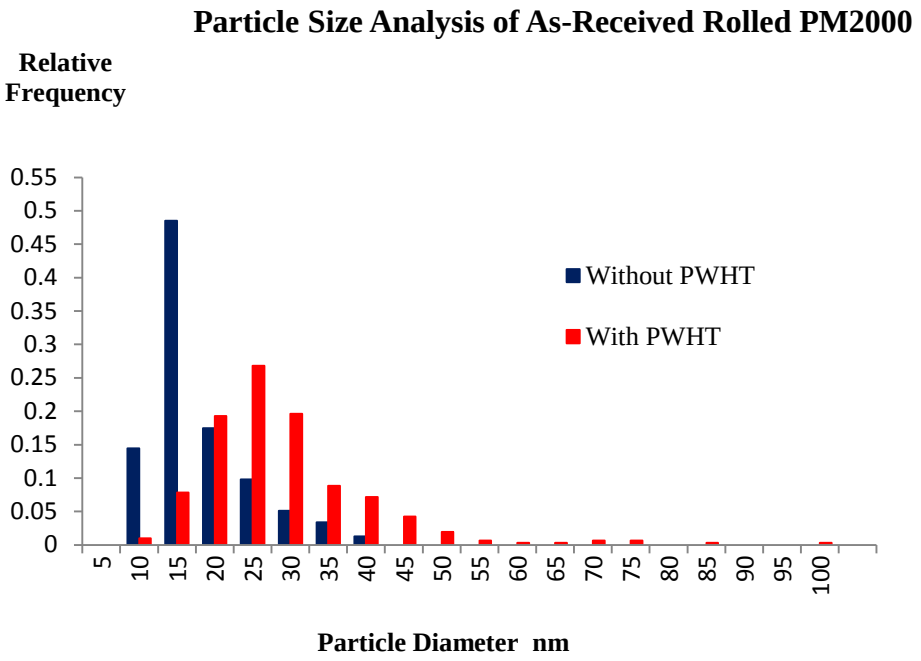

Figure 4.12 *Histogram of the particle size analysis of as-received rolled PM2000 with and without HT.*

The heat treatment has increased the average size of the dispersoid nanoparticles by more than two times and has slightly increased the spread of the size distribution i.e. the standard deviation of the range of sizes from 8nm to 11nm. Coarsening of the nanoparticles after the application of heat treatment is well documented in ODS steels and the above results are in line with literature [4, 95].

As Welded Condition

Two samples of BOP 7 cross sections, one with and one without PWHT were etched in order to reveal nanoparticles under an SEM microscope. Once again SEM images were processed using PEBBLES software and the data exported to EXCEL for analysis. Histograms are presented in Figure 4.13. The histogram of particle size analysis presented in Figure 4.13 shows the difference in the distributions of the particles within the TMAZ.

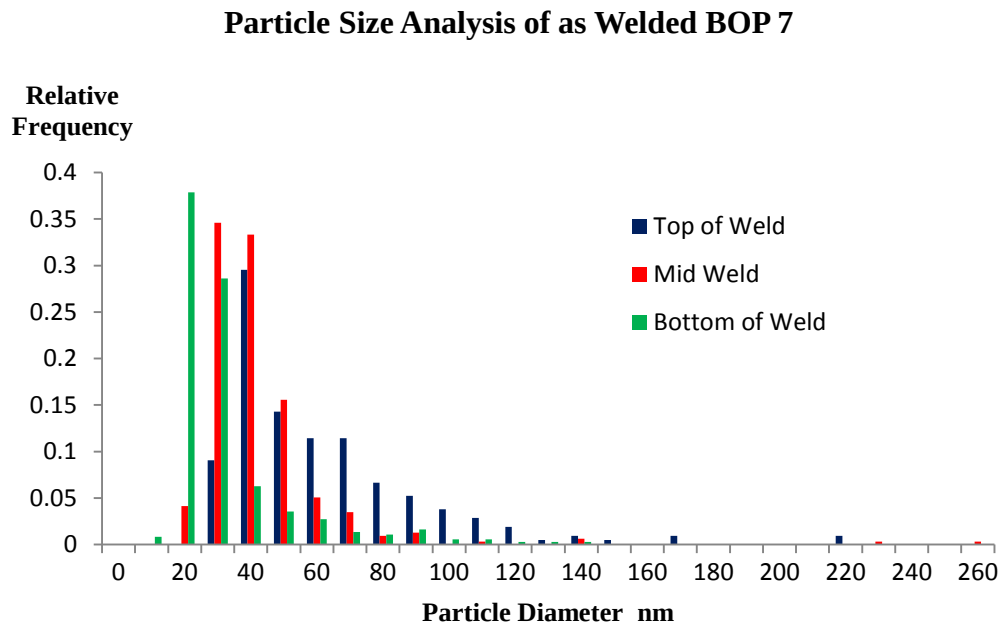

Figure 4.13 *Particle size analysis of BOP 7 from the top, middle and bottom of the TMAZ.*

Three regions were selected, top, middle and bottom of weld. The mean size for the top of the weld was 57nm with a standard deviation of 31nm. In the middle of the weld the mean size of nanoparticles was 37 nm and a standard deviation of 22nm. In the bottom of the weld the mean particle size was 35 nm with a standard deviation of 19nm.

The distribution is coarser near the top of the weld but as you analyse the particles further below the surface there is less coarsening. This could be related to the different temperatures between the top part of the weld and the rest of the stir zone, and the amount of time at that temperature that the particles experience in the different parts of the weld with a temperature difference of as much as 200°C [78, 96].

Post Weld Heat Treated Condition

A histogram of the particle size analysis is presented in Figure 4.14. Once again the three regions selected were, near the top of the weld, middle of the weld and bottom of the weld. Differences in the size distribution of the nanoparticles in the TMAZ of

the weld are seen corresponding to the differences in temperatures experienced during the FSW process.

The mean particle size of the nanoparticles near the top, middle and bottom of the weld was calculated to 99nm, 59nm, and 43nm respectively with a standard deviation of 35nm, 32nm and 11nm respectively.

PWHT is at a temperature of 1380^0C for 1 hour. In the FSW process, the maximum temperature experienced is in the region near the surface and is about 1000°C [96] and the duration at that temperature is much shorter as the tool bit is travelling at 100mm/m in the welding direction.

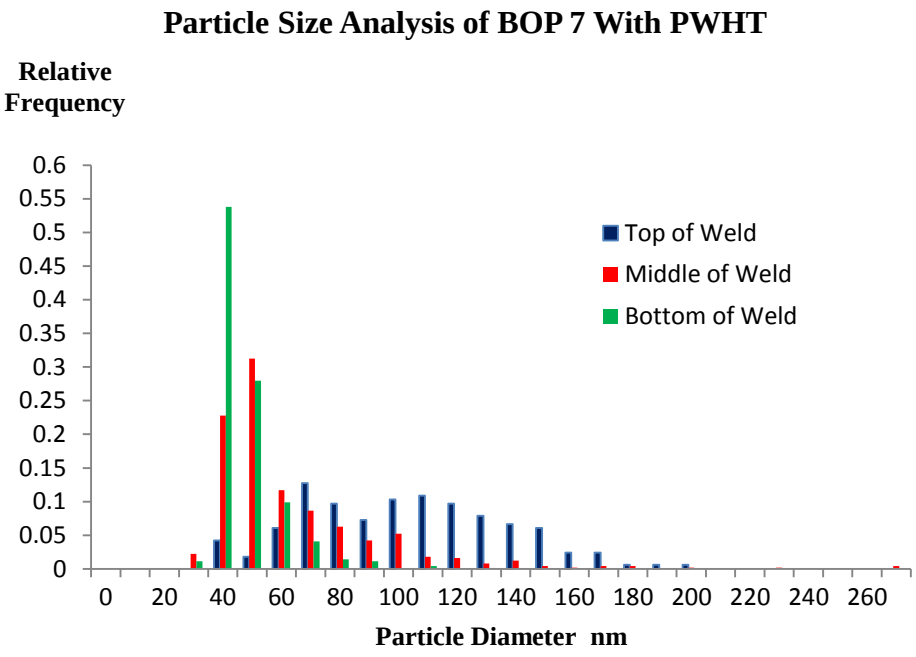

Figure 4.14 *Particle size analysis of BOP 7 with PWHT*

The longer exposure to the PWHT at the higher temperature would be expected to coarsen the particles much more than the friction stir process and therefore there should not be any significant difference in the particle size analysis between the three different regions of the weld. This is not the case as the histogram in Figure 4.14

shows. The PWHT has had a bigger effect in the size distribution of the particles near the surface of the weld than the middle and less so near the bottom of the weld.

In order to highlight the differences in particle size analysis a bar graph of the mean particle sizes in the as received sample and at the three regions with and without the application of heat treatment is illustrated in Figure 4.15. In the as-received condition, nanoparticles after heat treatment have coarsened by a factor of more than 2. In the as welded sample the effect of the FSW process is greater than the effect of the heat treatment on the as received sample. This seems to suggest that the stirring in combination with the heat experienced in the stir zone coarsens the nanoparticles more than the heat treatment alone.

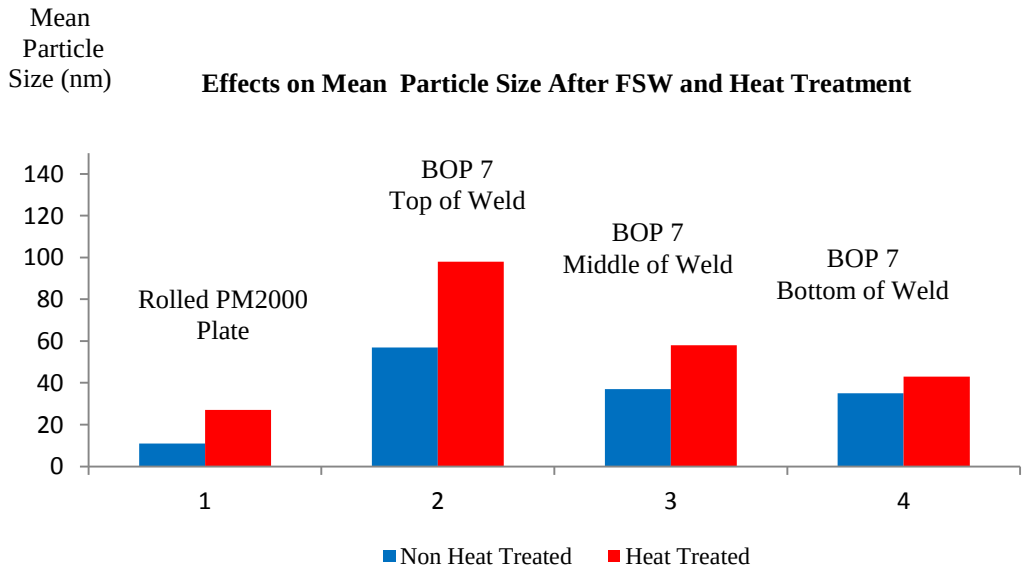

Figure 4.15 *A bar chart of mean particle size in the as received rolled PM2000 and the different regions of BOP 7 weld with and without the application of PWHT.*

The maximum temperature experienced by the particles deeper in the stir region is lower due to the distance away from the shoulder which is the main source of the frictional heat. Additionally the flow rate of the plasticised material is reduced deeper into the weld due to the smaller diameter of the tool.

The combination of the frictional heat generated by the rotation of the tool and the flow rate of material has resulted in particles near the surface to form a larger number of clusters, more than in the middle and bottom of the weld. Once PWHT is applied those clustered particles then consolidate and reform to an equilibrium shape depending on the type of particle that is formed. This results in a bimodal distribution as seen in Figure 4.14 in the top section of the TMAZ of the weld.

SEM images in SED mode of the three regions together with EDX of a particle is presented in Figure 4.16. Images a, c and d are of the top, middle and the bottom of the weld respectively.

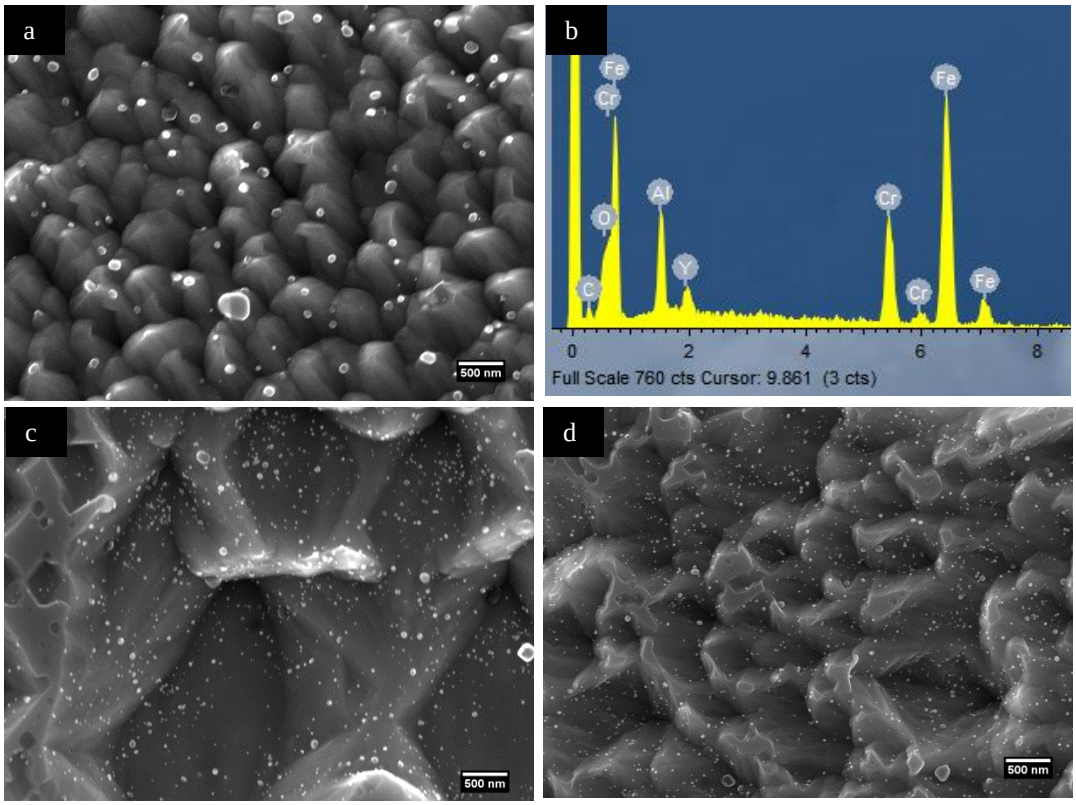

Figure 4.16 *SEM images in SED mode of a) the top, c) middle and d) bottom of the BOP 7 FSW. All images are at the same magnification. The EDX spectrum in (b) confirms the presence of Y-Al-O particles in image (a).*

Figure 4.16b is the EDX spectrum of a particle in image a. It is clear that, as all the images are at the same scale, there is a marked difference in the size distribution of

particles in the top of the weld compared to the middle and bottom regions of the TMAZ. The EDX analysis confirms the presence of Y-Al-O particles in the images.

4.6 Particle Phase Identification

The as-received sample was examined in the SEM in backscatter mode. EDX analysis was carried out to establish the nature of the nanoparticles seen. Figure 4.17 shows an image of the as received parent material with a mixture of both Al, and Al with Y rich oxide particles as confirmed by the EDX results (inserts).

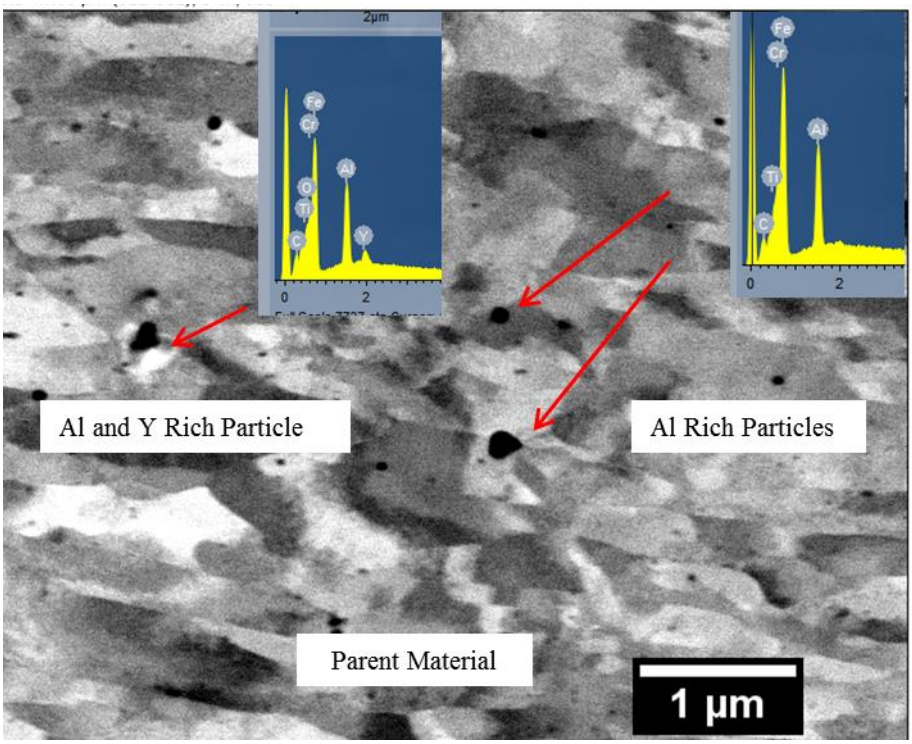

Figure 4.17 *Backscatter image of as received Rolled PM2000. EDX analysis has revealed a mixture of Al rich and Al Y rich oxide particles.*

Several particles were analysed at different locations in the sample. Particles were mainly Al rich oxides and Y-Al rich oxides. Further examination was undertaken to study the nanoparticles in PM2000. A carbon extraction TEM sample was prepared from the as received material. Carbon extraction lifts the nanoparticles from the

matrix and therefore allows the study of these particles without the presence of the matrix.

A carbon extraction replica from the as received rolled PM2000 was examined in the TEM. The low magnification image in Figure 4.18 shows the alignment of the nanoparticles along the extrusion and rolling direction. This alignment has been shown to be responsible for the elongated grain structure as they are a barrier for the grains to grow in other directions other than the rolling direction as discussed in the literature review in Section 2.5. This uneven growth of the grain boundaries along the rolling direction gives rise to the elongation of the grains [40].

HRTEM images of nanoparticles in the carbon extraction replicas in combination with EDX analysis was used to identify the phases.

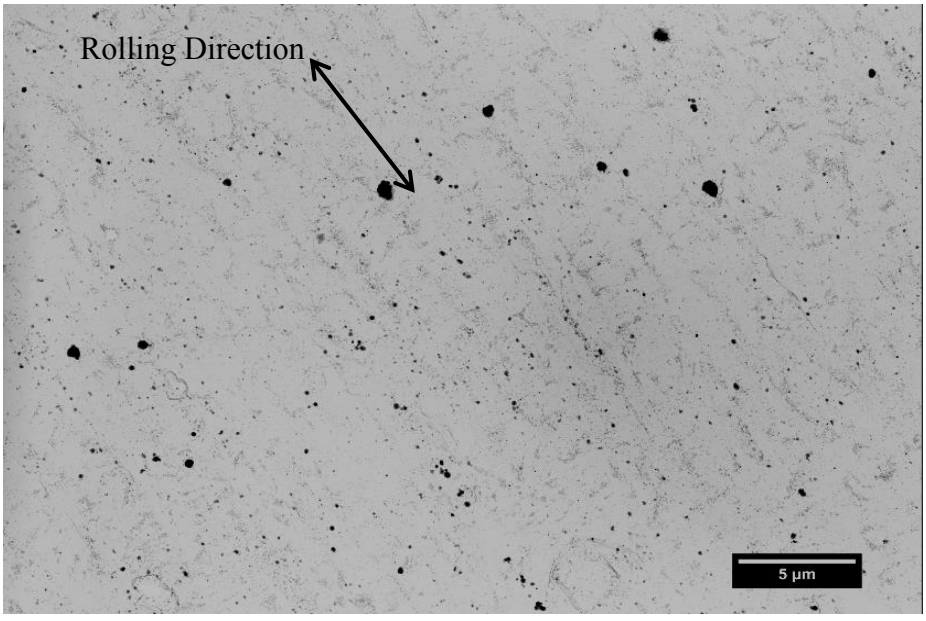

Figure 4.18 *A TEM image of nanoparticles in a carbon extraction replica of as received rolled PM2000 sample.*

Depending on the instrument used, lattice resolution images were used along with FFT of the images in order to measure d-spacing and angles between the spots to try to identify the phase of a particle. Diffraction patterns and in some cases CBED

patterns were used if HRTEM images were difficult to obtain, especially if some of the particles were too thick for HRTEM imaging. EDX analysis from the backscatter image in Figure 4.17 showed that the particles present are mainly of Al and Y Al oxides.

One of the easier particles to identify is aluminium oxide particles as they tend to be larger than the Y Al O nanoparticles. In Figure 4.19 a typical Al_2O_3 particle in a carbon extraction replica of the as-received rolled PM2000, is imaged in the TEM. SAD pattern was obtained and using crystallographic data the particle was resolved to be on the [-2, 8, -1] zone axis.

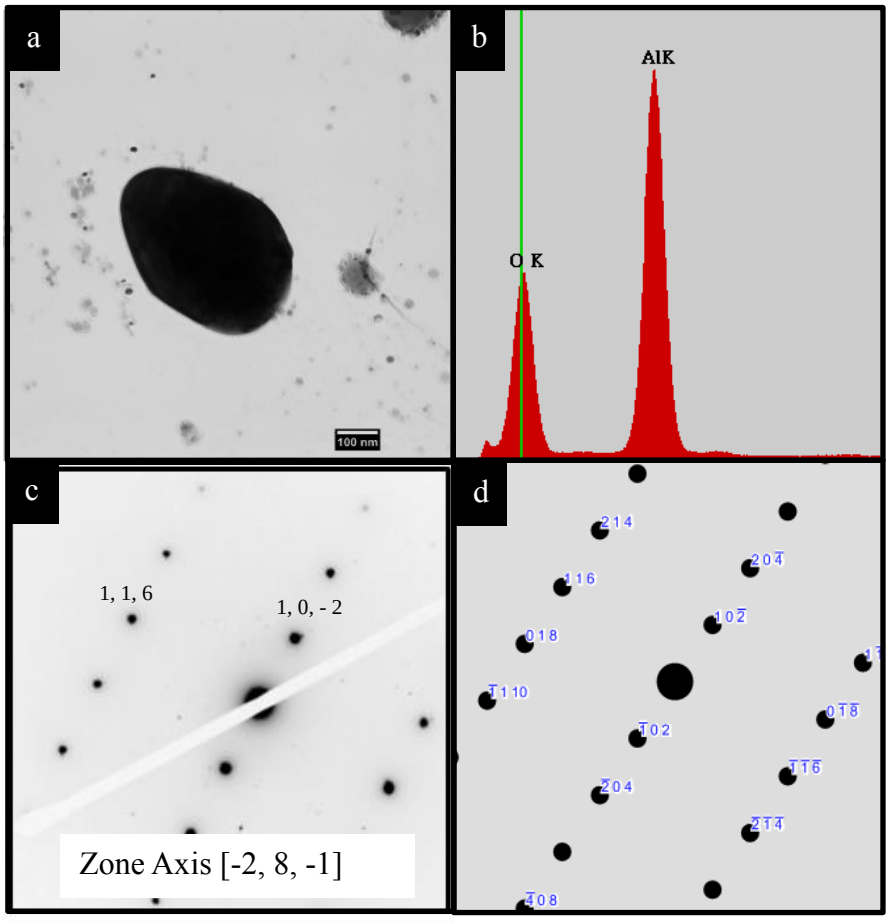

Figure 4.19 *A resolved Al_2O_3 particle from carbon extraction replica sample using a) TEM image, b) EDX analysis, c) diffraction pattern and d) simulated diffraction pattern using CrystalMaker software package.*

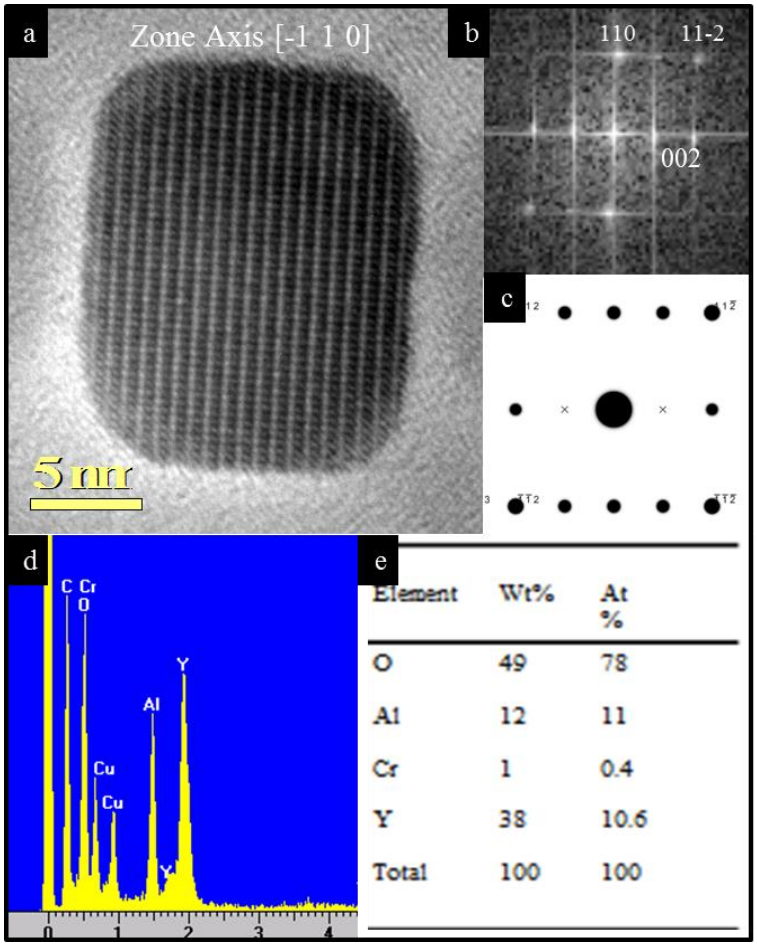

Figure 4.20 *A resolved YAP type particle with a) HRTEM image, b) FFT of the HRTEM image, c) a simulated diffraction pattern from CrystalMaker software, d) EDX spectrum analysis of the particle and e) quantification results of the EDX analysis of the particle. Note the rectangular shape of the particle.*

Another particle identified from the same TEM sample is a Y Al rich particle as seen in Figure 4.20. EDX analysis confirms the presence of Y, Al and O. The atomic % ratio, from the EDX analysis, of Al to Y ratio of 1 (11:10.6) suggests that the possible phases are YAP, YAP′ or YAH. A HRTEM image was obtained for the particle. From the FFT, lattice d-spacings were measured and using crystallographic data the particle was resolved to be a YAP phase with a zone axis [-1, 1, 0].

Several particles have been investigated, and YAG and YAP phases were the most common phases amongst the Y Al rich particles.

4.7 Study of Boron Nitride Tool Fragments

From the very first polishing steps of sample preparation of the BOP welds it became apparent that the TMAZ had inclusions embedded in it. These were much harder than the main body of the sample as the inclusions would scratch the surface of the sample as it was polished at each step. Figure 4.21 shows a DIC image of BOP 6 after the initial polishing steps using SiC papers.

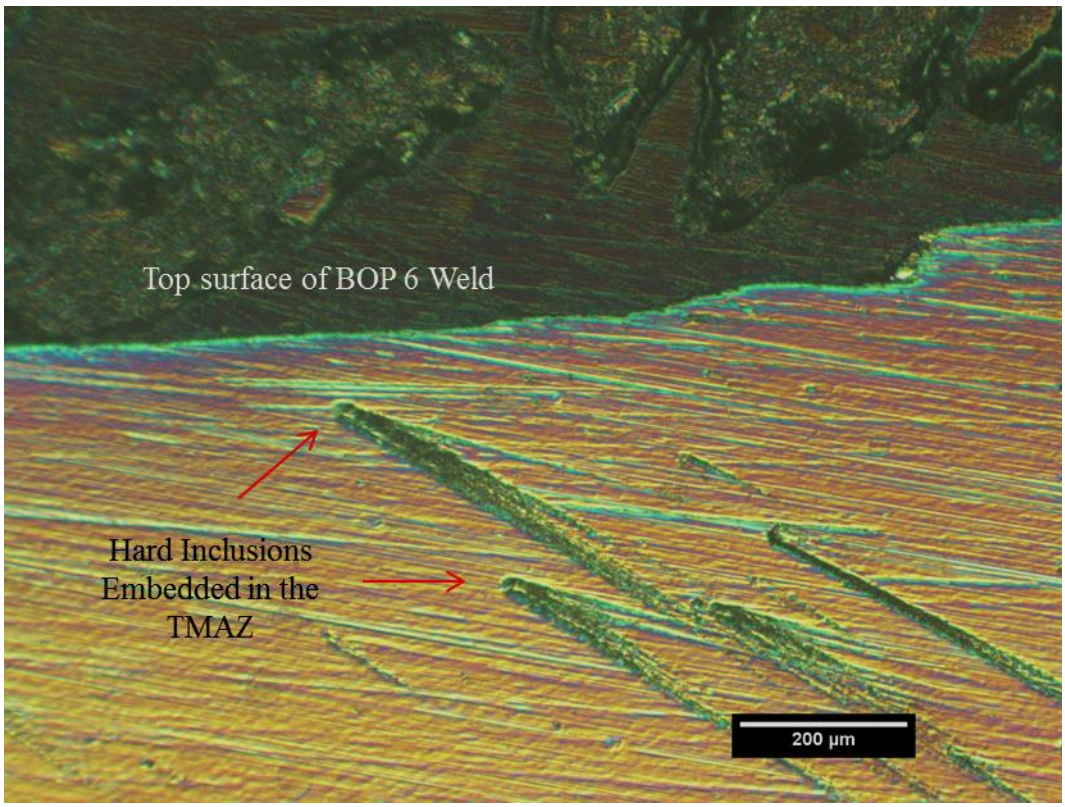

Figure 4.21 *DIC image of a cross section of BOP 6 weld showing hard inclusions embedded in the TMAZ.*

The DIC image in Figure 4.21 suggests that the inclusions were even harder than the SiC grains in the polishing papers because the inclusions are protruding above the surface and as they are polished away fragments of the inclusions are dragged across the sample causing the scratches on the polished surface.

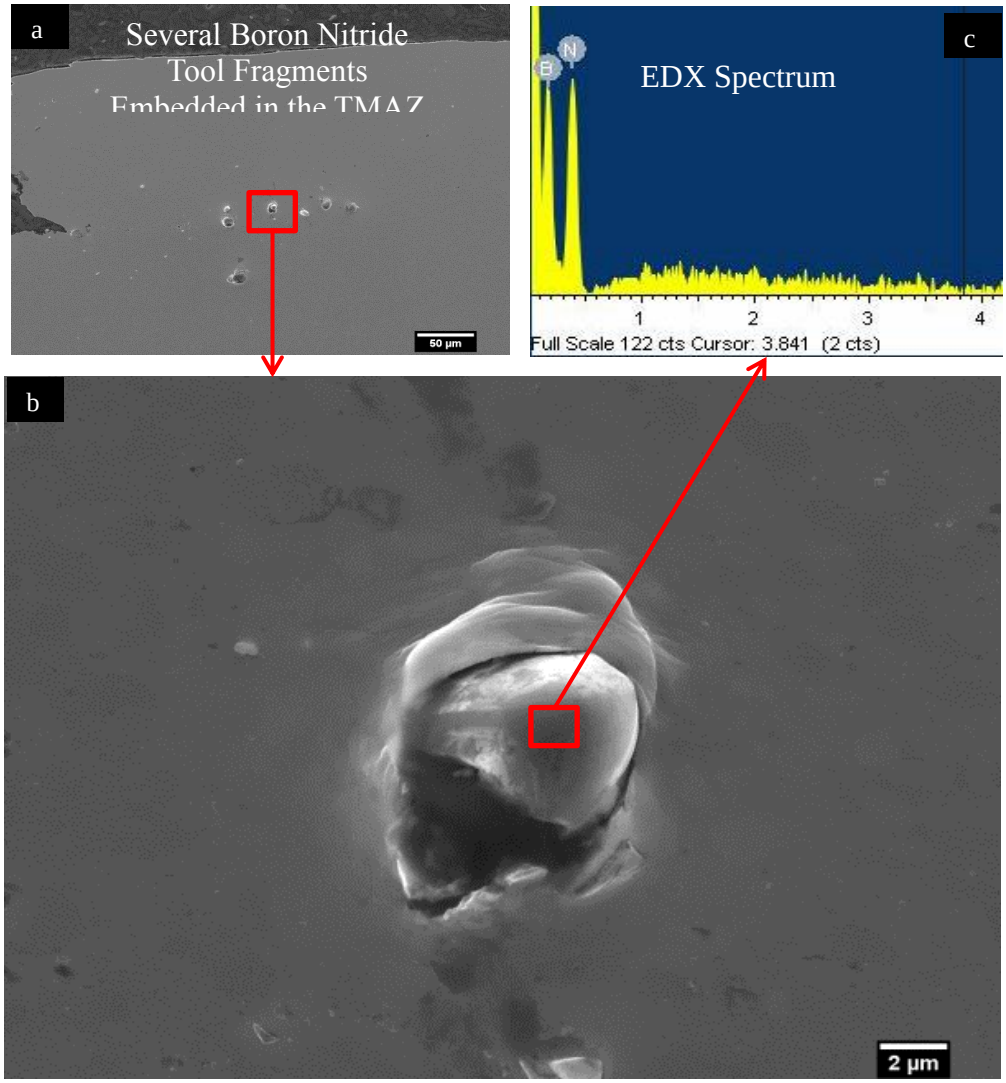

Figure 4.22 *SED images of a) fragments of the PCBN tool embedded in the weld b) closer look at a single fragment and c) EDX analysis confirming the presence of B and N in the fragment.*

The BOP 7 as welded cross section was analysed using the SED mode. Examination of the TMAZ revealed several fragments embedded mainly on the advancing side of the weld at the TMAZ boundary with the parent material. Fragments were also observed near the top surface of the weld and a few scattered within the TMAZ.

The sample seen in Figure 4.22b shows a typical tool fragment that was embedded near the top surface of the weld. EDX analysis confirmed the presence of B and N in the fragments as shown in Figure 4.22c.

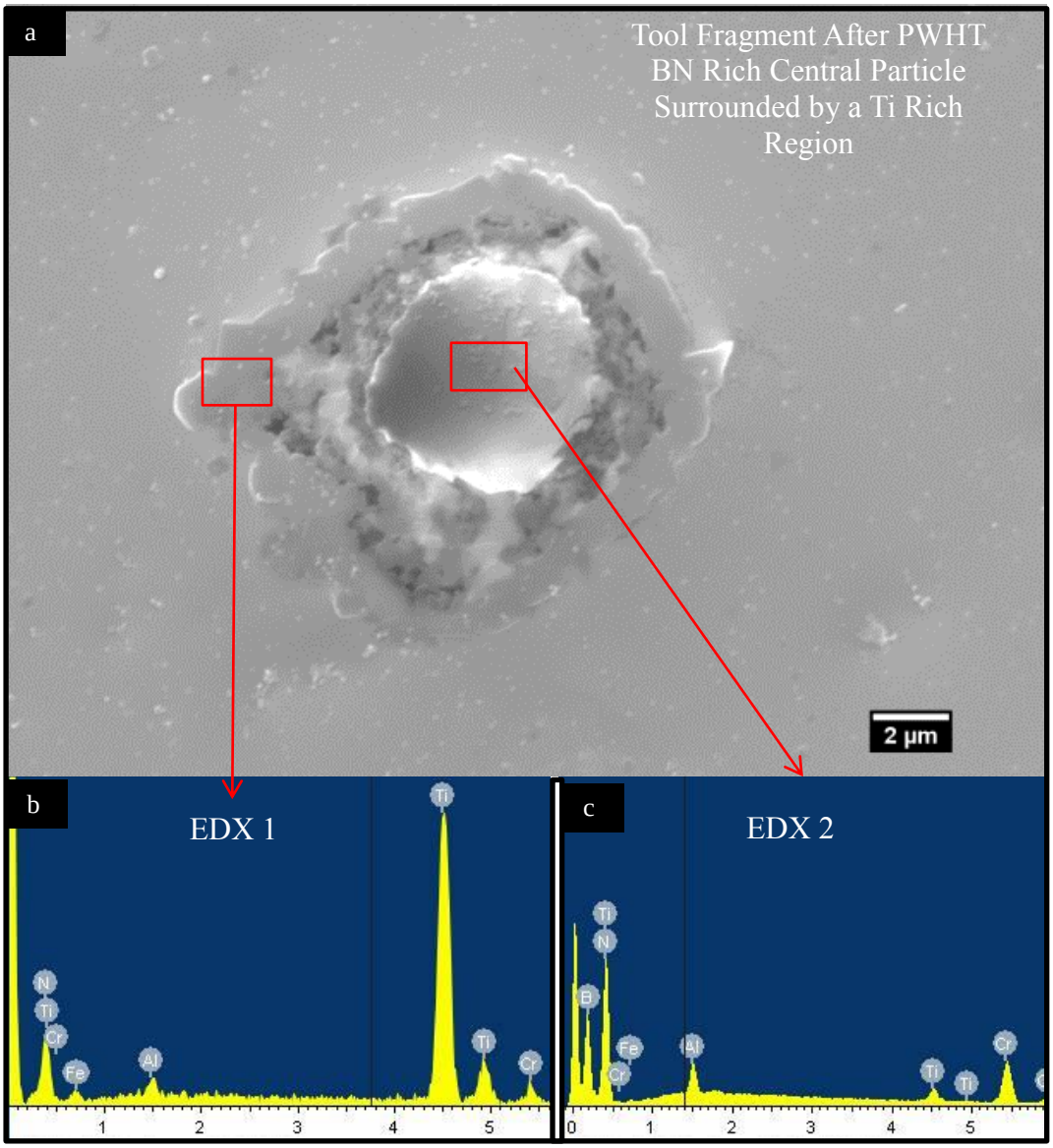

Figure 4.23 *SED image of BOP 7 with PWHT showing a) a tool fragment embedded in the TMAZ with EDX analysis of b) central region and c) area surrounding the fragment.*

The most likely source of these fragments is the PCBN tool which is used to perform the FSW. Tool wear is a major cost factor in the FSW process and in addition having tool fragments embedded in the weld could potentially have detrimental effects on the mechanical properties of the weld.

SEM analysis in SED mode of BOP 7 with PWHT has again revealed the presence of tool fragments embedded in the TMAZ. Figure 4.23a shows one such particle which, when compared to the previous image in Figure 4.21b, the fragment appears that it

has broken down around the edges. The region surrounding the tool fragment appears darker in contrast than the rest of the TMAZ. EDX analysis confirmed that the central region of the tool fragment is B and N rich, as expected, but the darker contrast region surrounding the tool fragment is Ti rich. It appears that Ti from the matrix is attracted towards the tool fragment.

In order to investigate further, two cross sections of FSW BOP 8 were heat treated at two different temperatures and comparisons made on the progress of the extent of the breakdown of the tool fragments. The heat treatments were set at 900°C and at 1100°C for 1 hour.

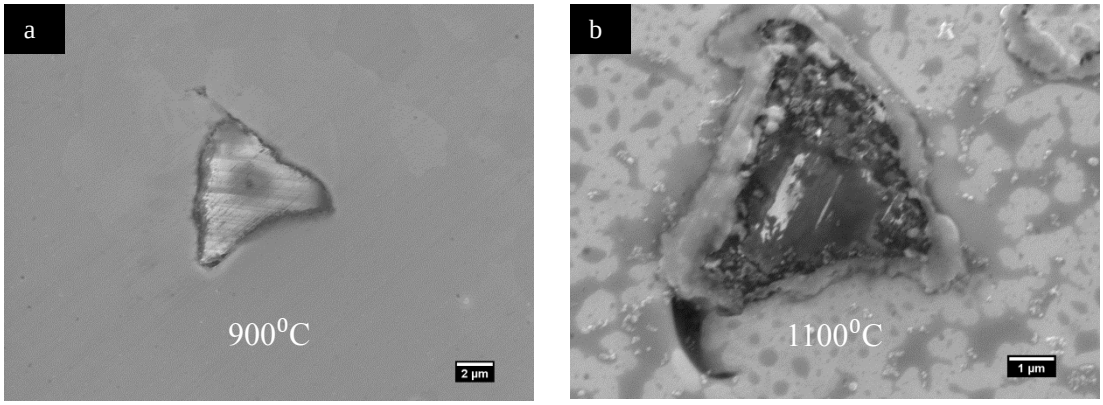

Figure 4.24 *Images of tool fragments in heat treated FSW BOP 8 at a) 900°C and b) 1100°C for 1 hour*

SED images of tool fragments in heat treated FSW BOP 8 cross sections shown in Figure 4.24 indicate that the BN tool fragments stay intact at 900°C but at 1100°C the fragments start to break down at the outer edges. The surrounding matrix area is similar to the outer Ti rich region around the tool fragment seen in Figure 4.23a. The breakdown of the BN tool fragment therefore initiates at a temperature above 900°C and below 1100°C.

FIB sections of the BN fragments in both the as welded and the PWHT samples were examined. The advantage of a FIB section is the fact that an exact point in the sample is chosen to be lifted.

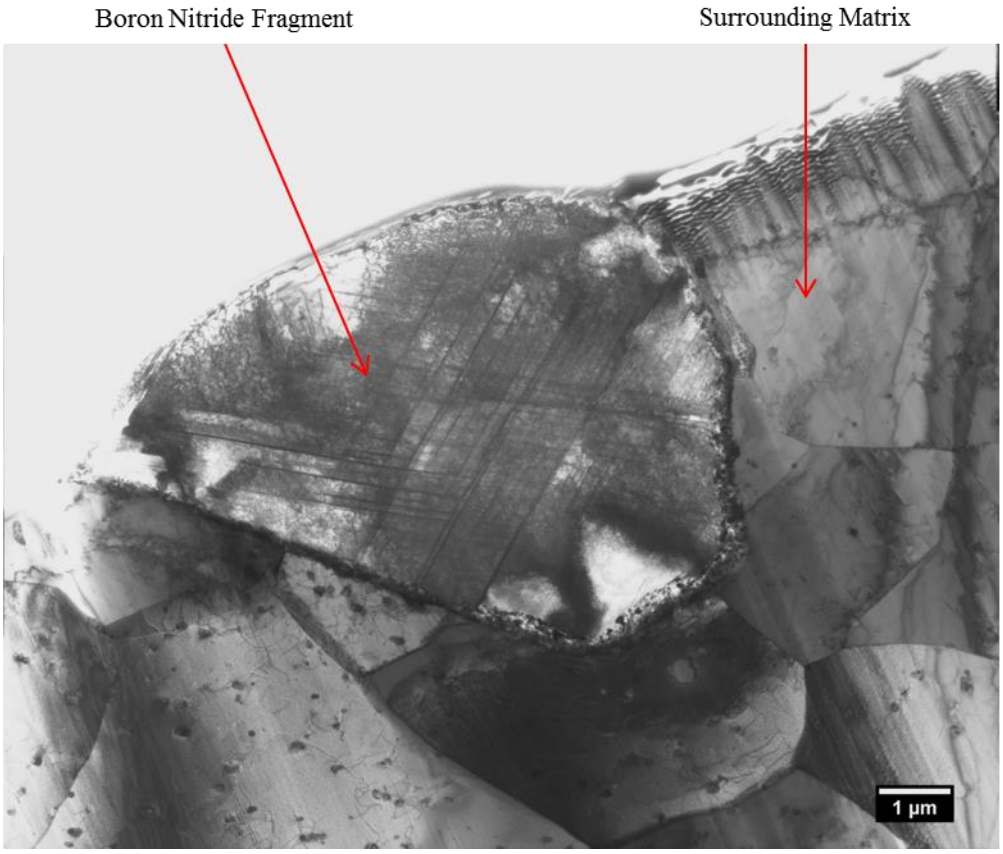

Figure 4.25 *BF TEM image of a FIB sample a PCBN tool fragment embedded in the TMAZ,*

A major disadvantage is that sometimes the samples are not as clean and that some material does get redeposited on the area of interest. In this particular instance both FIB samples were sufficiently clean and good images were obtained.

Figure 4.25 shows a TEM BF image from a FIB sample of a PCBN particle from BOP 9 FSW that is embedded in the matrix. The tool fragment can be seen protruding from the surface of the sample which confirms the observations in the sample preparation stage where the PCBN tool fragments were causing scratches to form at each stage of the SiC paper polishing steps. The TEM image clearly shows the matrix surrounding the tool fragment and the nanoparticles in the matrix. A Selected Area Diffraction (SAD) pattern of the tool fragment is shown with the simulated SAD pattern and the zone axis view of the crystal axis in Figure 4.26.

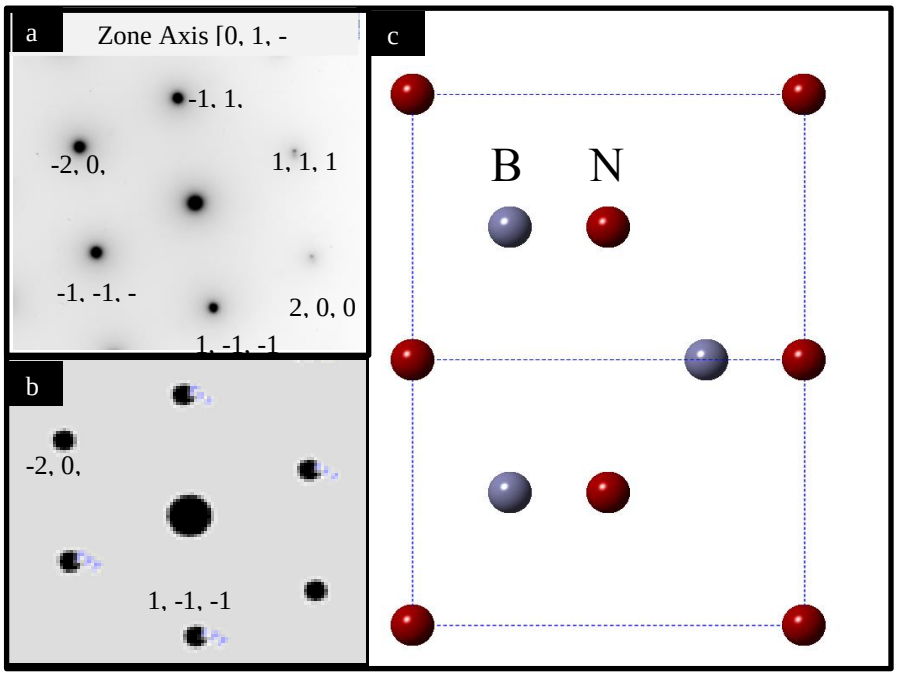

Figure 4.26 *a) SAD pattern of the PCBN tool fragment, b) simulated SAD pattern using Crystal Maker software and the simulated zone axis view of the crystal structure of cubic BN from Crystal Maker software.*

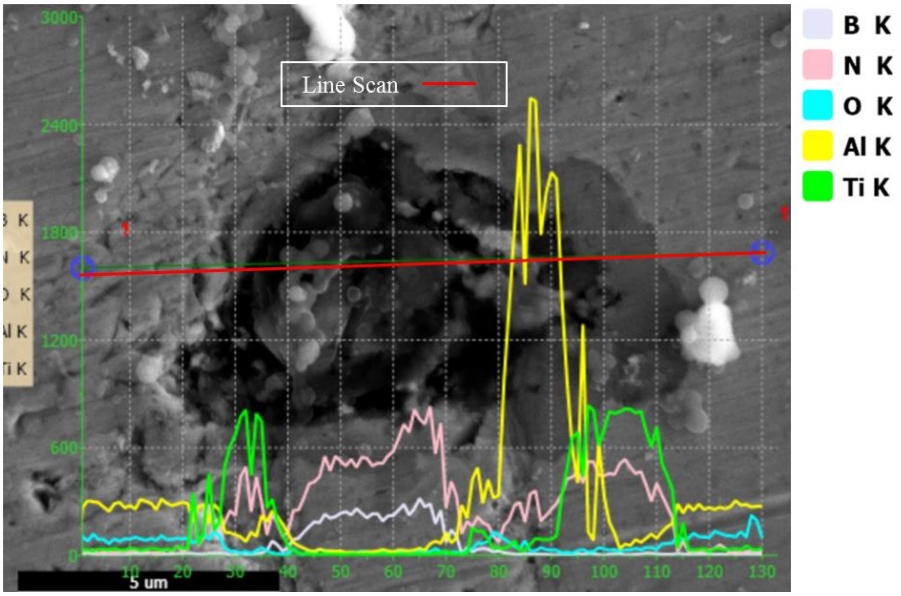

Figure 4.27 *SEM SED image of an embedded PCBN tool fragment in BOP 7 with PWHT. A line scan is indicated by the red line.*

Further investigation was carried out on the BOP 7 sample with PWHT. Initially a tool fragment was chosen for analysis and a line scan performed across the PCBN tool fragment for EDX analysis. Figure 4.27 illustrates the SEM SED mode image of the chosen region with the corresponding EDX line on the image.

As the scan approaches the tool fragment from left to right there is a peak in Ti signal in the matrix near and either side to the tool fragment which is the area with the darker contrast. This is the region rich in Ti identified in Figure 4.23. As the scan enters the outer part of the tool fragment the EDX signal for Ti and N is dominant. In the central region of the tool fragment only the B and N signals are seen. The scan is consistent with the breakdown of the PCBN tool fragment at the outermost region where there is contact with the matrix. An area rich in Ti surrounds the tool fragment and the outermost region of the tool fragment is rich in Ti and N which suggests the formation of titanium nitride layer.

The central part of the tool fragment the EDX signal is mainly of B and N indicating that the tool fragment is only partially broken down.

The large Al peak near the edge of the tool fragment is possibly due to the presence of an Al rich particle near the tool fragment.

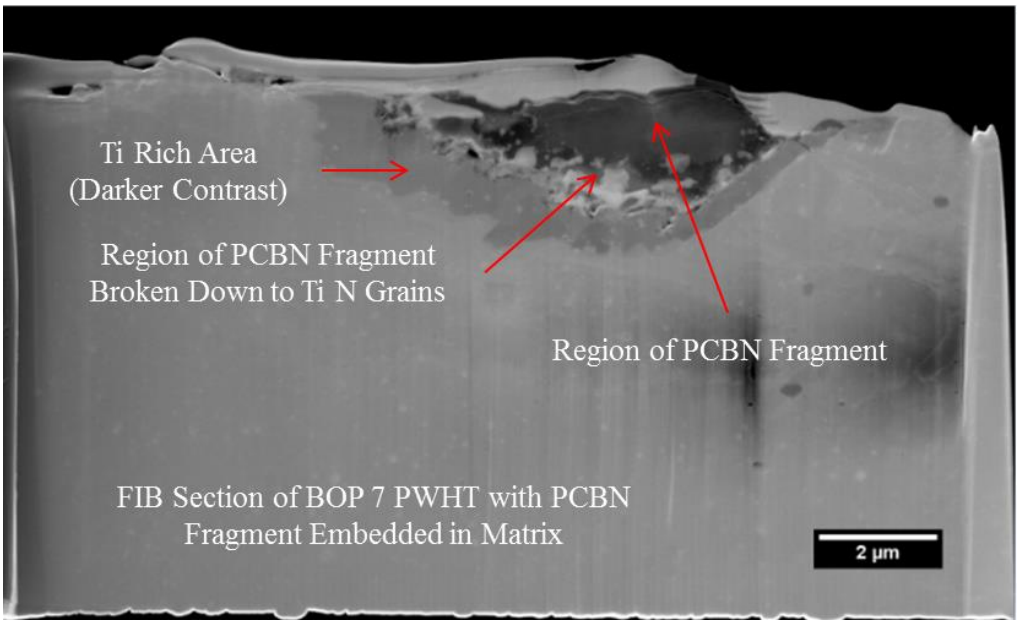

Figure 4.28 *SEM SED image of the FIB sample lifted from BOP 7 with PWHT.*

A FIB TEM sample was prepared from this particular fragment and the surrounding matrix and analysed in the TEM. Figure 4.28 shows an SEM image of the FIB sample that has been lifted from the BOP 7 weld with PWHT. The tool fragment can be seen in the central part of the image which is surrounded by a crystalline grain structure rich in Ti and N. A darker contrast region around the tool fragment is indicated as the Ti rich region.

TEM analysis of the FIB sample has revealed several regions of interest:

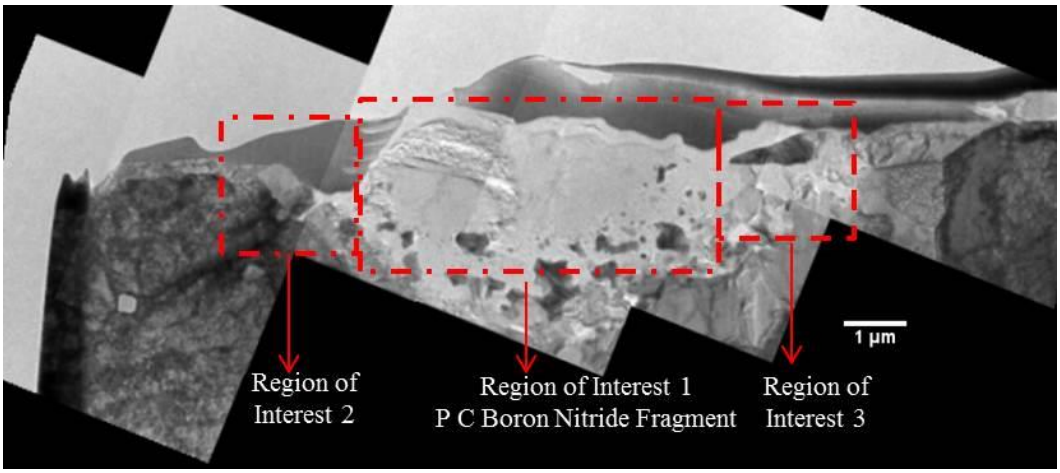

Figure 4.29 *A montage of TEM images of the FIB sample from BOP 7 PWHT with regions of interest 1 2 and 3 indicated for closer examination.*

Region of Interest 1

A closer look at ROI 1 in Figure 4.29, which is enlarged in Figure 4.30, shows the central part of the tool fragment that was still intact. A grain boundary near the middle of the region was visible as indicated. CBED patterns were obtained from both regions and presented in Figure 4.31.

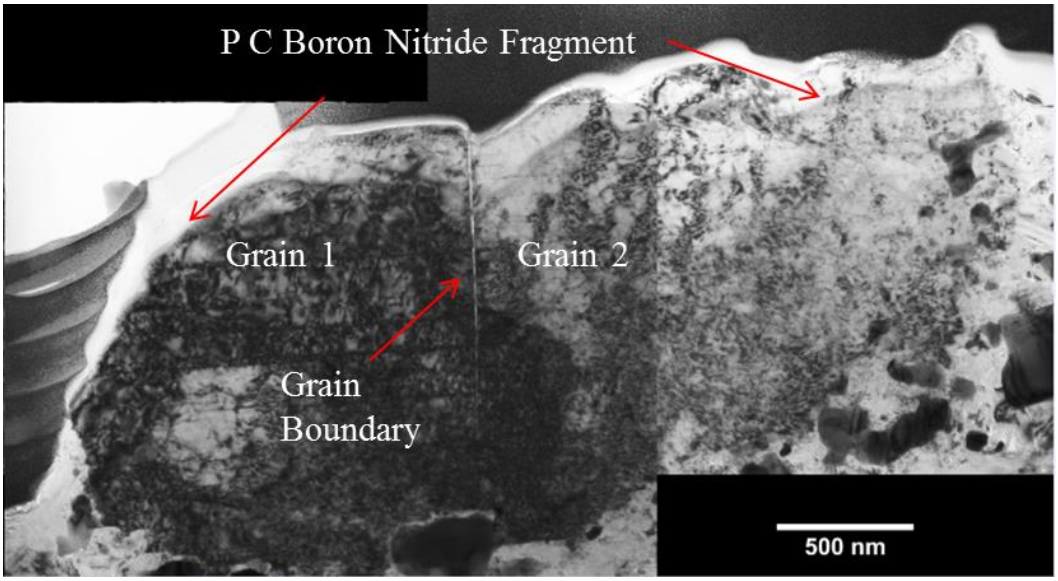

Figure 4.30 *Montage of TEM images of the central part of the PCBN tool fragment showing a grain boundary between two separate grains of PCBN.*

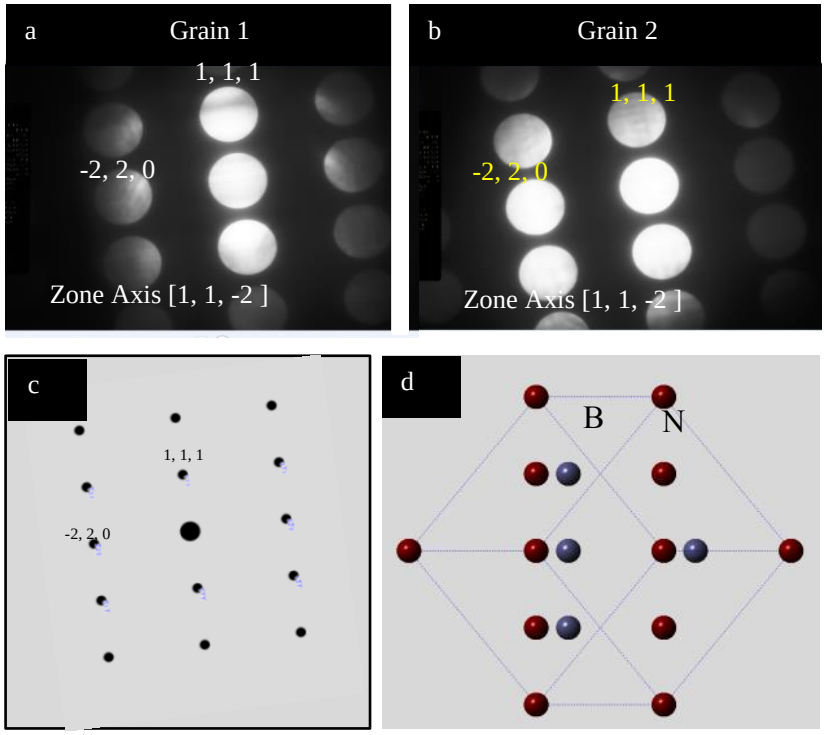

Figure 4.31 *CBED patterns for BN tool fragment at a) Grain 1 and b) Grain 2 with c) simulated SAD pattern and simulated crystal structure for the Zone Axis [1,1,-2]*

When tilting the specimen to the zone axis of Grain 1, there was a misorientation with regards to Grain 2. The goniometer positions were recorded from both CBED patterns and a misorientation angle was calculated using the formula [97]:-

$$Cos\ \gamma_m = Cos\ (Tx_2 - Tx_1) + Cos\ (Ty_2 - Ty_1) - 1 \qquad \textit{(Equation 4.1)}$$

Where γ_m is the misorientation angle between the two grains with goniometer coordinates Tx_1, Ty_1 and Tx_2, Ty_2. In the above case this misorientation angle was calculated at 24.4°. As the tool fragment is from the PCBN more than one grain of BN will be present in a fragment as shown in this case.

Region of Interest 2

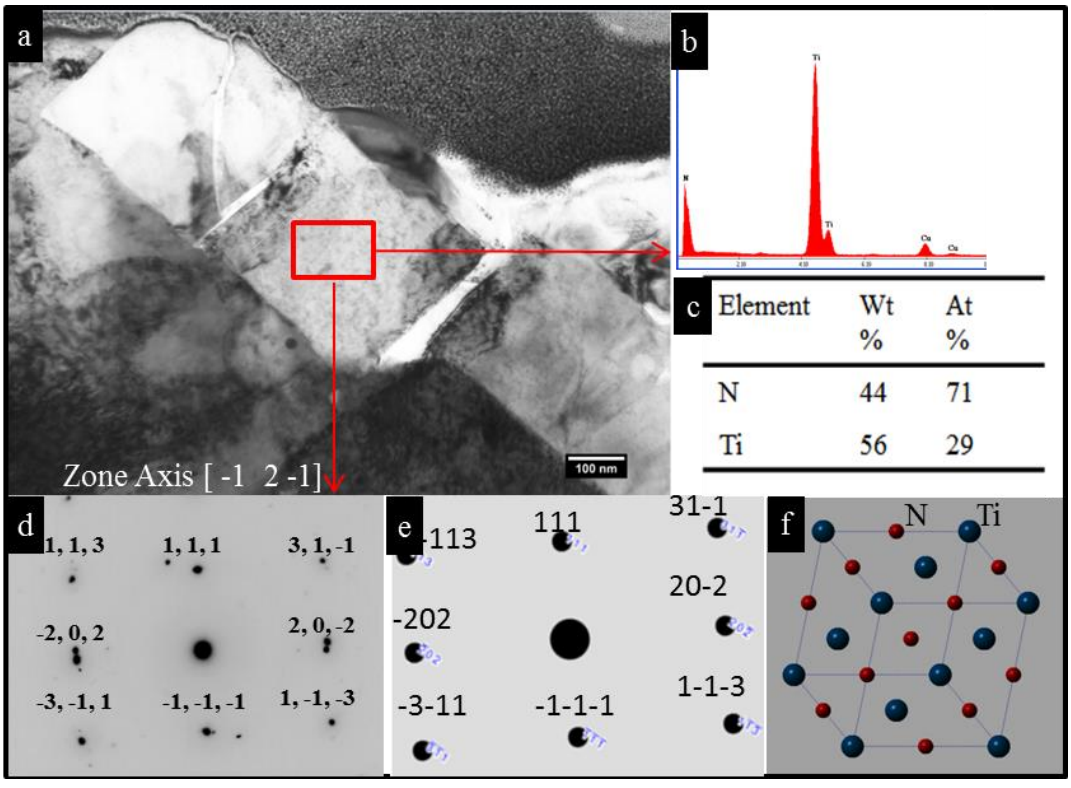

Figure 4.32 *ROI 2 showing a) TEM BF image of a TiN grain with b) corresponding EDX spectrum with c) quantitative analysis d) diffraction pattern e) simulated diffraction pattern and f) simulated zone axis view of the crystal structure of TiN.*

The TEM BF image of ROI 2, in Figure 4.32, a grain rich in Ti and N is confirmed by EDX analysis (Figure 4.32b). A diffraction pattern was obtained (Figure 4.32c) and it was resolved to a Ti N grain with a zone axis of [-1, 2, -1].

This confirms that at ROI 2, the broken down part of the B N fragment has been replaced by Ti N grain. The only source of Ti is from the matrix hence the Ti enriched region surrounding the B N fragment.

Region of interest 3

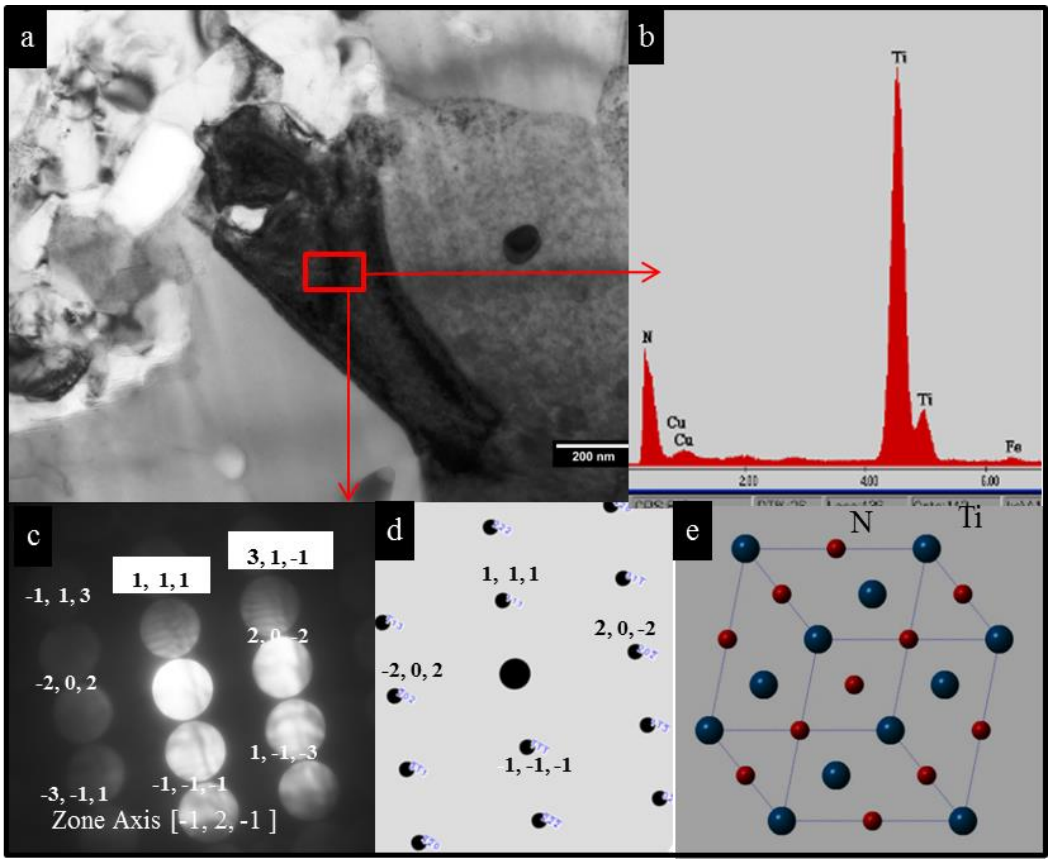

Figure 4.33 *ROI 3 showing a) TEM BF image of a TiN grain with b) corresponding EDX spectrum, c) CBED pattern, d) simulated diffraction pattern and e) simulated zone axis view of the crystal structure TiN.*

In ROI 3 another grain is examined just to confirm that the process is the same at both sides of the PCBN tool fragment. As seen in Figure 4.33 that is exactly the case.

All the area under the PCBN tool fragment that is in contact with the matrix is subject to the same process.

The only part of the process which has not been resolved is what happens to the B. All EDX analysis around the fragment has failed to indicate any presence of B other than from the tool fragment that has not broken down. Since B is an interstitial atom the most likely outcome is that the B is dissolved into the surrounding matrix and therefore an EDX signal could not be observed at this low concentration. Boron is known to increase the hardness of steels [98].

4.8 Summary and Conclusions

The BOP welds studied in this chapter were near end pieces and the results are an initial study of the FSW process to serve as a reference to the following chapters.

The aim of the FSW process of ODS steels was to produce good uniform welds with little or no defects in the weld region and to retain as much as possible the nanoparticle distribution in the welded region. PWHT is applied to the welds to promote secondary recrystallisation so that a large grain structure is obtained. The high temperature applications of these steels require a large grain structure with enough retained nanoparticle distribution in the matrix to provide high temperature creep resistance.

4.8.1 Optical and Microstructural Observations

General Observations

The welds appear to be well formed with few defects. Concentric circles appear on the surface of the welds as the shoulder passes across the weld line. Cross sections of the weld have revealed an altered microstructure from a slightly elongated sub-micron grain structure along the rolling direction to an equiaxed grain structure in the TMAZ of several microns. The application of PWHT has been successful in the formation of a large grain structure in the TMAZ but in the parent material region of

the welds, PWHT has only resulted in the recrystallisation of the grain structure with limited grain growth.

This was a disappointing aspect of the findings as to have low creep rate, at high temperature, a large elongated grain size is required. As the rolled plates used for the welds originated from as extruded rod of PM2000 it was decided to heat treat a test piece of as extruded PM2000 to see whether the sample would form a large elongated grain structure.

Figure 4.34 shows a montage of a DIC optical image of the test piece of as extruded PM2000. A large recrystallised grain structure is visible along the extrusion direction. The decision was taken that the next welds would be made with plates cut from the as extruded rod and that the subsequent PWHT should produce a large grain structure throughout the sample and not just in the TMAZ.

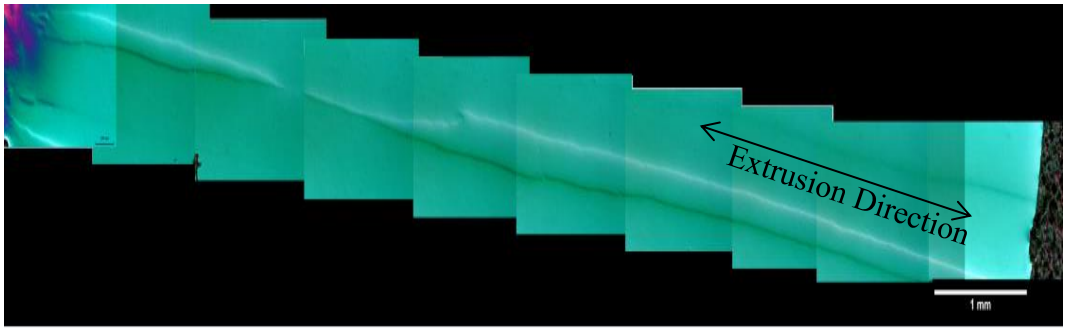

Figure 4.34 *A montage of DIC optical images of as extruded PM2000 test piece heat treated at 1380°C for 1 hour. Notice the large grain formation along the extrusion direction*

Hardness Profile

Mechanically alloyed ODS steels have a high density of dislocations and grain boundaries due to the stresses introduced by the alloying and rolling processes [94]. Any exposure to a higher temperature will have an impact on the hardness as some dislocations will diffuse out and any grain growth will affect its hardness due to the Hall Petch relationship. The extent of the reduction in hardness would depend on the temperature itself and the amount of time at that temperature.

The hardness profile of the as welded BOP 7 sample has the typical sharp reduction of hardness at the advancing side of the weld as opposed to the more gradual change in hardness in the retreating side which is in agreement with other authors of FSW [99-101]. This anisotropy in the hardness profile stems from the fact that the material is sheared away at the advancing side of the weld and then redeposited behind the tool at the retreating side as it moves along the weld line. This creates a sharp contrast in the grain size between the parent material and the TMAZ at the advancing side as the dynamically recrystallised grains in the TMAZ are larger in size than the grains in the parent material. This creates a noticeable difference in the hardness between the two regions due to the Hall-Petch relationship.

The HAZ is the area next to the TMAZ that is exposed to higher temperatures, due to the friction stir process, compared to the parent region. The temperature decreases the further away you are from the TMAZ. This creates an area with a temperature gradient. Heat will have an impact on the hardness so a gradual reduction in hardness number is seen as you approach the HAZ from the parent region.

Recrystallisation

In the parent material region there is a high amount of stored energy in the form of the high density of dislocations and the high grain boundary energy from the sub-micron grain structure. The question then arises as to why this region has not fully recrystallised after the application of PWHT. The main barrier to recrystallisation is due to the nucleation events being restricted by the pinning of the grain boundaries by the small grain structure. Even though there is a high level of stored energy there is also resistance to the recrystallisation process. PWHT recrystallises the parent region to form grains of several microns but the grains retain the elongated grain structure along the rolling direction of the parent material due to the particle alignment. A high number of nucleation sites results in a small recrystallised grain structure

The heat from the friction stir weld process will also have an effect on the number of nucleation sites for recrystallisation. After the application of PWHT, the recrystallised grain size of the HAZ was larger as you approached the TMAZ. The horizontally elongated grains observed were of varying length and of a high aspect

ratio which decreased in size as you moved away from the TMAZ. The average particle size in the HAZ with PWHT was measured as 28nm with a standard deviation of 12nm. This compared to an average size of 27nm with a standard deviation of 11nm in the parent region post heat treatment. The momentary heat increase due to the regions proximity to the TMAZ has not impacted on the particle size distribution. This suggests that the different recrystallisation behaviour of the HAZ was due mostly to the stresses from the shearing of material next to the TMAZ which are reducing as you move away from the TMAZ and the reduction in the grain boundary pinning due to a slight grain growth caused by the proximity of the region to the TMAZ. The particle distribution in the HAZ has not altered and the elongation of the grain structure was still evident.

In the PWHT sample, the partially dynamically recrystallised grain structure of the TMAZ has reduced the dislocation density and the driving force for nucleation and so has recrystallised to a large grain structure. This can be explained by the fact that nanoparticles have been rearranged and are no longer aligned, due to the stirring of the tool. There is less restriction in grain growth to a specific orientation and no other recrystallised grains to impede growth. The TMAZ has dynamically recrystallised prior to PWHT with a larger grain size than the parent region. The grains are no longer pinned down due to their sub-micron grain structure and in addition the coarsening of the nanoparticles means that their ability to pin down grain boundaries was reduced. The stored energy for recrystallisation was modified due to the energy input of the rotating tool [32] and the net effect is that the region recrystallised with a large grain structure due to the reduction of nucleation sites after the application of PWHT.

4.8.2 Particle Size Analysis

One of the interesting outcomes of the PSA results is the mean particle size bar graph and the effect on the coarsening of the nanoparticles purely because of the stirring of the tool in the TMAZ. The heat generated by the friction of the shoulder, which generates temperatures of about 1,000°C in the uppermost region of the TMAZ only

lasts for a few seconds but has more of an impact on the coarsening of the nanoparticles than the PWHT which is at 1380°C for 1 hour.

There are two main particle coarsening mechanisms

- Growth
- Agglomeration

Particles in ODS steels nucleate during the extrusion and rolling processes when the ODS powders are consolidated to form rods or plates. Particles in a saturated solution can grow by diffusion with time through a process called Oswald Ripening as mentioned in the literature review in section 2.7. The rate of growth is temperature dependent and is proportional to the radius cubed (R^3) as given by Equation 2.12. Agglomeration is when two particles are so close together that diffusion occurs between the two particles in order to reduce the surface energy of the particles [34].

All are possible in the TMAZ as the heat from the friction stir welding process should increase nucleation of new second phase particles and encourage coarsening of existing particles and agglomeration between neighbouring particles.

The PSA results though suggest that the FSW process actually has a bigger impact in the PSA than the PWHT alone. A possible explanation is offered below.

In a paper by Lifshitz and Slyozov [34] the concept of encounters is proposed when two different particles are within a distance smaller than their mean radius then by the process of Ostwald Ripening the larger particle will grow at the expense of the smaller one. As a particle grows then the chance of another encounter is increased due to the increase in the size of the particle. These encounters are more likely at higher temperatures as coarsening is temperature dependent.

In the TMAZ there is the increased temperature due to the friction of the shoulder but this is only a momentary temperature event and the application of PWHT should be much more profound in coarsening the particles.

The mechanical stirring must have an impact on the possibility of more encounters as material is sheared away from one side of the weld to the other. This would explain the much larger coarsening of the particles in the top of the TMAZ compared to the middle or bottom parts of the TMAZ. The larger flow rates of material in the top part must increase the likelihood of encounters with other particles nearby which would result in the formation of clusters or agglomerated particles and after the application of PWHT consolidate to form larger particles. If we consider the geometry of the tool the diameter of the shoulder is 25mm and the pin diameter is 4mm. If we assume that the number of encounters will depend on the relative motion between different regions of the TMAZ then one can assume that the number of encounters are much more likely at the top of the TMAZ due to the higher rotational speed of the shoulder relative to the bottom region of the TMAZ where the angular velocity of the pin governs the material flow and therefore the number of encounters. The additional encounters in the top part of the weld result in more agglomerations and this is reflected in the bimodal particle distribution seen in the histogram in Figure 4.14.

4.8.3 Boron Nitride Tool Fragment

The whole process of the tool fragments embedded in the matrix can now be summarised as follows. Boron nitride tool fragments were found in the TMAZ. These fragments were found near the top surface of the weld and at the advancing side of the weld. These fragments were found to have altered after the application of PWHT.

The cubic phase of BN is one of the hardest know materials along with diamond with a Vickers Hardness of over 4000 HV [102] and is the only stable phase at ambient temperatures and pressures. FSW of steels has only become a reality since the development of PCBN tools.

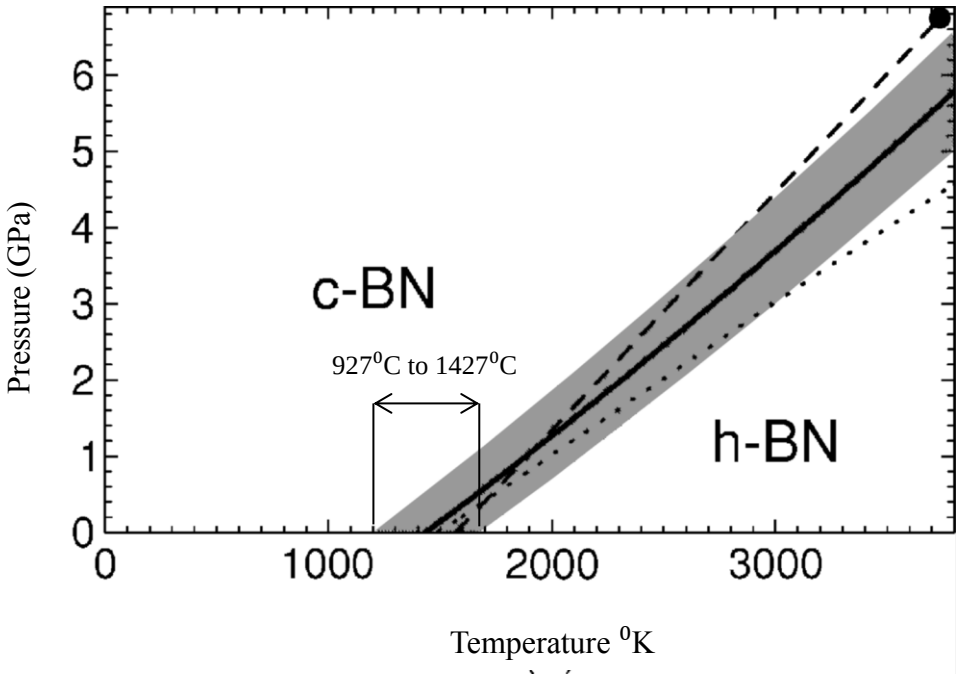

Figure 4.35 *Boron Nitride pressure temperature phase diagram (modified from Kern, Kresse et al. 1999) [103].*

The phase diagram of cBN and hBN phases shown in Figure 4.35 a temperature range of between above 900°C about 1400°C, cBN will transform into hBN depending on purity and on the grain size of the cBN with the transformation starting at the surface [103].

In a paper by Eremets et al. [104] the change in volume from the cBN phase to the hBN phase is $\frac{\Delta V}{V}$ = 0.53 so a large volume change occurs at the transformation. At the nucleation site of the new phase volume changes can lead to stresses and the fragmentation of the parent phase.

The PCBN tool fragment seen in the BOP 7 PWHT sample does show signs of fragmentation especially at the matrix / PCBN interface.

Using chemistry data tables [105] the enthalpy of formation for BN is -250.91kJ/Mol. and for TiN is -337.65kJ/Mol. The high affinity between N and Ti means that the Ti is attracted to the area of the matrix surrounding the tool fragment.

Since the recrystallisation temperature of 1380^0C takes the BN into the hexagonal phase, the breakdown of the fragment is most likely due to the volume change involved.

Park et al. [76] investigated tool wear in ferritic and austenitic steels and found evidence of Cr_2B and Cr_5B_3 particles in the TMAZ in the austenitic steels but no evidence of these particles were found in the ferritic 406 type steel.

No evidence was found of any region with EDX signal of B in the area surrounding the BN tool fragment in BOP7. Even though B has a very low solubility in ferritic iron (0.003%) [102, 106] the most likely outcome is that the B has diffused into the matrix. This would increase the hardness of the region with B but this could not be confirmed with any hardness measurements as the area in question was too small compared to the size of the indent produced by the diamond tip of the indenter in the micro-hardness instrument.

CHAPTER 5

Friction Stir Welding of As-Extruded PM2000

5.1 Introduction

Following the FSW of rolled PM2000 it was decided to try to produce a weld that would recrystallise fully across the TMAZ and the parent material. As mentioned previously in Chapter 4, the as-rolled PM2000 did not show an increase in grain size in the parent region. A test piece of as-extruded PM2000 was heat treated to 1380°C for 1 hour to promote recrystallisation. Large recrystallised grains were observed right across the sample. For this reason it was decided to proceed with the FSW of the as extruded PM2000 using plates that were cut from the as-extruded PM2000 rod. The objective was to induce a large grain structure in both the parent region and the TMAZ by avoiding the rolling process and by using the as-extruded plates. It would also be advantageous if the grains were to form across the parent material and TMAZ boundary. This would avoid boundary regions with different grain structures and therefore different mechanical properties that could potentially be detrimental to the joint.

In this chapter the FSW of the as-extruded PM2000 plates are characterised. The hardness profile of the weld and the grain structure of the weld were analysed. Particle size analysis was used to try and determine the effects of the FSW process on the nanoparticle distribution and the subsequent effects that it could have on the recrystallisation behaviour of the TMAZ in the weld. SEM analysis was used to determine the grain structure of the FSW and TEM analysis was used to study the effects of the FSW process on the particles themselves and their interactions with the matrix in the TMAZ.

The as extruded rod was cut into two 4mm thick plates measuring approximately 120mm x 44mm each.

5.2 The Friction Stir Weld Process

The weld was performed at TWI premises in Rotherham. The weld was designated as W34 and the two plates were placed on the welding jig and the weld line was aligned with the FSW tool.

Table 5.1 *Parameters provided by TWI of the W34 weld.*

W34 PM2000 ODS welded at 140mm/min, 200 rpm					
Start stable state position(mm)	13.0				
Stop stable state position(mm)	89.8				
	Average	Maximum	Minimum	%	St. Dev
X-Force (kN)	4.7	5.1	3.4	0.4	0.3
Y-Force (kN)	-2.7	-2.4	-2.9	-0.2	0.1
Z-Force (kN)	39.8	41.7	31.0	0.3	2.1
Spindle rotation speed (rpm)	-201.2	-199.0	-202.0	0.0	0.6
Spindle traverse speed (mm/min)	140.0	140.1	138.8	0.0	0.1
Torque (Nm)	152.3	158.5	144.7	0.1	3.5
Heat Input (kJ/mm)	-1.4	-1.3	-1.4	-0.1	0.0

Table 5.1 lists a summary of the parameters and the range of their values throughout the welding run. Stable state was achieved after 13mm of welding. This is the length of weld that was needed for the transverse speed to reach the 140mm/min. The negative sign on the rotational speed denotes anticlockwise rotation.

A graphical representation of the parameters as the weld was progressing is presented in Figure 5.1. In the top graph the various parameters are plotted against the distance travelled and in the bottom graph against the time. As multiple parameters are plotted on the same graph the units of the various parameters for clarity are listed in Table 5.1

From the data provided the process can be summarised as follows. The rotational speed (spindle speed) of the tool was gradually increased to 800rpm. The tool was lowered until it made contact with the plate to be welded. Keeping the rotational speed constant, the penetration depth was gradually increased to 3mm.

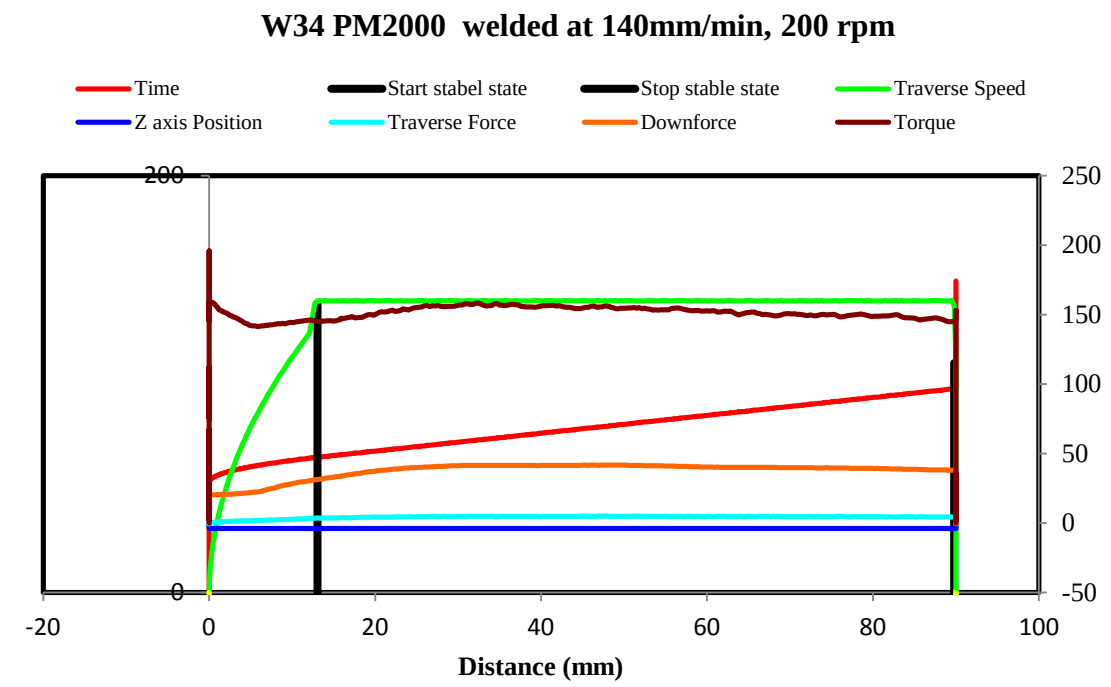

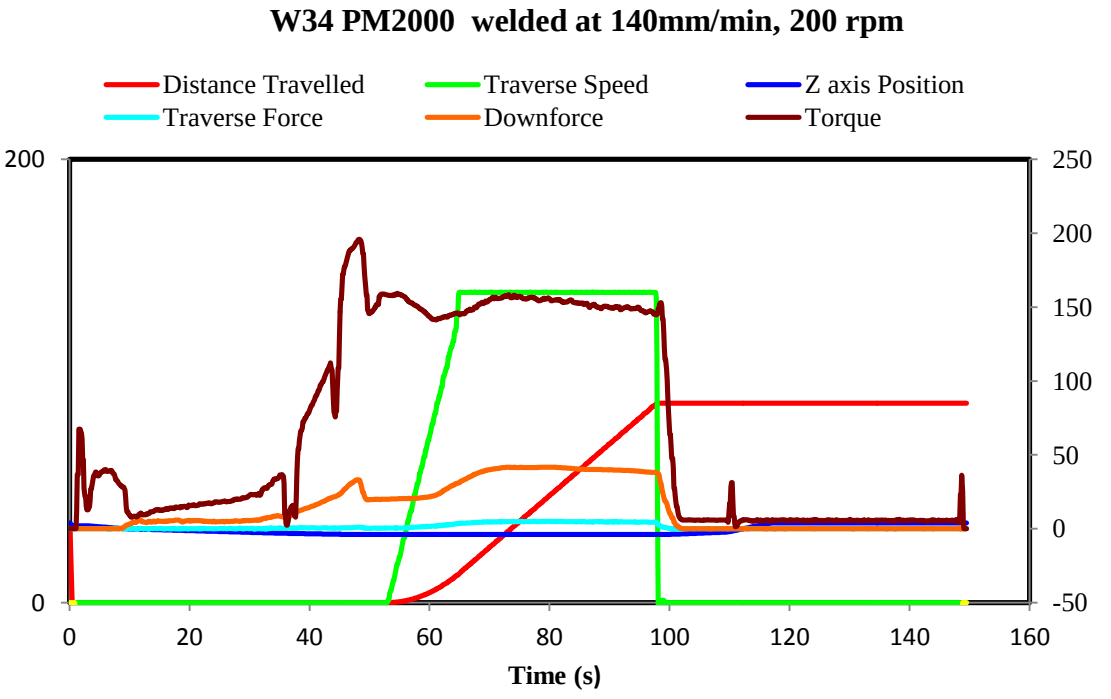

Figure 5.1 *Graph of the various welding parameters of W34 versus (above) distance in mm and (below) time is seconds. The y scale units are listed in Table 5.1.*

At this point the rotational speed was reduced gradually down to 200 rpm while still plunging the tool further into the plates to the depth of 3.9 mm. The tool was then allowed to move along the weld line gradually increasing the transverse speed to 140mm/min. As soon as the speed reached 140mm/min steady state in the weld was achieved. The parameters were held stable until the end of the weld line. At this point the rotational speed was maintained while the tool was slowly withdrawn. Once the tool exited the weld the rotational speed was reduced gradually and the weld was completed. It was then allowed to cool before removal.

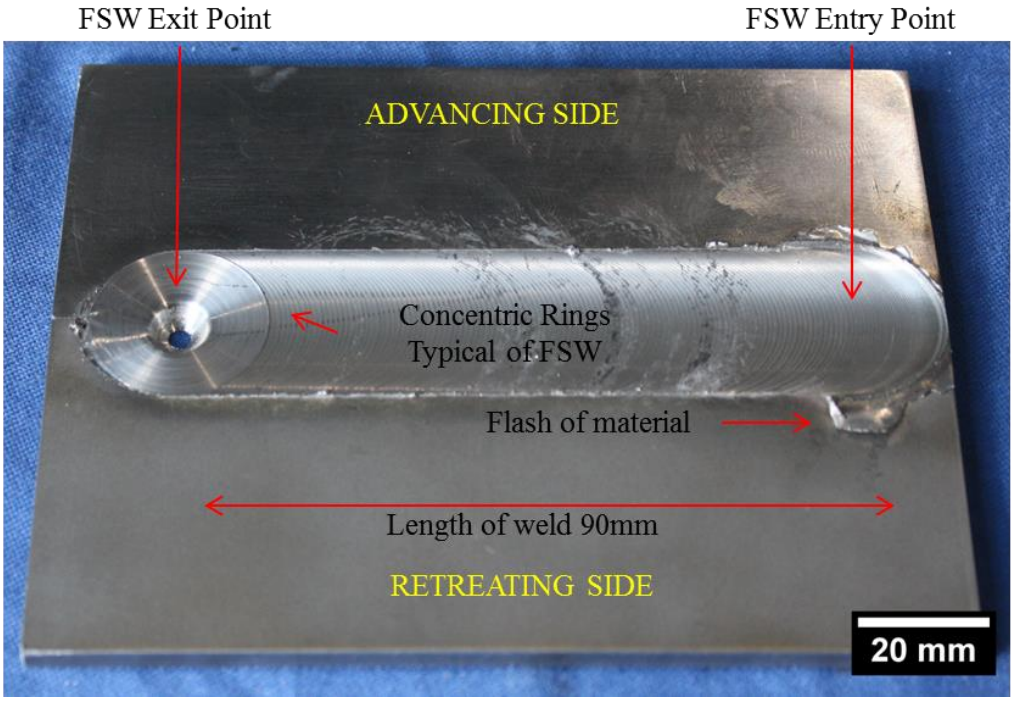

Figure 5.2 *Optical macrograph of the completed W34 weld. Notice the exit hole where the tool has penetrated right through the plates.*

A visibly sound weld was produced using as extruded plates of PM2000. Full penetration was achieved as can be seen by the exit hole in Figure 5.2. Typical of all FSW is the flash of material at the beginning of the weld which is caused by the entry of the tool bit at the start of the weld.

5.3 Optical Microscopy

Optical microscopy was used to examine the microstructure of the PM2000 as-extruded cut plates, before and after heat treatment and of the as-welded W34 before and after post weld heat treatment. All samples were polished to colloidal silica finish.

As-Extruded Condition

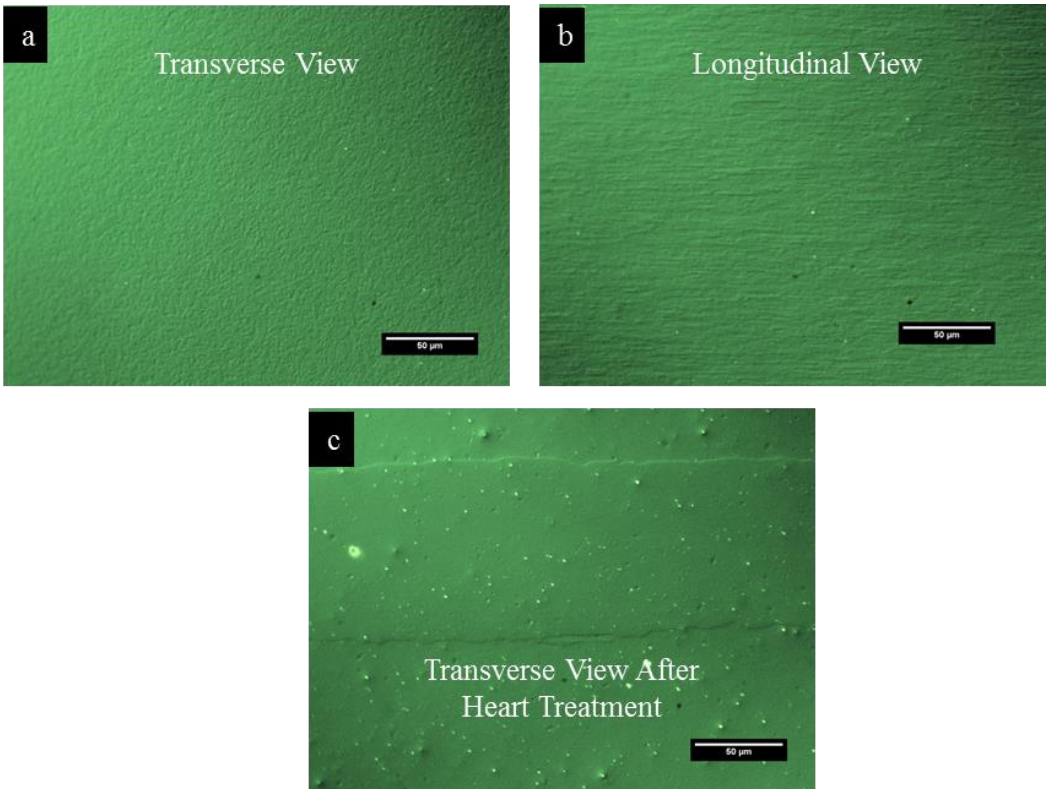

Figure 5.3 *DIC images of a) transverse, b) longitudinal views of as extruded PM2000 and c) longitudinal view of as extruded PM2000 with heat treatment.*

DIC images of the microstructure are shown in Figure 5.3. The transverse view grains in Figure 5.3a are equiaxed with a grain size of about 1 micron. Once again the longitudinal view grains in Figure 5.3b are elongated with an aspect ratio of about 3:1. Grains seem to form in bands in the direction of the extrusion direction. Once heat treatment was applied large (> cm) grains have formed right across the sample (Figure 5.3c) elongated along the extrusion direction. One slight difference

between the transverse view in the rolled plates in Chapter 4 and the as extruded plates is that the grains were slightly oval in the rolled plates whereas in the as extruded cut plates they were more rounded in shape. The shape difference could be a consequence of the rolling process.

W34 As-Welded Condition

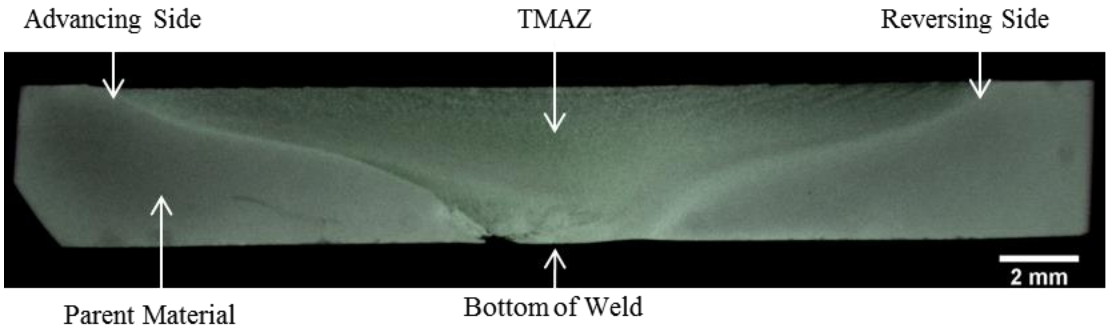

Figure 5.4 *Macrograph of the cross section of W34 weld (etched with 10%HCl in Methanol).*

A cross section of W34 was sectioned, polished and etched to reveal the microstructure of the weld as shown in Figure 5.4. As with the previous welds the outline of the TMAZ can be seen. Again the advancing side boundary with the parent material is more pronounced than the retreating side of the weld. At the bottom of the weld at the advancing side boundary with the parent material there is a small cavity. Overall the cross section of the weld looks fairly uniform and a good join was achieved.

W34 Post Weld Heat Treated Condition

The cross section of W34 heat treatment in Figure 5.5 has some very interesting features. The main aim was to promote the formation of large grains in both the parent region and the TMAZ. This has been partially achieved. In the TMAZ there are 3 distinct regions. The advancing side of the TMAZ has recrystallised but with small grains orientated in the direction of the material flow. Similar small grains

have formed in the retreating side of the TMAZ. The second region is the large recrystallised region with a small grain structure right across the middle of the TMAZ. This region was unexpected, as in all other welds the TMAZ was recrystallised with large grains. The third region is the fully recrystallised part of the TMAZ with some large grains that have grown right across the boundary between the TMAZ and the parent region at the retreating side, and to a lesser extend the advancing side, of the weld. The three regions will be discussed in more detail in the electron microscopy section.

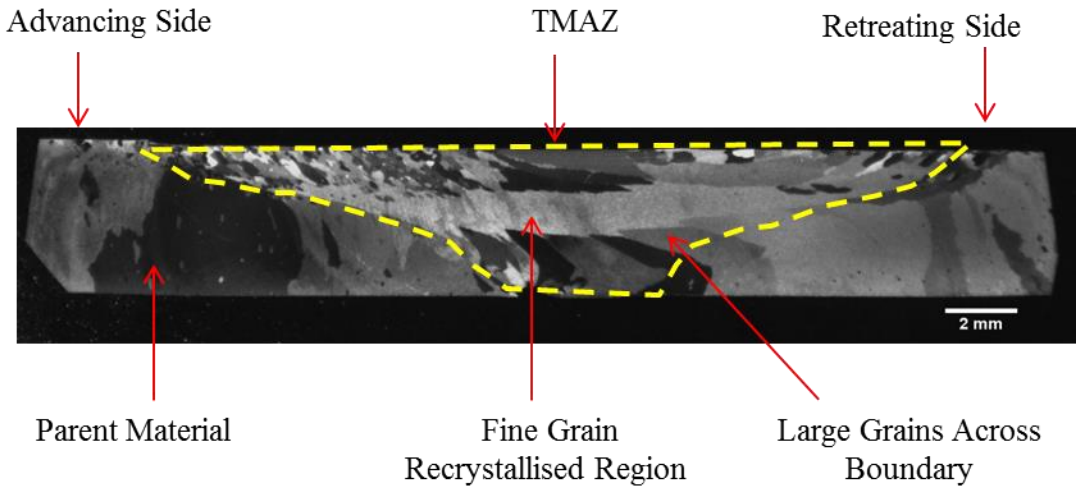

Figure 5.5 *Macrograph of the cross section of W34 with PWHT. The outline of the TMAZ is indicated by the dashed lines (etched with Kalling's Reagent).*

5.4 Hardness Profiles

As-Extruded Condition

Vickers hardness tests were carried out on the as extruded PM2000 plates. Samples with and without heat treatment were tested. The samples were from the as extruded rod sample which were cut into 4mm plates.

As can be seen from the hardness values listed in Table 5.2 there is very little variation in hardness between the 3 directions. This is unlike the rolled PM2000 plates tested in Chapter 4 where there was a difference of hardness in the as-received longitudinal direction.

Table 5.2 *Hardness profiles of as extruded PM2000*

Direction	No of Indents	Average HV	Standard Deviation HV
Plan	10	313	5
Transverse	10	313	7
Longitudinal	10	303	8
Plan HT	10	246	2
Transverse HT	10	242	9
Longitudinal HT	10	245	6

The application of heat treatment has had the effect of decreasing the hardness value by about 60 HV from the as-received value. The as-extruded hardness value was lower than the as-received, rolled PM2000 value to start off with and the reduction in hardness due to the heat treatment has very nearly resulted in the same hardness value as that of the heat treated as-received rolled PM2000.

W34 As-Welded Condition

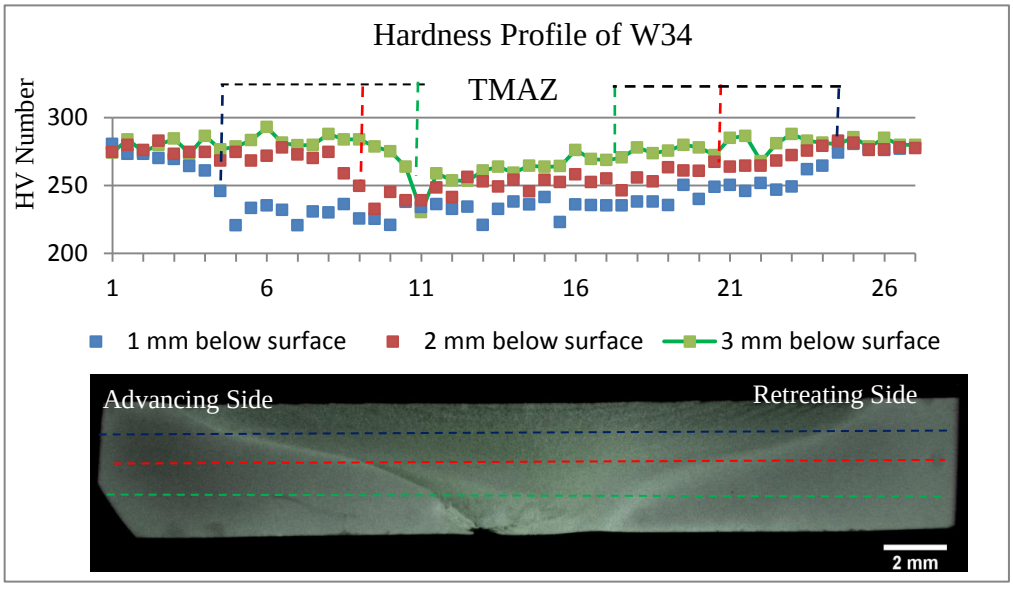

Figure 5.6 *Hardness Profile of the as welded W34 with the corresponding image of the cross section of the weld.*

Hardness measurements were taken at depths of 1mm, 2mm, and 3mm below the surface of the W34 as-welded sample as indicated by the dashed lines across the image in Figure 5.6. As with the rolled PM2000, there is a gradual decrease in hardness as you approach the TMAZ in all depths. The main difference between the extruded and the rolled samples is the amount by which the hardness drops i.e. a drop of 60 HV instead of 120 HV. The hardness profiles in the TMAZ are generally lower in the TMAZ of the as-extruded PM2000 cut plates than the as-rolled PM2000 plates.

W34 Post Weld Heat Treated Condition

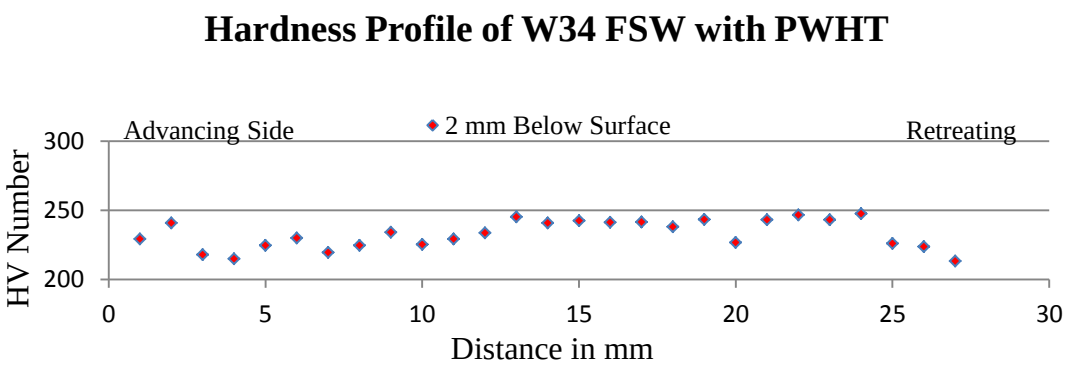

Number of Readings 27. Average Hardness 233 HV. Standard Deviation 10HV

Figure 5.7 *Hardness profile of W34 with PWHT.*

Hardness tests were carried out on the cross section of the as-extruded PM2000 FSW with PWHT. In all 27 tests were performed at intervals of 1mm apart at a depth of 2mm below the surface. As in the BOP 7 with PWHT results the readings were fairly uniform across the cross section with little variation in the value with position even when taking measurements in the fine recrystallised region in the middle of the TMAZ. The PWHT process has resulted in mostly large grains apart from a section in the middle of the TMAZ and the reduction in dislocations and stresses in the alloy has resulted in lower hardness values across the FSW.

5.5 Scanning Electron Microscopy

Colloidal silica polished samples were examined in the SEM in backscatter mode. Using channelling contrast images the microstructure and grain morphology of the samples was examined.

As-Extruded Material

Channelling contrast images of the transverse view and the longitudinal view of the as-extruded PM2000 are shown in Figure 5.8. The images show particles (dark spots in backscatter mode) which when analysed by EDX were found to be mostly oxides of aluminium (usually larger particles) and yttrium aluminium oxides (smaller particles) that were distributed within the grains and at the grain boundaries.

In the transverse view the particles seem to be more evenly distributed and the microstructure is made up of near equiaxed grains of about 1μm which is in agreement with the optical microscopy observations.

The longitudinal view image shows an elongated grain structure with bands of grains forming along the extrusion direction. Stringers of particles were also observed along the extrusion direction. Larger grains are observed in areas lacking particles creating bands of smaller grains and bands of larger grains in different regions of the sample.

The accepted standards for grain size measurement which are detailed in ASTM standard E112-12 involve measuring the number of grains intercepted by lines drawn over the image, known as the intercept method, or the number of grains counted in an area usually $1mm^2$ or a defined area, known as the planimetric method, from which the average area of the grains is then calculated. The grain size is then obtained by taking the square root of the average grain area which assumes that the grains are square. This of course is not the case but it is generally accepted practice.

Using channelling contrast images for the purpose of grain size calculations can be difficult as the contrast can vary in the same grain and sometimes the grain boundary is not well defined especially if the grain boundary is of a low angle boundary which would make a smaller difference in the contrast in the image.

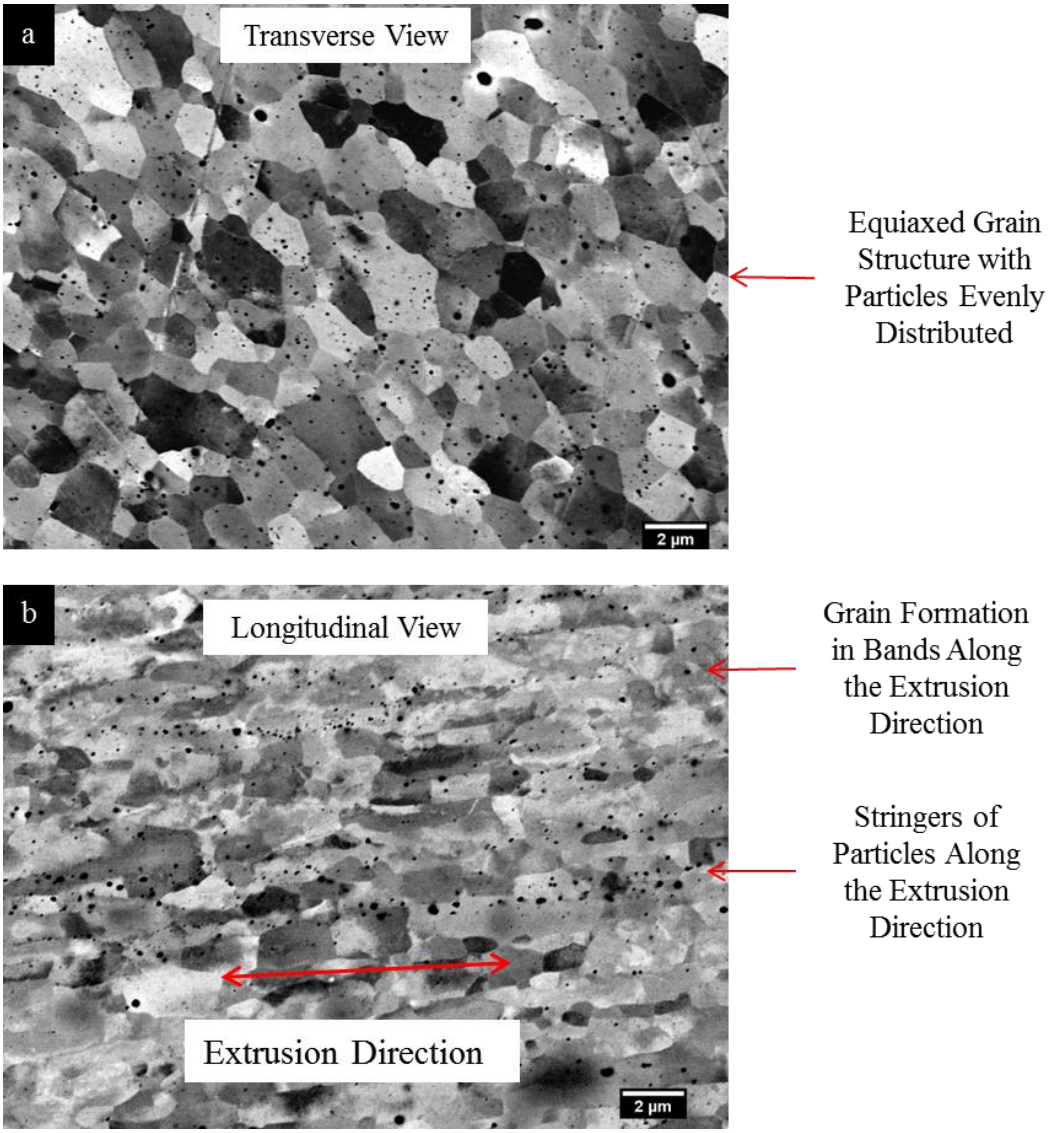

Figure 5.8 *Channelling contrast images of the as-extruded PM2000 showing, a) the transverse view and b) the longitudinal view. Notice the alignment of the particles along the extrusion direction.*

The method adopted for the purpose of working out the grain size is as follows. The outline of the area of the grain was traced and the number of pixels within the enclosed area was measured by using imageJ software. Using the scale from the SEM image the area of each grain was calculated in μm^2. Grains at the edge of the image and grains with boundaries which were not well defined were ignored. Figure 5.9 shows the frequency distribution of the grain size of the as extruded transverse

view with the corresponding image which was used with the individual grains outlined and numbered

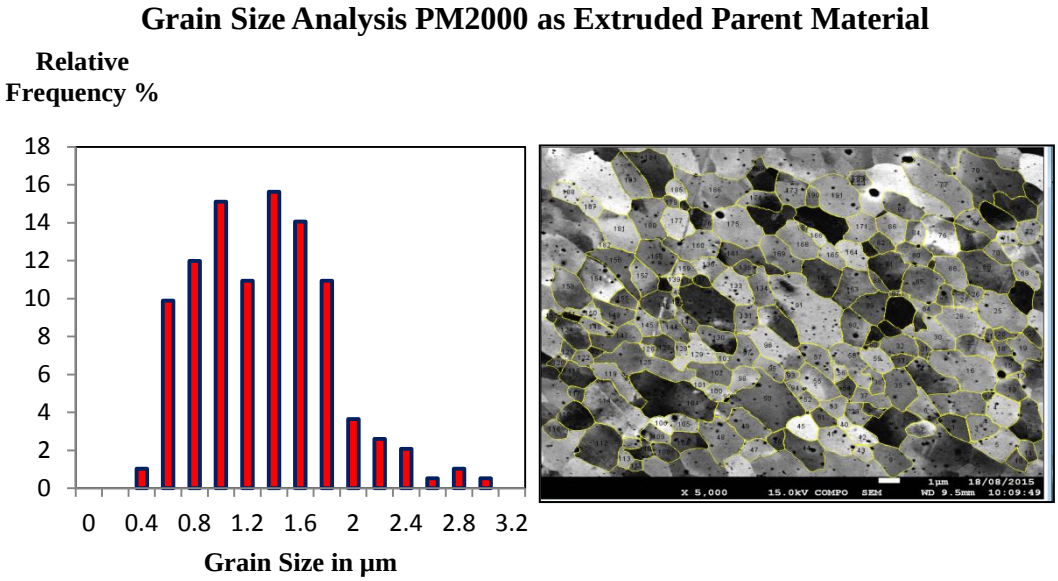

Figure 5.9 *Histogram of the grain diameter analysis of as-extruded PM2000 with the image used for the analysis (insert).*

There is a wide spread of grain size from 0.4µm to 3µm with an average grain size of 1.2µm. The ASTM E112 standard for grain size measurement for a uniform, randomly orientated, equiaxed grains which specify a Grain Size Number, G, ranging from 0 to14 with 14 being the smallest grain area specified of 7.9µm^2 which corresponds to a diameter of 2.8µm. Extrapolating the data a grain size G=16.5 corresponds to a grain diameter of 1.18µm. The distribution as shown in Figure 5.9 is close to a slightly asymmetric Gaussian type distribution and is in agreement with the microscopy observations of ≈ 1µm size grains from both the optical observations and the SEM channelling contrast observations.

W34 As-Welded Condition

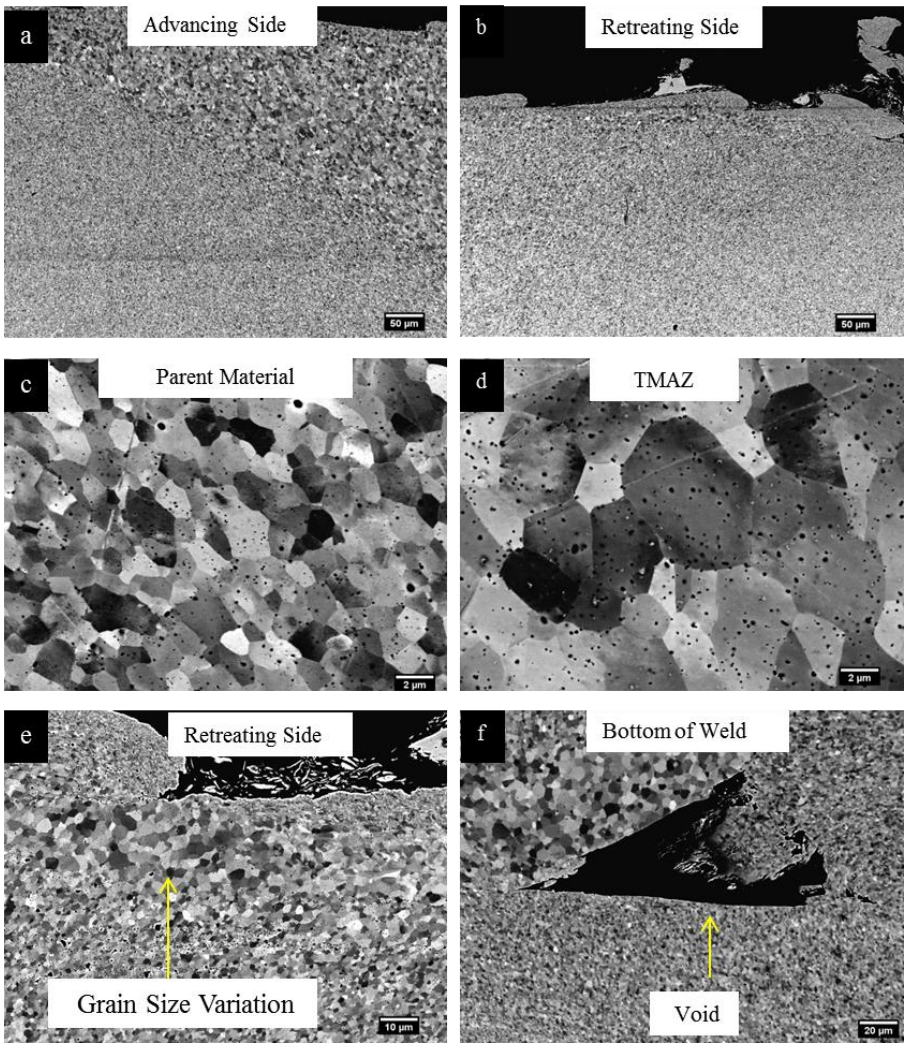

Figure 5.10 *Channelling contrast images of W34 as-welded showing a) Advancing side, b) Retreating side, c) Parent Material, d) TMAZ, e) Retreating side near the top surface of the TMAZ and f) Void at the bottom of TMAZ.*

A cross section of the as welded W34 was examined in the SEM in channelling contrast imaging using backscatter electrons. Figure 5.10 shows the channelling contrast images of the different areas of the weld. The advancing side grain structure of the sub-micron parent region contrasts sharply with the TMAZ grain structure of several microns in size as seen in Figure 5.10a.

The retreating side of the weld has a less pronounced boundary as seen in Figure 5.10b and in previous welds. In Figure 5.10 c and d, higher magnification of both the parent material and TMAZ grain structures respectively show the increased dynamically recrystallised grain size of the TMAZ compared to the parent region. On the retreating side of the TMAZ near the surface a local variation of the grain size was observed (Figure 5.10e). A closer look revealed a lack of particles in that particular area of larger grain size. Also seen were voids at the bottom of the TMAZ on the advancing side of the boundary with the parent material in Figure 5.9f. These voids will be investigated further in Chapter 6.

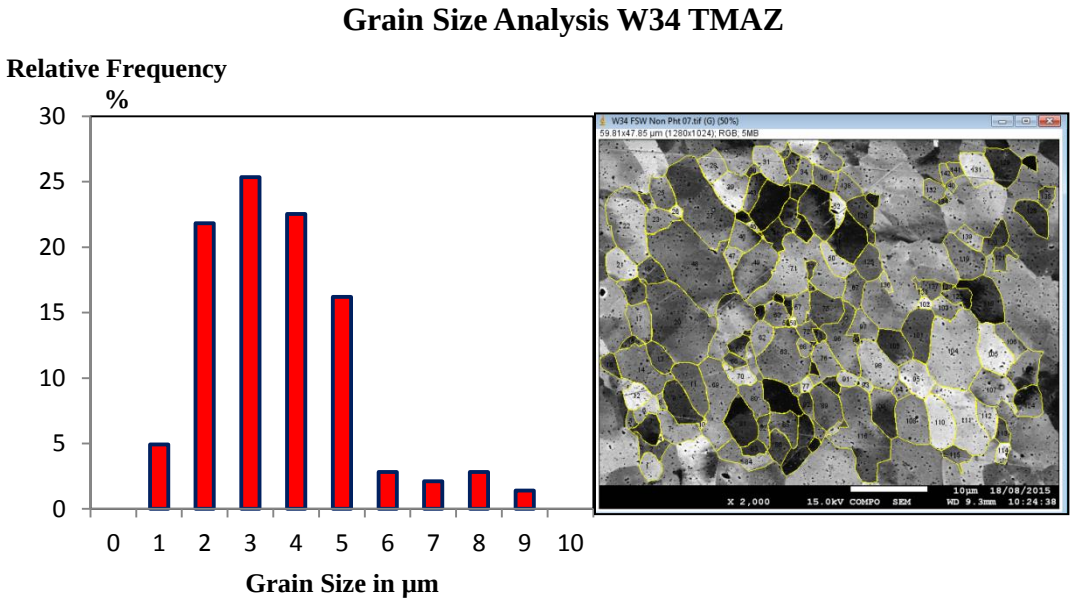

Figure 5.11 *Grain size analysis of the TMAZ of W34 with the image used for analysis inserted.*

Grain size analysis of the TMAZ of W34 as-welded has again shown a near symmetric Gaussian type distribution. The grains ranged in size from 0.6µm to 8.9µm with an average grain size of 3µm which corresponds to a grain size G 14, a near 3 fold increase in grain size of the TMAZ from the parent material region.

W34 Post Weld Heat Treated Condition

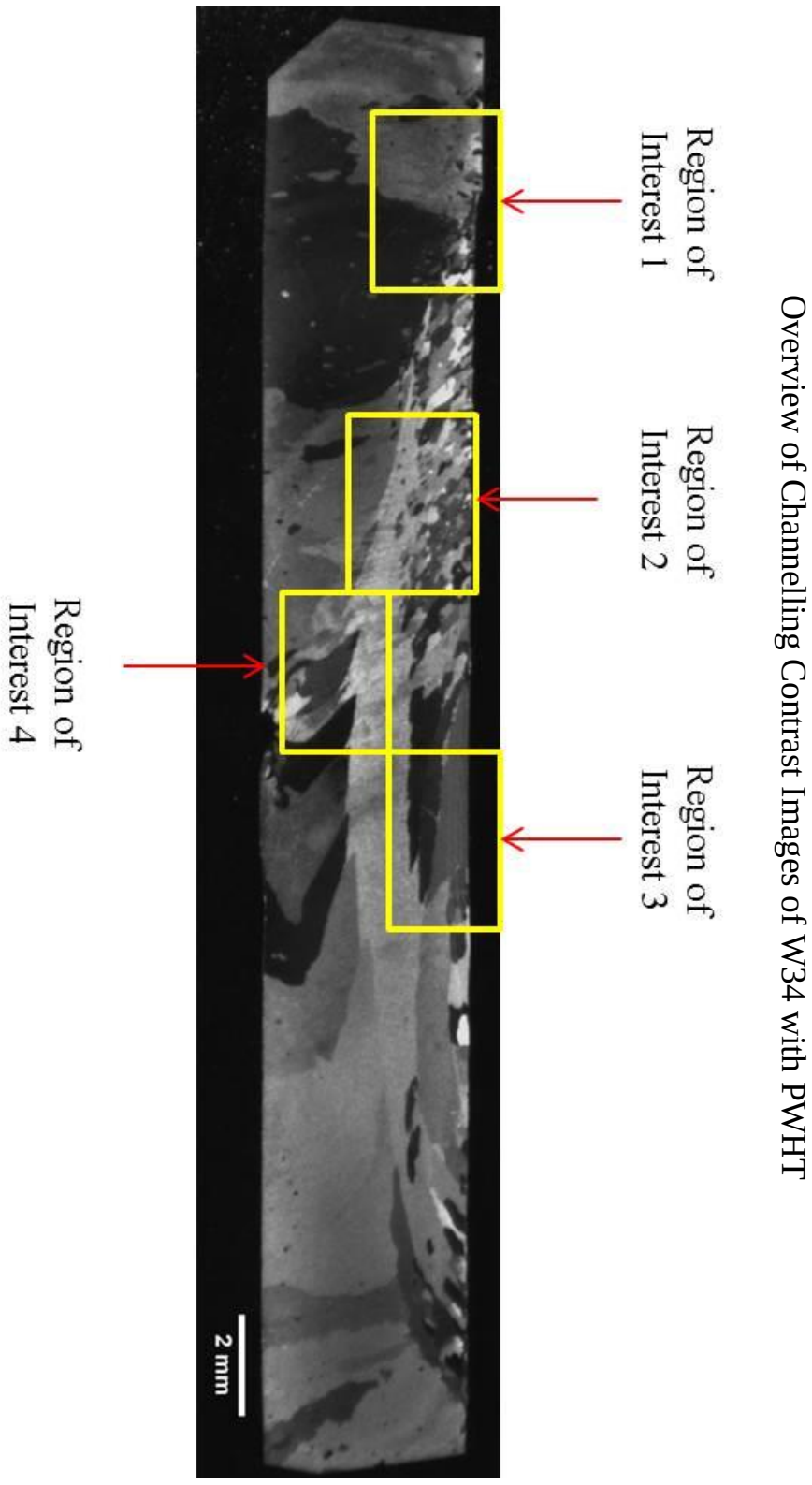

Figure 5.12 *An overview of the various Regions of Interest (ROI) indicated on an optical image of W34 with PWHT to be examined in detail.*

The cross section of W34 after the application of PWHT was examined in the SEM using channelling contrast imaging in backscatter mode. ROI 1,2,3 and 4 are indicated in the optical image in Figure 5.12 for clarity

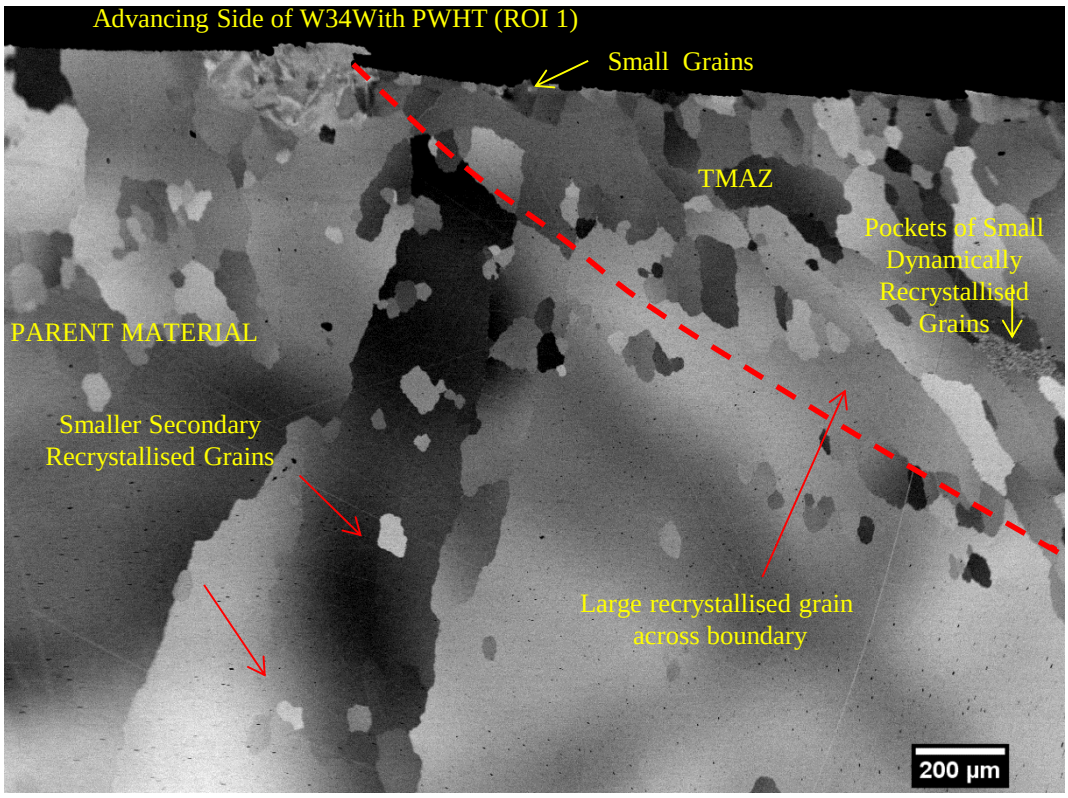

Figure 5.13 *Channelling contrast image of the advancing side of W34 with PWHT (ROI 1)*

A channelling contrast image of ROI 1 of the advancing side of the cross section of W34 with PWHT is shown in Figure 5.13. The red dashed line indicates roughly the position of the boundary between the parent region and the TMAZ as the boundary is not well defined as was in the BOP 7 weld with PWHT. A large recrystallised grain structure was obtained in the parent region unlike the cross section of BOP 7 with PWHT. Some of the large grains have grown across the boundary between the parent region and the TMAZ. Throughout the sample smaller grains of about 100 to 200 microns are seen in the parent region and in the TMAZ.

On the advancing side of the TMAZ next to the parent material boundary, grains have formed in a downward direction which reflects the material flow in that part of the weld. Similar grain growth is seen in the retreating side of the weld but in a much less profound way. As with the previous BOP 7 weld, small grains in the order of 20-50 microns have formed on the surface of the TMAZ.

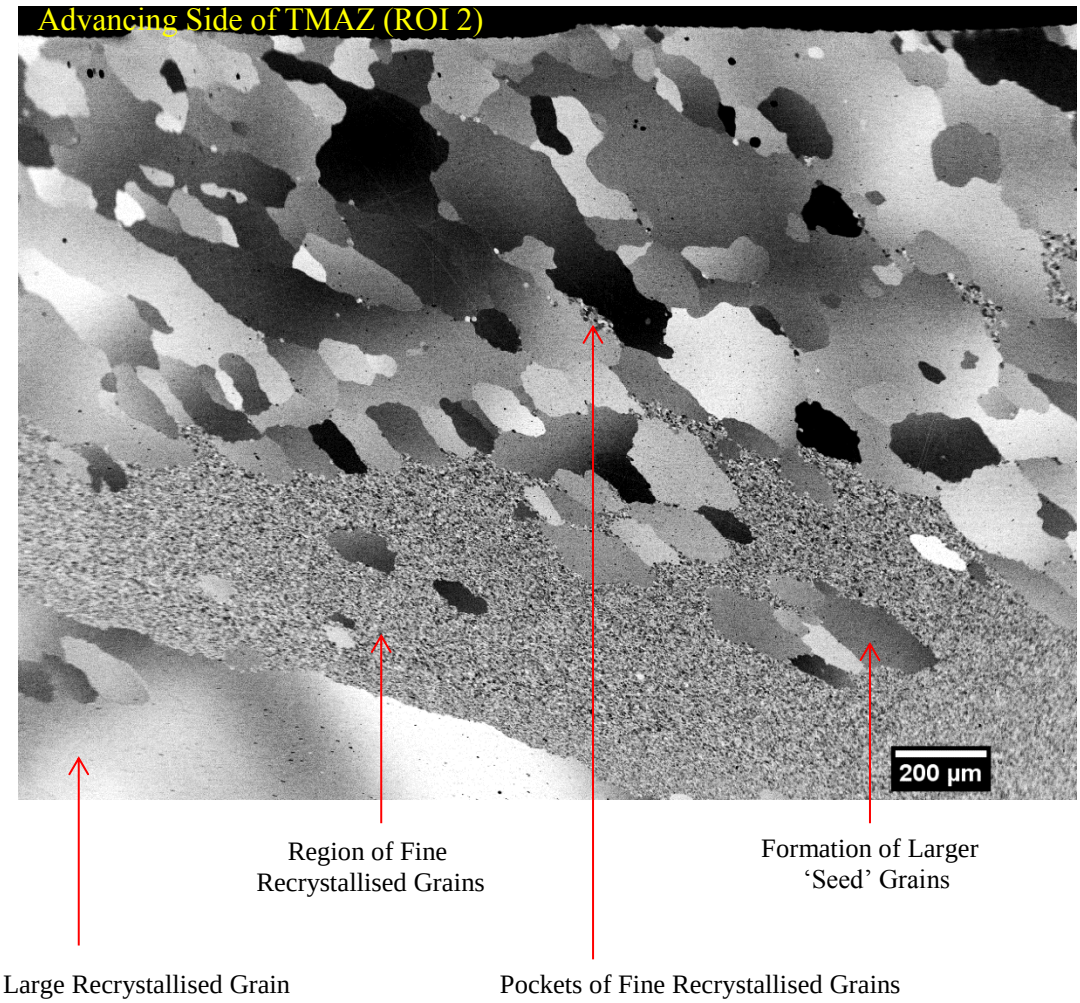

Figure 5.14 *Channelling contrast image of the advancing side of the TMAZ of W34*

These are grains which have formed because of a larger number of nucleation sites near the surface.

A large central region in the TMAZ has recrystallised but with a fine grain structure. This is a region in which the FSW process has induced dynamic recrystallisation, as seen in Figure 5.12 of ROI 2, but the subsequent heat treatment has not been successful in promoting a large recrystallised grain structure. This is very unusual as all the BOP welds with as-rolled PM2000 have fully recrystallised with a large grain structure in the TMAZ.

A higher magnification image taken towards the middle of the advancing side of the TMAZ is shown in Figure 5.15 which corresponds to the ROI 3 in Figure 5.12. Different regions of the TMAZ are arrowed.

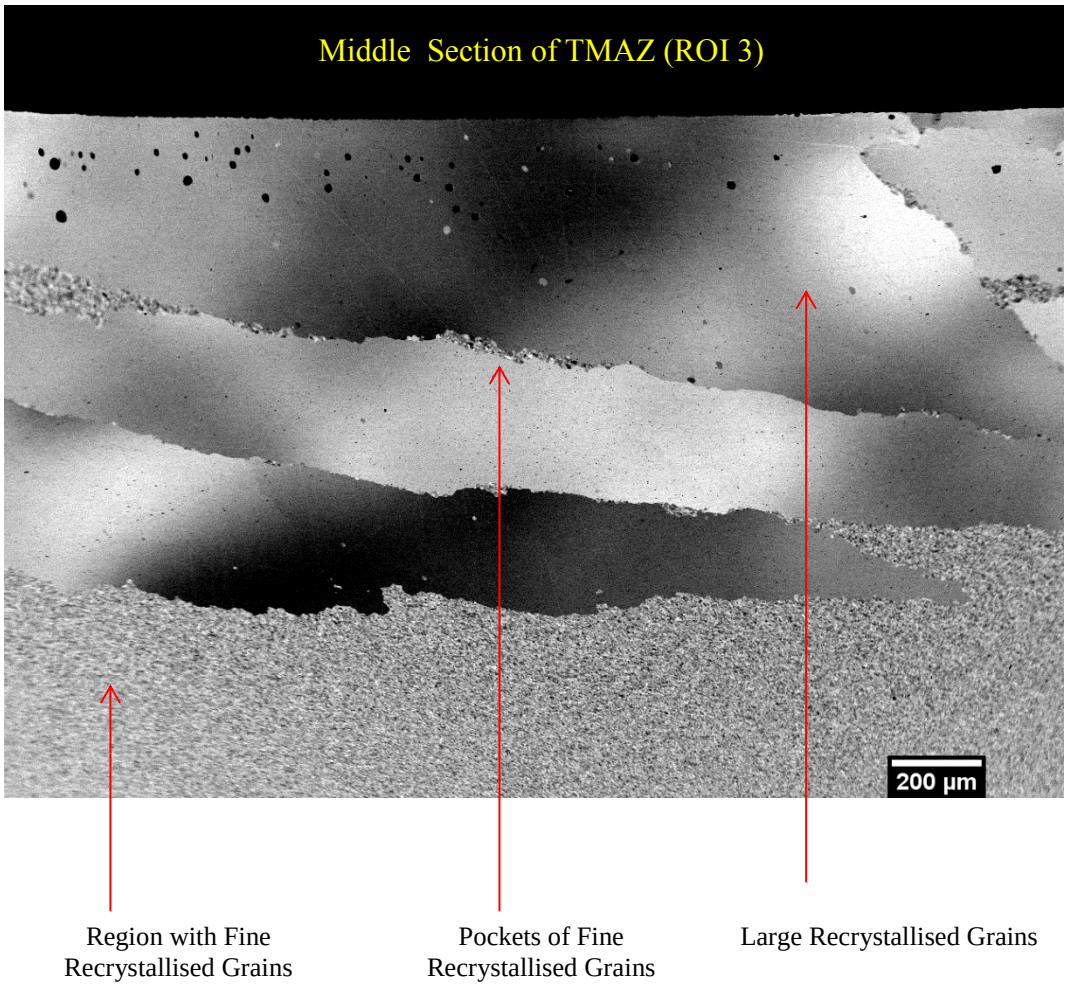

Figure 5.15 *Channelling contrast image of the middle of the top section of the TMAZ marked ROI 3in Figure 5.12.*

A large region of fine recrystallised grains can be seen. Above this region, large recrystallised grains have formed. Pockets of fine grains are observed between the larger grains. In the middle of the fine grain region several 'seed' grains have formed. These are grains that would normally consume the surrounding smaller grains and grow, but the driving force for growth into these regions to create a large grain formation was not sufficient.

At the bottom of the TMAZ, the channelling contrast image in Figure 5.16, which is a higher magnification image of ROI 4 of Figure 5.12, a cavity can be seen which was probably formed by the tool being too close to the bottom of the plate. As in the previous images, pockets of fine grains are trapped between recrystallised grains.

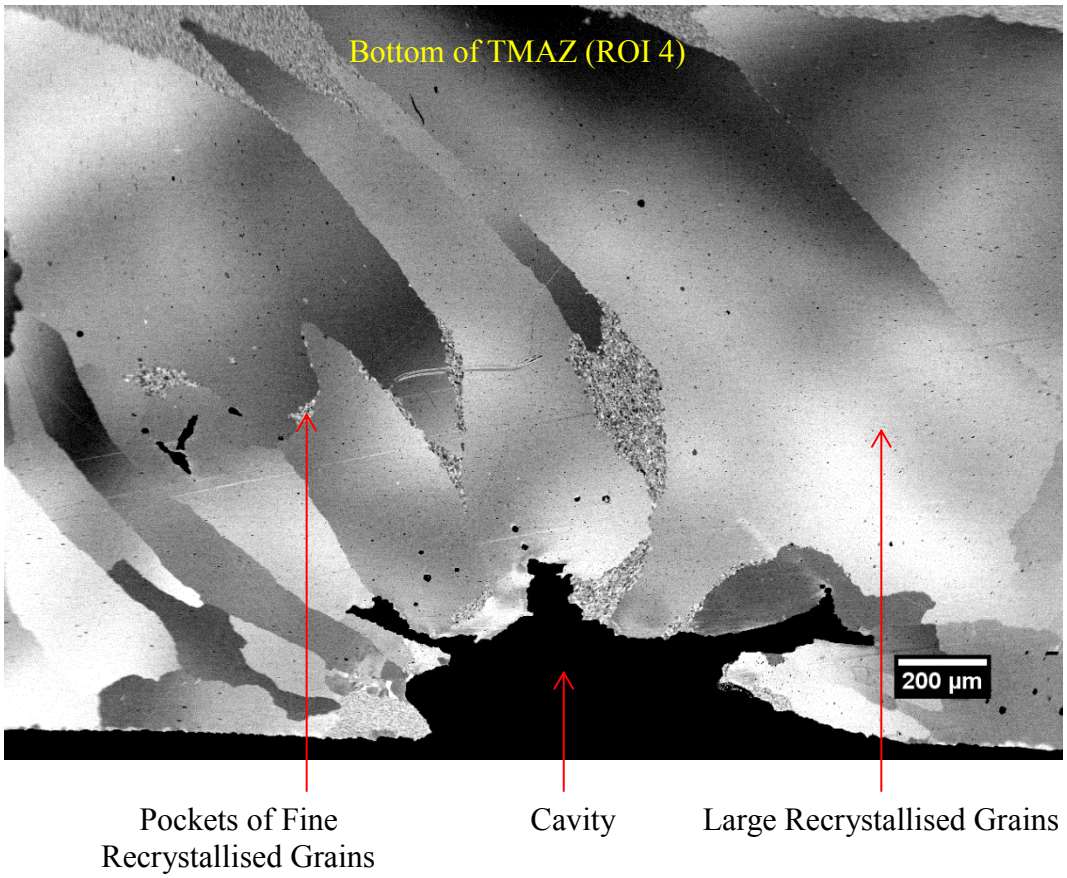

Figure 5.16 *Channelling contrast image of bottom of the TMAZ in W34 PWHT (ROI 4).*

Large recrystallised grains have formed but the interesting feature of this image is the inclination of the grains towards the advancing side of the weld. If you consider the

cross section of the weld, as the tool is rotating anticlockwise and moving away into the page, material is moving towards the advancing side and as the tool moves away, the flow stops as it cools down. This flow direction influences the growth direction of the recrystallised grains. Flow strains introduced by the FSW process influence the direction of the grain growth seen after the application of PWHT. These flow strains probably align the particles along the flow of material much like the extrusion process and the rolling process influence the elongation of recrystallised grains. Nucleation sites could also be aligned with the material flow creating an orientated recrystallised microstructure.

Further analysis of the grain structure is undertaken in the grain morphology section, which follows the particle size analysis section.

5.6 Particle Size Analysis

Two samples of as-extruded PM2000, one of which was heat treated at 1380° for 1 hour, were used for the analysis. Both samples were etched in 10% HCl solution in methanol in an ultrasound bath for 7 minutes. The samples were then analysed in the SEM in SED mode. The magnification of the images used depended on the size and number of particles in the image. Regions with larger particles were analysed at lower magnifications. This resulted in less accurate measurement of the smaller particles as they were only a few pixels in size in the image. Pebbles software was used to measure the diameter of the particles and the data was exported to Excel for analysis.

As-Extruded Condition

As with the previous analysis on the as-received rolled PM2000 in Chapter 4, the application of heat treatment has altered the particle size distribution of the sample. The particle size distribution analysis is shown in Figure 5.17.

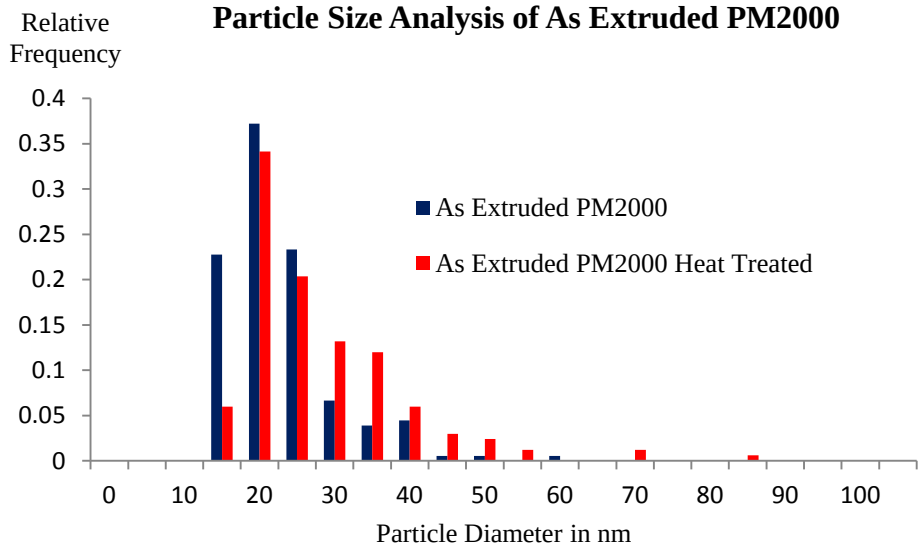

Figure 5.17 *Particle size analysis of as extruded PM2000 with and without heat treatment.*

The average size of the particles analysed was 21nm with a standard deviation of 7nm before the application of heat treatment and an average particle size of 25nm with a standard deviation of 11nm after the application of heat treatment. Once again the coarsening effect of the heat treatment is evident but the extent of the coarsening is minimal.

W34 As-Welded

Two samples were analysed from the TMAZ in the as-welded condition. PWHT was applied to one of the samples. As with the BOP weld, three regions were selected in the TMAZ. The top section was selected about 0.5mm below the surface and then the middle of the weld and finally just above the bottom of the weld.

The particle size analysis data are presented in Figure 5.18.

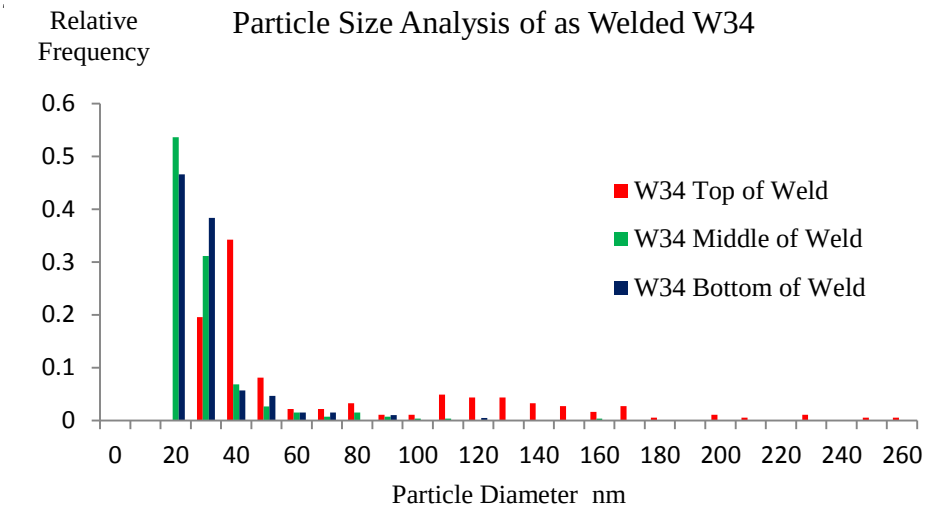

Figure 5.18 *Particle size analysis of each of the three different regions of the TMAZ of the as welded condition.*

The average particle size in the top part of the weld was 68nm with a standard deviation of 52nm whereas the middle and bottom parts both with an average particle size of 24nm and a standard deviation of 16nm and 13nm respectively.

The interesting feature of the analysis is that unlike the BOP sample, the particles in the middle of the weld have not coarsened as much as expected but there is only a negligible difference between the middle and the bottom of the weld. Particle size analysis for the top part of the weld has again shown that there is a definite increase in the coarsening of the particles as seen previously in the BOP welds. The increased agglomeration of the particles in the top part of the weld is again evident from the data presented.

W34 with Post Weld Heat Treatment

The particle size analysis performed at the top middle and bottom of the TMAZ of W34 weld is presented in Figure 5.19. From the channelling contrast images in Figure 5.14 one can see the smaller grain structure of the dynamically recrystallised region which did not then undergo subsequent recrystallisation after the application of PWHT. The middle of the weld particle size analysis data was from this region.

Once again the results mirror the results from the BOP weld from the previous chapter.

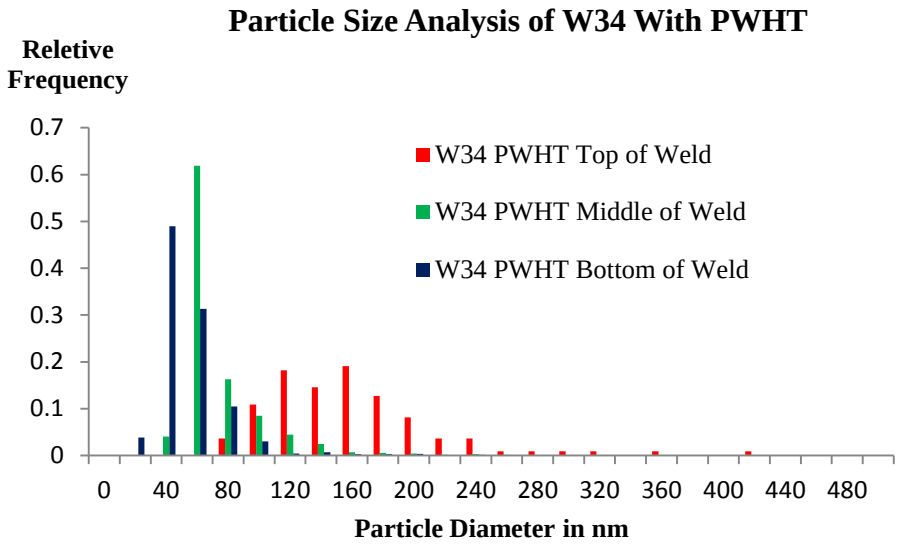

Figure 5.19 *Particle size analysis of each of the regions from the top, middle and bottom of W34 with PWHT.*

The average particle size in the top part of the weld was 150nm with a standard deviation of 55nm. In the middle part of the weld it was 84nm with a standard deviation of 48nm and in the bottom part of the weld it was 62nm with a standard deviation of 28nm.

The main point is that near the top of the weld the coarsening is much more pronounced than the other two regions due to the agglomeration of the particles seen in the TMAZ. When particles agglomerate they can then consolidate to form larger particles which can then give rise to the bimodal particle size distribution that is observed.

5.7 Grain Morphology of W34 with PWHT

From the observations of the channelling contrast images of the grain structure and from the particle size analysis of the three different regions of the weld, the different types of grain formed are analysed further and some explanation as to the processes

involved in forming the different types of grains is attempted. From the observations of the SEM study of the PWHT condition of W34 the grain morphology of the sample can be categorised to 4 distinct types.

1. Large recrystallised grains formed due to limited nucleation sites
2. Smaller recrystallised grains surrounded by larger recrystallised grains in the Parent Material
3. Fine dynamically recrystallised grains
4. Fine dynamically recrystallised grains 'trapped' between larger recrystallised grains

The resultant microstructure after the application of PWHT is very dependent on the starting microstructure of the region being studied and the effects of the FSW process on the particle size analysis. The grain structure of each of the different regions of W34 with PWHT is analysed further and explained with regards to the starting microstructure and the particle distribution.

1. Large Recrystallised Grains

These are large recrystallised grains that have formed in the parent material and partly in the TMAZ as seem in Figure 5.15. The large amount of deformation in the parent material results in large amounts of stored energy that provides the driving force for recrystallisation. The small number of recrystallised grains is indicative of the small number of nucleation sites for recrystallisation. The new grain structure grows at the expense of the surrounding deformed grains to form very large grains sometimes as long as the sample itself. This large grain size is desirable for high temperature applications and the ultimate goal is to be able to form a large microstructure throughout the whole of the sample.

2. Smaller Recrystallised Grains Surrounded by Larger Recrystallised Grains in the Parent Material

As soon as grains nucleate, competitive grain growth will dictate the final grain structure. Some of the grains will be orientated in such a way that they are able to grow into very large grains whereas the growth of grains of a different orientation might be hampered by other grains nearby blocking their advance.

Another possible explanation is that these are large grains that have infringed just above the surface of the larger grains in view.

Figure 5.20 shows a number of smaller grains in the region of 50 to 200 + microns have formed surrounded by a much larger secondary recrystallised grain in the parent material after the application of PWHT. The irregular shape of the smaller grains suggest that there was no 'pressure' to be consumed by the larger grain in view as all the grains are recrystallised with low internal stresses within the grains. It is also possible that these are nuclei of recrystallised grains that have formed late in the process and were then engulfed by the larger recrystallised grain. The driving force for any one grain to consume another, now being too low as all the grains are recrystallised.

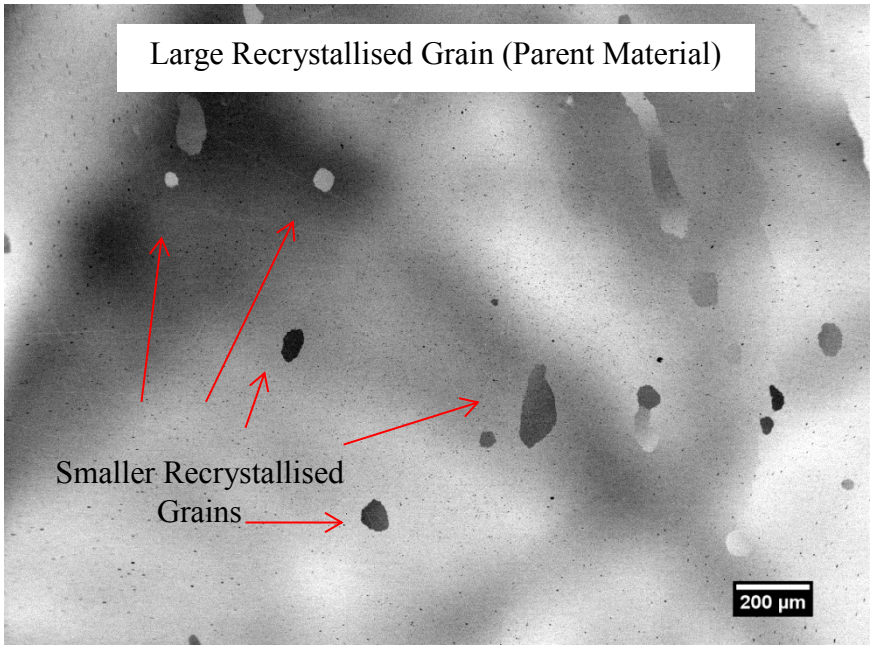

Figure 5.20 *Channelling contrast image showing a number of smaller secondary recrystallised grains that have formed surrounded by a much larger secondary recrystallised grain in the parent material of W34 after the application of PWHT.*

3. Fine Recrystallised Grains

This microstructure is from the TMAZ part of the sample where the FSW process has resulted in the dynamic recrystallisation of the region. In the previous BOP welds this microstructure has resulted in recrystallisation with a large grain structure in the

TMAZ after the application of PWHT. In the case of W34 only part of the TMAZ has recrystallised into large grains. There is a large region in the middle of the TMAZ that has recrystallised with a fine grain structure. This is indicative that a large number of nucleation sites have formed in this region. At the retreating side of the TMAZ, there is a well-defined boundary between the fine recrystallised grains and the very large recrystallised grains. At the advancing side of the TMAZ several large grains can be seen in the middle of the fine recrystallised grain region. These are grains that had the potential to grow even larger but not enough driving force was available for these grains to do so.

In the as welded condition the grain size of the dynamically recrystallised TMAZ was in the order of between 2 to 5 microns in size. After the application of PWHT the grain size of the fine recrystallised region in the TMAZ has not changed which may suggest a low dislocation density and so a lack of driving force in this region is more likely the reason for not undergoing large grain recrystallisation. Internal stresses introduced by the FSW process may have an impact on the recrystallisation behaviour of the different regions in the TMAZ which may explain the fact that the central part of the TMAZ has not undergone large grain recrystallisation.

4. Fine Dynamically Recrystallised Grains 'Trapped' by Secondary Recrystallised Grains

These are grains that were dynamically recrystallised in the TMAZ by the FSW process and after the application of PWHT have not been consumed by the much larger grains that have undergone recrystallisation because there is insufficient difference in dislocation density to drive the grain boundary movement..

The channelling contrast image in Figure 5.21 shows extensive bowing of the grain boundary between the larger recrystallised grains and the smaller recrystallised grains next to them. From several observations from different cluster of grains the grain structure of the smaller recrystallised grain region has not changed. 'Pressure' from both the larger grains has resulted in flattening of some of these grains due to the diffusion process involved in the grain growth of recrystallised grains, resulting in an increase in their aspect ratio.

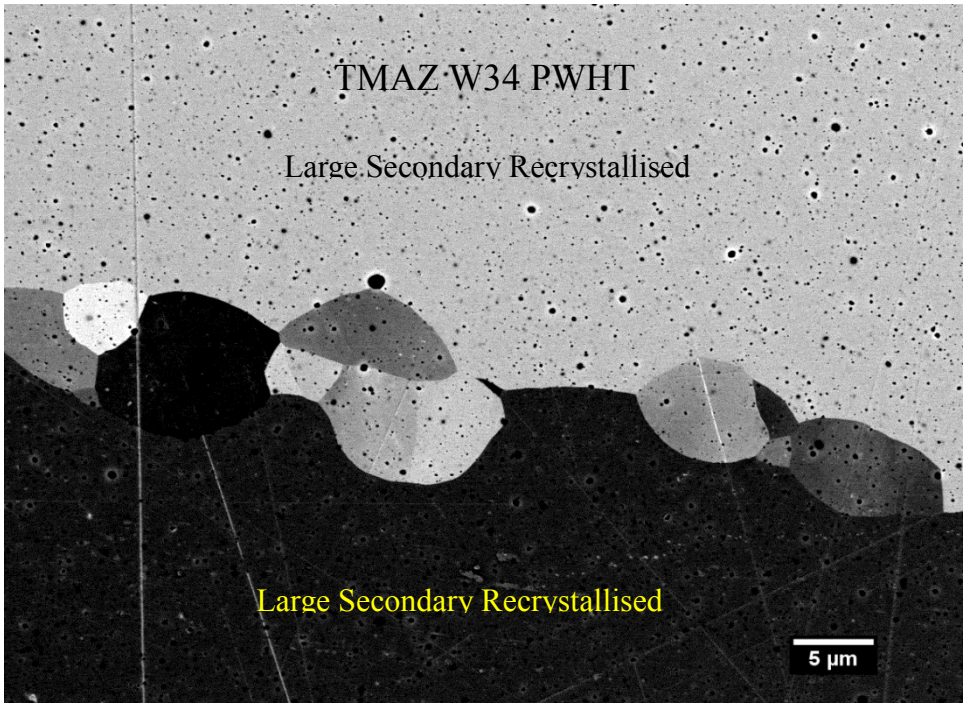

Figure 5.21 *Channelling contrast image of a region in the TMAZ showing smaller dynamically recrystallised grains, surrounded by secondary recrystallised grains.*

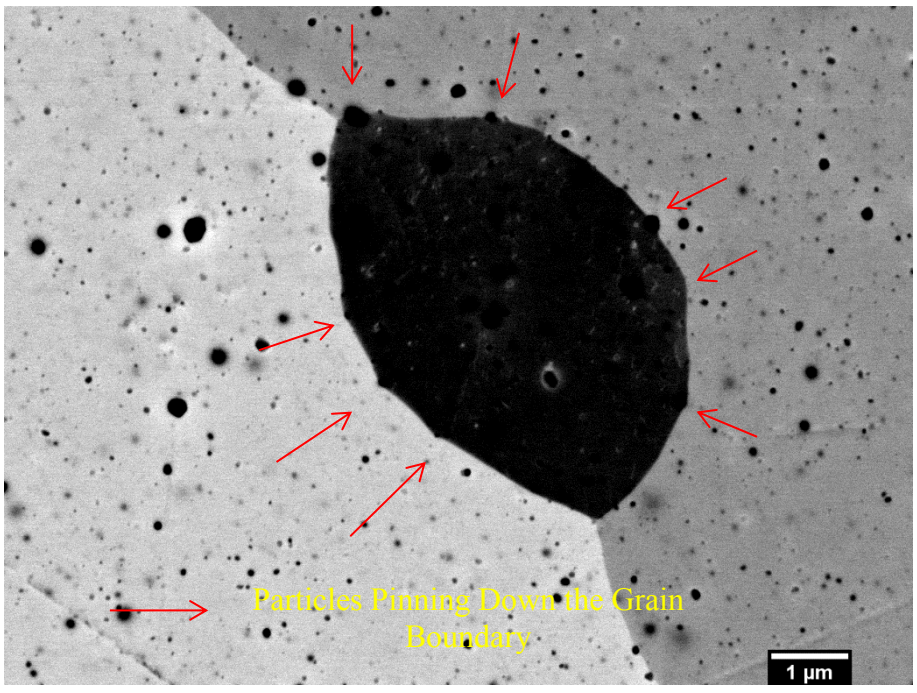

Figure 5.22 *Channelling contrast image of a single dynamically recrystallised grain surrounded by two large secondary recrystallised grains. Particles pinning the grain boundary can be seen causing the bowing of the boundary between the particles.*

Another channelling contrast image in Figure 5.22 shows a single recrystallised grain between two much larger recrystallised grains. As the recrystallisation process is a short range diffusion lead process, the grain boundary of the smaller grain is curved and as it reduces in size it interacts with particles that pin down the grain boundary. Bowing of the grain boundary in between the particles can be clearly seen all along the grain boundary. Eventually given enough time the smaller recrystallised grain would be consumed completely.

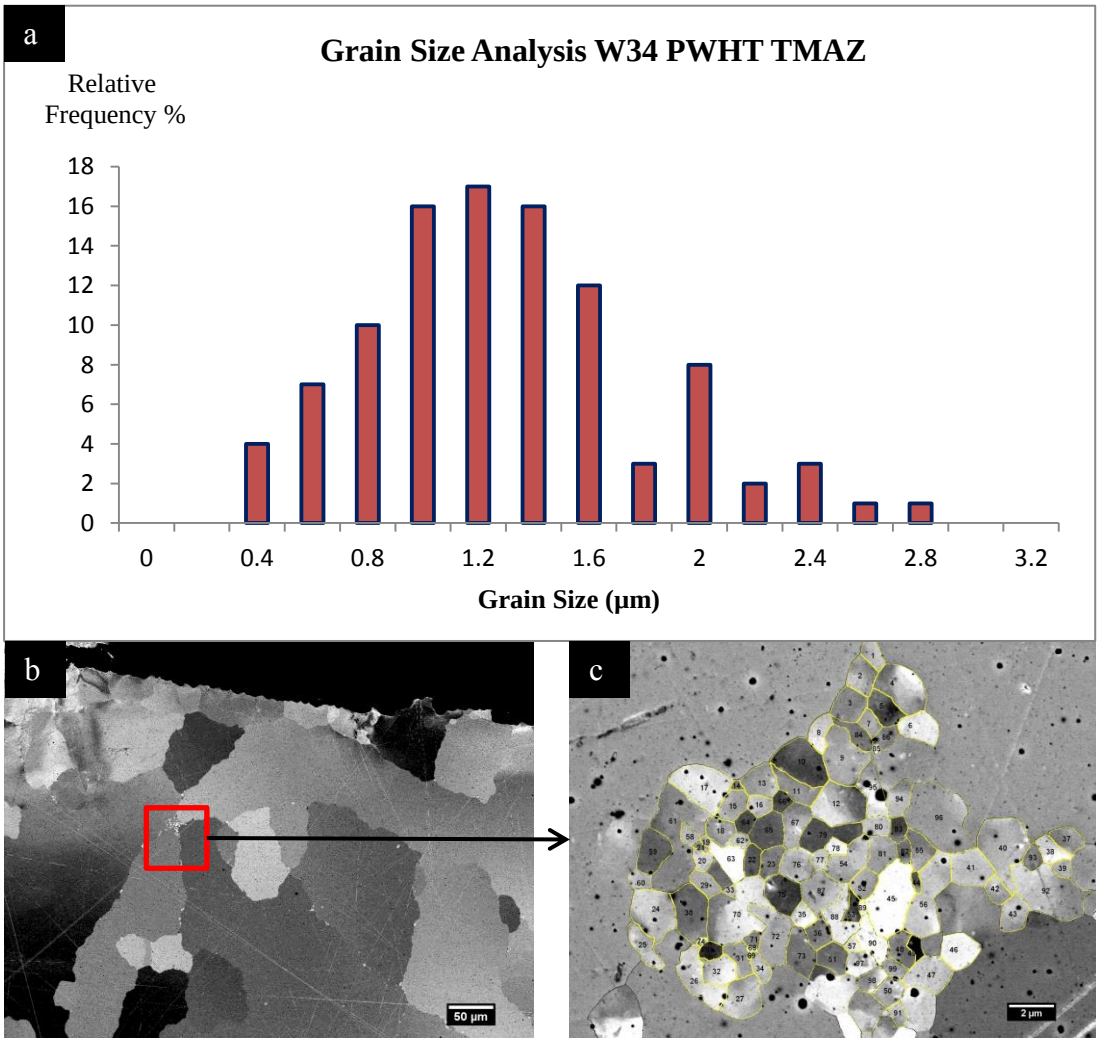

Figure 5.23 *a) Grain size distribution of region of interest from the channelling contrast images b and the higher magnification image (c).*

One particular region of interest is shown in Figure 5.23b which is near the top of the advancing side of the weld. A small cluster of fine recrystallised grains (Figure 5.23c) are observed surrounded by large recrystallised grains. The main difference with this cluster was the small size of the grains. In order to determine the grain size, analysis was performed on this cluster and the results are presented in the histogram in Figure 5.23a.

The grain size analysis results give an average grain size of 1.2 μm which suggests that this region is recrystallised with a fine grain structure that has not increased in size from the parent grain structure. From the channelling contrast image in Figure 5.23b it is difficult to know exactly where the boundary between the parent material and the TMAZ is. The cluster of grains observed between the much larger recrystallised grains in the W34 PWHT sample can be observed in both the parent material and the TMAZ even though in the TMAZ dynamic recrystallisation has increased the average grain size from 1.2 μm to 3 μm. The most likely explanation is that there is a variation in the particle distribution and a cluster of particles that can form in some regions prevents the formation of larger recrystallised grains by the severe pinning of the grain boundaries. Stringers of particles were observed in the longitudinal view of the parent material along the extrusion direction as observed in Figure 5.18. These regions were concentrated with particles and they would therefore impart a larger pinning force in these small areas. When you consider the transverse view the stringers would occupy small regions where large grain recrystallisation would be prohibited, as observed with the small clusters of recrystallised grains.

5.8 TEM Study of Second Phase Particles

Second phase particles play an important role in providing additional creep strength at high temperatures. These particles pin dislocations and grain boundaries and hinder their movement. The effect is known as Zener drag and the magnitude of the drag dependents on their size and number density of the particles [24]. A large number density of very small particles is more effective in pinning the dislocations and grain boundaries. Needless to say that anything which alters their size and

distribution will have an impact on their effectiveness and will therefore alter the materials mechanical properties and its recrystallisation behaviour. The particle size analysis in this chapter and in the previous chapter has indicated that the FSW process agglomerates the particles which then consolidate to larger particles after the PWHT process. Although some work has been done in Chapter 4 identifying the types of particles present in PM2000, in this section a more detailed study of the particles was undertaken. In particular the interaction between particles and grain boundaries and between particles and dislocations were studied. In addition particles in the TMAZ of W34 before and after the application of PWHT were focused on.

5.8.1 Particle-Grain Boundary Interactions

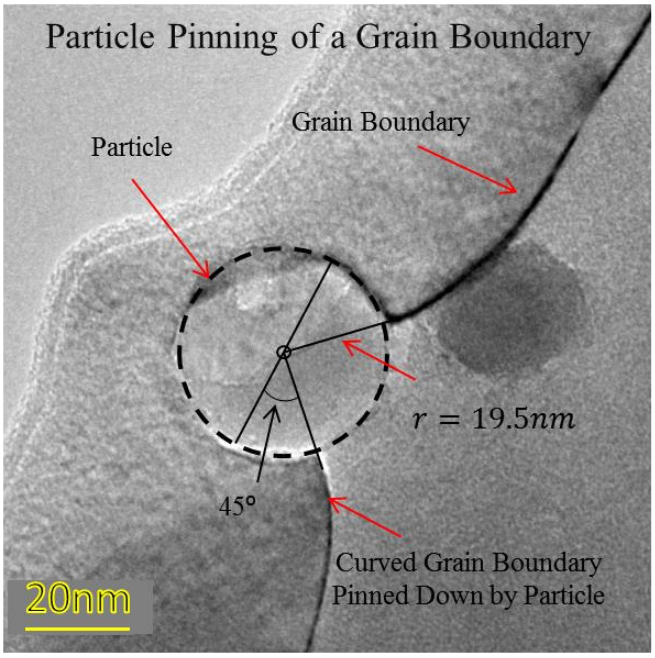

Figure 5.24 *A bright field TEM image of W34 as welded TMAZ region showing a particle pinning a grain boundary with the characteristic curvature of the grain boundary around the particle.*

When grain boundaries migrate due to grain growth or recrystallisation processes, second phase particles are encountered. The grain boundaries are then pinned due to the Zener drag as discussed in the literature review in Chapter 2 Section 2.7. One such particle interaction with a grain boundary is shown in Figure 5.24.

The image is from W34 as welded sample, and the particle which is 39.8 nm in diameter can clearly be seen in a typical pinning position with the grain boundary curved towards it. The grain boundary is attracted to the particle as it lowers the overall energy of the system. For a non-coherent particle the pinning force attributed to the particle is given by the equation

$$F_p = 2\pi r_p \gamma_{GB}\, cos\beta\, sin\beta \qquad \textit{(Equation 5.1)}$$

The maximum force exerted is when the angle $\beta = 45°$ as is the case in Figure 5.24. Angle β was measured at 45° in which case the pinning force is then given by,

$$F_p = \pi r_p \gamma_{GB} \qquad \textit{(Equation 5.2)}$$

Where r_p is the radius of the particle (19.9 nm) and γ is the grain boundary energy which for PM2000 [40] is taken as 0.5 J/m^2. The pinning force due to this size particle that is not coherent was calculated to 3.1 x10^{-8} J/m.

Particles present in the matrix can be coherent, incoherent or semi-coherent. In the case of semi – coherent particles there is a slight mismatch between an orientation of the matrix and the particle which can result in Moiré fringes. Figure 5.25 shows one such particle that is semi-coherent in Grain 1 but the particle is not coherent with respect to Grain 2 and the result is that Moiré fringes are observed only on one half of the particle.

The Moiré fringes observed are a combination of translational and rotational type fringes. For small misorientations the Moiré spacing can be calculated using the following formula [87]:

$$d_m = d_1 d_2 / ((d_1 - d_2)^2 + d_1 d_2 \beta^2)^{\frac{1}{2}} \qquad \textit{(Equation 5.3)}$$

Where d_m is the moiré fringe spacing, d_1 is the matrix d spacing, d_2 is the particle d spacing and β is the misorientation angle in radians.

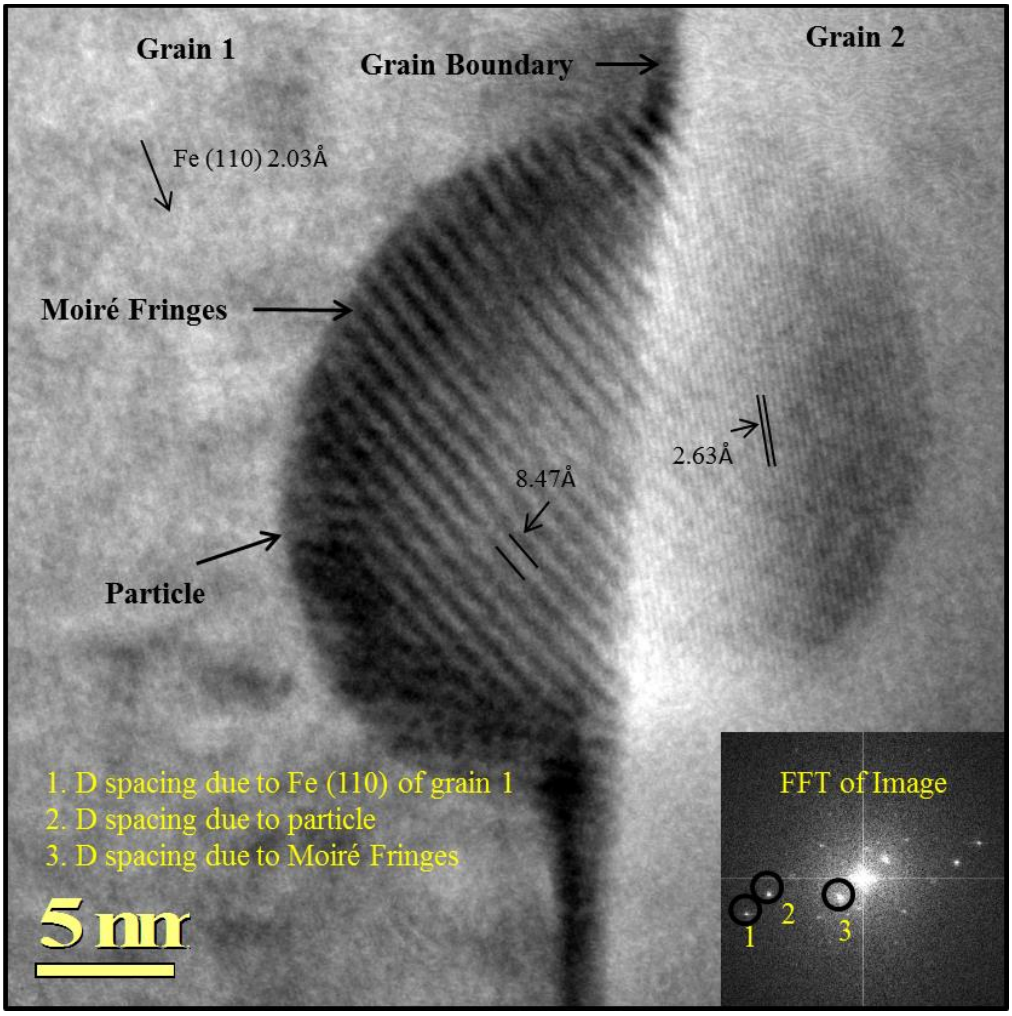

Figure 5.25 *HRTEM image taken from W34 as welded sample showing a particle pinning a grain boundary with moiré fringes visible in grain 1 but not in grain 2. Insert shows FFT of image with diffraction fringes, due to grain 1 and the particle, producing moiré interference.*

Using d_1= 2.03Å for the Fe (110) d spacing, d_2 = 2.63Å for the particle d spacing and 7.0° as the misorientation angle as measured from the FFT of the image, the calculated d_m = 8.05 Å. The measured d_m = 8.16 Å which is in good agreement with the calculated value.

5.8.2 Particle-Dislocation Interactions

Second phase particles hinder the movement of dislocations in the matrix. The dislocations can shear through the particles but in the case of hard particles such as

oxides, nitrides and carbides the dislocations can loop around and bypass particles, a process called Orowan Bowing [63].

The bright field TEM image in Figure 5.26 shows several dislocation interactions with the particles present in the matrix. The variety of the shape and size of the different phases of particles present in the matrix is evident from the image. Orowan bowing of the dislocations and dislocation pinning by particles is evident in the image.

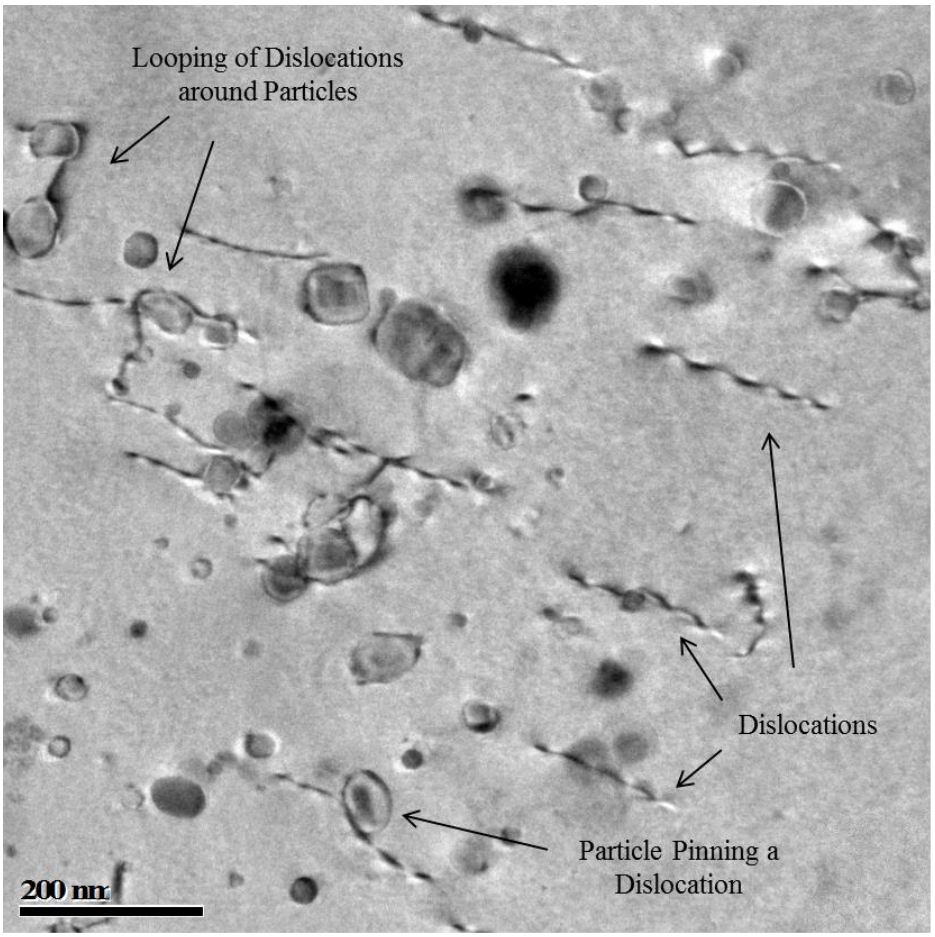

Figure 5.26 *TEM bright field image of the TMAZ in W34 with PWHT showing a number of dislocations, particles pinning dislocations and the looping of dislocations around particles Notice the low density of dislocations.*

As the dislocation line encounters an array of particles Orowan bowing around the particles allows the dislocation line to progress beyond the particle array. Dislocation

lines can attract each other and by a process known as the Orowan mechanism, as discussed in the literature review in Chapter 2, it results in a ring of dislocation around each of the particles and the continuation of the dislocation past the particle array.

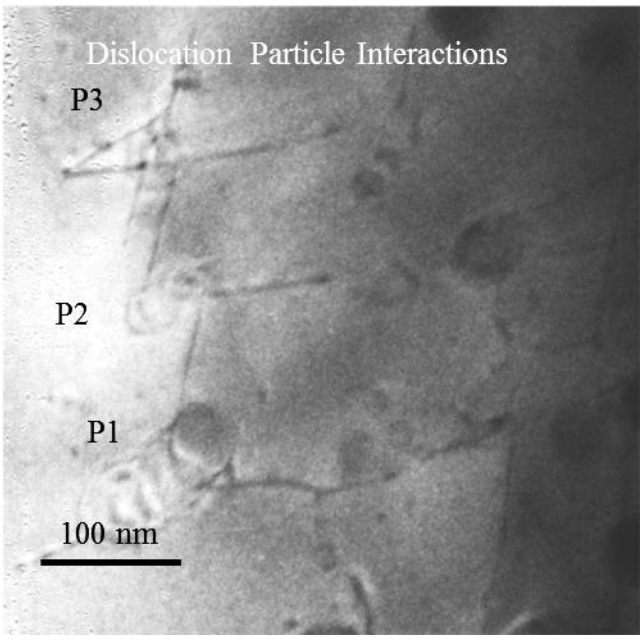

Figure 5.27 *TEM bright field image of W34 as welded TMAZ sample showing an array of particles with complex arrangement of dislocation lines.*

The TEM bright field image in Figure 5.27 shows one such array of three particles but with a different outcome with regards to the dislocation line. The following description is speculative but the image shows an unusual arrangement of dislocations.

A possible explanation could be that when the second phase particles are close together the distance of the bowing dislocation lines between two particles can be shorter than the distance of the dislocation lines either side of a single particle which is further reduced if the angle between the dislocation line and the array of particles is not perpendicular. The two dislocation lines between two particles can be attracted to each other but particles are attractive to a dislocation line as the dislocation line energy can be reduced further. This could result in the formation of two near

perpendicular lines of dislocations with each one attached to a particle at one end as observed in the image in Figure 5.27. This could be a contributory process to strengthening as the average distance between the particles is near to the actual size of the particles then the dislocation lines may not be able to bypass the particle array.

5.8.3 Particle Morphology

A fine distribution of second phase particles with a high number density imparts a big enough drag force that combined with the small grain size of ODS steels, which themselves provide a pinning force to the migration of grain boundaries, is the main reason why ODS steels have a very high recrystallisation temperature (0.9Tm). The driving force for recrystallisation has to overcome the Zener drag from the second phase particles and from the pining effect of the small grain structure as mentioned in the literature review (Chapter 2, Sections 2.5 and 2.7). Any thermal mechanical process such as FSW which alters the size and distribution of the second phase particles will have an effect on any subsequent recrystallisation treatment.

Following the particle size analysis of both as-rolled and as-extruded PM2000, particle coarsening through agglomeration especially in the top section of the TMAZ was attributed partly to the rotation of the shoulder of the tool creating more encounters with neighbouring particles. In this section TEM analysis was used to investigate in depth the particle agglomeration and in particular any orientation relationship that exists between the agglomerated particles with each other and with regards to the matrix and the subsequent consolidation of these particles after the application of PWHT.

W34 As-Welded Condition

TEM investigation of the W34 as-welded sample has revealed the extent of the particle agglomeration that has occurred due to the effects of the FSW process. The bright field TEM image in Figure 5.28 shows clearly several clusters of agglomerated particles the TMAZ of W34. Particles were observed to have agglomerated to more than one other particle. In most cases even 4 or more particles have agglomerated together although you can still see a few single phase particles in the image. When investigating agglomerated particles it was difficult to identify with

a high degree of confidence the type of the particle under observation as the FFT of the HRTEM images would contain information from more than one set of lattices. In addition any EDX analysis would also be affected by several particles due to the interaction volume of the analysis of a thin foil.

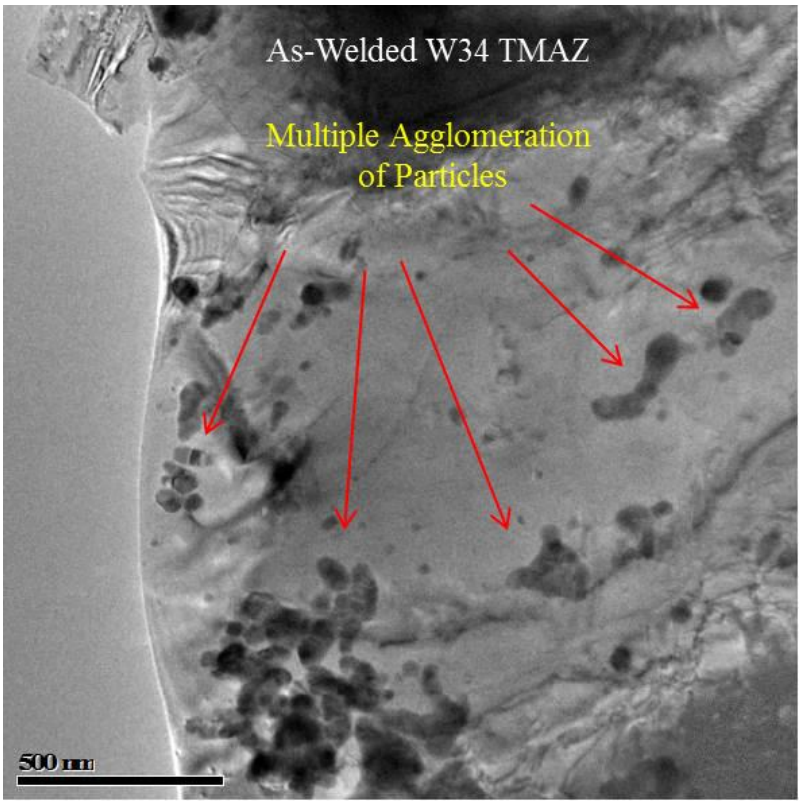

Figure 5.28 *A TEM bright field image of the TMAZ in the as welded W34 sample. Please note the number of large agglomerations of particles.*

On the other hand, two particles joined would not necessarily be the product of agglomeration due to FSW as many two phase particles are present in the as received PM2000 anyway. The particles selected have several regions of different lattice structure that indicate that the particles have probably agglomerated due to the FSW process.

In Figure 5.29a two particles on a grain boundary that have agglomerated can be seen. In the higher magnification image in Figure 5.29b, the particles are named P1 and P2 with the region of interest marked ROI 1.

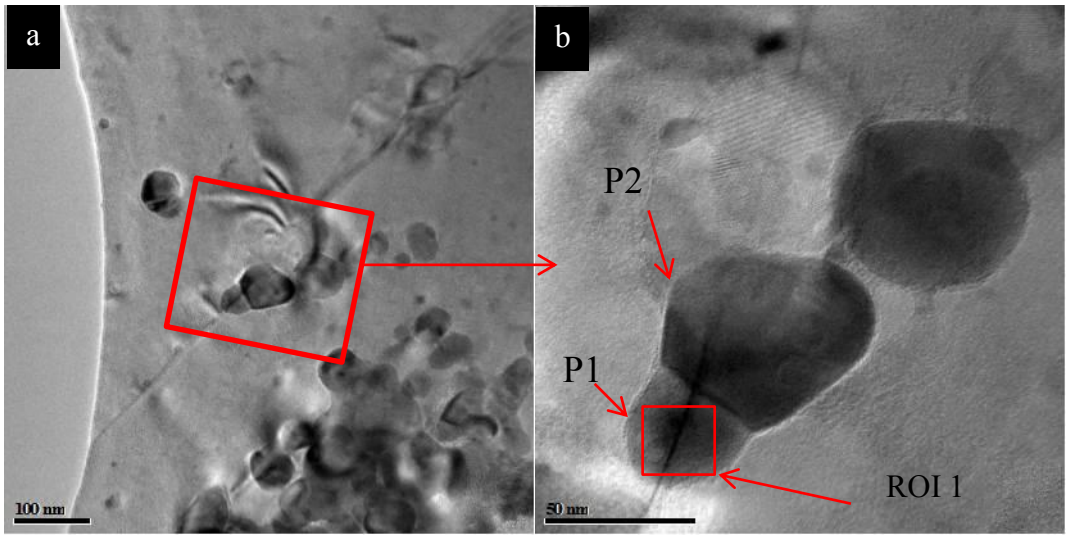

Figure 5.2*9 Bright field TEM images of the TMAZ in the as welded W34sample with a) agglomerated particles and b) a higher magnification image of a particle outlined showing two agglomerated particles on a grain boundary with Region of Interest marked.*

EDX analysis of both particles has indicated the presence of Y Al and O but the relative quantities of each of the elements were inconclusive with regards to determining the composition of the particles. This is not surprising as on closer investigation of the HRTEM bright field image of ROI 1 as observed in Figure 5.30 one can see lattice arrangements of different orientations in different parts of P1. FFT of 5 different regions reveal 5 different diffraction patterns but all with a common orientation which is marked on all the FFT‘s taken. This highlights the difficulty in determining the phase of the particle as more than likely several phases are present in any agglomeration of particles.

The extent of the agglomeration is evident from the fact that there is a multitude of lattice orientations that is an indication of the number of different phases or particles attached to each other. The common orientation arrowed in Figure 5.30 could be any of a number of possible phases and therefore the particle has not been resolved. The YAP, YAG, YAM and Y_2O_3 phases all have a d-spacing of 1.63Å or very near to it, and all with strong reflections as listed on Table 5.3, and as shown in Figure 5.31.

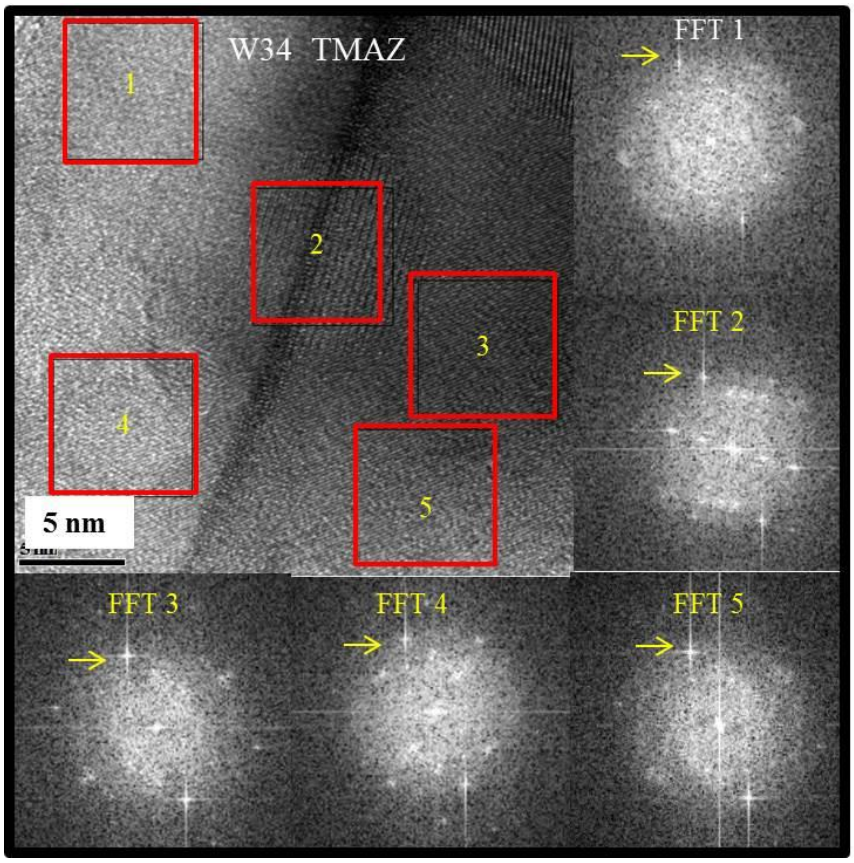

Figure 5.30 *HRTEM image of ROI showing lattice resolution of P1, and 5 areas with their corresponding FFT. The common lattice orientation is arrowed.*

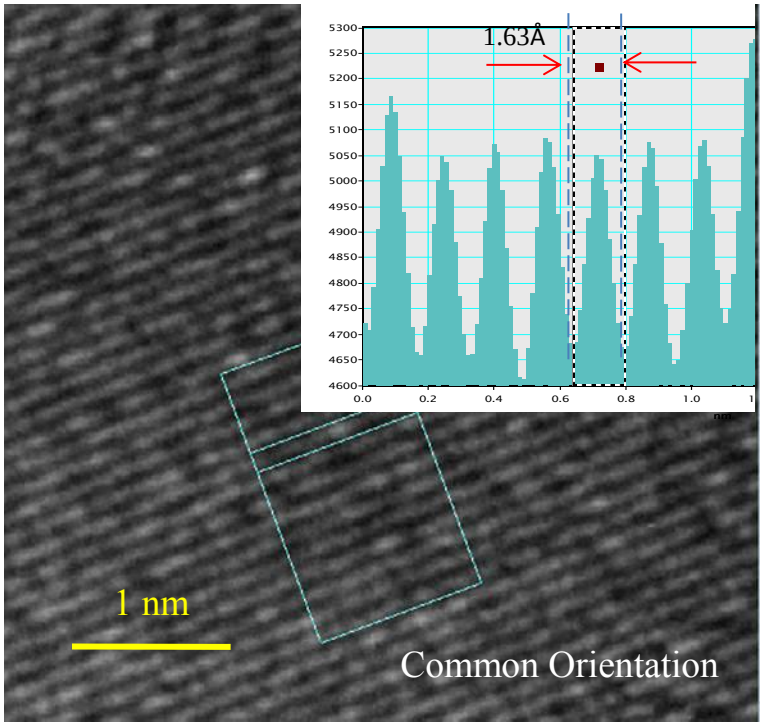

Figure 5.31 *Above HRTEM bright field image of the common lattice in P1 with the line intensity measurement tool from Digital Micrograph software measuring the d spacing at 1.63Å.*

Table 5.3 *Below a table listing the different phases of particles with the common (or near to) orientation of 1.63Å with corresponding h, k, l and I/I Max intensity of each orientation*

Phase	D-spacing (Å)	(h ,k ,l)	I/Imax (%)
YAP	1.63	(1, 3, 1)	24
YAG	1.60	(6, 2, 4)	28
YAM	1.63	(3, 2, 3)	27
YAM	1.62	(-2, 3, 6)	28
Y_2O_3	1.60	(2, 2, -6)	23

This is an indication of the complexity of the formation of particle clusters that can form in the TMAZ of the weld. In the bright field TEM image of the particles it seems that there are only two particles that have agglomerated but closer examination of the lattice resolution image reveals several lattice orientations.

As well as agglomerated particles a number of single phase particles were observed. One such particle observed is a YAP phase particle seen in Figure 5.32. The HRTEM image was taken from a TEM foil from W34 as-welded sample. This is a single particle that is semi coherent with regards to the matrix. As the matrix is only present in the left hand side of the particle one can see the moiré fringes in two directions which suggests that there is an orientation relationship in not just one direction but two.

The orientation relationship with the $(1\bar{1}\,\bar{1})$ YAP || (110) Fe plane and along the [110] YAP || [002] Fe direction and the $[\bar{1}1\bar{2}]$ YAP || [1-10] Fe direction. In a paper by Foxman et al. [107] the orientation relationship $(2\bar{1}0)$ YAP ∥ $(\bar{1}10)$ Fe, [121] YAP ∥{111}Fe was reported between a YAP particle and Fe matrix.

The moiré fringes observed are of the translational type which is due simply to the difference in d spacing between the two orientations in the relationship. FFT of the HRTEM image in Figure 5.32 is shown in Figure 5.33.

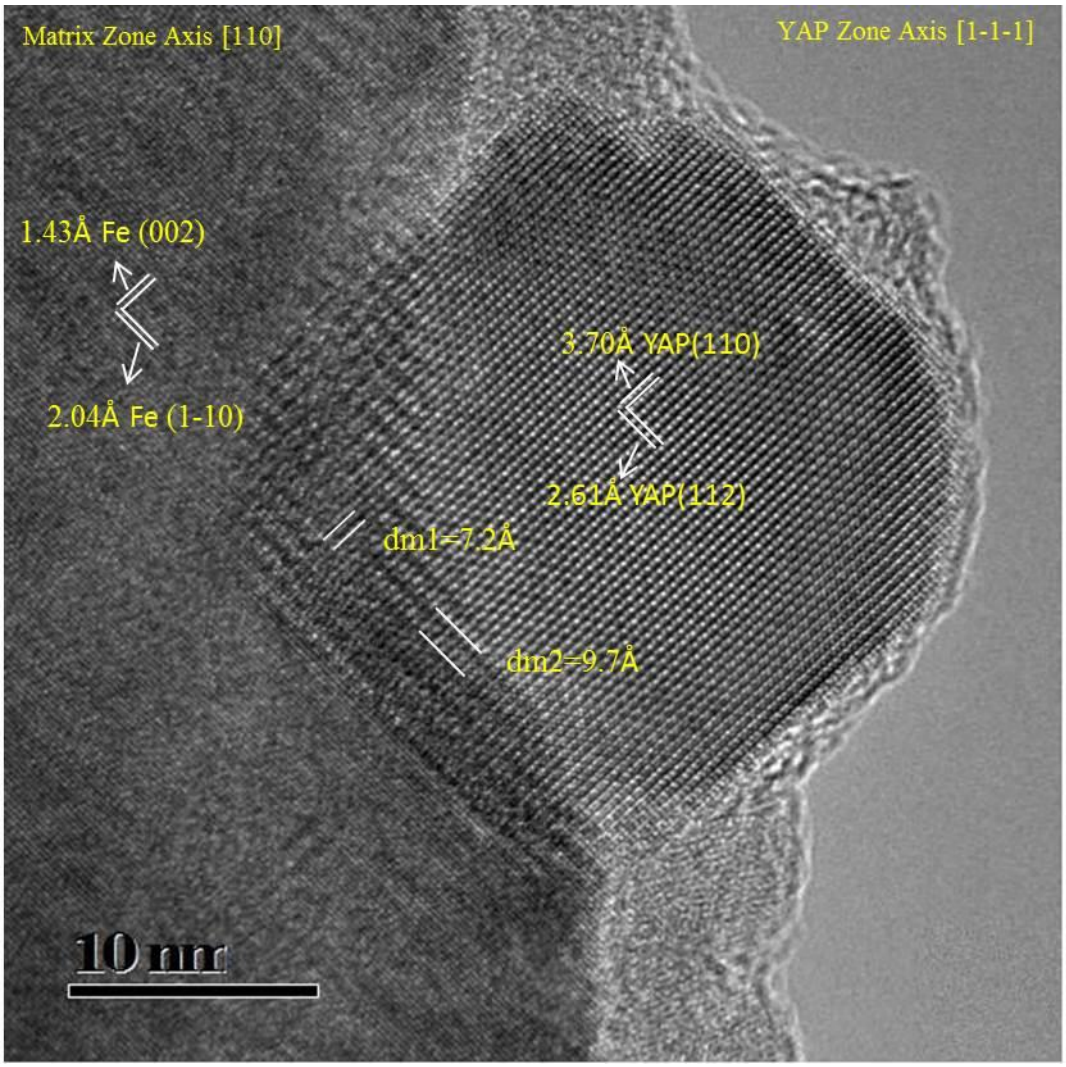

Figure 5.32 *HRTEM image of a semi coherent YAP particle with translational moiré fringes in two directions due to the orientation relationship between (1-10)Fe//(112)YAP and (002)Fe//(1-10)YAP*

In order to calculate the translational moiré d spacing equation the following equation is used [87].

$$d_m = d_2 d_1/(d_1 - d_2) \qquad \textit{(Equation 5.4)}$$

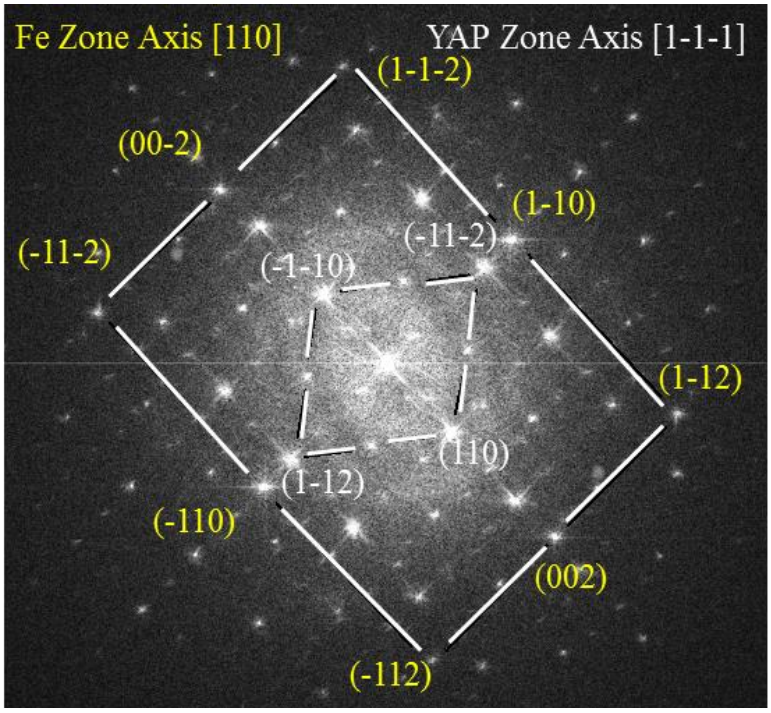

Figure 5.33 FFT of the bright field TEM image in Figure 5.32 showing the orientation relationship between the matrix and the YAP particle.

Where d_m is the moiré d spacing and d_1, d_2 are the d spacing of the two lattices. The calculations using Equation 5.4 are in very good agreement with the measured moiré fringe spacing. For the $[\bar{1}1\bar{2}]$ YAP || $\{1\bar{1}0\}$ Fe orientation relationship the calculated $d_m = 9.7$Å (measured $d_m = 9.8$Å) and for the [110] YAP || [002] Fe relationship the $d_m = 7.2$Å (measured $d_m = 7.7$Å).

W34 with PWHT

Samples of W34 cross sections were heat treated at 1380° for 1 hour. TEM samples were prepared in the usual manner.

The low magnification images of the matrix in Figure 5.34 indicate that the many agglomerations are no longer observed but instead there are many large mainly single phase particles. Many two phase particles or multiphase particles are still seen but they are all uniform in shape and not clustered together as in the as-welded samples.

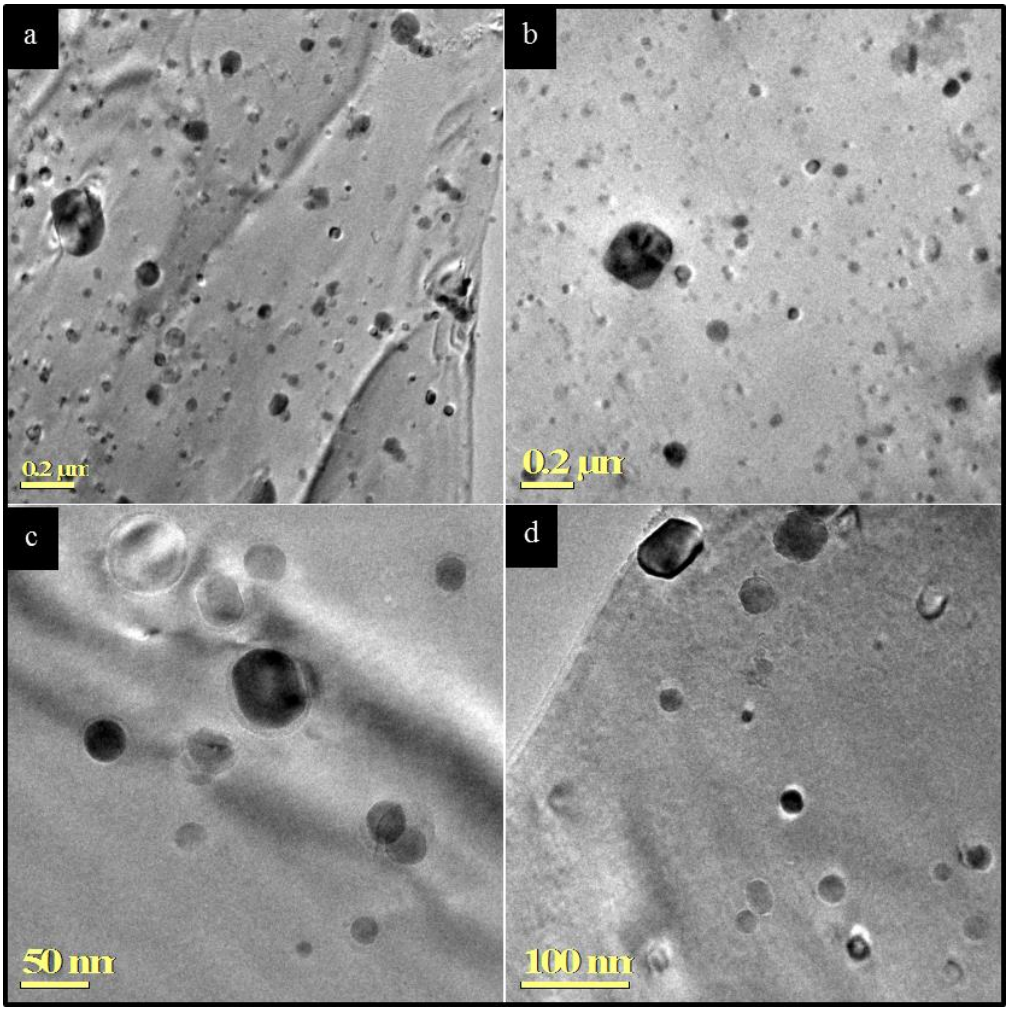

Figure 5.34 *Bright field TEM images of W34 PWHT sample with a) and b) low magnification and c) and d)higher magnification of the matrix showing the second phase particles. Note the lack of dislocations present in the PWHT sample.*

The particles tend to be bigger in size than in the as welded W34 sample. Also notable is the lack of dislocations in the matrix which is expected as the PWHT process allows for recrystallisation to take place which forms a new larger grain structure that is mostly defect free. It seems that the particles have had enough time to consolidate to form mainly single phase particle with some two or multiphase particles which are no longer odd in shape but uniformly shaped. Evidence of the bimodal particle distribution can be seen where there are present a number of much larger particles in the images. It seems very likely that the cluster of particles formed in the TMAZ have combined to form many large single phase particles.

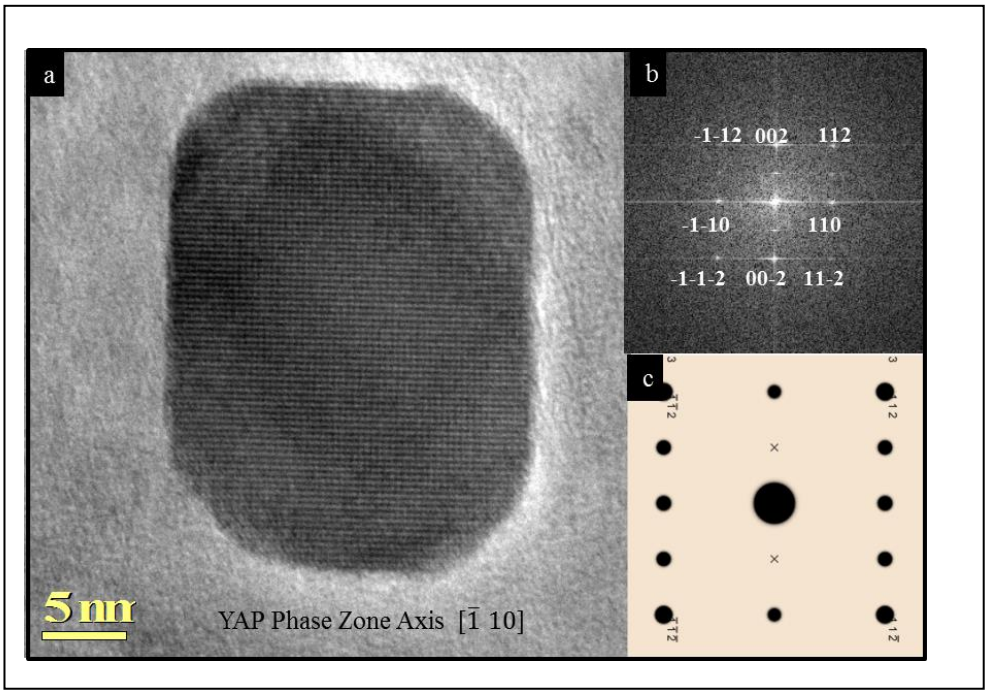

Figure 5.35 *A HRTEM image of a single phase particle resolved to a YAP phase with a zone axis [$\bar{1}$10]*

The clusters are likely to be of different compositions but as both yttrium and aluminium are present in the matrix it is not inconceivable that there might be a preference for a particular phase to form. From the number of particles studied it was not possible to draw any conclusions as to a preferred phase but some authors have indicated that YAP phase is the dominant phase after the application of PWHT [85].

The bright field TEM image in Figure 5.35 shows a YAP phase particle in the [$\bar{1}$10] zone axis with dimensions of 22nm by 30nm.

A number of particles could not be identified as the d spacing data and angles between spots in the FFT of the image did not match any of the known phases of yttrium aluminium oxides. Similar observations have been reported previously in SLM builds with PM2000 [108].

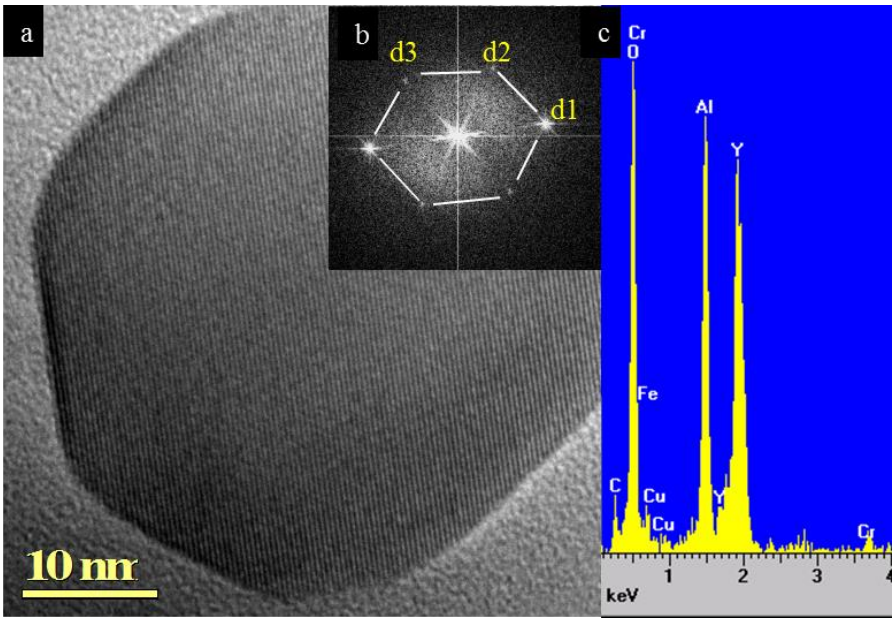

Figure 5.36 *Bright field TEM image of an unidentified particle with the FFT of the image. EDX analysis indicates the presence of Y Al and O with an Al: Y ratio of 61%.*

The bright field TEM image of an unidentified particle is shown in Figure 5.36 with the FFT of the image and the EDX spectrum EDX analysis indicates the presence of Y, A and O with a ratio of Al:Y of 61%. This would strongly indicate the YAG phase but the d-spacings measured from the FFT of the unidentified particle did not match with the d-spacings of the YAG phase from crystallographic data tables. Table 5.4 lists the nearest d-spacings, which clearly indicate that the particle is not a YAG phase and therefore remains unidentified.

Table 5.4 *d-spacing data for the unidentified particle and the nearest d-spacings for YAG phase particle.*

Al: Y At %	Unidentified Particle 61:39	YAG 62.5:37.5
d 1	3.80Å	3.21Å (1 2 3)
d2	4. 43Å	4.25Å (0 2 2)
d3	4.54Å	4.90Å (1 2 1)

5.9 Summary and Conclusions

The analysis carried out on W34 has is now summarised into the following categories

5.9.1 General Observations

The welding of as extruded PM2000 has been successful in that the process has resulted in a good join with the minor cavity section in the bottom of the TMAZ and some void areas. The question of voids will be covered in the next chapter. The one micron size grain structure slightly elongated along the extrusion direction, of the parent material has changed into a 3 micron equiaxed grain structure in the TMAZ with the characteristic smaller grains at the surface of the weld. The formation of these small grains can be attributed to the increased number of nucleation sites near the surface of the weld. The application of PWHT has resulted in a large grain structure in the parent material but in the TMAZ a large central region had failed to recrystallise with a large grain structure as expected. This was a setback as it was hoped that the whole cross section would undergo recrystallisation with a large grain structure. Some explanations as to why this has not been the case will be attempted in the particle size analysis summary.

5.9.2 Hardness Profile

The hardness number of the as-extruded PM2000 of 245 HV (average of the three directions) is much lower than the hardness value of as-rolled PM2000 of 380 HV. This can be attributed to the rolling process introducing further dislocations and therefore increasing the hardness value of the as-rolled PM2000 as compared to the as-extruded PM2000. On the application of HT the hardness value of the as-extruded PM2000 averaged over the three directions was 244HV. That was slightly above the hardness value for the as rolled PM2000 figure of 233HV. So in both cases once HT was applied then the hardness number reduced to the de-stressed state that is the hardness of the alloy after all the internal stresses have been reduced by the HT.

5.9.3 Particle Size Analysis and Grain Morphology

The recrystallisation behaviour of the W34 can be explained mostly by the particle size distribution.

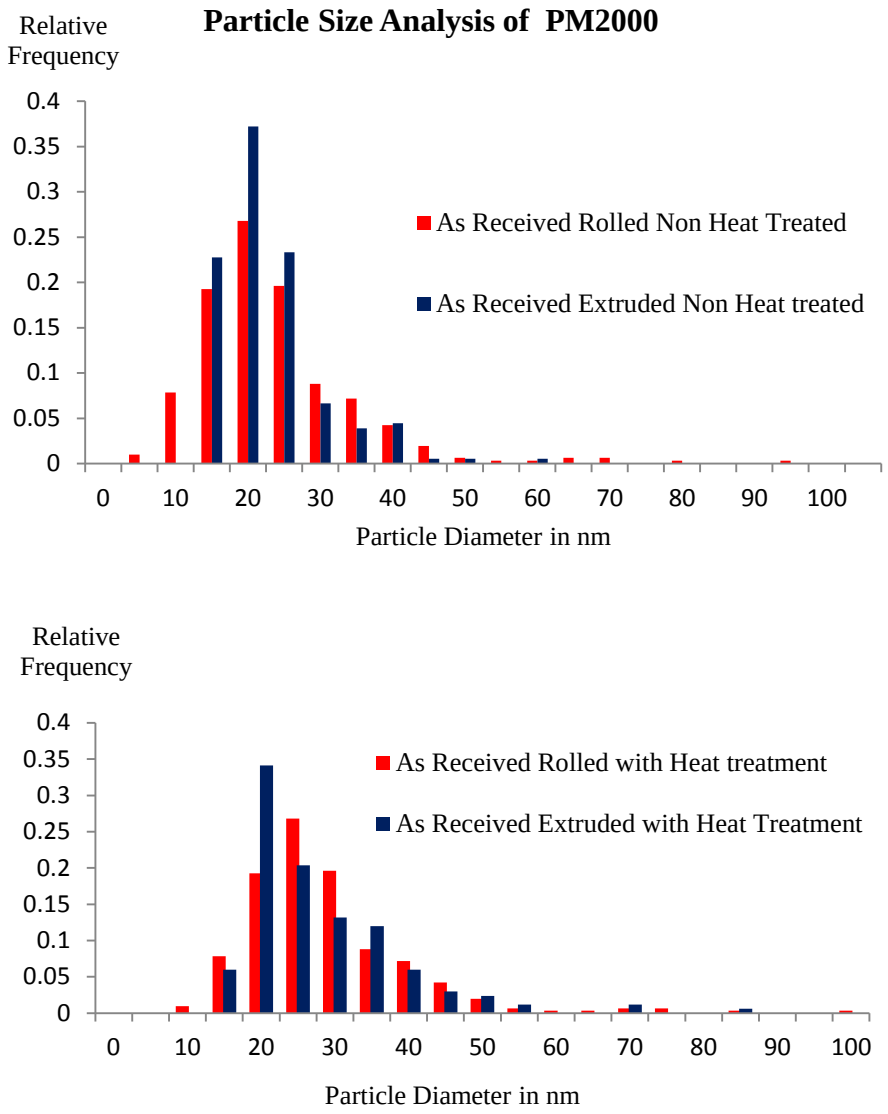

Figure 5.37 *Particle size analysis of as received rolled and as received extruded PM2000 with and without HT*

Parent Material

The parent region of W34 has undergone recrystallisation with a large grain structure which was the desired outcome. This is in line with expectations as the test piece of as extruded PM2000 in Chapter 4 had undergone recrystallisation with a large grain

structure. If we compare the particle size analysis of the non-heat treated, as-extruded and as-rolled PM2000 in Figure 5.37 then we can see that in the as-rolled and the as-extruded PM2000 have very similar distributions above 15nm but below this size there are no particles smaller than 15nm in the as-extruded PM2000 whereas in the as-rolled PM2000 there is a number of particles at 10nm and at 5nm present in the as-rolled PM2000 than the as-extruded PM2000. This difference in the size distribution could explain why the parent region in the BOP weld did not recrystallise with a large grain structure after the application of PWHT. The refinement of the microstructure due to the rolling process with the additional pinning force imparted by the smaller particles present along with an increase in nucleation sites in the as-rolled PM2000, has resulted in recrystallisation with a small grain structure. The question that arises is why is there an amount of smaller particles in the as-rolled PM2000 than in the as-extruded PM2000? One possible explanation is that the rolling process could bring about the precipitation of smaller particles from the matrix than a process of extrusion on its own. This would explain the fact that as-rolled PM2000 did not recrystallise with a large grain structure whereas as-extruded PM2000 recrystallised with a large grain structure after the application of HT. It is well known that the mechanical alloying process dissolves the Y_2O_3 powder into the matrix [52, 109] and that in the extrusion and rolling process result in the precipitation of Y Al O particles. The extrusion process may not have the same effect as the rolling process with regards to the size of the precipitated particles. The fact that the rolling process must deform the as-extruded material may in fact limit the size of the precipitated particles whereas the extrusion process may allow the precipitated particles to grow slightly bigger.

TMAZ region

The recrystallisation behaviour of the as-welded W34 in the TMAZ is in line with expectation in that the microstructure is one of dynamically recrystallised equiaxed grains of about 3 microns in diameter. With the application of PWHT the TMAZ has not fully recrystallised with a large grain structure as expected.

There is a large region across the middle of the TMAZ which has retained the the previously dynamically recrystallised grain structure present before the application of PWHT. The particle size analysis in the middle of the weld, for both the BOP weld

and the W34 weld are very similar and therefore cannot explain the difference in behaviour in the two welds. Residual stresses by way of lattice d-spacing variations have been measured by Mathon et al. [48] by neutron diffraction technique in both the transverse and longitudinal directions using the d-spacing of the (110) planes as a strain gauge.

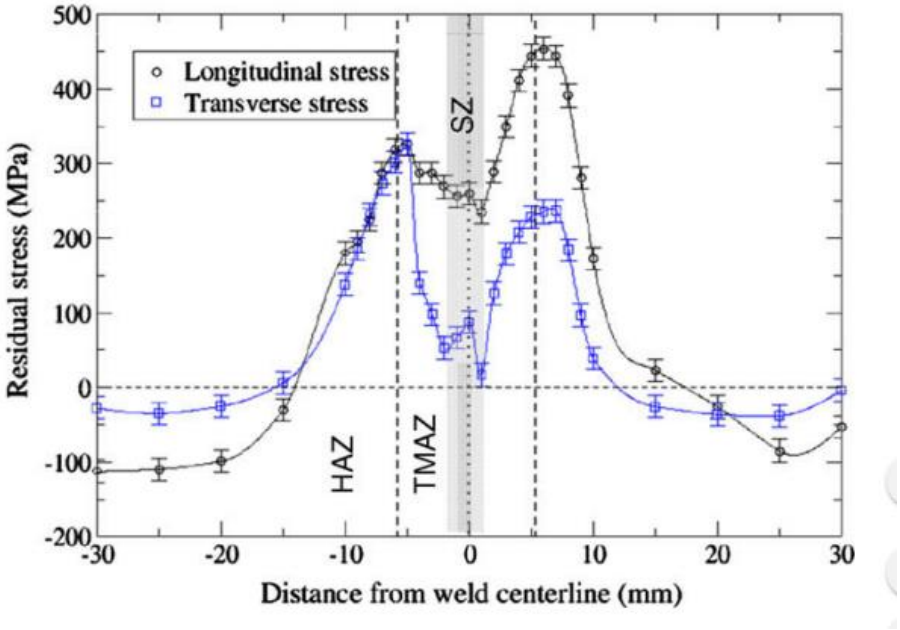

Figure 5.38 *Longitudinal and transverse residual stresses versus distance from the weld centre line (from Mathon et al Ref 26)*

In this particular study the results show a characteristic 'M' profile of the residual stress in both the directions but more so in the longitudinal (parallel to the weld line) than the transverse directions as shown in Figure 5.38. This residual stress profile has been observed by several authors in steels [83, 110] and in aluminium FSW [111]. A more recent study by Brewer et al. [110] has investigated a FSW of MA956, an alloy very similar to PM2000 bar a few minor alloying additions. They observed the correlation between the residual stress in the THAZ and the heat input which is the ratio between the rotational speed and the transverse speed of the weld parameters. The residual stresses increased with the decrease in the heat input of the FSW. Keeping the rotational speed constant, it translates to an increasing stress with

increasing transverse speed. This makes sense as the higher cooling rate of the tool moving away faster gives less time for stresses to relax before the TMAZ is set. In their investigation heat inputs of 4 and 20 were used on a single weld by altering the parameters as the weld progressed. The longitudinal stresses which were found to be tensile in nature peaked just outside the TMAZ and then were slightly reduced inside the TMAZ. The FSW with a heat input of 4 has resulted in a residual stress in the longitudinal direction close in the TMAZ up to 40% of the yield stress.

With W34 the heat input was set at 1.4 which would indicate that the stresses in the TMAZ could be higher than 40% of the yield strength. Another consideration is that the methods employed to measure the residual stresses do average the amount of stress across the thickness of the weld. As Mathon et al. mentioned in his paper there could be differences in the residual stresses with regards to the thickness of the weld. This inhomogeneous stress profile in the cross section of the weld could be responsible for the unrecrystallised region in the TMAZ in W34 with PWHT.

5.9.4 Coarsening of Second Phase Particles

One of the unexpected outcomes from the results is the extent of the agglomeration of the particles in the TMAZ. This has been reported previously [101, 112] but the agglomeration observed is extensive. The process of particle encounters due to rotation of the tool was proposed as a possible mechanism in the discussion section in Chapter 4 especially in the top part of the weld. The agglomeration was in many instances multi particle but a few two particle agglomerations have been observed. This is different from two phase particles that are present in PM2000 anyway. Wang et al. [112] has made similar observations in MA754 a nickel based ODS steel but on a lesser scale. Necking of particles was also observed. After the application of PWHT, the agglomerated particles consolidate to form mainly single phase particles which would explain the reason why a bimodal distribution of particles is observed in the top part of the TMAZ as that is the region with the highest number of agglomerations as confirmed by the particle size analysis. Kang et al. [113] proposed a mechanism for the agglomeration of certain large Al_2O_3 or Ti/CN particles which are surrounded by smaller Y_2O_3 particles that were attached by the plastic flow in the

TMAZ. A reduction in surface energy with the matrix would drive the agglomerated particle to form irregular shaped particles. The application of PWHT consolidates the agglomerated particle to form mainly single phase and/or two phase particles as observed in W34 PWHT sample.

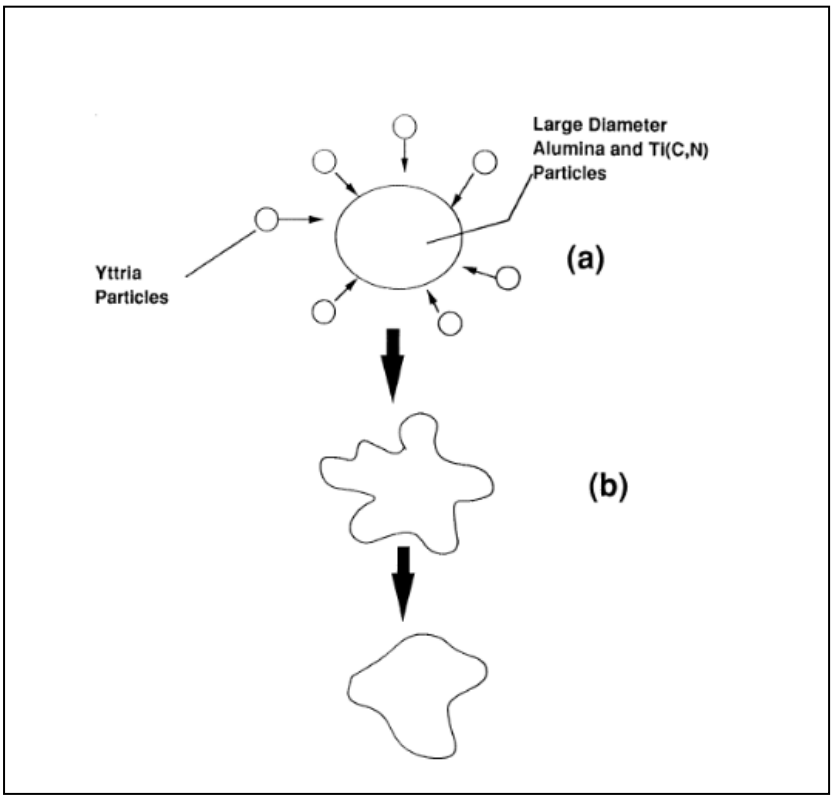

Figure 5.39 *Schematic of proposed mechanism of agglomeration of smaller Y_2O_3 particles with the larger Al_2O_3 or Ti(C, N) particles [113].*

As mentioned in the literature review the formation of yttrium aluminium oxides originate from the Y_2O_3 which is mechanically alloyed into solution in the matrix. The extrusion process facilitates the following reactions to take place.

$$3Y_2O_3 + 5Al_2O_3 \rightarrow 2Y_3Al_5O_{12} \quad \text{(YAG)} \qquad \textit{(Equation 5.5)}$$

$$Y_2O_3 + Al_2O_3 \rightarrow 2YAlO_3 \quad \text{(YAP)} \qquad \textit{(Equation 5.6)}$$

In effect the Y_2O_3 combines with Al_2O_3 both present in solution in the matrix to form the various phases of Y Al O. If we consider the thermodynamics of the formation of the different particles, the reaction enthalpy for Equation 5.1 is -2.4eV and for equation 5.2 is -0.05eV [114]. Clearly the formation of YAG is thermodynamically favoured over the formation of YAP. Another possible reaction route for the formation of YAG is:

$$Al_2O_3 + 3YAlO_3 \rightarrow Y_3Al_5O_{12} \quad (YAG) \qquad \textit{(Equation 5.7)}$$

The reaction enthalpy of the reaction in Equation 5.3 is -1.6eV. This is an additional route to form the YAG phase from YAP phase by combining with Al_2O_3. The FSW process could indeed promote the formation of YAG particles by the mechanical stirring of the parent material. Indeed this agrees with the findings of Chen et al. [115, 116].

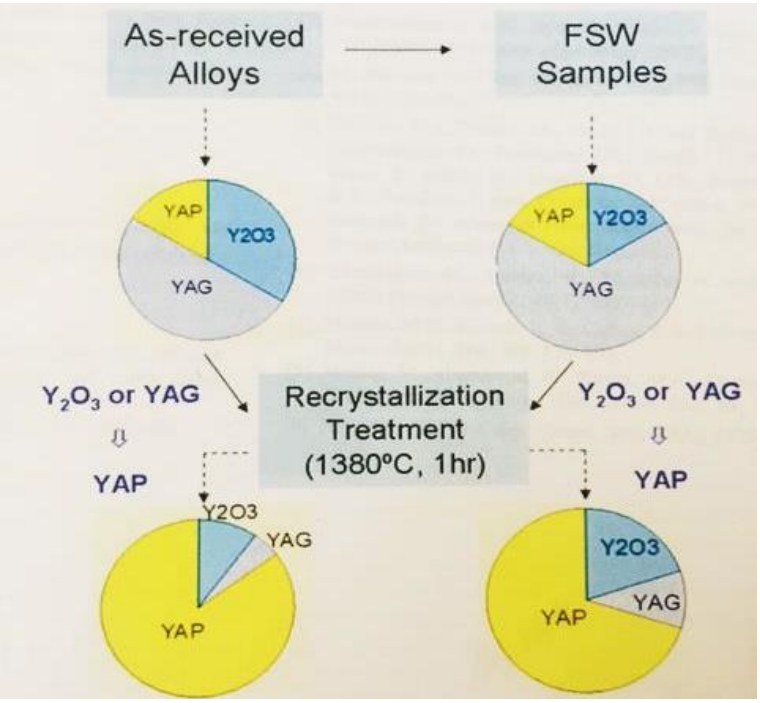

Figure 5.40 *Pie chart representation of the frequency of YAG, YAP and Y_2O_3 phases of as received PM2000, with heat treatment and FSW processes [115].*

The FSW process increases the proportion of YAG in the alloy but any subsequent heat treatment favours the formation of the YAP phase. This could be due to the

depletion of the aluminium reservoir due to the formation of the protective aluminium oxide scale that forms on the surface of the alloy after the application of either HT or PWHT. The coarsening of particles might also result in the local depletion of aluminium which would favour the formation of YAP particles. Another possible reason could be that the high temperatures during the heat treatments could favour the formation of YAP thermodynamically.

5.9.5 Particle Matrix Orientation Relationship

The addition of Y_2O_3 to matrix powder at the mechanical alloying step of the production step of ODS steels actually dissolve the Y_2O_3 into the matrix. The process of consolidation by extrusion results in the precipitation of various Y Al O phases through reaction with Al present in the matrix. These precipitates provide the additional creep strength at high temperatures as they pin dislocations and grain boundaries. The particle size analysis results found that particles, < 10 nm were present in the rolled PM2000 compared to the as extruded PM2000. The rolling process could be a possible reason for the precipitation of these smaller particles. In a recent study of FSW of PM2000 by Dawson et al. [101] suggested that an element of mechanical alloying was a possible mechanism where particles were dissolved into the matrix and precipitated after FSW and PWHT. This would explain why some of the particles studied were coherent or semi-coherent with the matrix.

CHAPTER 6

Friction Stir Weld of Kanthal™ APMT Alloy

6.1 Introduction

Kanthal™ APMT is a FeCrAlMo alloy which is manufactured via the gas atomisation process where powder is produced from the melt of the alloy mix and combined with rare earth additions such as hafnium and zirconium to provide some additional creep strength at high temperatures. The production process is much more cost effective than the mechanical alloying process route but the particle distribution in the matrix is inferior to mechanical alloying. The result is an alloy that is highly oxidation and corrosion resistant at high temperatures with limited high temperature creep strength.

In this chapter, due to the abundance of the material that was available, the focus will be on the FSW process itself, the mechanical properties of the welds and the microstructural variations with regards to the FSW parameters.

6.2 Friction Stir Welding Process

Three large 5mm plates of APMT were purchased from Kanthal which were cut to facilitate 2 BOP welds and 3 butt welds. The welds were performed at TWI.

Table 6.1 *List of the FSW parameters for Kanthal™APMT welds*

Weld No	RPM	Speed mm/m	Heat Index	Weld Type	Heat Input kJ/mm	Weld Depth Mmb
W26	200	100	2	BOP	1.08	3.75
W27	200	125	1.6	BOP	1.02	3.85
W29	200	125	1.6	Butt	1.37	3.85
W30	200	150	1.33	Butt	1.20	3.85
W31	200	140	1.43	Butt	1.24	3.85

The welds were named W26, W27, W29, W30 and W31. The parameters used are listed in Table1. The BOP welds were placed next to each other and it was mainly to ensure that the parameters were optimised for the subsequent FSW. In all the welds the rotational speed was kept at 200rpm.

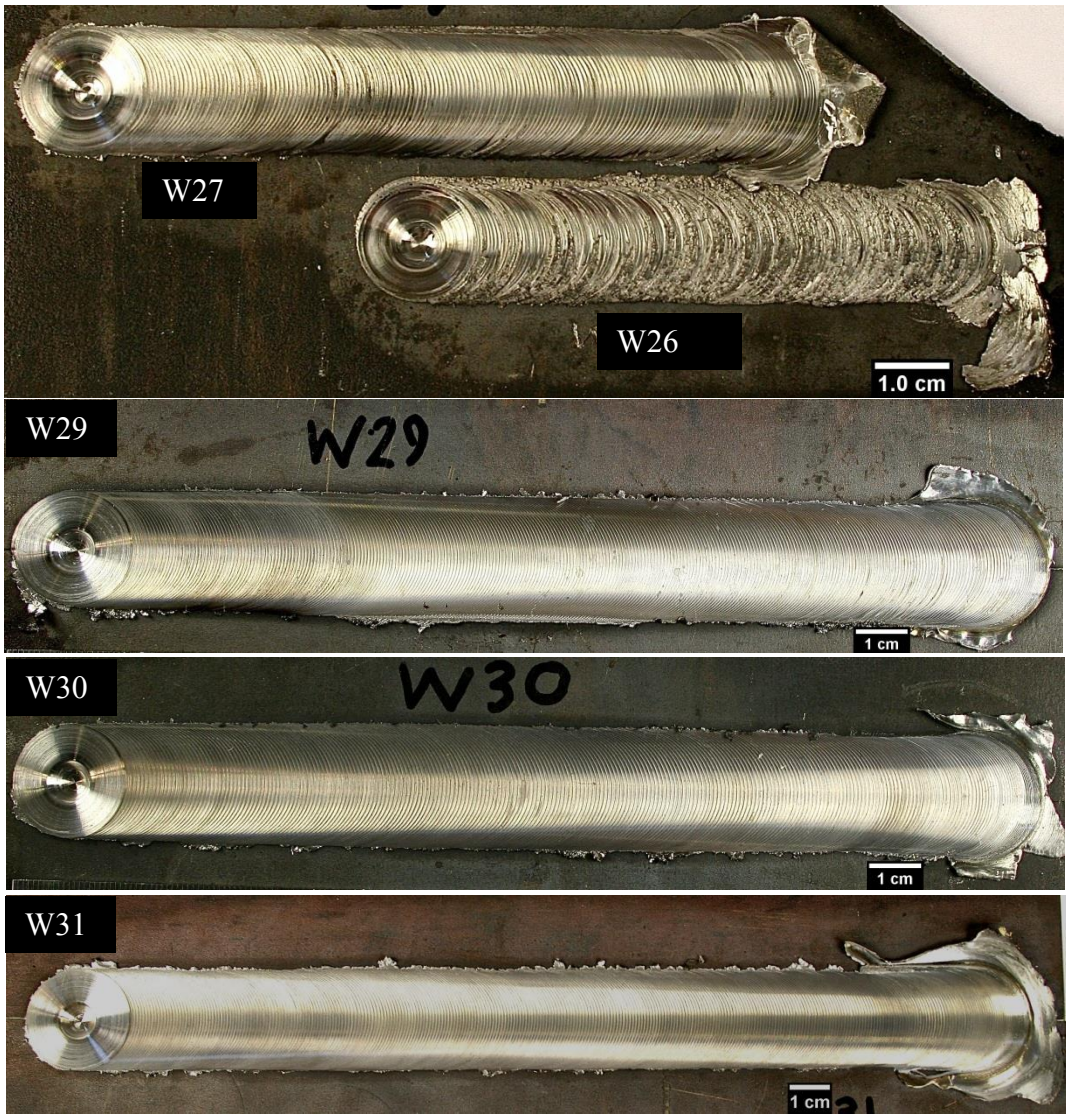

Figure 6.1 *Optical macrograph of the BOP welds W26 and W27 and the butt FSW W29, W 30 and W 31.*

Figure 6.1 shows the BOP welds W26 and W27 and the butt FSW W29, W30 and W31. From the images one can see that the surface quality of W27 has been improved compared to W26 by increasing the penetration of the tool and by reducing the heat input of the weld. This was achieved by increasing the transverse speed from

100mm/m to 125mm/m. The parameters for W29 were the same as W27 with the main difference being that W29 was a butt weld whereas W27 was a BOP weld. Further adjustments were made for the other two FSW. With W30 the transverse speed was increased to 150 mm/m further reducing the heat input and with W31 the transverse speed was adjusted to 140mm/m which slightly increased the heat input from W30 but less than W31. The result was that all three butt welds were visually of good surface quality as observed in Figure 6.1. Typical of all the BOP and butt welds is the flash of material seen at the tool pin entry point. All the welds featured the concentric rings typical of FSW.

6.3 Optical Microscopy

Optical microscopy was used to analyse the microstructure of the as received and the HT conditions of the APMT plate, the as welded and with PWHT conditions of the two BOP welds W26 and W27, and the as welded and PWHT conditions of the three butt FSW, W29, W30 and W31. All samples were polished to colloidal silica finish.

As Received APMT Plate With and Without PWHT

The microstructure of the as received APMT is one of a typical rolled plate with an elongated grain structure along the rolling direction.

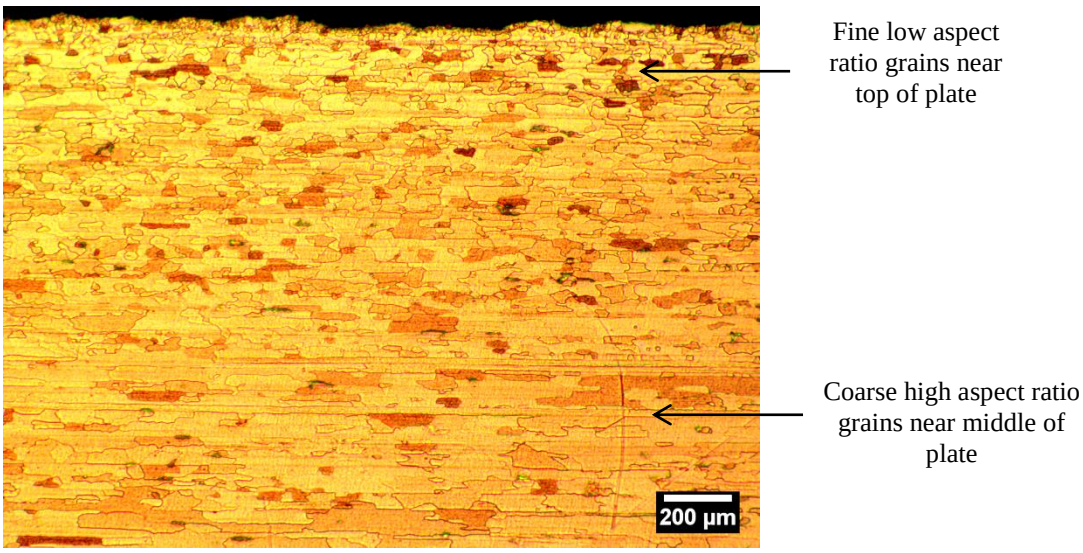

Figure 6.2 *Optical image of the longitudinal view of as received APMT plate showing a wide variation in the grain size with depth of the plate (etched with 10%HCl with methanol).*

The optical micrograph in Figure 6.2 shows the view from the longitudinal direction. There is a wide variation in the grain structure with the depth of the plate. At the top and bottom of the plates the microstructure differs from the middle of the plate.

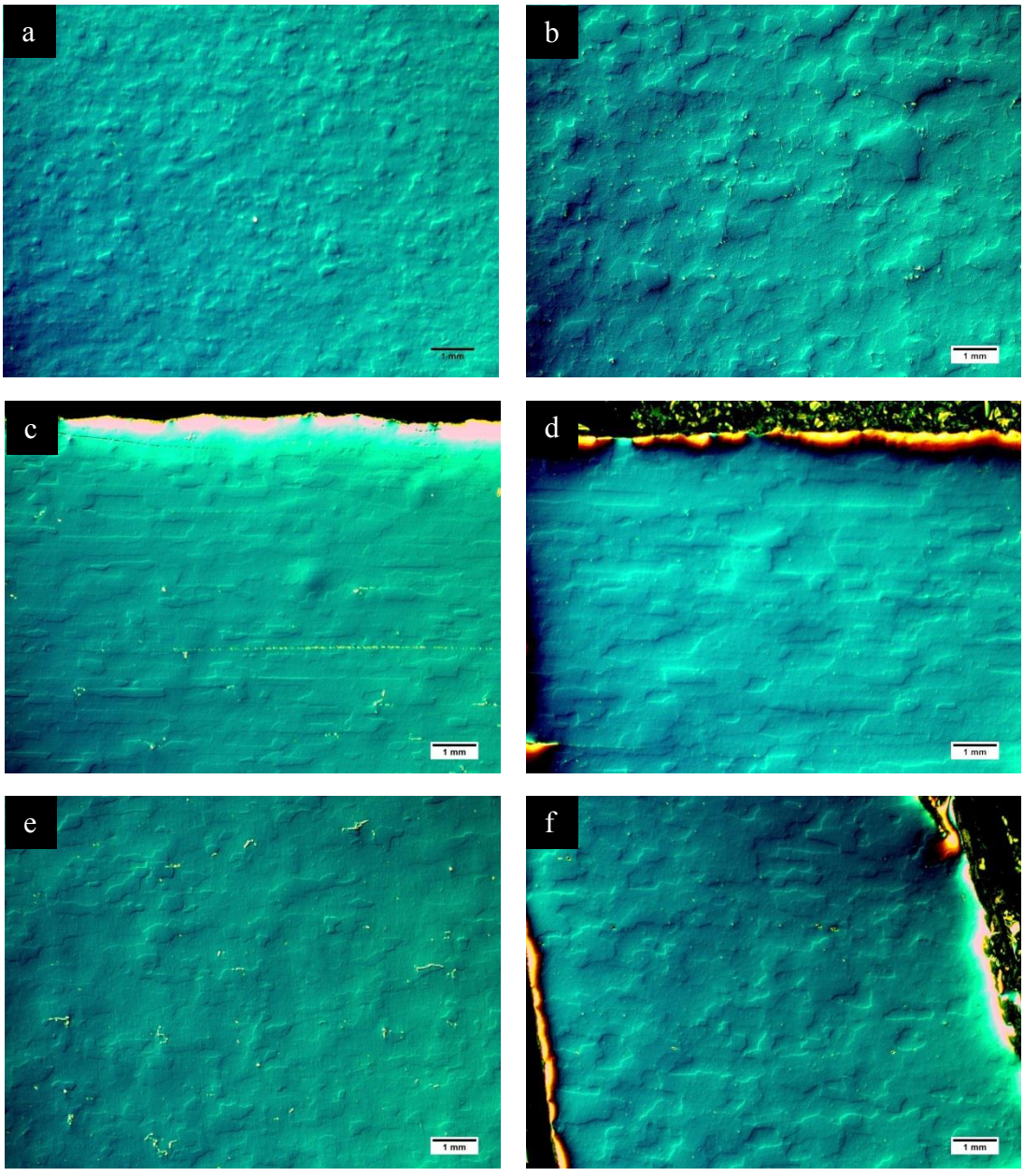

Figure 6.3 *DIC images of a) c) e) as received APMT plan, longitudinal and transverse views and b) d) and f) APMT with HT plan, longitudinal and transverse views.*

Fine grains of about 20 to 100 microns across with an aspect ratio of about 1 to 3 can be seen near the top of the plate with the size and aspect ratio of the grains gradually

increasing as you move near to the middle of the plate. Some of the grains near the middle of the plate can be longer than 2mm with an aspect ratio of 10 or more.

DIC images of APMT, as received and with HT are shown in Figure 6.3. Again the variation in the grain size with depth can be seen. Grain growth is observed after the application of HT with the elongated grain size of the middle of the plate (longitudinal view) increasing in size with a similar aspect ratio. Some grains that were measured were as long as 4mm and 0.5mm wide giving an aspect ratio of 8. Grain growth was uniform in the three directions.

As welded Condition

The orientation of the plates with regards to the welding line for all the welds apart from W31 were along the transverse view so that the cross sections of the welds would reveal the longitudinal elongated grain structure with the TMAZ grain structure. With W31, the welding line was along the longitudinal view so that the cross section of the weld would reveal the transverse view of the APMT plate along with the TMAZ.

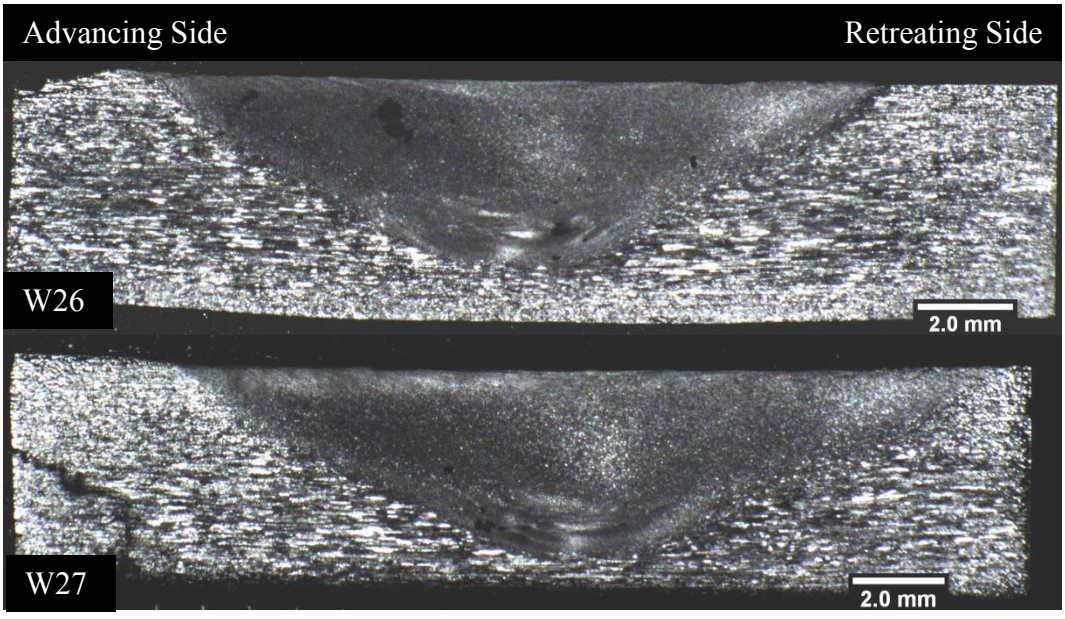

Figure 6.4 *Optical macrographs of the cross sections of BOP welds W26 and W27 (etched with 10%HCl in methanol).*

Figure 6.4 shows the optical macrographs of the cross sections of both W26 and W27. Note the difference in the depth of the two welds as specified in Table 1. Both

BOP welds show the longitudinal elongated grain structure of the parent material. The grain structure in both welds in the TMAZ has altered from the elongated structure into a fine grain structure.

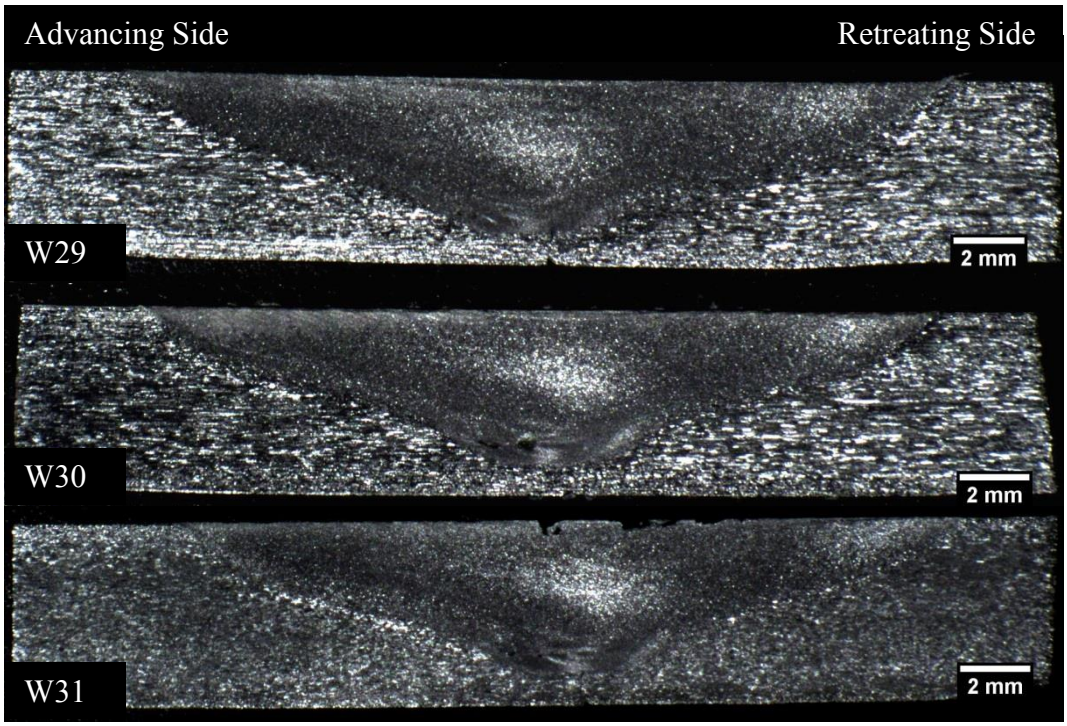

Figure 6.5 *Optical macrographs of the cross sections of W29, W30 and W31. Note the different parent grain structure of W31due to the different orientation of the weld line with the APMT plate (etched with 10%HCl in methanol)*

The optical macrographs of Figure 6.5 show the cross sections of W29, W30 and W31 FSW. All three welds show that a good join was achieved. The cross section of W31 shows the parent material transverse view as the weld line was performed along the longitudinal direction. In all the FSW there seems to be changes in the microstructure of the TMAZ from the parent material with clear defined boundaries between both regions in all the welds.

Post Weld Heat Treated Condition

The application of PWHT has altered the grain structure of the TMAZ of the BOP FSW W26 and W27 as presented in Figure 6.6.

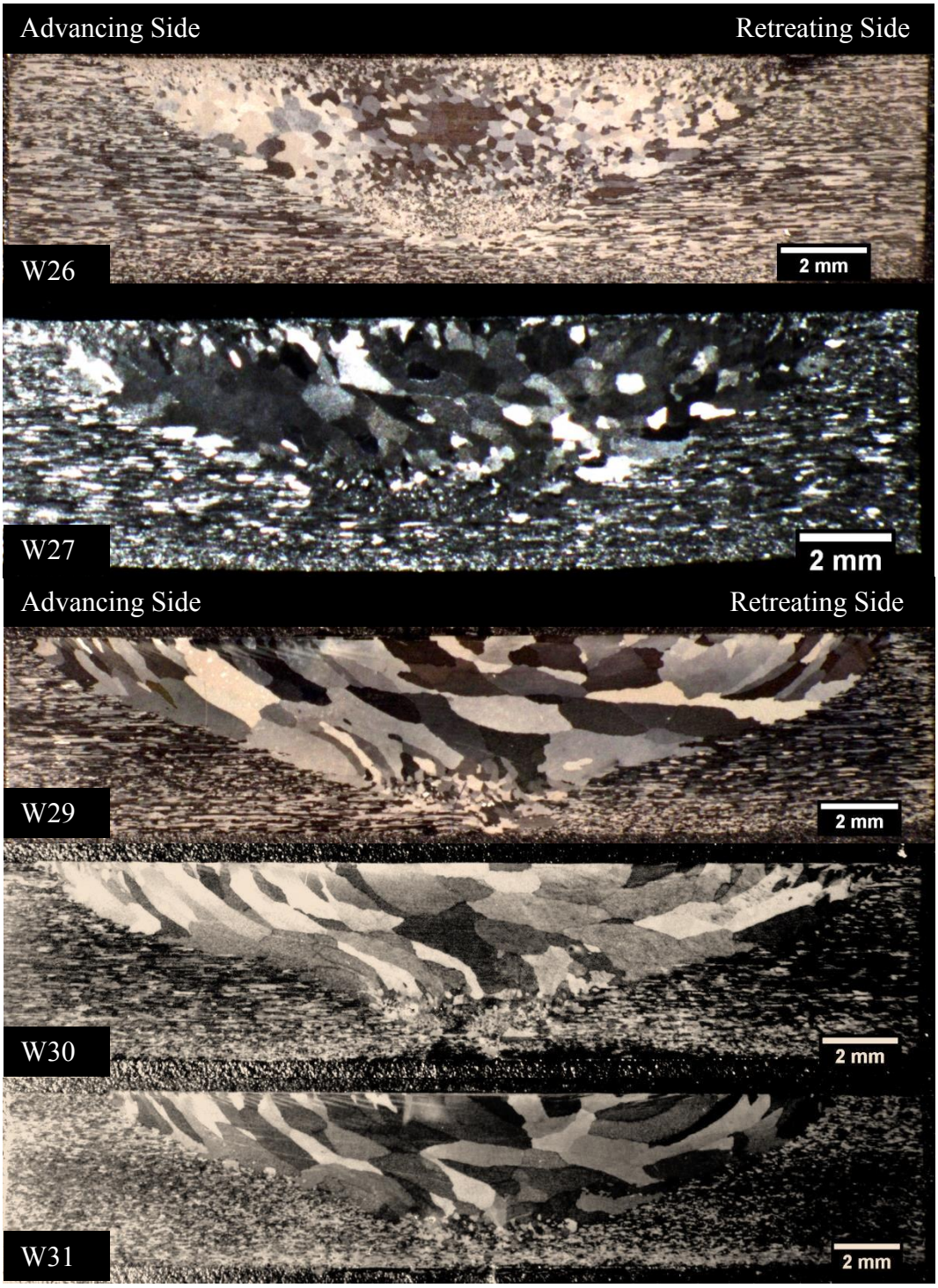

Figure 6.6 *Optical macrographs of the BOP W26 and W27 FSW with PWHT and of butt configuration FSW with PWHT of W29, W30 and W31. Notice the difference in the grain size achieved in the TMAZ between W26 and W27 as compared to the rest of the welds*

The larger grain structure of W29, W30 and W31 compared to W26 and W27 is attributed to the difference in the heat input which is a measure of the amount of deformation in the welds. This in effect determines the number of nucleation sites

which in turn determines the grain size. The increase in the heat input was achieved by increasing the down force applied to W29, W30 and W31 even though the transverse speed was increased in these welds. The downforce increased the amount of friction hence the heat input by more than the increase in the transverse speed reduced the time the tool spent at any specific point on the weld.

Closer observations of the flow pattern of material in the TMAZ using the elongation of grains as a guide, reveals three distinct regions. The schematic in Figure 6.7 illustrates the likely flow of material with arrows. The advancing side region has strong flow patterns downward, extending as far down towards the base of the weld. On the retreating side of the welds, the flow indication is again towards the base of the weld but then the flow is diverted towards the middle region of the weld. The direction of flow in the middle of the weld region could be formed from the contraflow of the two opposite sides of the weld but this is difficult to determine just from the grains formed.

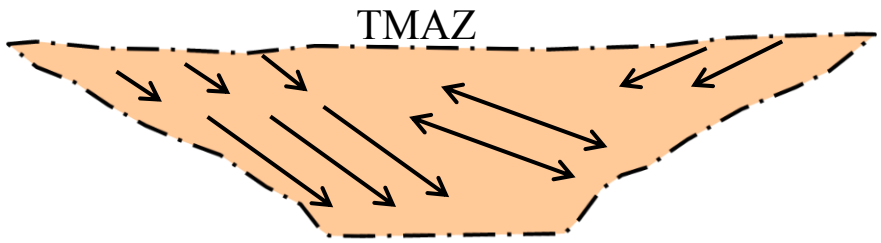

Figure 6.7 *A schematic of the TMAZ indicating the possible flow pattern determined from the elongation of the grain growth as a guide. .Author's own schematic.*

6.4 Hardness Profile

Hardness tests were performed on the as received APMT plate in the three directions with and without HT. The results, which are presented in Table 6.2, indicate that the APMT as received plate has an average hardness value, over the three directions, of 226HV without HT and an average hardness value of 225HV with HT. Although there are some variations in the HV valuer with the 3 directions overall the HV value is relatively uniform even after HT. This is an indication that the microstructural

changes due to the HT do not alter the hardness compared to the as received APMT. This is unlike PM2000 as-rolled or as-extruded PM2000 hardness results.

Table 6.2 *HV hardness test of the as received APMT plate with and without HT*

APMT/ Direction	No of Indents	Average HV	Standard Deviation HV
Plan	10	229	6
Transverse	9	238	9
Longitudinal	10	222	8
Plan HT	10	216	9
Transverse HT	6	231	10
Longitudinal HT	7	228	7

As-Welded Condition

Hardness tests were carried out on all the welds and since very similar results were obtained for all the welds in order to avoid repetition, only W29 data is presented in this section.

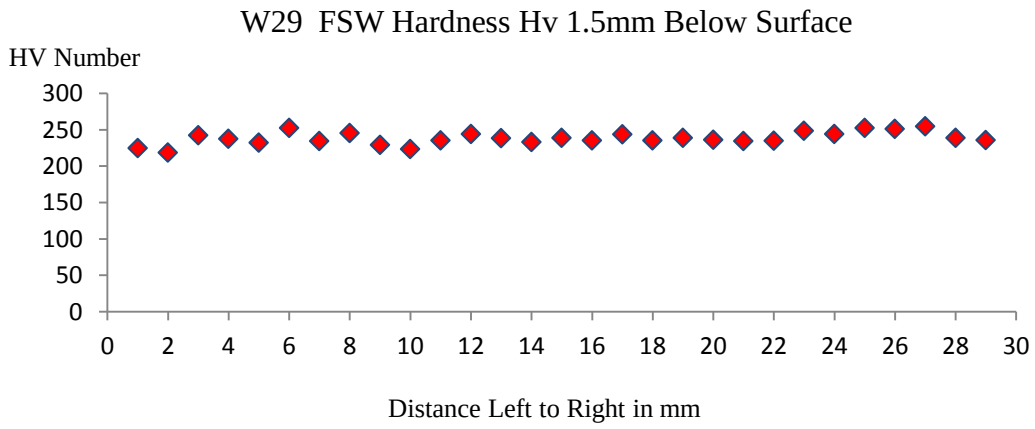

Figure 6.8 *Vickers hardness profile of W29 taken at 1.5mm below the surface of the weld.*

The hardness profile of W29 is presented in Figure 6.8. There is little variation in the hardness readings across the cross section of W29. Going from the parent material to the TMAZ there is no change in the hardness at all. What little variation there is in the readings can be attributed to errors when taking the measurements.

Post Weld Heat Treated Condition

The hardness profile of W29 with PWHT is presented in Figure 6.9. In all 24 measurements were taken 1mm apart and at 1.5 mm below the surface, across the cross section of the weld. From the results one can see that the hardness number is again fairly uniform with no difference detected from the parent material to the TMAZ.

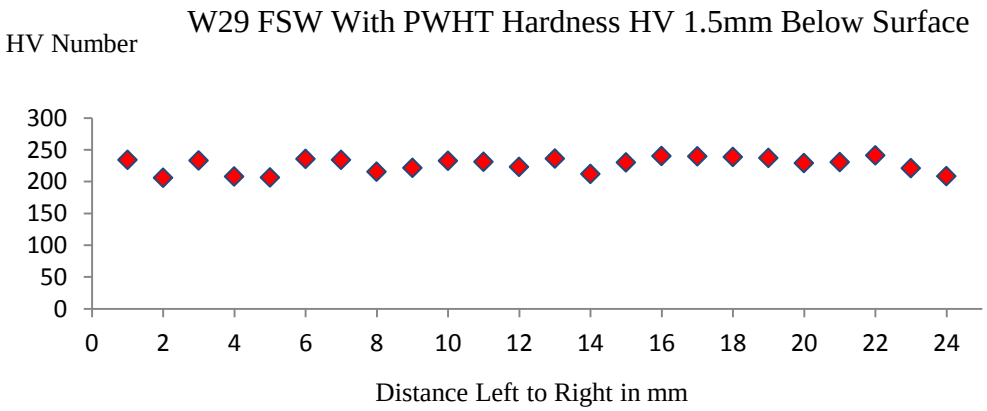

Figure 6.9 *Vickers hardness profile of W29 with PWHT taken at 1.5mm below the surface.*

6.5 Scanning Electron Microscopy

Channelling contrast imaging was used to show the grain morphology of as received APMT with and without HT and the W30 APMT welds with and without PWHT. All samples were polished to colloidal silica finish. Enhanced grain boundary images were achieved by etching samples with 10%HCl in methanol and re-polishing to colloidal silica finish taking care not to polish away completely the previously etched grain boundaries.

As received APMT

As seen in the optical images, the as received APMT has an elongated grain structure along the rolling direction. This is confirmed by the channelling contrast images in Figure 6.10 Near the top and bottom of the plates, as seen in the longitudinal top view in Figure 6.10a, the grains are much smaller and equiaxial in shape. Deeper into the plate, the grains become larger and more elongated in structure.

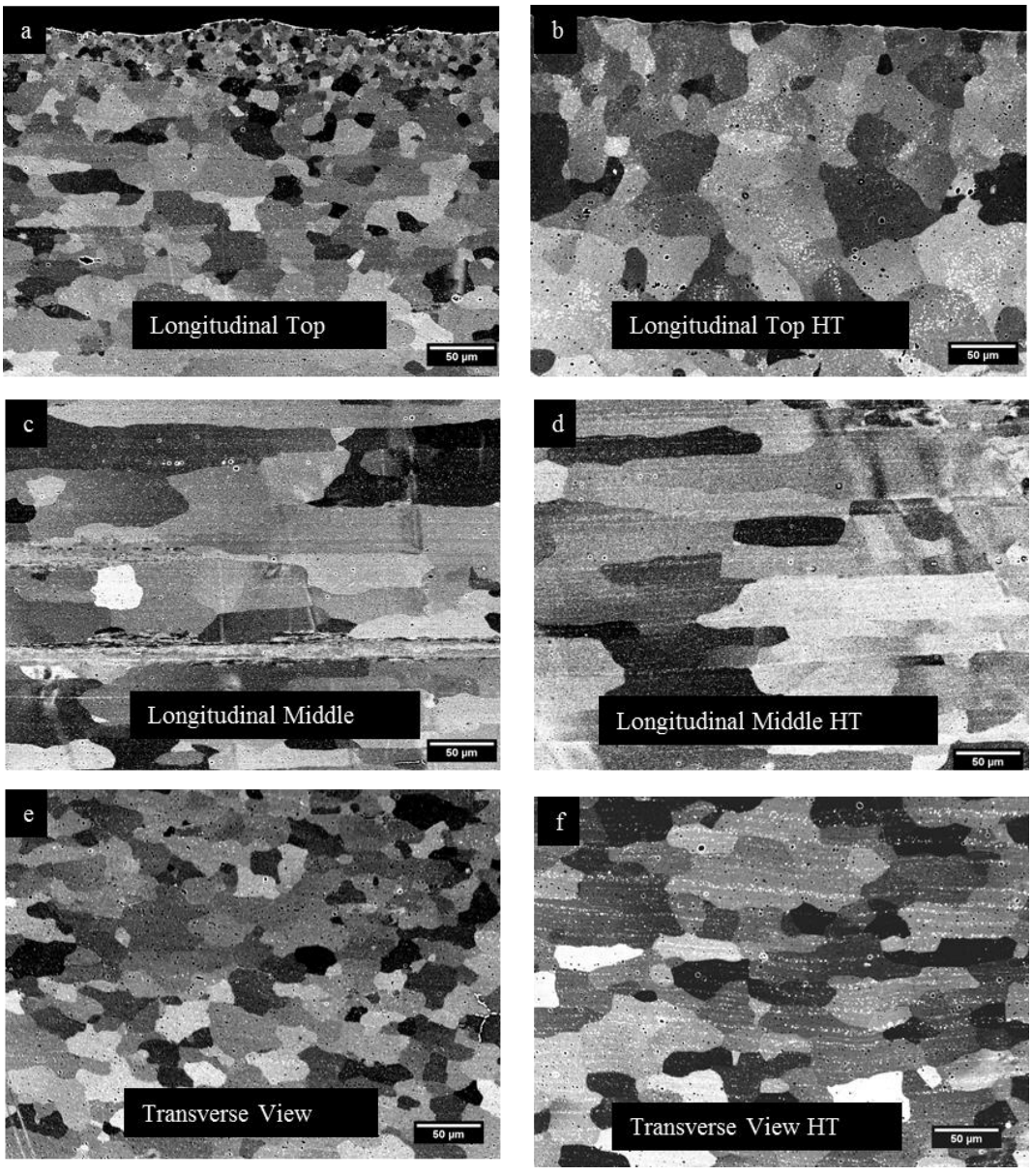

Figure 6.10 *Channelling contrast images of a) the longitudinal top, b) with HT, c) longitudinal middle view, d) with HT, and e) the transverse view and f) with HT, of the as received APMT plate.*

Grains are in the order of 20 to 50 microns wide as seen in the transverse view in Figure 6.10e, with lengths of over 500 microns in the middle of the plate (Figure 6.10c) which gives an aspect ratio greater than 10 in some grains. This is a highly elongated grain structure. The application of HT does not alter the shape of the grains but there is a noticeable grain size increase observed, due to recrystallisation, especially in the transverse view (Figure 6.10f) and the plan view which is observed in the top longitudinal view (Figure 6.10b). The longitudinal middle view with HT in Figure 6.10d does not look much different to the non HT image in Figure 6.10c. There is such a wide variation in the length of the grains that without carrying out measurements over a number of images it would be difficult to say if there was any grain growth due to recrystallisation in this direction.

W30 As-Welded Condition

The advancing side and retreating side of the as welded W30 sample is shown in Figure 6.11

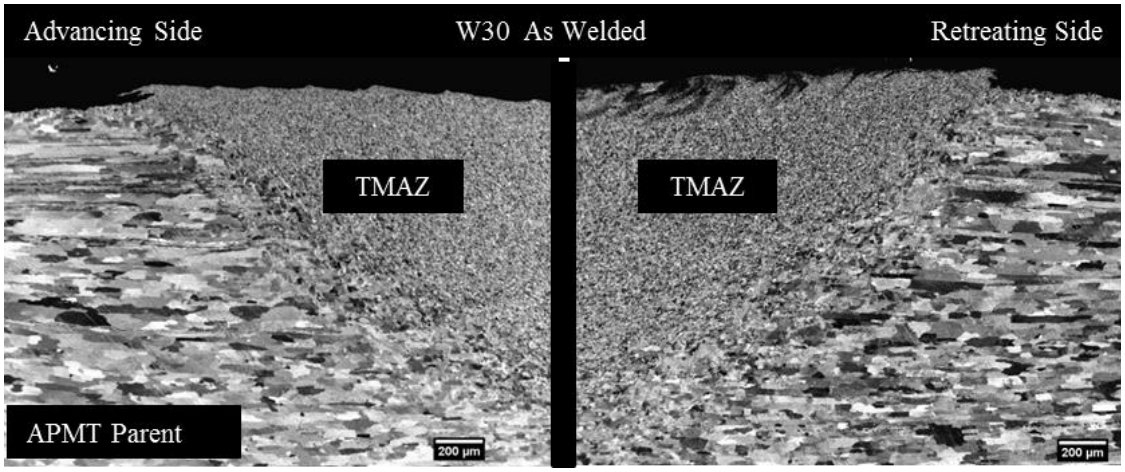

Figure 6.11 *Channelling contrast images showing the grain structure of the advancing side and the retreating side of W30 as welded.*

The elongated grain structure of the parent APMT has altered to a much smaller equiaxed grain structure in the TMAZ due to dynamic recrystallisation during the FSW process. The boundaries between parent APMT and the TMAZ are well defined on both the advancing side and retreating sides. This is due to a large grain difference between the parent region and the TMAZ.

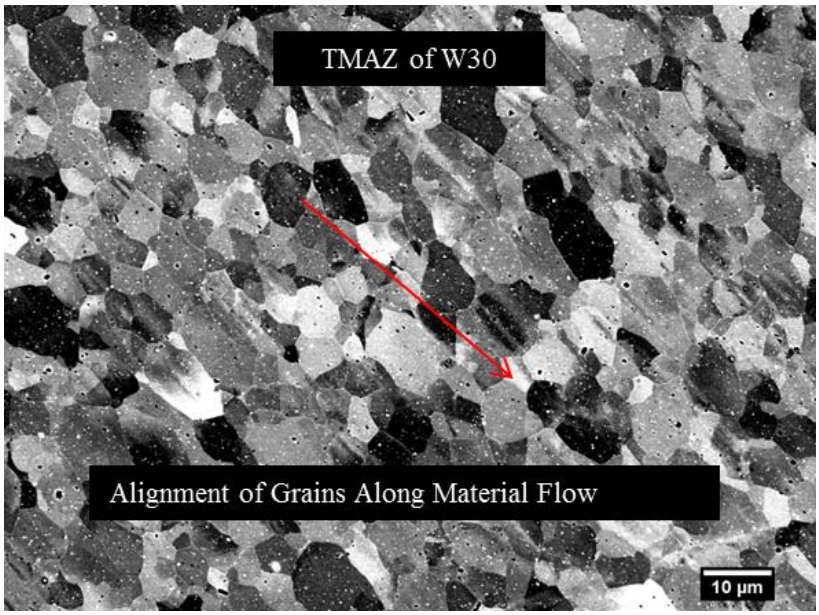

Figure 6.12 *Channelling contrast image of the TMAZ of W30showing the alignment of grains with the material flow.*

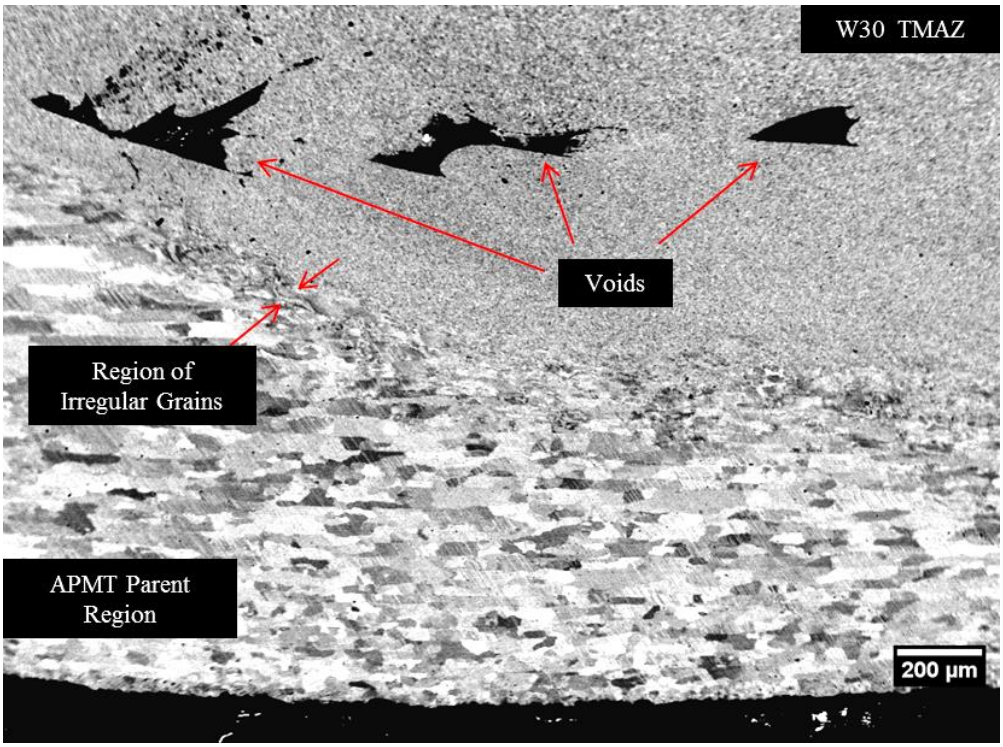

Figure 6.13 *Channelling contrast image of the advancing side boundary between the Parent region and the TMAZ in W30 as welded showing voids present in the TMAZ.*

In the TMAZ next to the advancing side, the grain size varies from about 5 to 10 microns and the structure is equiaxed with an alignment with the material flow as illustrated in the channelling contrast image in Figure 6.12. Similar flow patterns were reported by Wentuo et al. [117].

Near the bottom of the weld, at the advancing side several voids were observed. These voids are not on the boundary between the parent APMT and the TMAZ but within the TMAZ. This suggests that the voids are not caused by lack of cohesion between the parent APMT and the TMAZ as all the voids observed were always at the advancing side of the TMAZ and at the same region. All the way round the boundary there seems to be very good cohesion indeed between the two regions. Further investigation of the voids is covered in Section 6.4 of this chapter. The elongated grains of the parent APMT, near the TMAZ are irregular as some grains seem to have been partly stirred and dynamically recrystallised.

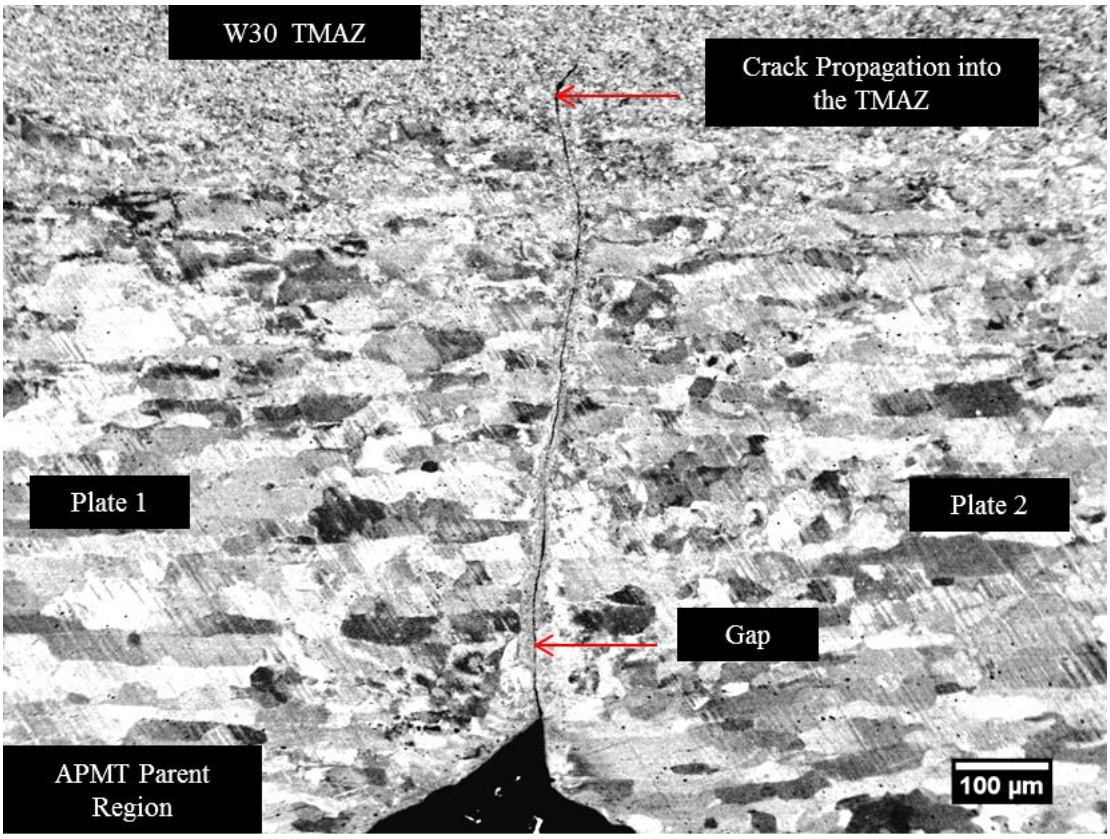

Figure 6.14 *Channelling contrast image of the base of W30 as welded. A crack originating from the gap between the plates can be seen in the TMAZ.*

Another interesting area to note is the bottom of the TMAZ as seen in the channelling contrast image in Figure 6.14. As mentioned the APMT plates were 5mm thick, where the tool was designed to weld 4mm plates. The plates were not welded at the bottom leaving a gap between the two plates. As can be observed in Figure 6.14 this gap in the plates can result in a crack which in this case has propagated into the TMAZ. This could possibly be due to vibrations experienced during the FSW process as the weld was progressing. In any case it confirms the importance of using the right tool for the required thickness of weld.

W30 with Post Weld Heat Treated Condition

After PWHT the parent APMT remains with the same elongated grain structure but some growth after recrystallisation is observed. The TMAZ has recrystallised to a very large grain structure as observed in Figure 6.15.

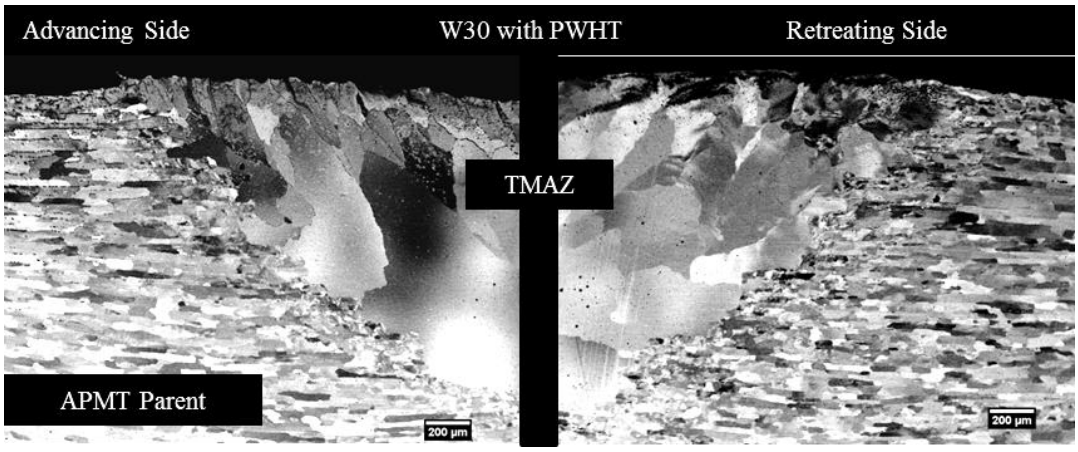

Figure 6.15 *Channelling contrast image of W30 with PWHT. A large grain structure is observed in the TMAZ. Grain boundaries were enhanced by polish, etch and re-polish technique.*

The grains are aligned inclined to the vertical, elongated along the material flow especially at the advancing side of the weld. There is a region next to the TMAZ where the grains are somewhat interleaved between the parent grain structure and the large grained recrystallised structure of the TMAZ. The grain structure of the TMAZ is one of larger grains with increasing depth.

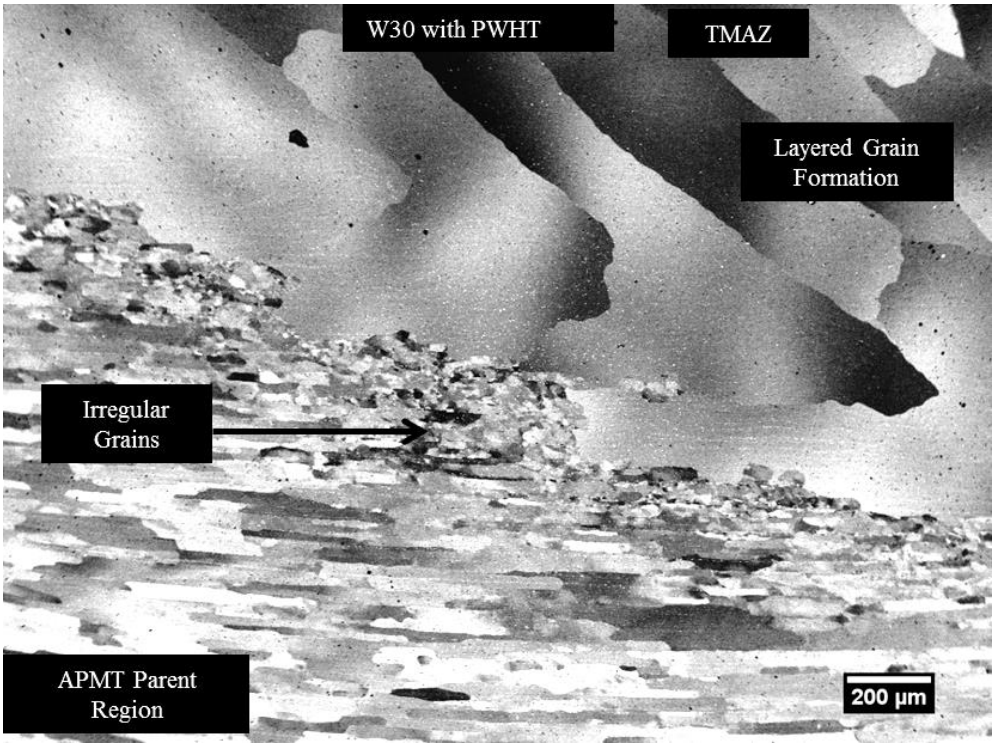

Figure 6.16 *Channelling contrast image of the boundary of the Parent APMT with the TMAZ near base of advancing side of W30 with PWHT showing a large layered formation of secondary recrystallised grains in the TMAZ.*

Nucleation sites are lower in number as you go deeper into the weld. The nucleation sites increase in number near the surface of the weld. The final grain structure is governed by the distribution of the nucleation sites and competitive growth.

As observed in Figure 6.16, a layered grain structure can be seen where the secondary recrystallised grain structure seem to form in overlapping layers. There is again visible a region next to the TMAZ where the grain structure is not elongated as the parent region is but smaller more equiaxed grains can be seen at this boundary.

In the area surrounding the voids near the base of the TMAZ, as shown in Figure 6.17 one can observe a variation in grain size. Smaller grain structure next to the void area is then surrounded by a larger grain structure moving towards the parent region of the cross section. A difference in the formation of nucleation sites for recrystallisation has resulted in a difference in grain size. Further away the cooling rate is slower allowing grains to grow slightly larger as seen in Figure 6.16.

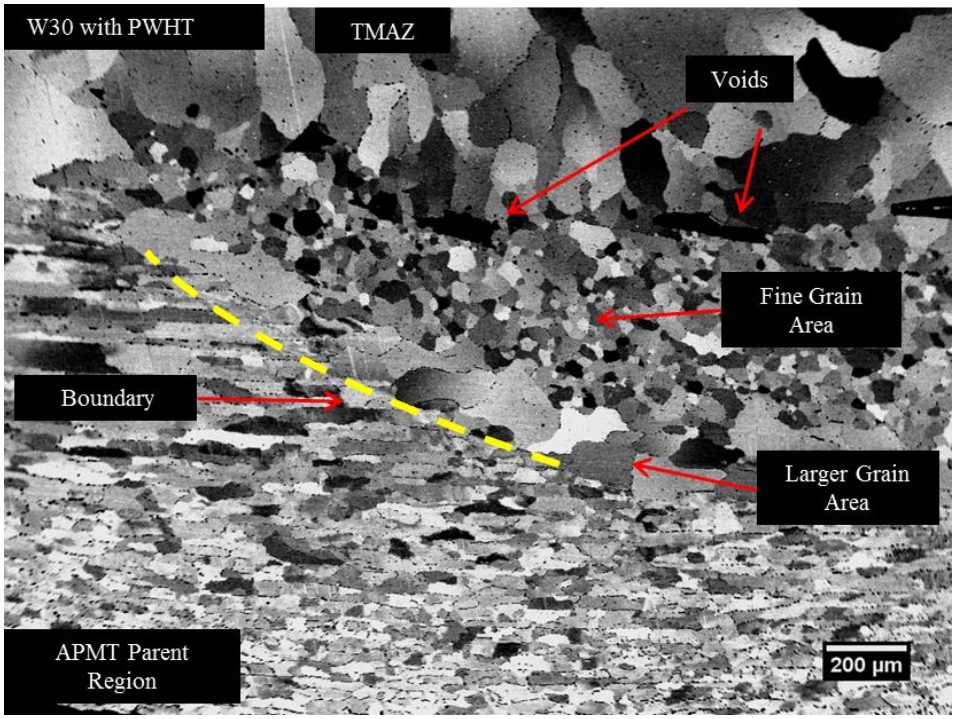

Figure 6.17 *Channelling contrast image of W30 with PWHT at the void region in the TMAZ of the weld. (Grain boundaries enhanced by polish etch and re-polish process)*

Another region of interest is the gap between the two plates at the base of the weld as observed in Figure 6.18. In the as welded sample of W30 a crack has propagated from the gap into the TMAZ possibly due to stresses subjected to during the FSW process. The grain formation in the parent region either side of the gap seems to have recrystallised with a larger grain size compared to regions further away from the gap. One possible explanation is that the gap has allowed vibrations to cold deform the two surfaces either side of the gap which has then provided the driving force required to nucleate recrystallisation. The large grain size is due to the lower number of nucleation sites. Some grains within the TMAZ, near the base of the weld, which were deformed by the FSW process, have recrystallised but with a smaller grain size. This could be due to the lower temperatures experienced during the FSW process, being further away from the tool.

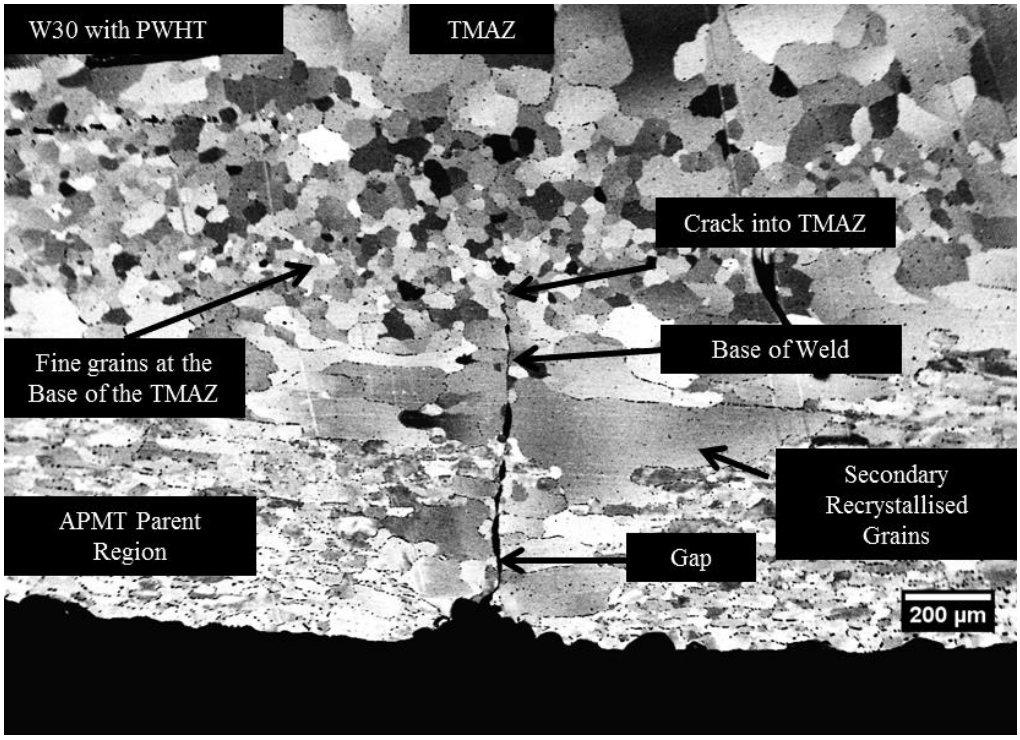

Figure 6.18 *A channelling contrast image of the base of W30 with PWHT showing the grain structure near the gap between the two APMT plates.*

6.6 Particle Size Analysis

Particle size analysis was undertaken for all the welds. The results were consistent across all the welds so only the results from W29 will be presented to avoid repetition. Samples were polished to 0.25 microns and then etched in 10%HCl in methanol in an ultrasonic bath for 7 minutes. SEM images in SED mode were taken at 10,000 magnification setting and 'Pebbles' software package was used to analyse the particle distribution.

As-Received APMT

The particle size analysis of the as received APMT plate with and without HT is presented in Figure 6.19. Immediately one can observe that the particles present in APMT are much larger than in PM2000. The average particle size of the as received APMT plate is 107nm with a standard deviation of 66nm. This is larger than the reported size in literature of 75nm [118]. A wide spread of particle sizes was measured. They ranged from 29nm to 259nm and the total number of particles

counted was 259. After the application of HT, coarsening of the distribution was observed. The average particle size was 141nm with a standard deviation of 123nm. The particle size ranged from 36nm to 766 nm. The total number of particles counted was 161.

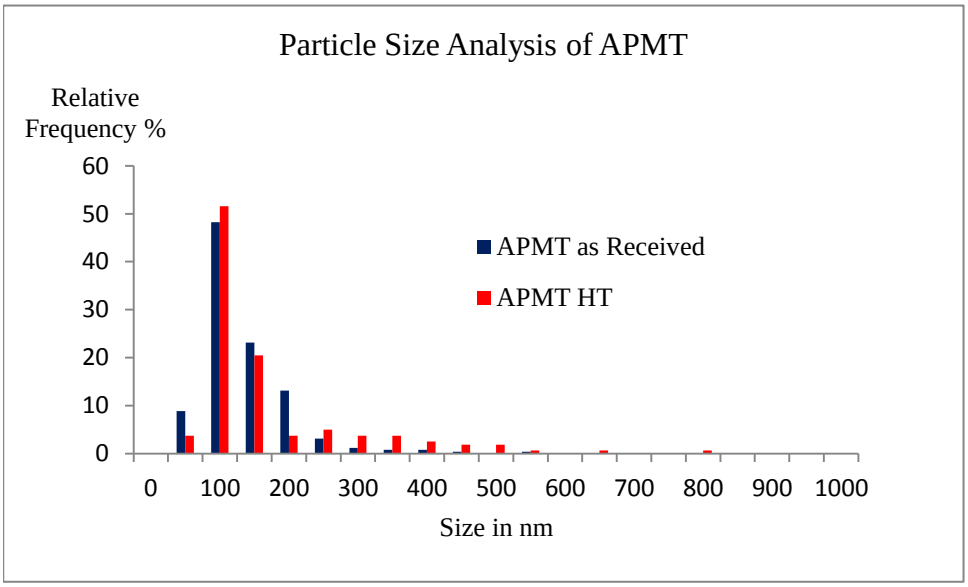

Figure 6.19 *Particle size analysis of the as received APMT plate with and without HT.*

W29 As-Welded

The results of the particle size analysis of the W29 weld are presented in Figure 6.20. The average size of the particles measured in the TMAZ of W29 was 83nm with a standard deviation of 50nm. The particle size ranged from 35 nm to 417nm. The actual number of particles measured was 362. The application of PWHT has coarsened the particle distribution as expected. The average particle size has increased to 130nm with a standard deviation of 117nm with the particle size range from 38 nm to 605nm. The sample size was 187 particles.

It seems that the FSW process has refined the particle size distribution slightly compared to the as received APMT plate. This in effect can mean that either the FSW process somehow breaks up the larger particles increasing the numbers of the smaller particles in the TMAZ or that the FSW process causes the precipitation of

smaller particles increasing their numbers in the distribution. From the range of the particle size data, it is unlikely that precipitated particles would be as big as 35nm in size as this is the size of the smallest particles measured in the TMAZ. The FSW process increases the temperature of the sample for only a short amount of time. It is more of a possibility that an element of dissolution has taken place or that there is a naturally large variation in the particle distribution in APMT plate and the decrease of about 25% in size between APMT plate and the TMAZ of W29 is not a result of the FSW process.

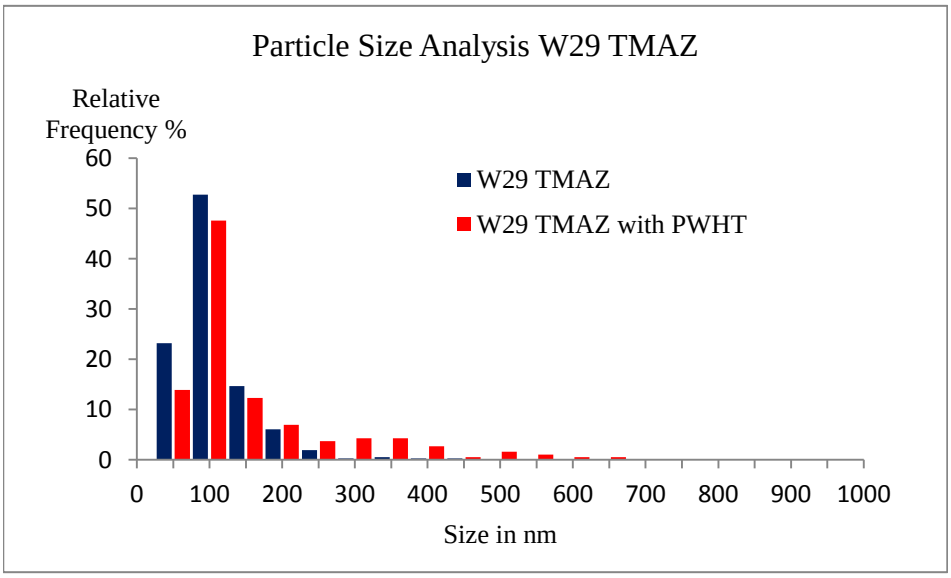

Figure 6.20 *Particle size analysis of W29 with and without PWHT.*

Once again the effect of PWHT on the particle distribution is to coarsen the particles from their pre PWHT size to approximately 1.5 X original size and the spread of the size distributions in both the as welded and as received APMT has increased in both cases.

6.7 Mechanical Testing

Mechanical testing of W31 was performed at the ORNL in the USA. Tensile testing samples were prepared from the parent region and the TMAZ region as illustrated in

the schematic in Figure 6.21. The APMT plates were aligned so that rolling direction was along the weld direction. Two tensile tests pieces were prepared from each, the as received plates and from W31.

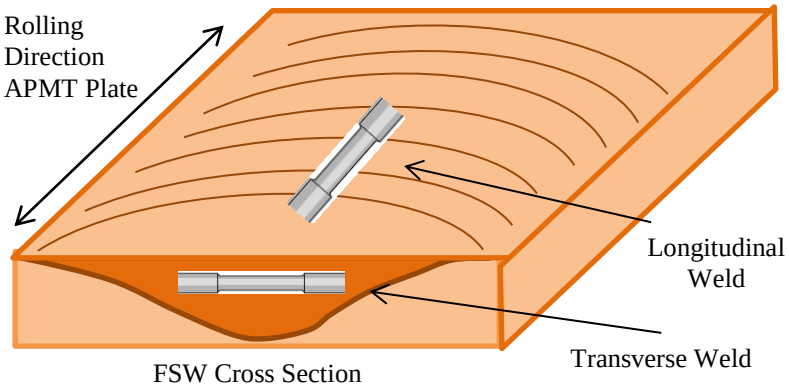

Figure 6.21 *A schematic showing the alignment of the tensile test pieces that were prepared from the APMT as received plate and W31 FSW.*

The results of the tensile tests are presented in Figure 6.22. The first point to note is that there is a marked difference in the tensile test results for the longitudinal and the transverse directions in the APMT plate.

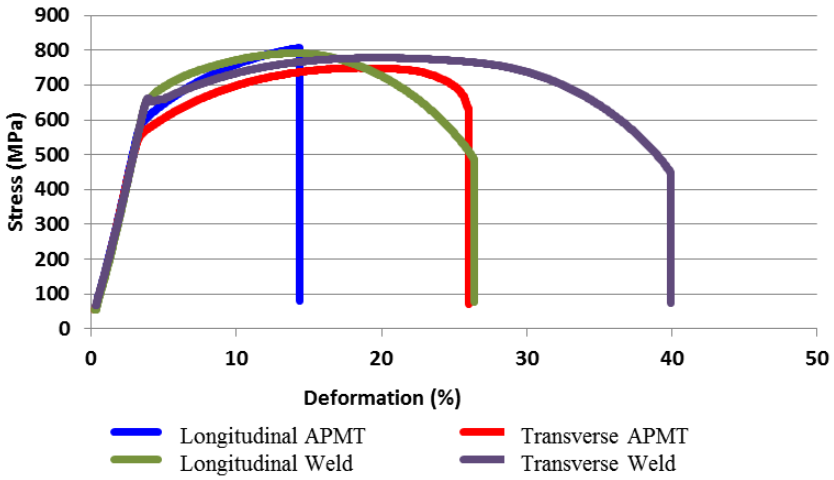

Figure 6.22 *Stress strain graph for as received APMT along longitudinal and transverse direction and W31 along direction of weld and transverse directions.*

This can be attributed to the elongated grain structure along the rolling direction. As previously mentioned the aspect ratio of the longitudinal grains can be as much as 10

and even higher in some cases. The number of grain boundaries opposing the longitudinal direction of stress is drastically reduced compared to the transverse direction. The deformation of the transverse direction of 26% is nearly double the deformation in the longitudinal direction of 14%. The tensile strength of the longitudinal direction is 805MPa and in the transverse direction it is slightly lower at 750MPa. After the FSW process, the ductility of both directions in the TMAZ of W31 has increased considerably. In the longitudinal direction which is the direction of the weld line the deformation was 26% and in the transverse direction nearly 40%. From the large elongated grain structure of the as received APMT the FSW process has altered the grain structure into a more equiaxed 10 micron size grain structure. The tensile strength of the longitudinal weld direction has reduced slightly to 790MPa but the transverse weld direction the tensile strength has increased to 777MPa. The effects of the texture of the plates in the different directions may contribute to the differences in hardness observed.

6.8 Charpy Impact Test Fractography

Charpy v-notch impact tests were carried out on the as received APMT plate and on the FSW W31 with and without PWHT samples.

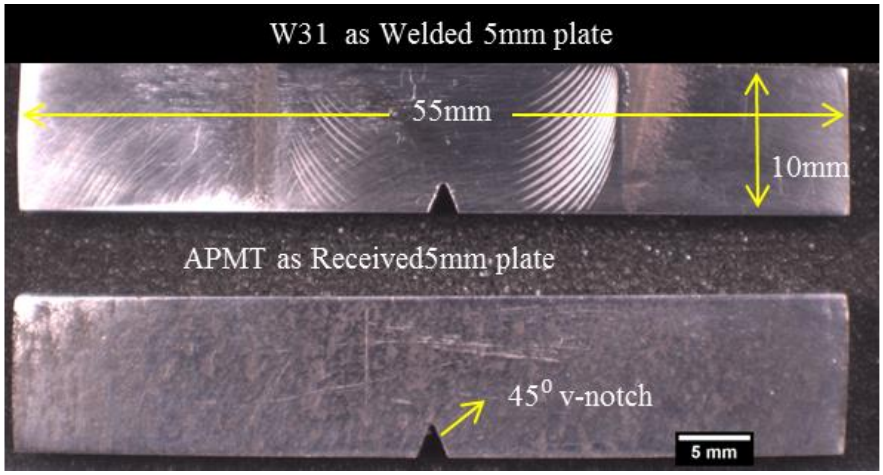

Figure 6.23 *W31 as welded and APMT as received samples prepared for Charpy v-notch tests using the non-standard specifications stated in ASTM E23 12c Standard Test Methods for Notched Bar Impact Testing of Metallic Materials.*

The three v-notch samples were prepared for the tests using ASTM E 23 12c standards. The standard dimensions for Charpy tests are 55mm X 10mm X 10mm but since the APMT and therefore W31 plate thickness is 5mm the alternative sub size dimensions were used instead which were 55mm X 10mm X 5mm as specified in the non-standard specimen recommendations.

As shown in the optical image in Figure 6.23 the v-notch was cut so that the break in the sample would be along the longitudinal direction which is also the weld direction in W31. The samples were examined using SEM analysis.

As-Received APMT

The fracture surface of the as received APMT Charpy v-notch impact test is shown in the optical macrograph in Figure 6.24. A uniform brittle cleavage type fracture surface is observed.

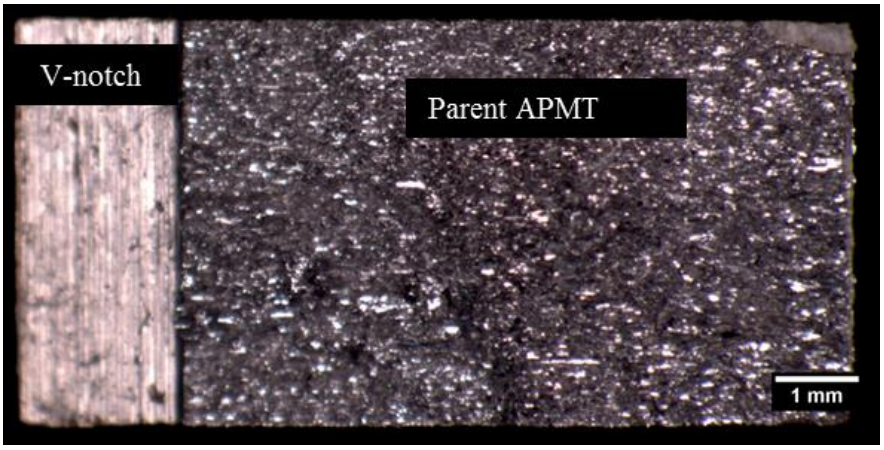

Figure 6.24 *Optical macrograph of the fracture surface from a V-notch Charpy impact test of the as received APMT plate.*

Further analysis using higher magnification SEM images is shown in Figure 6.25. The SEM fractograph shows the fracture surface detail. The rolling /longitudinal direction is indicated. On the right hand side of the image in Figure 6.25b, the v-notch can be seen. The main features that can be observed are the transgranular crack and the brittle cleavage fracture type features in Figure 6.25a, and the grain boundary crack in Figure 6.25b.

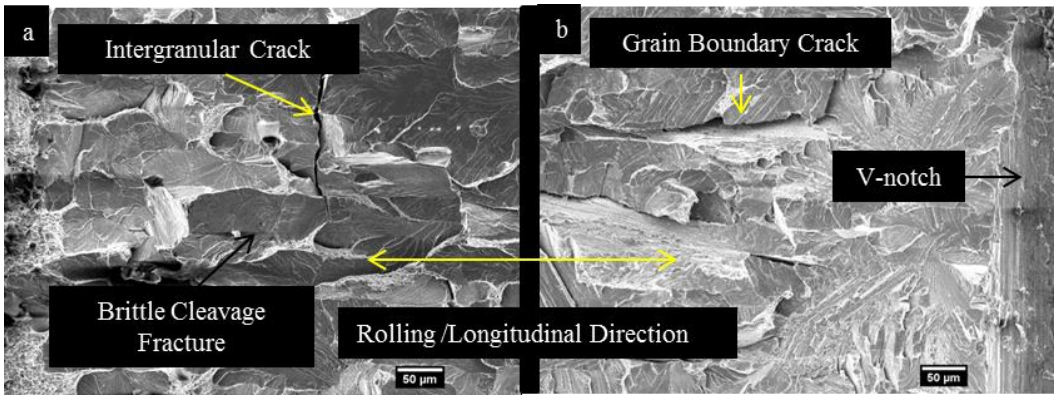

*Figure **6.25** SEM fractographs of as received APMT showing a) intergranular crack and brittle cleavage fractures and b) grain boundary crack.*

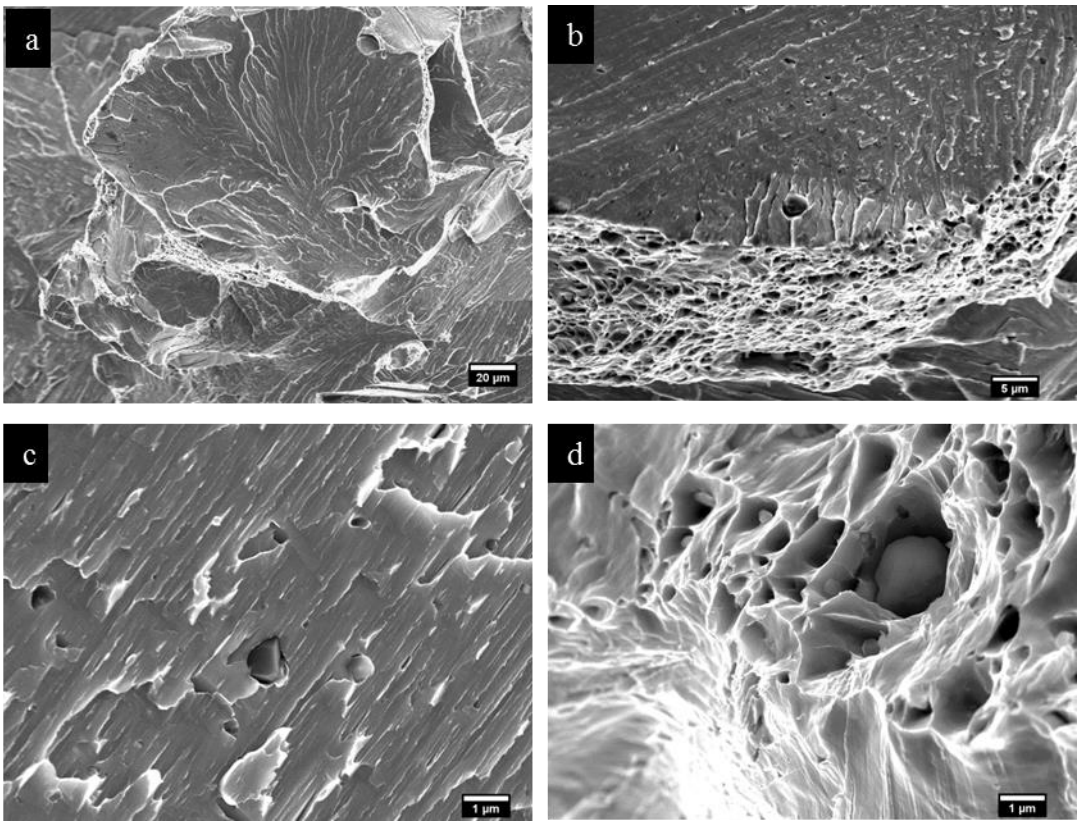

***Figure 6.26** SEM fractographs of as received APMT showing a) brittle cleavage fracture region surrounded with ductile fracture regions, b) a higher magnification image of a region with both, brittle cleavage and ductile fracture modes, c) particles extruding from cleavage fracture area and d) particles embedded in dimple fracture microvoid regions*

Figure 6.26a shows a fractograph of a brittle cleavage fracture and some areas of ductile dimple fractures. Figure 6.26b is a higher magnification fractograph of a cleavage fracture surrounded by an area of ductile dimple fracture. Figure 6.26c is a

close up fractograph of a cleavage fracture region with a protruding particle. Figure 6.26d is a fractograph which shows an area of ductile dimple fracture with particles embedded in pits. The overall fractured surface is one of mainly brittle cleavage fracture features surrounded by ductile dimple structures with particles in the microvoid areas.

W31 As-Welded

An optical macrograph of the Charpy v-notch impact test fracture surface of W31 as welded is presented in Figure 6.27. The fracture surface has several cracks visible in the TMAZ part of the weld. Also visible are several void regions with a number of cracks originating from them. The elongated microstructure of the parent APMT at the base of the weld contrasts strongly with the finer more equiaxed microstructure of the TMAZ.

Figure 6.28 shows an SEM fractograph of the area next to the v-notch. Notable features are the voids in the TMAZ and the cracks that have originated from them. The parent APMT regions varies in appearance as the area next to the v-notch has a smoother surface but further away from the v-notch as in Figure 6.26, details of the elongated microstructure can be seen.

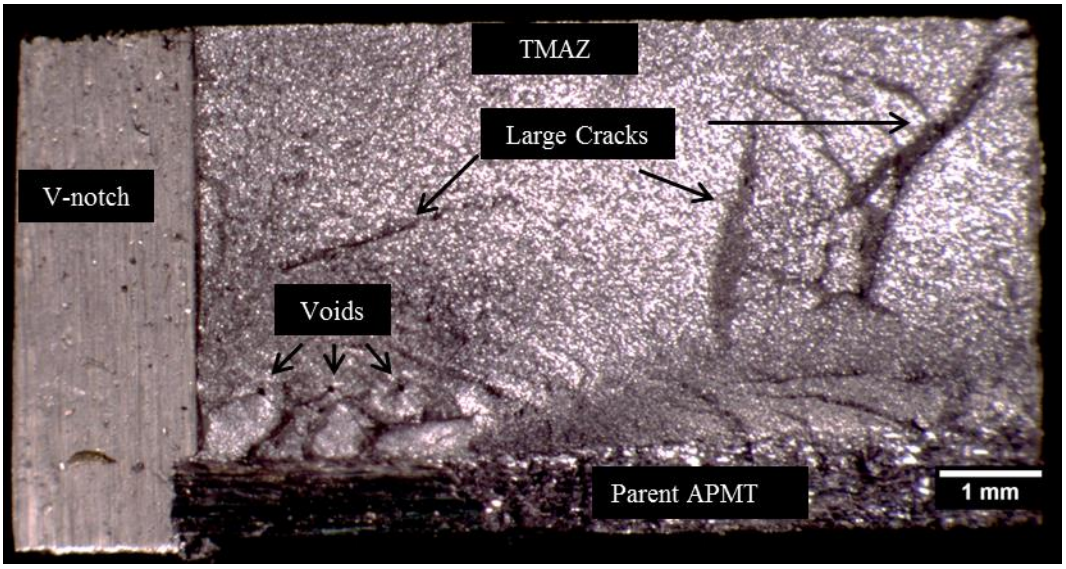

Figure 6.27 *Optical macrograph of the Charpy v-notch impact fracture surface of W30 as welded sample.*

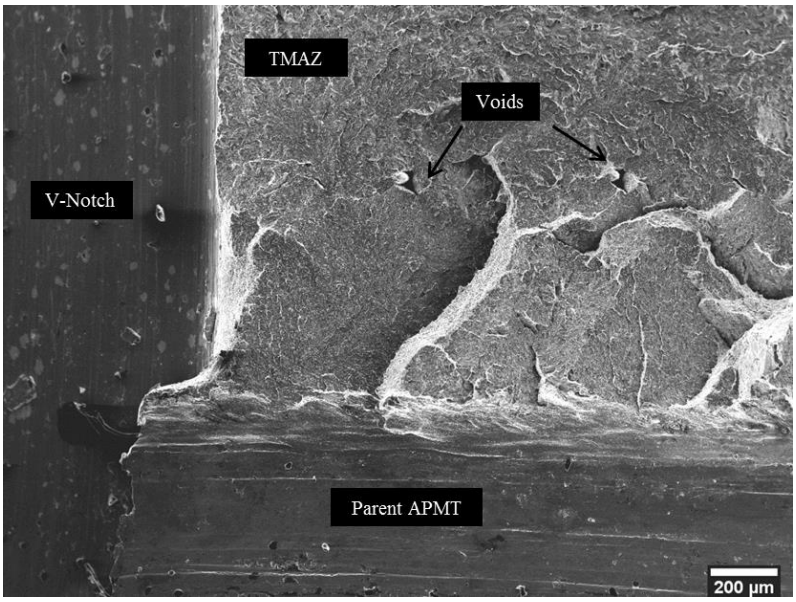

Figure 6.28 *SEM fractograph of the Charpy v-notch impact fracture surface of W30 as welded sample.*

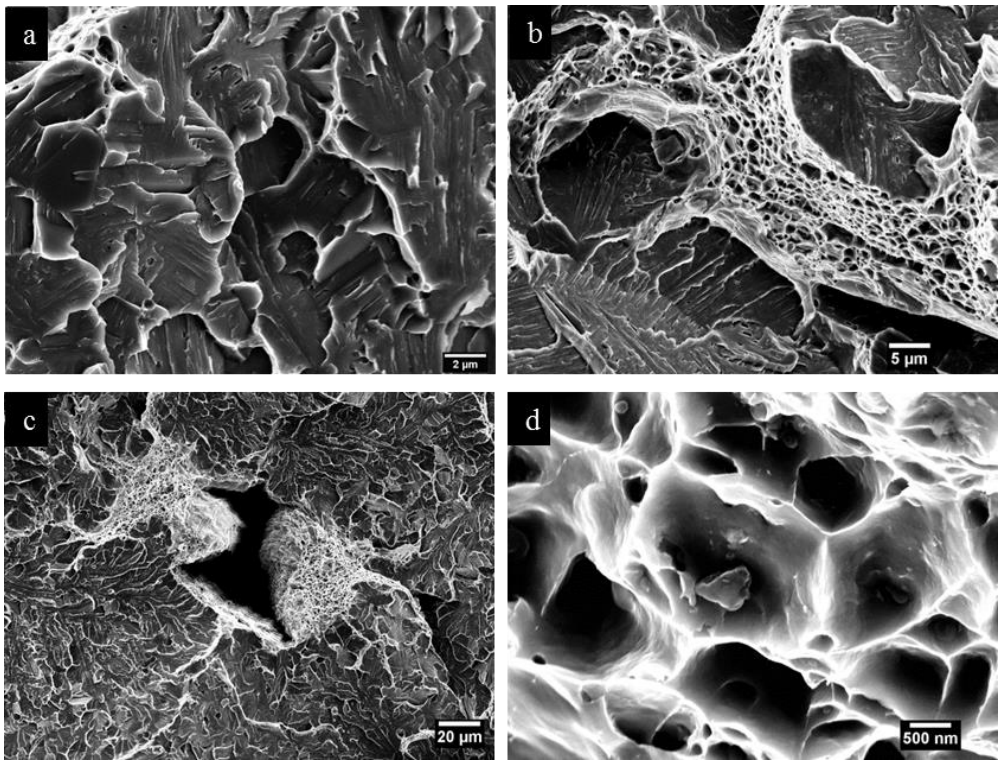

Figure 629 *SEM fractograph images of APMT W30 as welded fracture surface showing a) brittle cleavage fractures in the TMAZ, b) higher magnification image showing the larger ductile fracture regions surrounding the brittle cleavage regions, c) fracture surface around a void and d) a higher magnification image of the ductile fracture region next to void area showing particles in the microvoid areas.*

The higher magnification SEM fractograph in Figure 6.29a show the smaller sized brittle cleavage fracture features in the TMAZ which correspond to the smaller grain size of the microstructure in the TMAZ of W30. Another notable difference observed is that the ductile regions surrounding the cleavage features, as seen in Figure 6.29 b, is wider. In effect there is more ductility in the TMAZ of the as welded W30 than in the parent APMT. Figure 6.29c a void with ductile features are observed and in Figure 6.29d a closer look at the ductile fracture features showing particles at the base of the microvoid areas.

W31 Post Weld Heat Treated Condition

Channelling contrast image of the fracture surface of the base of W31 with PWHT is shown in Figure 6.30. The large grain structure of the TMAZ is reflected in the size of the brittle fracture cleavage features in the top part of the image in contrast with the parent APMT part of the image at the base.

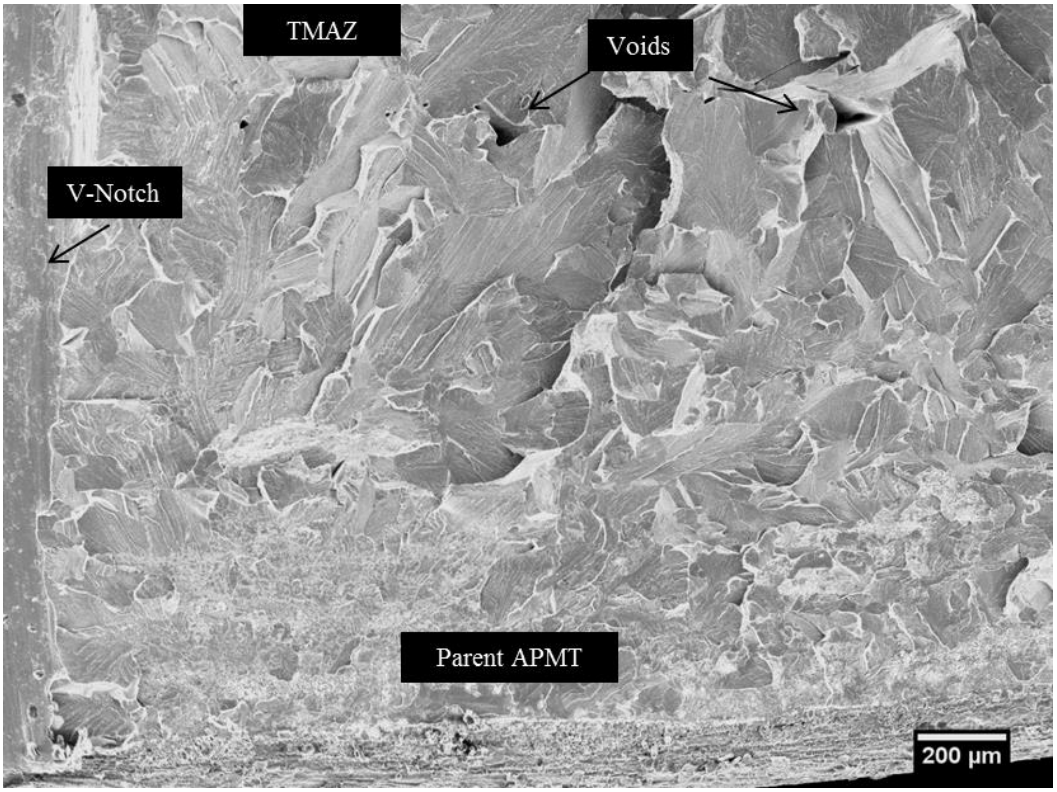

Figure 6.30 *Channelling contrast image of the base of the fracture surface of W31 with PWHT. Note the cracks around the void region.*

The v-notch is marked at the left hand side of the image. Two voids are marked just above the boundary region between the parent APMT and the TMAZ of W31. Several cracks can be seen at the void regions.

The top part of the fracture surface is shown in Figure 6.31. In contrast with the fracture surface of W31 as welded, the brittle fracture cleavage features are larger which corresponds to the larger grain structure of the TMAZ. Additional features are the cleavage steps as indicated and the river lines which originate from local crack regions as the surface is separated by the impact of the tester. These cracks propagate from grain to grain and as the grain orientation changes so does the direction of the river lines which are steps between parallel planes.

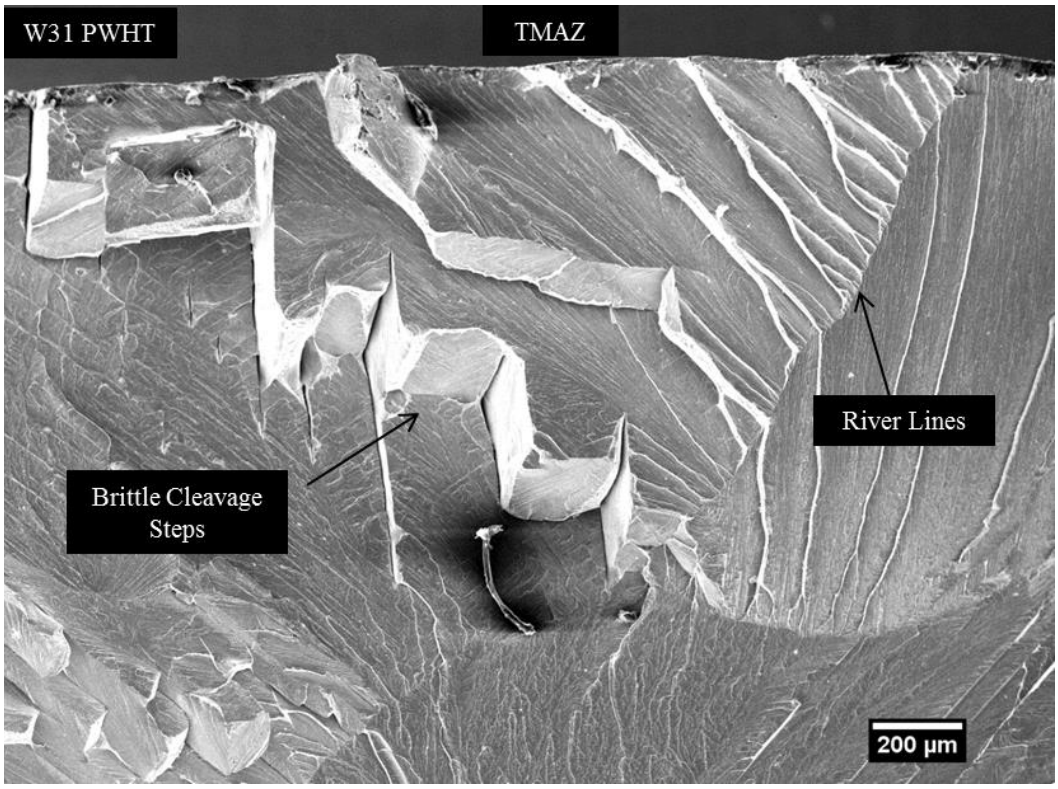

Figure 6.31 *Channelling contrast image of the top part of the fracture surface of W31 with PWHT. Brittle cleavage steps and river lines are clearly visible.*

6.9 The Formation and Analysis of Voids

The void formation in FSW was further examined in order to determine their source and to determine whether it was controlled by the parameters or whether it was a design feature that could be eliminated by improving design aspects of the tool. All voids observed were located at the advancing side near the base of the weld. The schematic in Figure 6.32a illustrates the several longitudinal cuts made from the reversing side to the advancing side of the weld in order to look at the grain structure of the W30 weld but also to try and cut at the right point to see if there was a pattern to the voids or whether they were a random effect. The DIC image in Figure 6.32b shows the longitudinal view of a section just at the advancing side of the base of the W29 weld which confirms that the voids are a regular occurrence across the longitudinal cross section as shown. The distance between the voids was measured at 0.76mm.

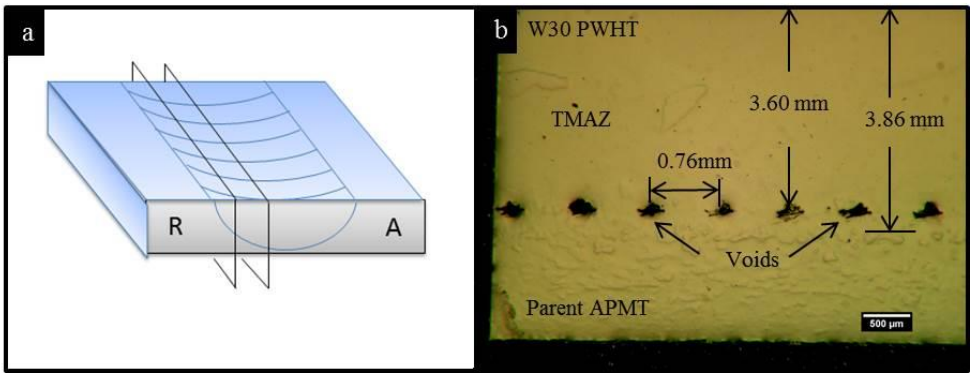

Figure 6.32 *a) Schematic illustrating the longitudinal cuts made on W30 with PWHT section of the weld and b)the DIC image of a of the longitudinal cross section showing a series of voids at regular intervals.*

Using data from Table 6.1 the time taken to travel along the sample by 0.76mm is:

$$t = d/s \qquad \textit{(Equation 6.1)}$$

where t is the time in seconds d is the distance in mm and s is the transverse speed in mm/m

$$t = 0.76 \div (150 \div 60)$$

$$t = 0.304 \text{ s}$$

Number of revolutions R for a given time,

$$R = t \times s_r \qquad \textit{(Equation 6.2)}$$

Where s_r is the rotational speed, so that:

$$R = 0.304 \times (200 \div 60) = 1.01$$

This confirms that the voids coincide with the rotation of the tool in the W30 weld. A similar calculation was performed with the W29 weld and the voids again were spaced out exactly one revolution of the tool apart.

From the DIC image in Figure 6.32b, voids are formed just above the base of the weld boundary with the parent APMT.

In order to investigate the voids further, a section of W29 with PWHT was polished from the base of the weld carefully removing the parent APMT. When the region with the voids was near optical examination of the sample was regularly undertaken until voids could be seen. The sample was polish to a 0.25µm finish and then etched to reveal the grain structure at that depth of the weld.

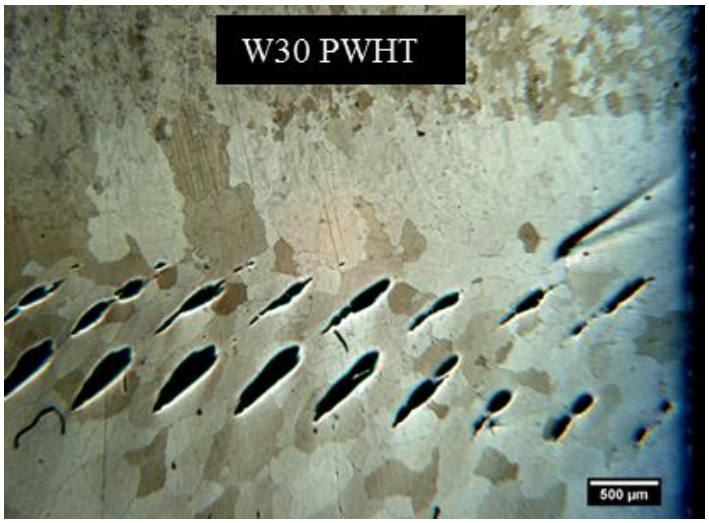

Figure 6.33 *Plan view from the base of the weld which had been polish progressively until voids could be observed. The voids follow a spiral trajectory.*

Figure 6.33 shows an optical image of the plan view from the base of W30 with PWHT. The voids seem to follow a spiral trajectory as the tool rotates and moves

along the longitudinal direction. As an approximation, if a rotating tool moved along the weld, then the voids would form a set of rings as illustrated by the schematic in Figure 6.34. Depending on the line of view, which corresponds to the polished cross section of the weld, the distance between each successive spiral, most of the time several voids would be visible.

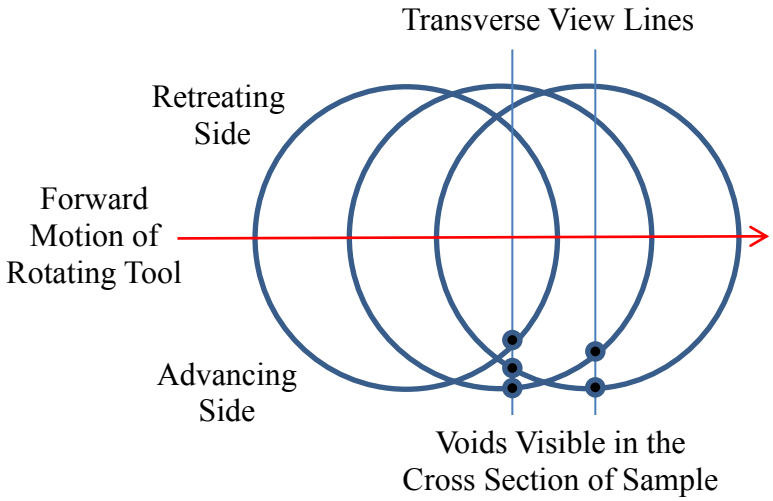

Figure 6.34 *Schematic of the rings of voids formed and the number of voids that could be visible depending on the position of the view line. Author's own schematic*

The best approximation of the radius of the rings would be the distance between the centre of the weld and the void that is furthest from the centre.

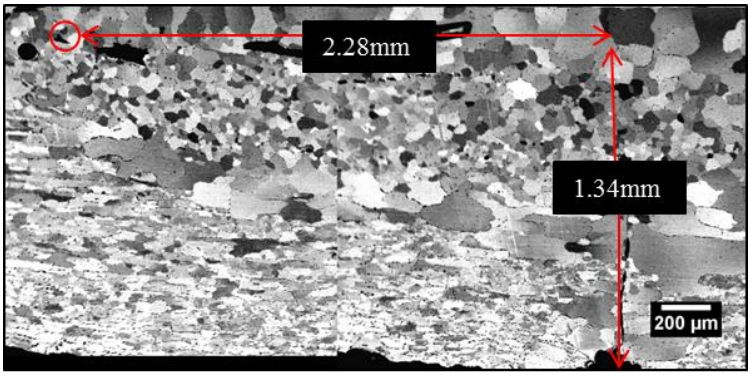

Figure 6.35 *A montage of two channelling contrast images of W30 with PWHT showing the centre of the weld and 4 voids in total. Distance of the furthest from centre void is 2.28mm*

The channelling contrast montage from two images in Figure 6.35 show the cross section of W30 with PWHT and 4 voids that are visible. The distance of the void furthest away from the centre is 2.28mm.

Another method is to assume that the arcs formed by the voids are circular i.e. to ignore the forward motion of the tool and assume that the voids form a perfect circle. In reality the forward motion of the tool would have the effect of elongating the arc and therefore increasing the radius of the void rings. To calculate the radius from the height and the width of the arches the following formula is used:

$$R = \frac{H}{2} + \frac{W^2}{8H} \qquad \textit{(Equation 6.3)}$$

Where R is the radius, H is the height, and W is the width of the section of arc as illustrated in Figure 6.36.

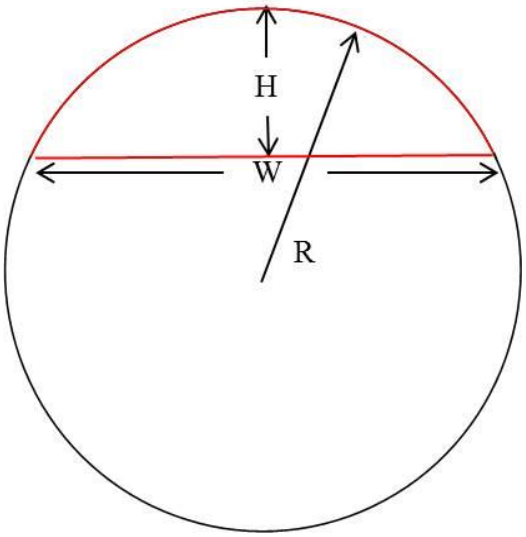

Figure 6.36 *Schematic of the width and height measurements used to calculate the radius of an arc.*

Of the ten arcs that were visible in the DIC image in Figure 6.33, only 6 measurements were made with some degree of accuracy. The results are presented in Table 6.3

Table 6.3 *Calculations of the radius of the voids observed in the DIC image in Figure 6.33*

Arch No	Width (mm)	Height (mm)	Radius (mm)
1		Could not determine	
2		Could not determine	
3	1.41	0.08	3.1
4	1.08	0.06	2.46
5	1.08	0.07	2.12
6	1.12	0.08	2.0
7	1.13	0.05	3.22
8	1.06	0.06	2.37
9		Could not determine	
10		Could not determine	
		Average	2.54

The average radius of the arches was calculated to be 2.54mm. In reality the true radius could vary and is a region of between 2.28mm as a minimum and 3.22mm which was the maximum measured in the calculation of radius from the arc dimensions.

As mentioned in the literature review, the tool used for the welds was a Q70. In a paper by J Perrett et al. [119], a study was conducted on the effects of wear on several tool compositions including Q70 which is the tool used on the APMT welds.

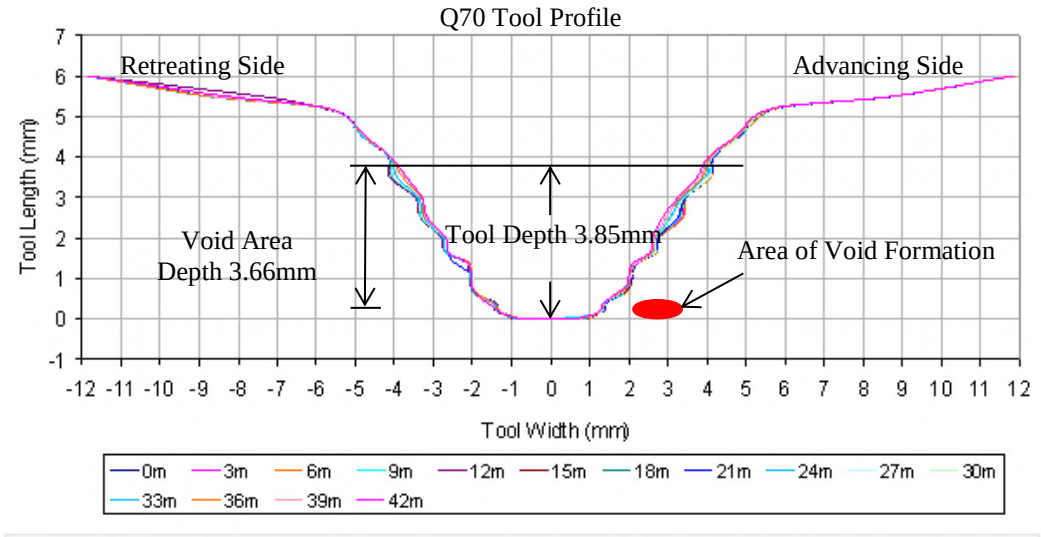

Figure 6.37 *Profile of Q70 tool with the position of the void areas superimposed on the profile of Q70 tool taken from J Perrett et al. [119] .*

Using the profile of Q 70 from the paper as a guide, the position of the void area is marked using the measurements of the depth and radius of the voids. A specific region just beyond the tool bit is where the voids are formed. This could be due to a specific feature of the tool bit such as a groove or similar type of feature that as the tool rotates is causes voids to form and as the tool moves along the weld line these voids are flung off the tool due to the centrifugal force of the rotating tool. These voids are only visible in the advancing side of the weld. The likely reason for that is at the advancing side the material is sheared away by the tool and at the retreating side material is moved back behind the advancing tool. Any voids formed at the retreating side would them be 'filled' by the rush of material moved by the tool.

6.10 Second phase particle characterisation

The second phase particles in APMT are made up of a combination of carbides, nitrides, oxides of aluminium and yttrium, yttrium aluminium oxides and oxides of hafnium, and zirconium. Larger particles tend to be the carbides and nitrides along with aluminium oxides. These particles can be up to several microns in size. The carbon extraction technique had been attempted in order to study the morphology of the particles present in APMT but due to the size range of the particles, the etching of the carbon film post deposition did not prove successful. Analysis was therefore performed on various TEM samples and some EDX analysis was performed on polished surfaces in the SEM.

SEM Analysis of Second Phase Particles

Several particles observed in the SEM image in Figure 6.38 of W30 as welded were analysed by EDX and the results are presented in Figure 6.39. As can be seen from Figure 6.38 there is a wide range of size of particles.

EDX analysis also confirms that there is a wide range in types of particles as well. From the literature review on the production methods of APMT, nitrogen is used to facilitate the atomisation of the APMT melt and therefore it is inevitable that nitrides will form during this process.

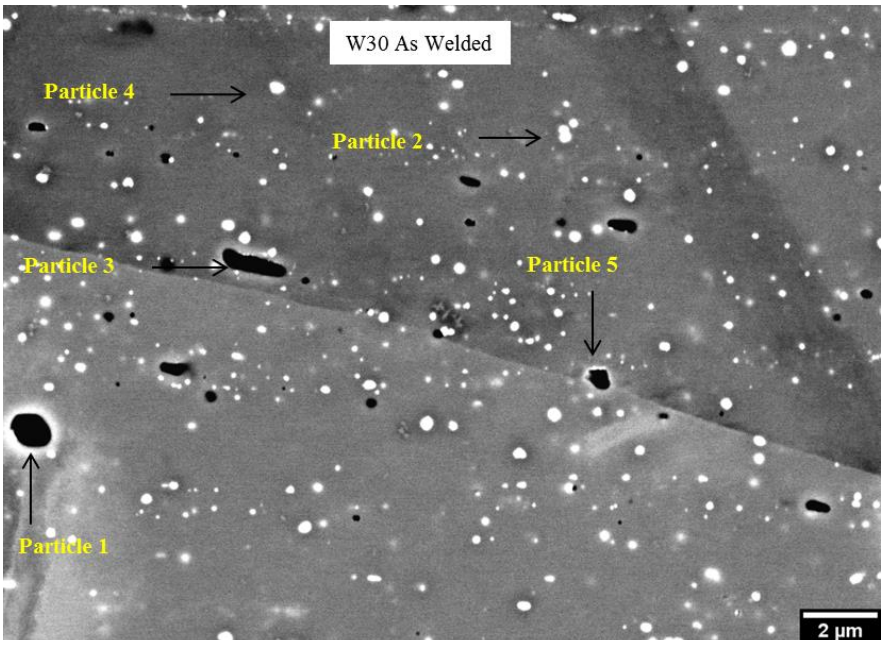

Figure 6.38 *SEM image of W30 as welded with different types of particles labelled Particle 1 to Particle 5.*

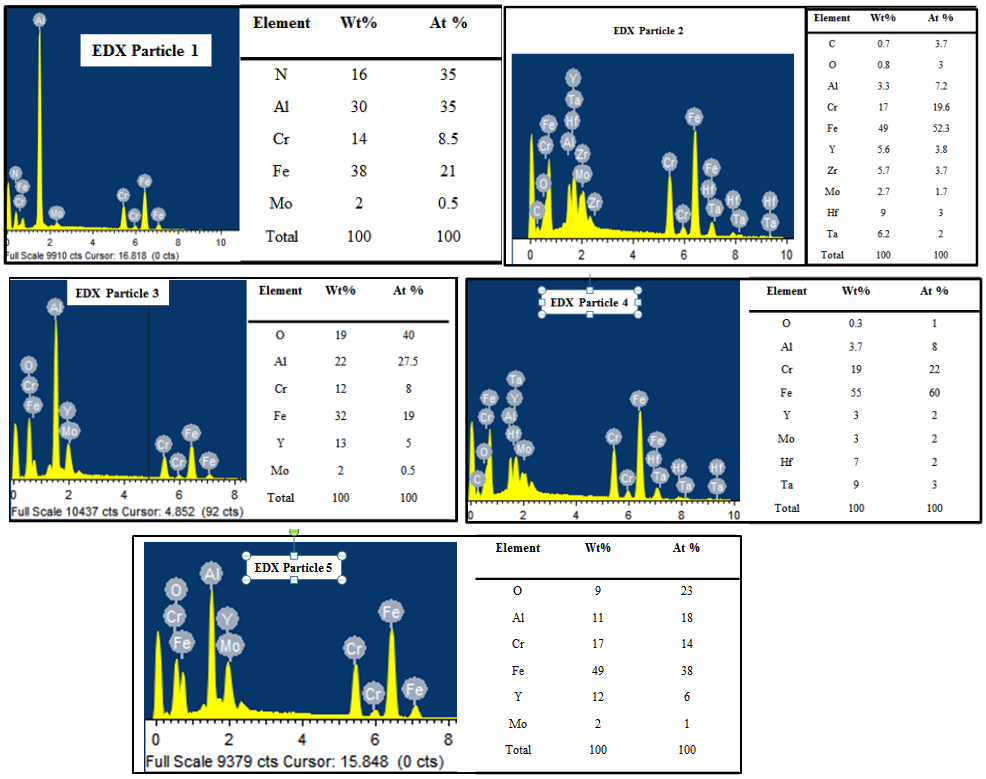

Figure 6.39 *EDX spectrum and quantitative results of the 5 different particles observed in W30 as welded sample in Figure 6.38*

As with PM2000 the addition of yttrium oxide powder to the production during consolidation produces a reaction with the aluminium in the matrix to form Y Al O particles but not all of the yttrium oxide is consumed. Several different types of particles had been selected for EDX analysis. Particle 1 is most likely aluminium nitride Al N. The EDX analysis of particle 2 indicates the presence of Zr, Hf, Ta, and Y which is a typical EDX of many of the smaller particles in APMT. Particle 3 is most probably a Y Al O type particle. Particle 4 is very similar to particle 2 and particle 5 is most likely an Al O type particle (dark contrast) with a Y Al O type particle attached (bright contrast). The main point is that there is a large variety of particles present in APMT with a wide range of size distributions

TEM Analysis of APMT

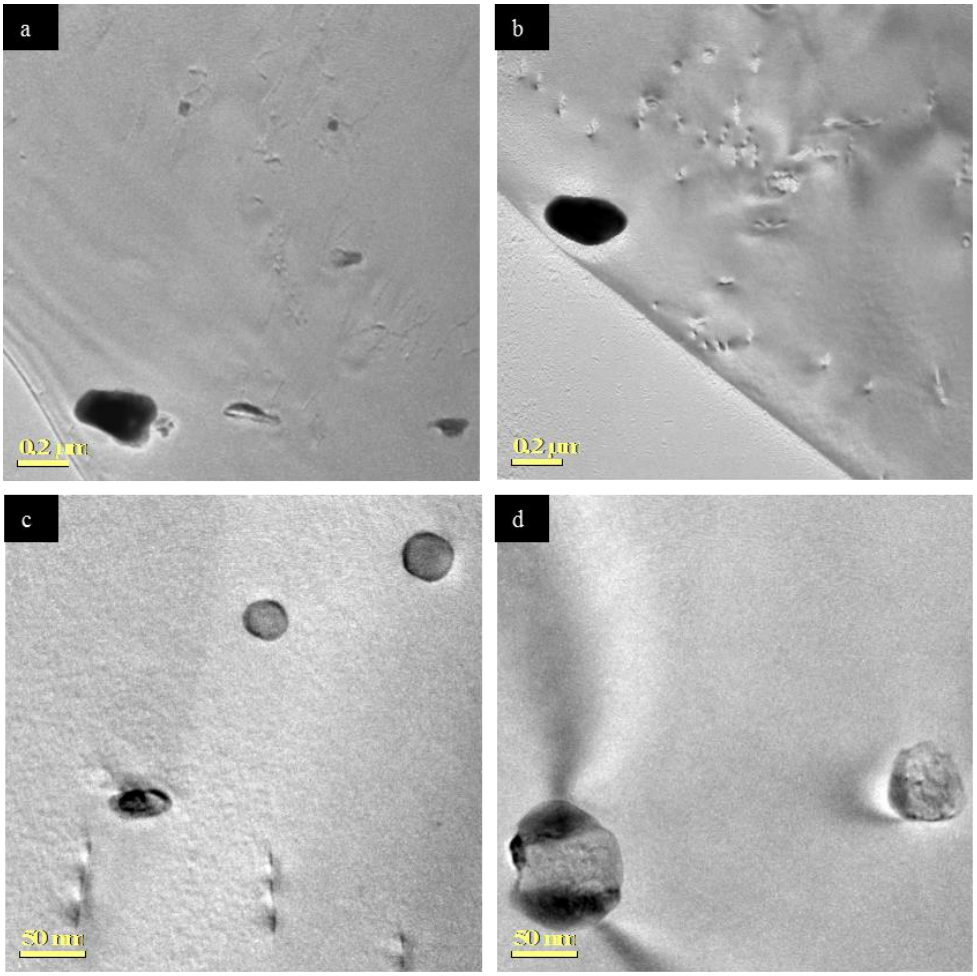

Figure 6.40 *Bright field TEM images of APMT as received showing the lack of particles in the matrix compared to PM2000.*

The bright field images in Figure 6.40 show the matrix with very few particles present. This is in stark contrast to the equivalent images of PM2000 matrix shown in Chapter 5. There is abundance in carbide type particles but in most cases only one set of FFT spots from the particle could be resolved, therefore not enough information was available to calculate the zone axis of the particles.

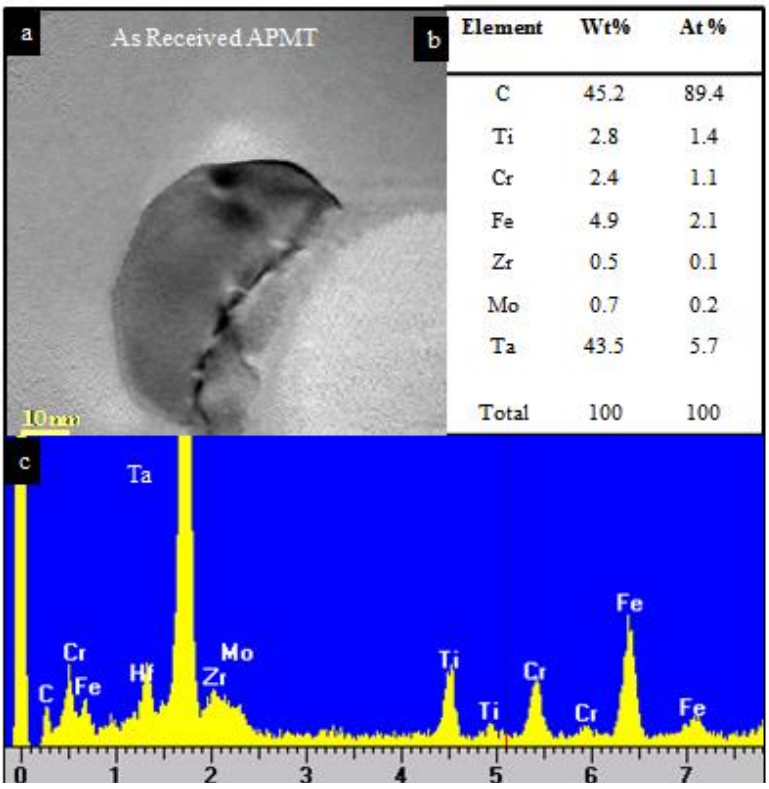

Figure 6.41 *a) A bright field TEM image of a carbide type particle, b) the quantitative data of the EDX analysis, and c) the corresponding EDX spectrum.*

One such particle is shown in the bright field image in Figure 6.41a. The corresponding EDX (Figure 6.41b and c) spectrum indicates the presence of Ta, which is a very strong carbide former. Ta is not listed in the composition table of APMT but has been detected in several particles examined, which was unexpected. On closer examination of the US patent document for the RSP process [23]. Ta is used in the production process and as a result APMT contains 0.05% to 0.5% Wt Ta. This is not stated in the data sheets available from Kanthal™ website. Hf and Zr are also detected in the EDX spectrum as seen in the quantitative data in Figure 6.41b

both being strong carbide formers. The TEM image in Figure 6.41a shows a dislocation in a single particle or a grain boundary between two different particles.

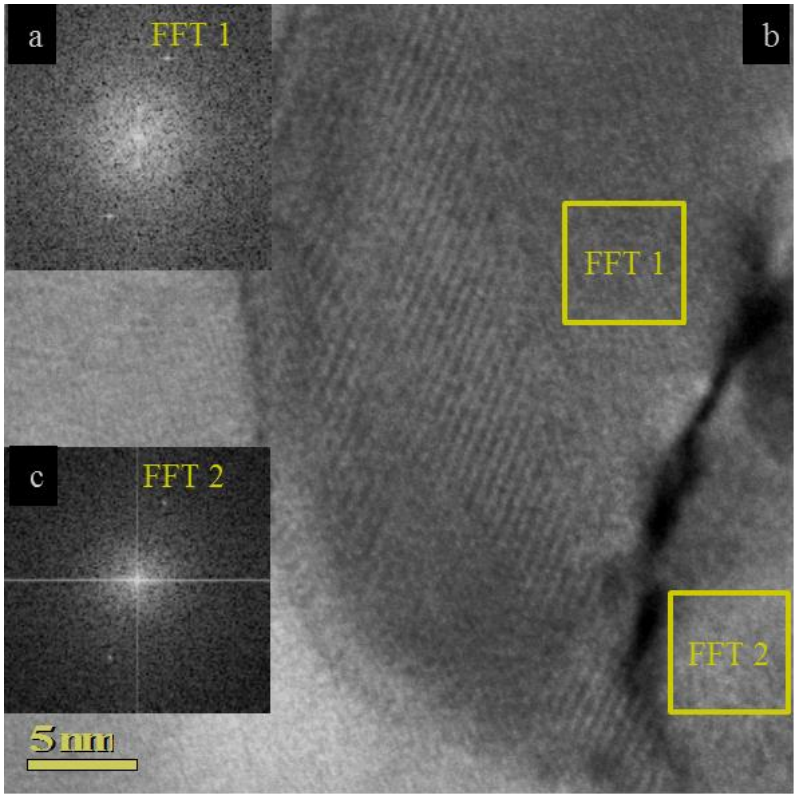

Figure 6.42 *a) HRTEM image of the particle in Figure 6.41with b) FFT of region marked FFT1 and c) FFT of region marked FFT2.*

A HRTEM image of the particle in Figure 6.42 with the corresponding FFT of the regions marked FFT1 and FFT2 either side of the boundary indicate that the lattice orientations are identical but a slight shift in the diffraction spots was detected. Taking an FFT of the whole image has confirmed that there is a shift in the diffraction spots as shown in Figure 6.43 with the expanded view showing a small difference in the d-spacing which was measured at 0.09Å. When taking measurements from expanded FFT of HRTEM images the accuracy of the data is much reduced but this difference matches the difference between the (002) planes of HfC (002) = 2.3 Å and the TaC(002) = 2.22 Å. As the carbides of Ta, Zr and Hf are all soluble, the difference in the d-spacing is somewhat surprising as diffusion should have homogenised the particle. This would suggest that the boundary observed was

indeed a grain boundary as possibly two particles have nucleated adjacent to each other with the same orientation but with slightly different compositions and therefore the slight difference in d spacings observed. The EDX analysis could not indicate any difference in composition as the two regions are too close together for the spacial resolution of the EDX signal to be able to differentiate between the two regions.

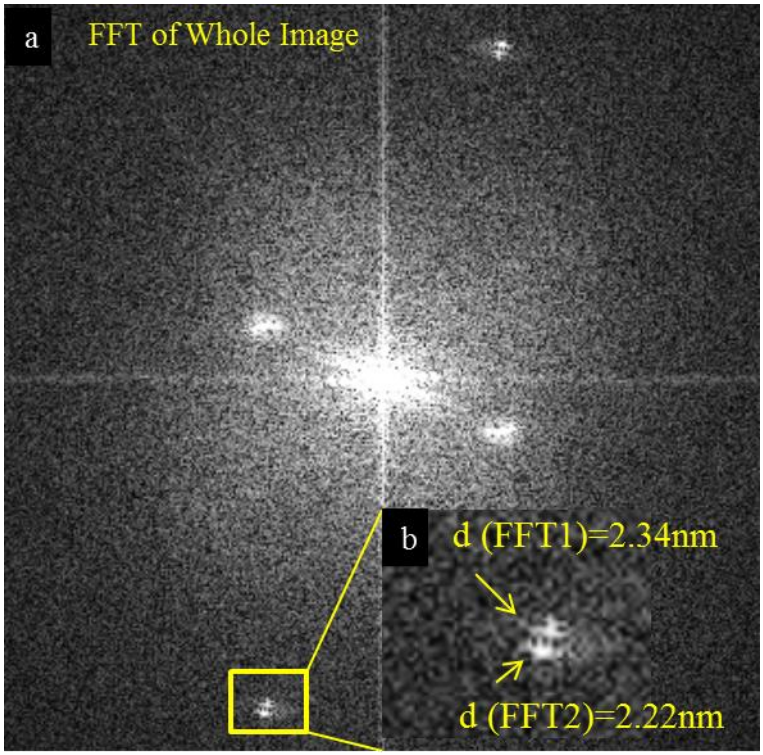

Figure 6.43 *FFT of the whole HRTEM image in Figure 6.42with an expanded view showing the difference in the d-spacing observed.*

6.11 Summary and Conclusions

The large size of the as-received APMT plate made more material available for additional characterisation that was not available for the PM2000 welds. Fractography of the fracture surfaces were examined using a Charpy v- notch impact tester. Tensile testing was performed in the USA by ORNL. In addition void formation was investigated using the APMT FSW samples.

6.11.1 General Observations

The FSW of APMT has resulted in several visually good quality joins with the minor defects in the form of voids and some cracks that appeared in the TMAZ. The surface quality of all the welds apart from W26 was very good with minimal amount of flash material around the welds. The weld depth of W26 is lower than the weld depth of the rest of the welds indicating that the downforce was not sufficient to provide enough frictional force to plasticise the weld region.

Cracks appeared at the base of the welds. APMT is a rolled 5mm plate which is thicker than the 4mm plate required for the type of tool available for FSW, which meant that there was a gap at the base of the welds. This gap was the source of a crack line that appeared in the TMAZ of the welds.

6.11.2 Hardness Profile

APMT has a much lower Vickers hardness number than PM2000 as there is little contribution to the hardness to APMT from the large grain size and the large particle distribution compared to PM2000. Consequently the FSW process also has little or no effect on the hardness profile as it is already at a low level. The application of PWHT also has no impact on the hardness value to any significant degree.

6.11.3 Particle Size Analysis and Grain Morphology

The particle distribution of APMT is considerably coarser and with a larger standard deviation than PM2000. Figure 6.42 shows the average particle sizes and the standard deviation in APMT with and without HT and of W29 with and without PWHT.

The unusual result in the particle size analysis of APMT is the reduction of the average size of the particle distribution after the FSW process. Starting with an average size of 107nm before the application of FSW the average size is reduced to 83nm after the FSW process. A published average particle size of 75nm is reported

in literature [118]. The FSW seems to have reduced the average size of the distribution. This could be due to some dissolution of carbides and/or nitrides during the FSW process which re-precipitate after the tool passes through or that the range in the size distribution means that there could be a large variation of the average size in APMT which might also be a likely explanation.

The coarsening effect of the HT and of the PWHT in both APMT and in the W29 sample is consistent with the coarsening observed in PM2000 where the average size increased but in addition the spread of the size distribution is also increased after either HT or PWHT

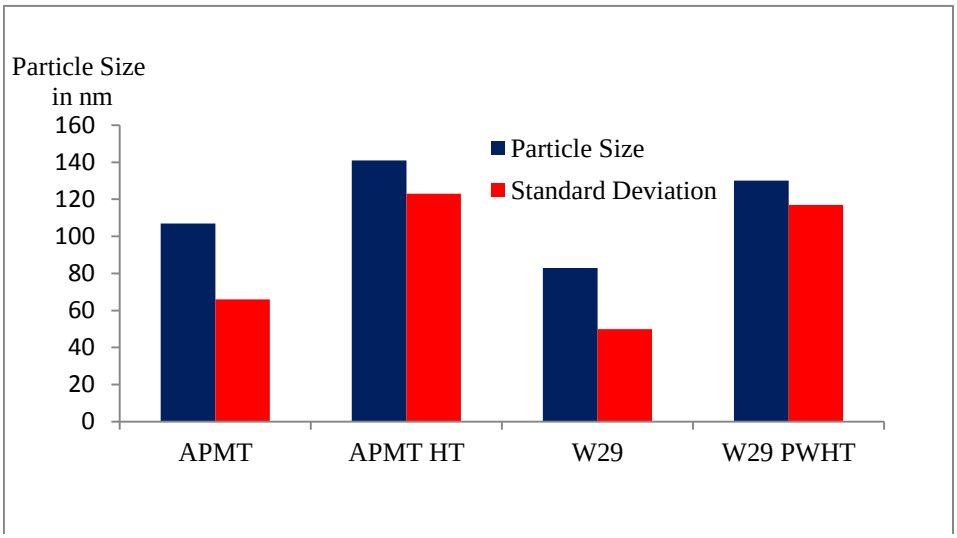

Figure 6.41 *Bar graphs of the average particle size and standard deviation for APMT, APMT with HT, W29 and W29 with PWHT.*

The particle size analysis did not reveal any differences of the distribution of the TMAZ from the different regions. This could be because the particle size and the spread of the size distributions were so large to begin with that any coarsening effect from the agglomeration of particles as observed with PM2000 would not be distinguishable.

6.11.4 Parent Material Microstructure

The grain structure of APMT is one of elongated grains along the rolling direction. Top and bottom of the APMT plate the microstructure is of much smaller grains that are equiaxed suggesting that an element of dynamic recrystallisation had taken place during the rolling process. The large elongated grain structure is mainly due to the alignment of the large average particle size and the low particle density of the distribution (12 ± 2 μm^{-3}) [118]. In effect it offers little hindrance to grain growth during consolidation due to the lack of any pinning force to the grain boundaries. This is also confirmed by the hardness data. With the application of HT grain growth was observed in all three directions.

6.11.5 TMAZ Microstructure

The grains in the TMAZ of all the APMT welds have undergone dynamic recrystallisation with a grain size in the region of 10µ. The grains are equiaxed but slightly aligned to the material flow. The differences arise after the application of PWHT. W26 and W27 have a much smaller secondary recrystallised grain structure to the rest of the welds.

Looking at Table 6.1 which lists the parameters of the welds, the only parameter that is different in W26 and W27 but not the rest of the welds is the Heat Input (HI). This is a measure of the energy input per mm of weld. W29, W30 and W31with a heat input of 1.37kJ/mm, 1.20kJ/mm and 1.24kJ/mm respectively, have an increased amount of deformation but also an increased amount of heat and therefore a higher temperature is reached and so more recovery occurs. This limits the number of nucleation sites and creates a large recrystallised grain size

W26 and W27 have a similar heat input of 1.08kJ/mm and 1.02kJ/mm respectively. The lower amount of energy input in these two welds compared to the rest of the welds corresponds to a lower amount of deformation in the TMAZ, so one would expect that W27 with the slightly lower heat input would have an even smaller secondary recrystallised grain structure than W27. Looking at the transverse speed of the two welds W26 at 100mm/m and W27 at 125mm/m could be a possible

explanation. The slower transverse speed of W26 allows the TMAZ to set at a slower pace enabling some relaxation of the stresses that drives the recrystallisation process.

6.11.6 Defects and Void Formation

The use of the correct tools for a specific purpose cannot be emphasised enough. As received APMT plates were supplied in 5mm plate. The tool used for the FSW was designed for 4mm welds. The butt FSW namely W29, W30 and W31, all had a gap at the base of the welds where the tool could not reach. This gap had propagated into the TMAZ of the welds probably due to the vibrations of the rig while the FSW was progressing.

Void formation was investigated and was found to be linked with a feature on the tool bit. This could have major implications on the design of the FSW tools as a minor adjustment of the design could in theory eradicate some or possibly all the voids observed in the TMAZ of the welds. The features on the tool such as grooves help stir material to facilitate the welding. From the Q70 tool profile as presented in Figure 6.37, one can observe that the biggest change in the dimensions of the tool over time is near the top of the tool and near the middle. These regions probably play a bigger part in stirring the material in the TMAZ as they are worn down more than regions of the tool at the base. A change in the design of the tool at the base could have little effect on the ability of the tool to stir material around and could prove beneficial in terms of the reduction of voids.

6.11.7 Mechanical Properties

Tensile tests and Charpy v-notch impact tests have indicated that the FSW process increases the ductility of the TMAZ compared to the parent APMT without compromising the tensile strength of the material. This increase in ductility was evidenced in the fractographs. The ductile regions surrounding the brittle cleavage fractures have increased in size in the TMAZ compared to the parent APMT.

Fractographs of the TMAZ of W30 with and without PWHT indicated several cracks originating from the void regions which could prove problematic in stressed conditions.

6.11.8 Second Phase Particles

There is a wide variety in the size and composition of the particles investigated in APMT. The larger particles are mainly carbides, nitrides and aluminium oxide whereas the smaller particles tend to be yttrium aluminium oxides and yttrium oxides.

A number of particles that were analysed by EDX had strong signals for Hf, Zr, and Ta. These elements are strong carbide and nitride formers and in addition the carbides and the nitrides of these elements are completely soluble with each other [120]. In effect a particle could be a nitride, carbide or a carbonitride with a combination of Hf, Zr and Ta. This of course makes it extremely difficult to distinguish between them.

CHAPTER 7

Dissimilar Metal FSW between APMT and As-Extruded PM2000

7.1 Introduction

The main reason for the study of APMT FSW in Chapter 6 was the attractive prospect of welding an ODS alloy to a less critical component which still has excellent oxidation and corrosion properties but does not have the high temperature creep properties that is required for stressed high temperature applications. APMT fulfils the role perfectly and so a FSW between APMT and as extruded PM2000 is a logical step that can minimise costs by using the high cost PM2000 only for parts of a design that require the high temperature creep performance and attaching APMT to parts of a design that only require the high temperature oxidation and corrosion performance. In this chapter the focus will be the boundary areas in the TMAZ between the two different alloys. This weld was performed at TWI and designated as W35.

7.2 The FSW Process

In order to perform the FSW between APMT and PM2000, the APMT plate had to be ground down to 4mm in thickness so that the two plates would be of the same thickness. The parameters chosen are listed in Table 7.1.

The APMT plate was placed at the advancing side of the weld. The reason for this was that any voids usually form at the base of the advancing side of the weld. The idea was to keep the voids in the part of the weld that is not critical in terms of the high temperature creep resistance. The weld line was arranged along the transverse direction of the APMT plate and along the extrusion direction of the as extruded PM2000.

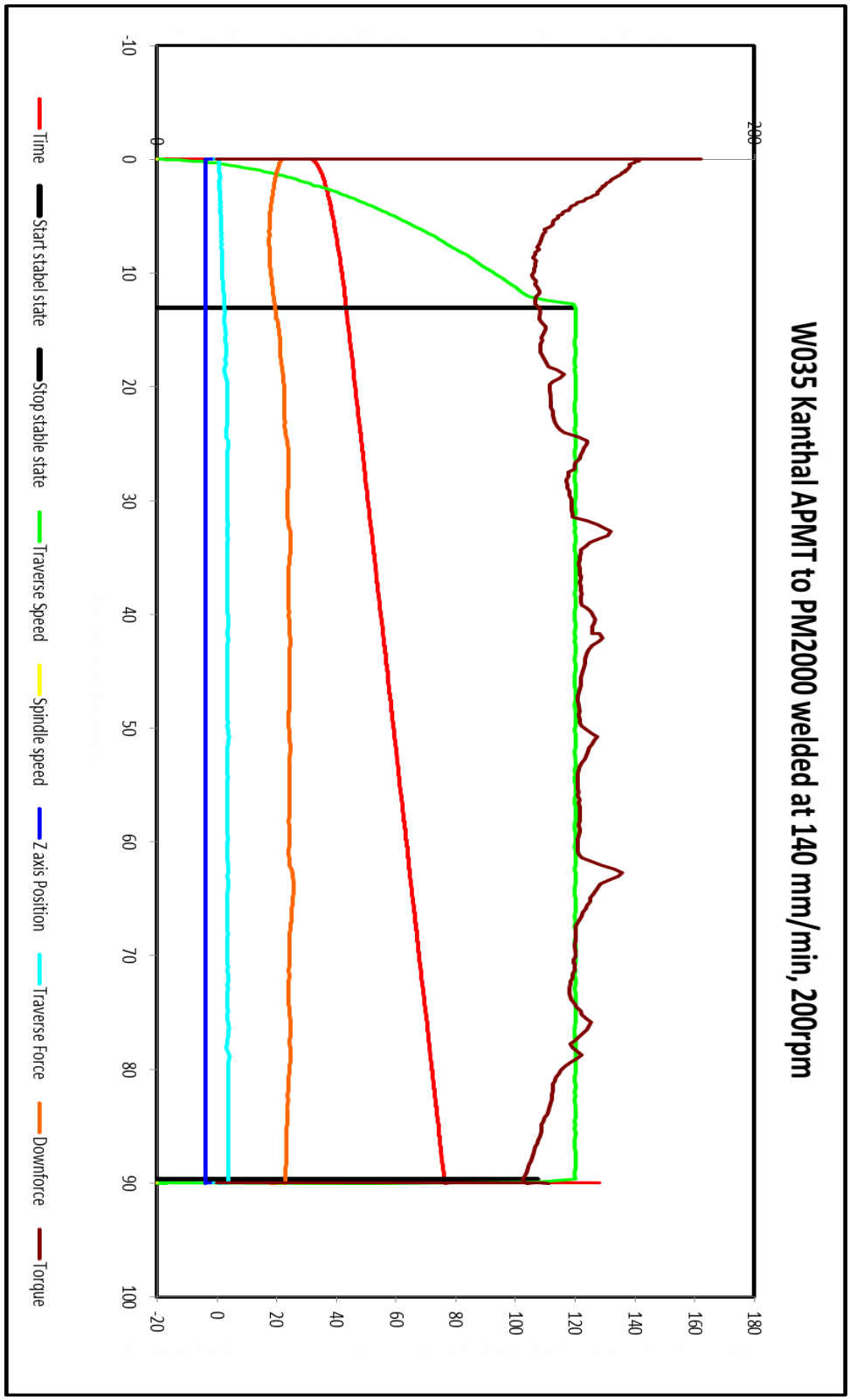

Figure 7.1 *Chart of the parameters versus distance for W35. The units used are listed in Table 7.1*

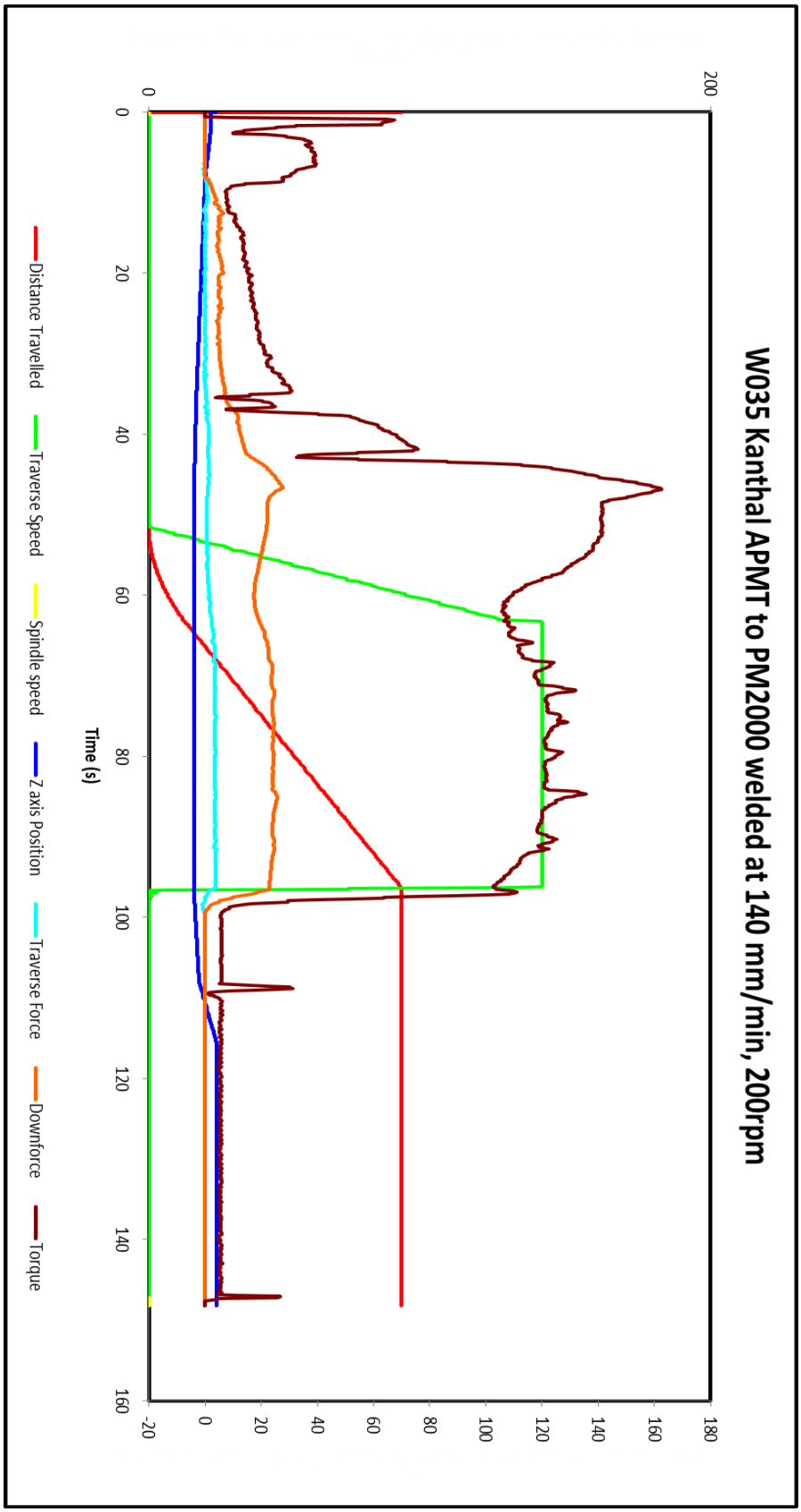

Figure 7.2 *Chart of the parameters versus time for W35. The units used are listed in Table 7.1*

Table 7.1 *List of the parameters used for the dissimilar metal FSW between APMT and PM2000 designated W35*

W035 Kanthal APMT to PM2000 welded at 140 mm/min, 200rpm					
Start stable state position(mm)	13.1				
Stop stable state position(mm)	89.7				
	Average	*Maximum*	*Minimum*	*%*	*St. Dev*
X-Force (kN)	3.5	4.2	2.3	0.5	0.3
Y-Force (kN)	-3.7	-2.6	-4.8	-0.6	0.4
Z-Force (kN)	23.8	25.7	19.4	0.3	1.1
Spindle rotation speed (rpm)	-201.2	-197.0	-202.0	0.0	0.8
Spindle traverse speed (mm/min)	140.0	140.1	139.4	0.0	0.1
Torque (Nm)	119.1	135.6	103.7	0.3	6.3
Heat input kJ/mm	-1.1	-0.9	-1.2	-0.3	0.1

Table 7.1 lists the parameters and units used for the weld and the charts in Figure 7.1and 7.2 are plots of the various parameters versus distance and time respectively as the weld was progressing. Figure 7.3 shows an optical image of the weld. The surface quality of the weld is not as good as the previous welds namely, the as-extruded PM2000 W34 weld and the APMT welds.

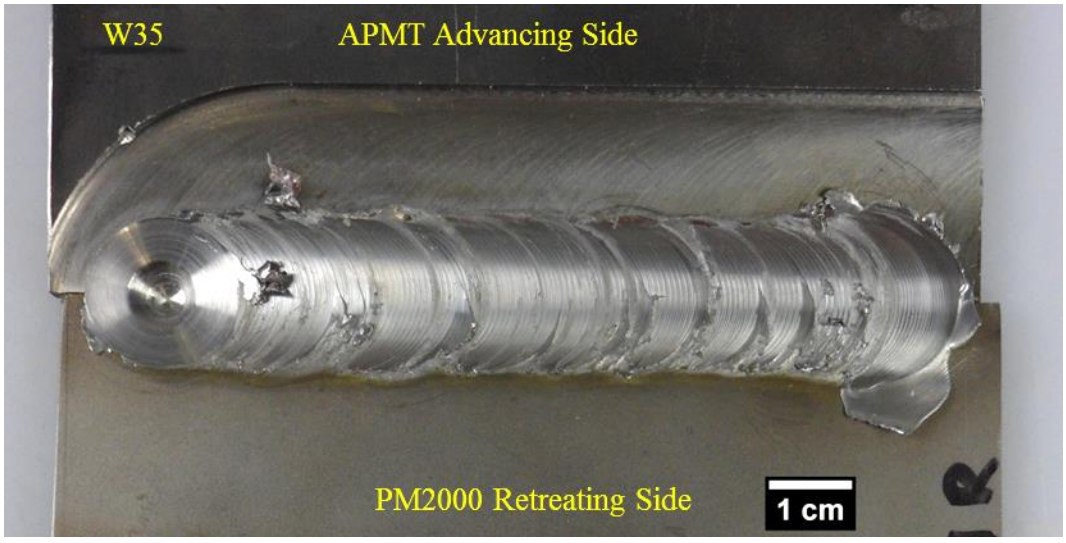

Figure 7.3 *Optical image of the dissimilar metal weld between APMT and PM2000 designated as W35.*

In addition there is more flash of material along the weld than in the previous welds mentioned. Excessive downforce can sometime cause more flash of material to form in a FSW.

7.3 Optical Microscopy

W35 As-Welded Condition

A montage from optical images of the cross section of the W35 is presented in Figure 7.4. Several observations can be made from the image. The flow of material is indicated by the yellow arrows. There is a region of APMT top section that is moved along to the retreating side of the weld and the middle section there is a region of PM2000 that is moved along towards the advancing side of the weld.

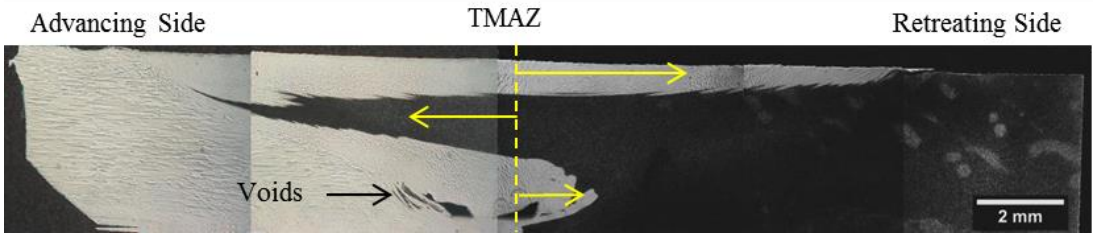

Figure 7.4 *Montage from optical images of the cross section of W35. The material flow is indicated by the yellow arrows. Voids are visible near the base of the weld (polished to colloidal silica finish).*

At the base of the weld a short intrusion of APMT is moved across into the PM2000 half of the weld. The longitudinal elongated grain structure of APMT parent region is visible.

Apart from the two larger than usual voids that are present, a good join was achieved. There is a marked difference in contrast of the APMT and PM2000 plates in the image as it shows quite clearly the material flow between the two parts of the weld. This is due to the difference in grain size between APMT and PM2000.

W35 Post Weld Heat Treated Condition

Figure 7.5 shows a montage of optical macrographs of the cross section of W35 after PWHT. As expected the parent region of APMT at the advancing side has undergone recrystallisation leading to a smaller rain size and the parent region of PM2000 at the retreating side has recrystallised to form a large grain size.

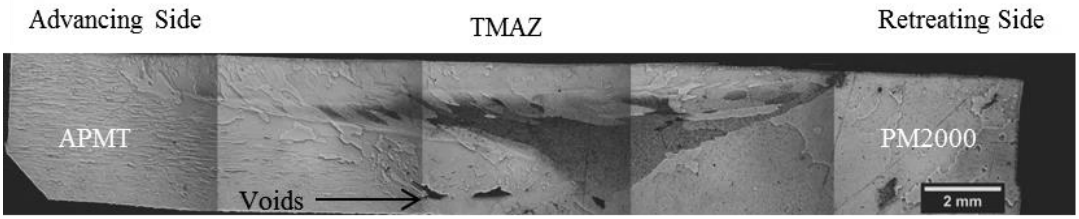

Figure 7.5 *Montage from optical images of the cross section of W35with PWHT (polished to colloidal silica finish).*

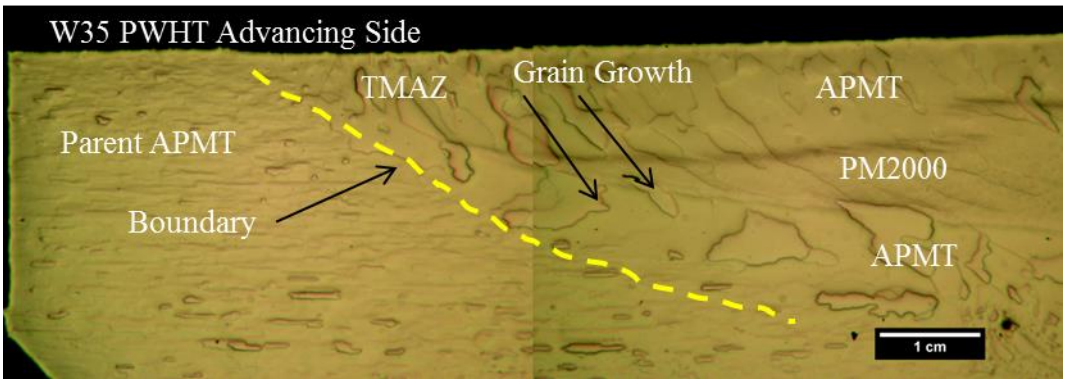

Figure 7.6 *A montage of two DIC images of the advancing side of W35 with PWHT. The secondary recrystallised grains in the TMAZ have grown across the APMT/PM2000/APMT boundaries (polished to colloidal silica finish).*

In Figure 7.6 a montage of DIC images of the advancing side of W35 is presented. The boundary between the APMT parent region and the TMAZ is well defined. The APMT has recrystallised with an elongated grain structure and the TMAZ has recrystallised with a much larger rain size.

Also visible in the montage is the TMAZ recrystallised grains that have grown across the APMT/PM2000/APMT region as indicated in Figure 7.6.

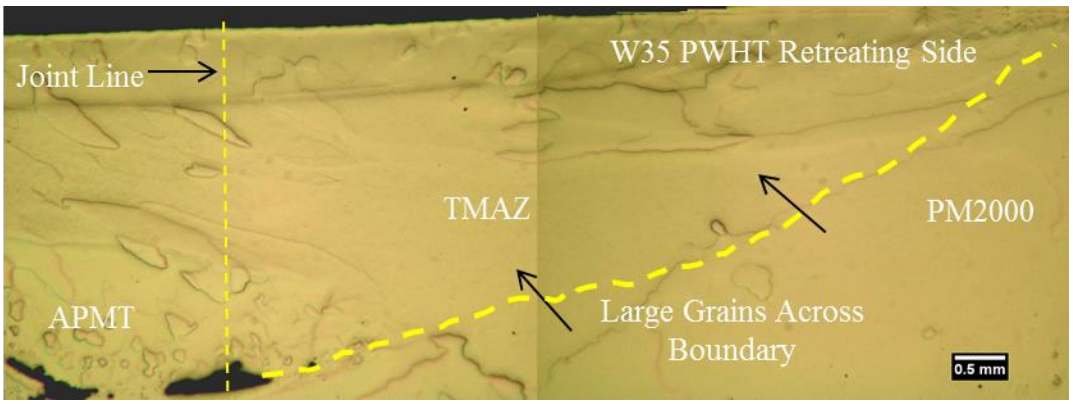

Figure 7.7 *A montage of two DIC images of the retreating side of W35 showing large grains that have formed across the parent region and the TMAZ (polished to colloidal silica finish).*

The retreating side of W35 is presented in Figure 7.7. A montage of DIC images clearly shows large grains that have formed across the TMAZ boundary with the parent region. Two large voids are also visible near the base of the weld. Unlike the advancing side there is no clear boundary between the TMAZ and the parent region.

7.4 Hardness Profiles

Vickers hardness tests were performed on W35 with and without PWHT. The results are presented in Figure 7.8. As expected the results are the combination of hardness of the two different regions. With the as welded sample the advancing side hardness is similar to the hardness profile of APMT until the PM2000 is reached in the TMAZ when an immediate increase in hardness is apparent. Similarly in the PWHT sample, the hardness values depend on whether the indenter is sampling the APMT region or the PM2000 region, although after the application of PWHT there is little difference in the hardness values.

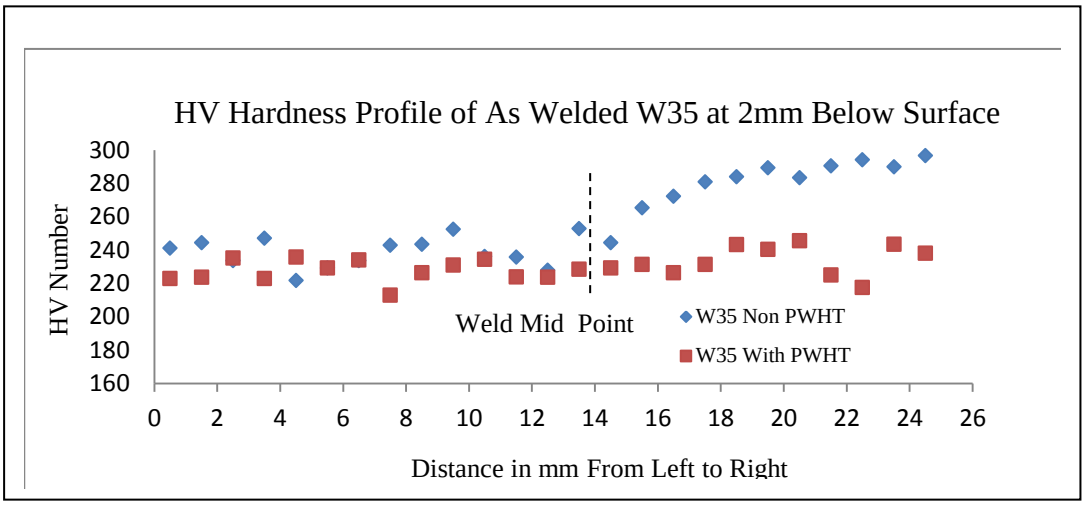

Figure 7.8 *Vickers Hardness profile of W35 with and without PWHT.*

7.5 Scanning Electron Microscopy

Samples were polished to colloidal silica and examined in the SEM using channelling contrast imaging.

W35 as Welded Condition

The channelling contrast images in Figures 7.9 and 7.10 show the boundary at the advancing side of W35. The parent APMT boundary with the TMAZ is as expected and as seen in Chapter 6 with the FSW of APMT. The TMAZ grain structure is simply the dynamically recrystallised grain structure of the APMT and PM2000 in their respective regions. The PM2000 region of the TMAZ extends nearly up to the edge of the boundary at the advancing side. There is a clear difference in the grain size in the TMAZ in the two regions with the APMT grain size of about 10 microns and the PM2000 region with grains of several microns in size. This difference in grain size is probably due to the difference in the particle distributions which pin down grain boundaries and modify the nucleation events that lead to recrystallisation. The channelling contrast images in Figure 7.8a and b show the

region at higher magnification. In certain areas the boundary is well defined in other areas a jagged boundary is observed.

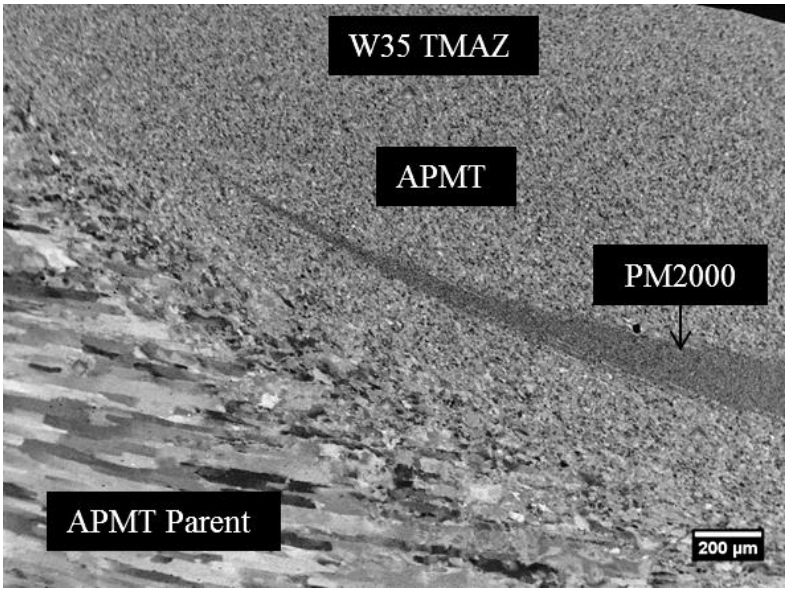

Figure 7.9 *Channelling contrast image of the TMAZ of W35 showing the PM2000 region at the advancing side of the weld.*

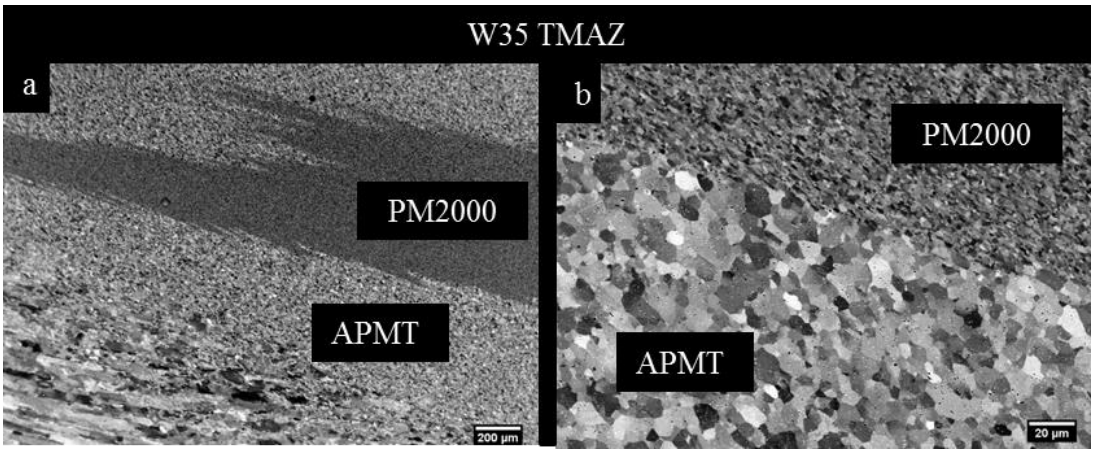

Figure 7.10 *Channelling contrast images of the TMAZ in W35 showing the PM2000 region at the advancing side of the weld, a) low magnification image and b) higher magnification image.*

The FSW process is a rapid one where the rotation of the tool together with the motion along the weld line does not allow enough mixing to take place. This creates an interesting area at the advancing side of the weld where clear regions of each of the alloys can be observed.

W35 Post Weld Heat Treated Condition

The channelling contrast image of W35 with PWHT in Figure 7.11 shows a large grain recrystallised structure of the TMAZ.

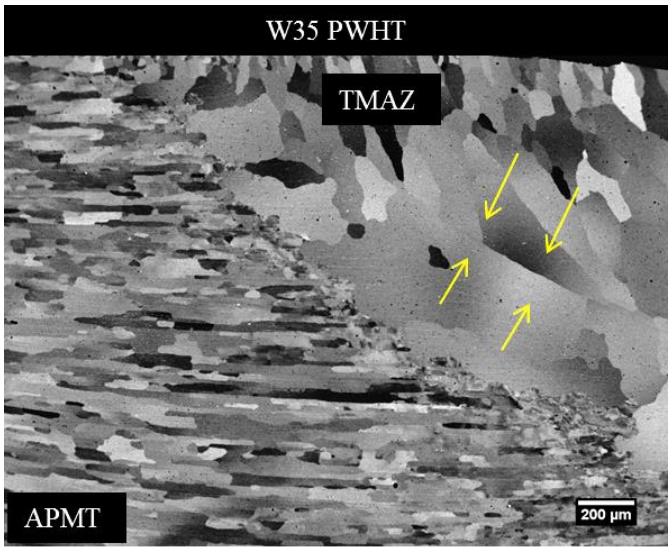

Figure 7.11 *Channelling contrast image of the advancing side of W35 with PWHT showing the recrystallised TMAZ. There is a grain boundary at the PM2000 region indicated by arrows.*

In Chapter 5, the FSW of the as extruded PM2000, W34 with PWHT, a region in the TMAZ appears to have had a large number of nucleation sites for recrystallisation and the grain structure was the same as that of the as welded W34 TMAZ grain structure, i.e. the dynamically recrystallised grain structure. With W35 the main difference is that the whole of the TMAZ has undergone recrystallisation to form a large grain size even though some corresponding regions with the as extruded PM2000 have not done so in W34.

Another feature of interest observed in the image is the grain boundary that is indicated by the arrows in the PM2000 region. This appears to be two recrystallisation fronts either side of this boundary which then meet to form this grain boundary at the APMT/PM2000/APMT junction.

The channelling contrast image in Figure 7.12 shows the base of the weld and once again voids could be seen. These are located near the bottom of the weld and as seen with W34 the grains are smaller just below the voids compared to the grains above the voids. A large recrystallised grain (arrowed) of PM2000 can be seen just below the right hand side void. This is the original join line between APMT and PM2000.

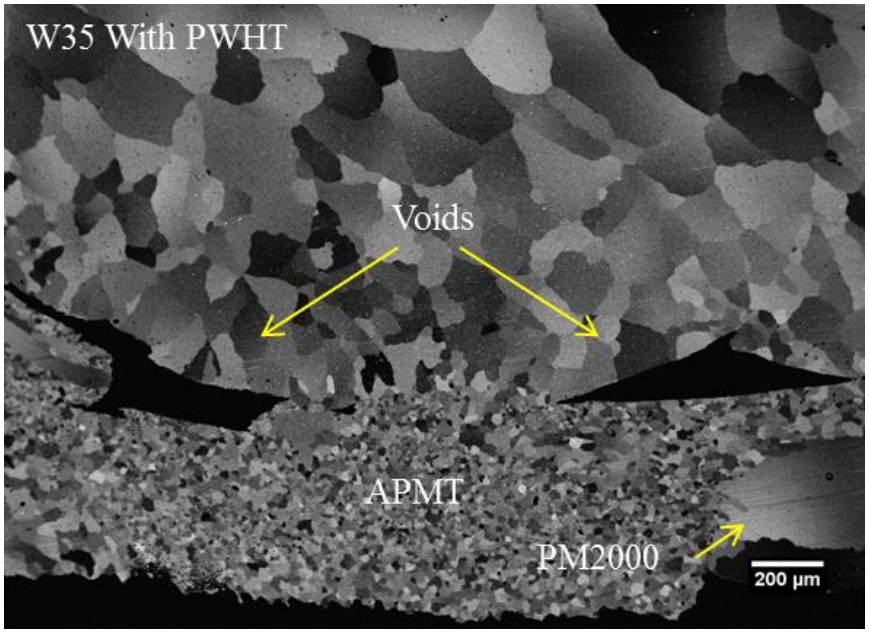

Figure 7.12 *Channelling contrast image of the base of W35 showing the voids and the surrounding grain structure.*

In order to determine the progress of the recrystallisation front, an as-welded sample was annealed at 1380°C for 10 minutes instead of the usual 1 hour. It was hoped that this would give an indication of the progress of the grain growth in the TMAZ region of interest.

The channelling contrast image in Figure 7.13 shows the cross section of W35 with PWHT for 10 minutes only. This image confirms that the APMT in the TMAZ

recrystallises first, forming two recrystallisation fronts either side of the PM2000 region in the TMAZ.

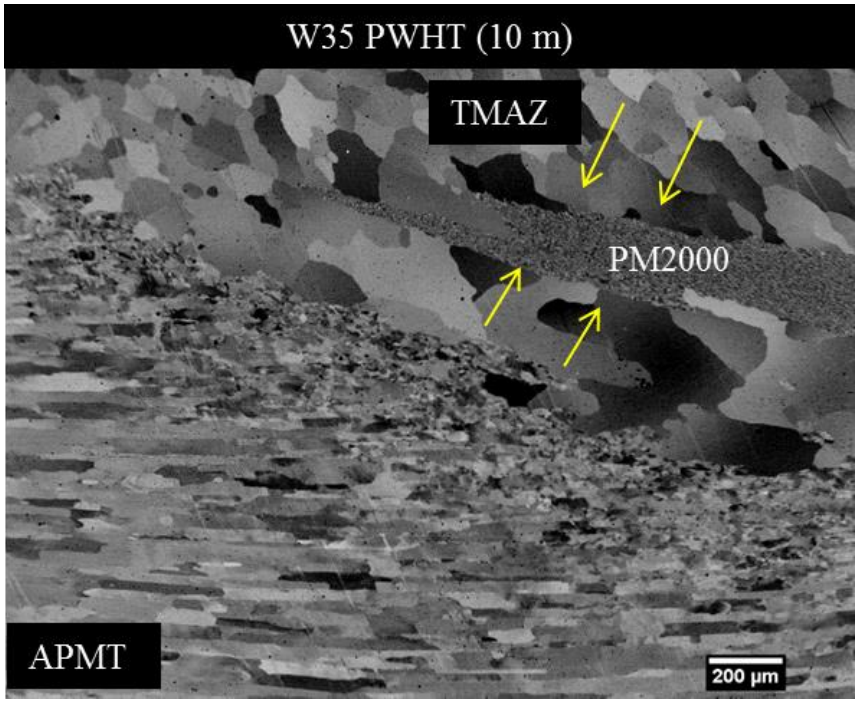

Figure 7.13 *Channelling contrast image of W35 with PWHT (10m). The APMT in the TMAZ undergoes secondary recrystallisation first with either side of the PM2000 region forming a recrystallisation front as shown by the arrows.*

EDX Mapping of the APMT/PM2000/APMT region of interest in the TMAZ was undertaken for the 3 different samples in order to investigate any diffusion due to the differences in the composition between APMT and PM2000. The samples were as follows, W35 as-welded, W35 with 10 minutes of PWHT and the W35 1 hour PWHT. The results are presented in Figure 7.14.

The results were as expected for the Fe, Cr, and Mo as there is clear evidence that diffusion takes place after 10 minutes of PWHT and more so after the full hour of PWHT and at different rates for each of the elements mentioned. Fe diffuses out of the PM2000 region into the APMT while Cr and Mo diffuse out of the APMT into the PM2000.What was unexpected was the EDX map for Ti. In this case, the map suggests that the Ti is diffusing away from the central PM2000 region as might be

expected but as it approaches the prior APMT/PM2000 boundaries either side of the region of interest there seems to be an increase in the Ti signal at the boundary.

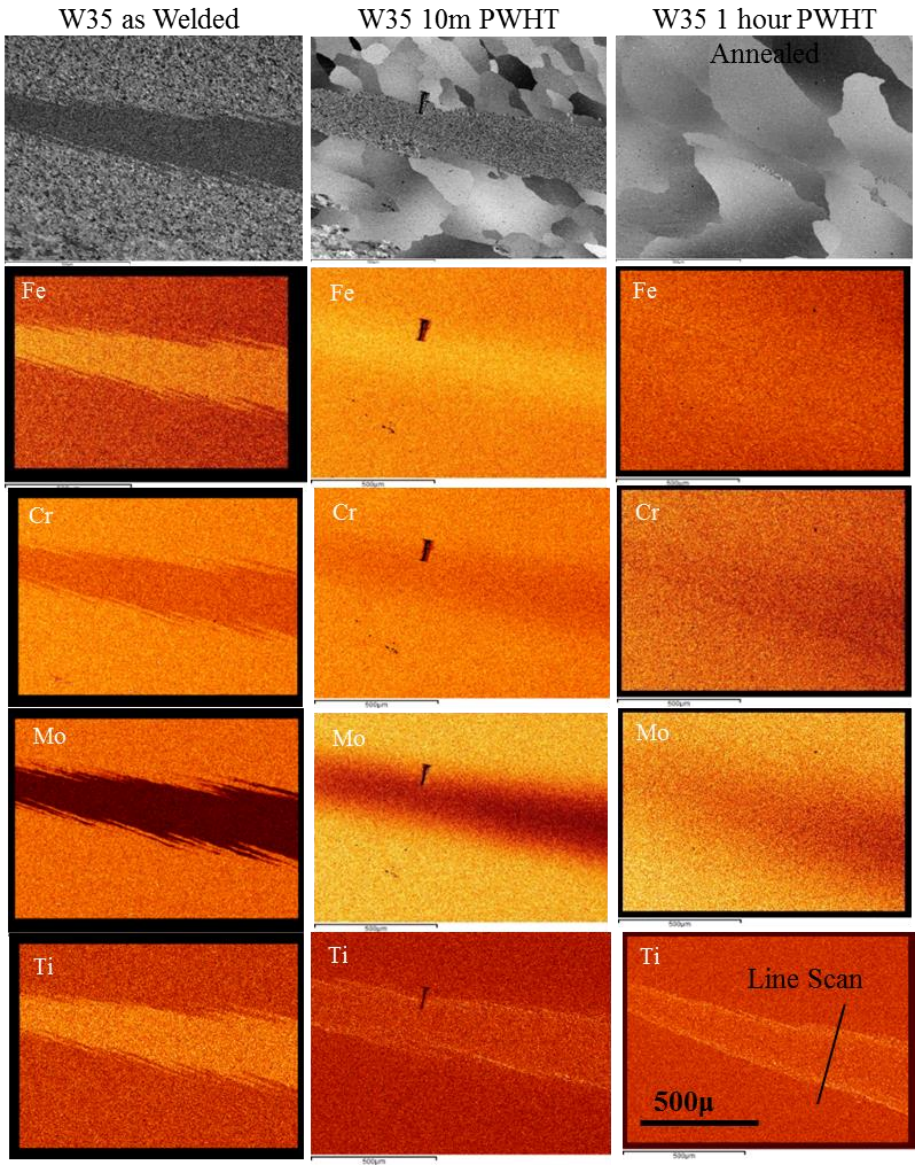

Figure 7.14 *EDX mapping at the APMT /PM2000 /APMT region of interest for the W35 as-welded, W35 10m PWHT and the W35 1 hour PWHT. A line scan of the Ti map was taken at the indicated position of the W35with 1 hour PWHT*

A line scan of the Ti map of W35 with 1 hour PWHT is presented in Figure 7.15. The Ti Kα1 signal peaks at each of the prior boundaries as indicated in the line scan,

even though the channelling contrast image shows that the grains have secondary recrystallised.

The Ti is concentrated in particles at this region. The boundary region between APMT and PM2000 was further examined in the SEM in backscatter mode in channelling contrast imaging in Figure 7.16.

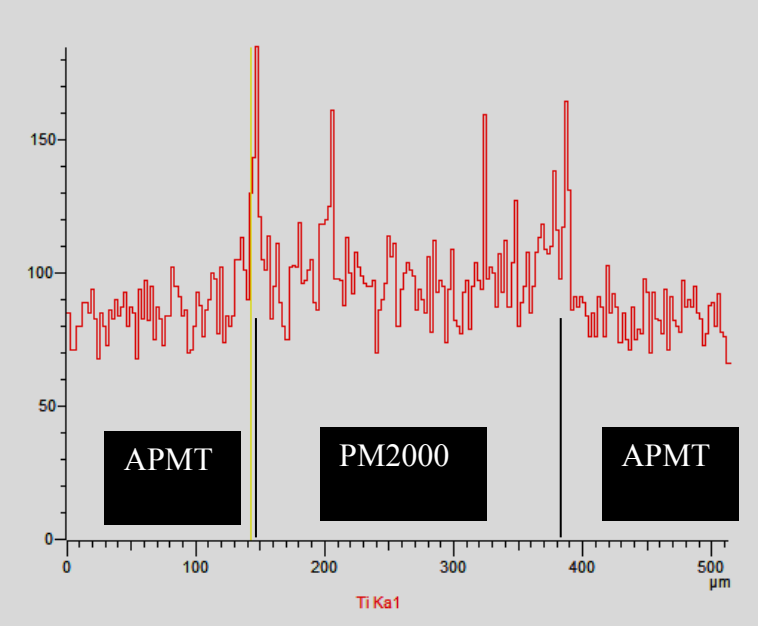

Figure 7.15 *Line scan of Ti Kα1signal across the APMT/PM2000/APMT boundary as indicated by the line in the Ti map in Figure7.13. The signal peaks at the two boundary edges.*

There is a clear difference in the particles within the boundary regions. In the APMT region most of the particles observed were light in contrast (yellow circles) and in the PM2000 region the particles were mostly of a dark contrast (red circles). EDX analysis of a typical particle in each of the two regions revealed a difference in the composition of the particles. In APMT, as previously mentioned EDX of some of the smaller particles indicate the presence of Zr, and Hf. In the PM2000 side of the boundary a high proportion of the particles indicated the presence of Ti. The spectrum peak indicating the presence of N suggests the formation of TiN or even the formation Ti (CN). However care is needed since there is a peak overlap between

N and Ti. For Ti Lα = 0.4522keV and N K α = 0.3924keV, which makes it difficult to distinguish between the two elements.

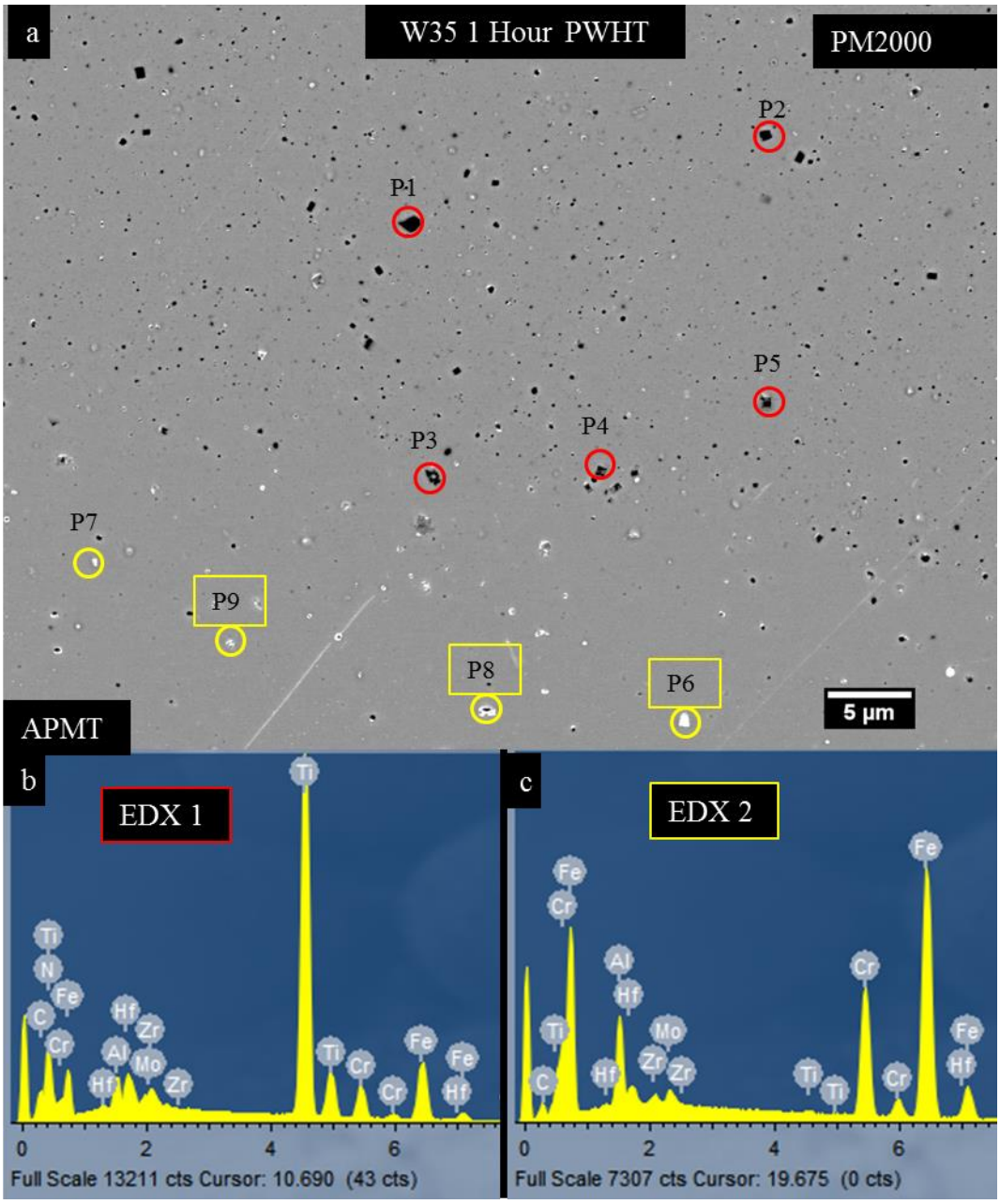

Figure 7.16 *a) Back Scattered Channelling contrast image of the boundary region of interest between APMT and PM2000in W35 with PWHT for 1 hour, b) EDX spectrum of a typical particle (red circles) and at the PM2000 side of the boundary and c) EDX spectrum of a typical particle (yellow circles) in the APMT side of the boundary*

The main point of the EDX analysis is that it suggests that some of the Ti present in the matrix in the PM2000 region between the two APMT regions has diffused away from the centre of the PM2000 and has been captured in particles near the boundary with the APMT.

In order to investigate this further, EDX mapping of Ti Kα1 at a higher magnification (shown in Figure 7.17a) was undertaken. The EDX map in Figure 7.17b confirms that indeed the Ti is present in particles in the region. The most likely scenario is that the difference in activity/concentration of carbon and nitrogen between APMT and PM2000 is the driving force for diffusion of both elements from APMT towards the PM2000 region. However given the strong affinity of Ti for nitrogen and carbon a combination of TiC or TiN or Ti (CN) particles are formed along the prior boundary.

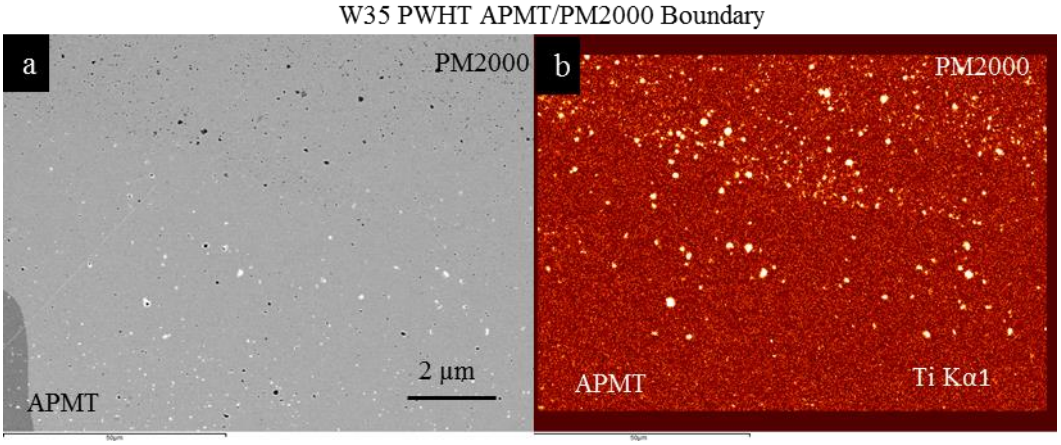

Figure 7.17 *a) Channelling contrast image of a boundary region between APMT and PM2000 with b) The corresponding EDX map for Ti Kα signal indicating the presence of Ti in particles.*

7.6 TEM Analysis of W35 with 10 Minutes PWHT

The TEM analysis was focused on the 10 minute PWHT sample as there appeared to be partial consolidation of some of the particles and there were some regions with the formation of carbides, nitrides and/or carbonitrides at the APMT/PM2000 boundary that were analysed further.

FIB samples were prepared for the boundary region with limited success since the samples were not particularly clean with considerable redesposition. Hence a TEM sample was prepared from the boundary of the weld. A thinned cross section of W35 10 minute PWHT was slightly etched to reveal the thin APMT/PM2000 region. From this region a 3mm disc was then punched out and polished away to remove any traces of the etchant but also to thin discs before electropolishing. Fortunately the electro polish process had etched away just at the right area i.e. the boundary region between APMT and PM2000 as can be seen by the optical image in Figure 7.18

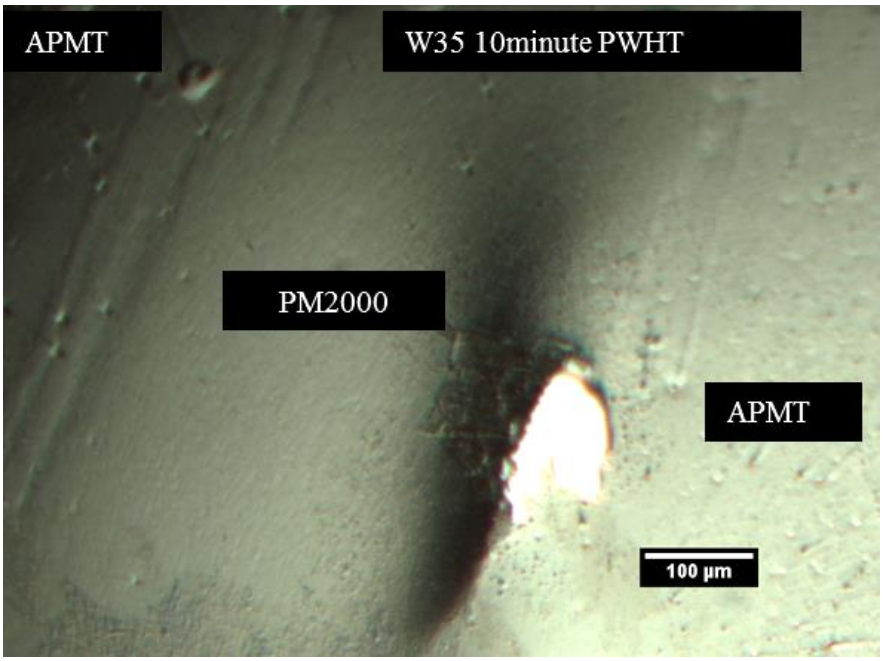

Figure 7.18 *Optical image of the 3mm TEM sample that was electro polished. Image shows the electron transparent region at the boundary between APMT and PM2000.*

In Chapter 5 the agglomeration of particles in the TMAZ due to the FSW process was discussed as most of the particles analysed in the as extruded PM2000 with PWHT were singular with well-defined boundaries. As this TEM sample was subjected to PWHT for only 10 minutes, there was the possibility that this was not enough time to consolidate at least some of the particles. The HRTEM image in Figure 7.19 shows one such particle. Unfortunately the particle could not be identified as the EDX analysis was inconclusive but one can observe that the edges

of the particle are not as well formed. It seems that the particle was not in equilibrium yet especially around the edge of the particle.

Another HRTEM image presented in Figure 7.20 is of two nearby particles that seem to be in the process of consolidation. The two particles clearly have different d spacing and orientation of lattice arrangement which suggests that they were clearly two separate particles but due to the FSW and the partial application of PWHT have started to consolidate.

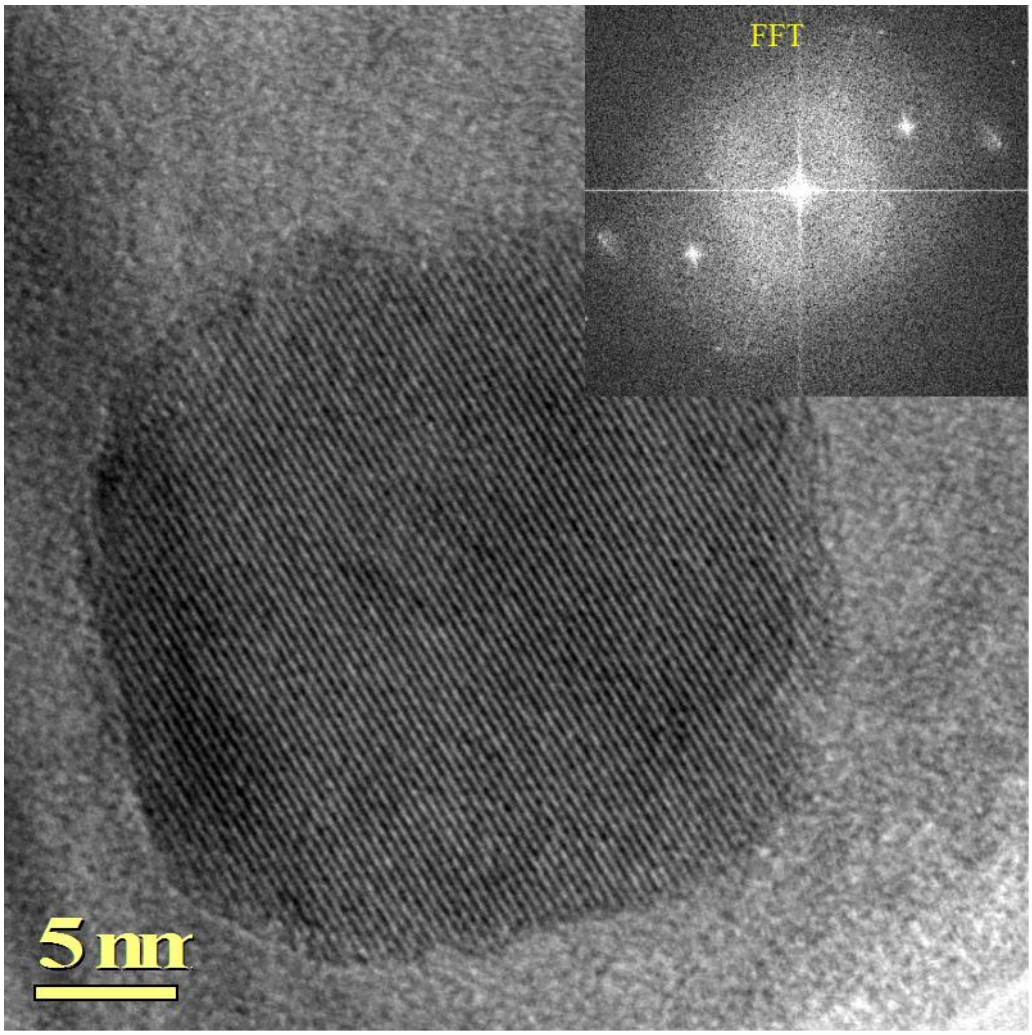

Figure 7.19 *Bright field TEM image of W35 with 10 minutes PWHT showing a particle that is not fully consolidated. FFT of the image shows a variation in d spacing and orientation on some of the diffraction spots*

Necking between the particles is clearly visible. The EDX and quantitative analysis suggest that P2 is a YAG type particle with a Y to Al ratio of 37:63. P1 was too small for EDX analysis. The FFT of the particles did not reveal more than one set of diffraction spots which makes a positive identification difficult.

As mentioned in the SEM analysis of W35 with PWHT, EDX mapping has indicated that Ti diffuses from PM2000 towards the APMT at the boundary between the two alloys.

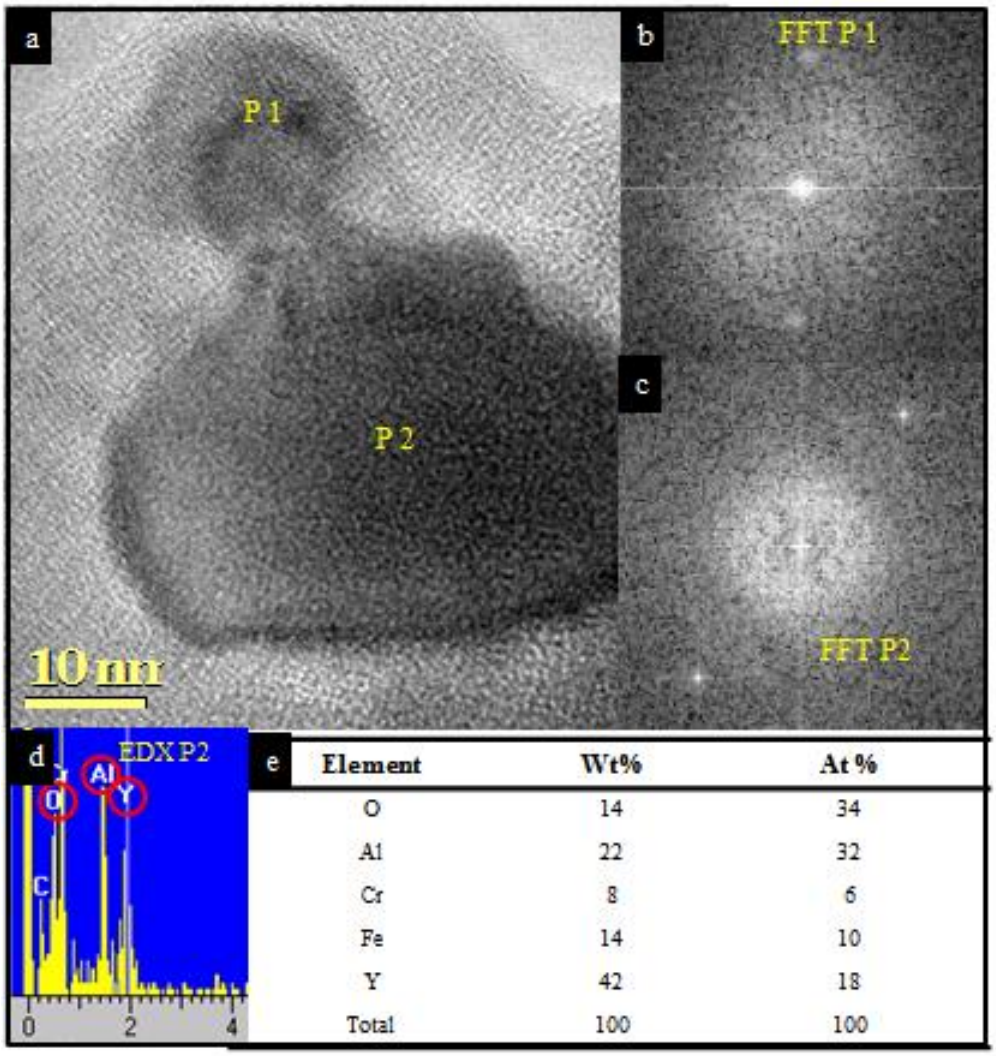

e

Element	Wt%	At %
O	14	34
Al	22	32
Cr	8	6
Fe	14	10
Y	42	18
Total	100	100

Figure 7.20 *a) bright field TEM image from W35 with 10m PWHT showing two particles P1 and P2 in the process of consolidation, b) FFT of P1, c) FFT of P2, d) EDX spectrum of P2 and e) quantification data of the EDX on P2.*

One such particle is presented in the bright field TEM image in Figure 7.21a and the HRTEM image in Figure 7.21b. Several particles are agglomerated as can be seen but the EDX analysis on the central part of the particle shown in the spectrum analysis and the quantitative analysis in Figures 7.21d and 7.21e indicate the presence of Ti. The FFT of the HRTEM image (Figure 7.21c) only reveals one set of diffraction spots which does not provide enough information to calculate the zone axis of the particle. The diffraction spots reveal a d spacing of 2.49Å which is consistent with the (111) plane of T(CN) although due to the similar d spacing data it could also be a possibility that the particle could in fact be TiN or TiC.

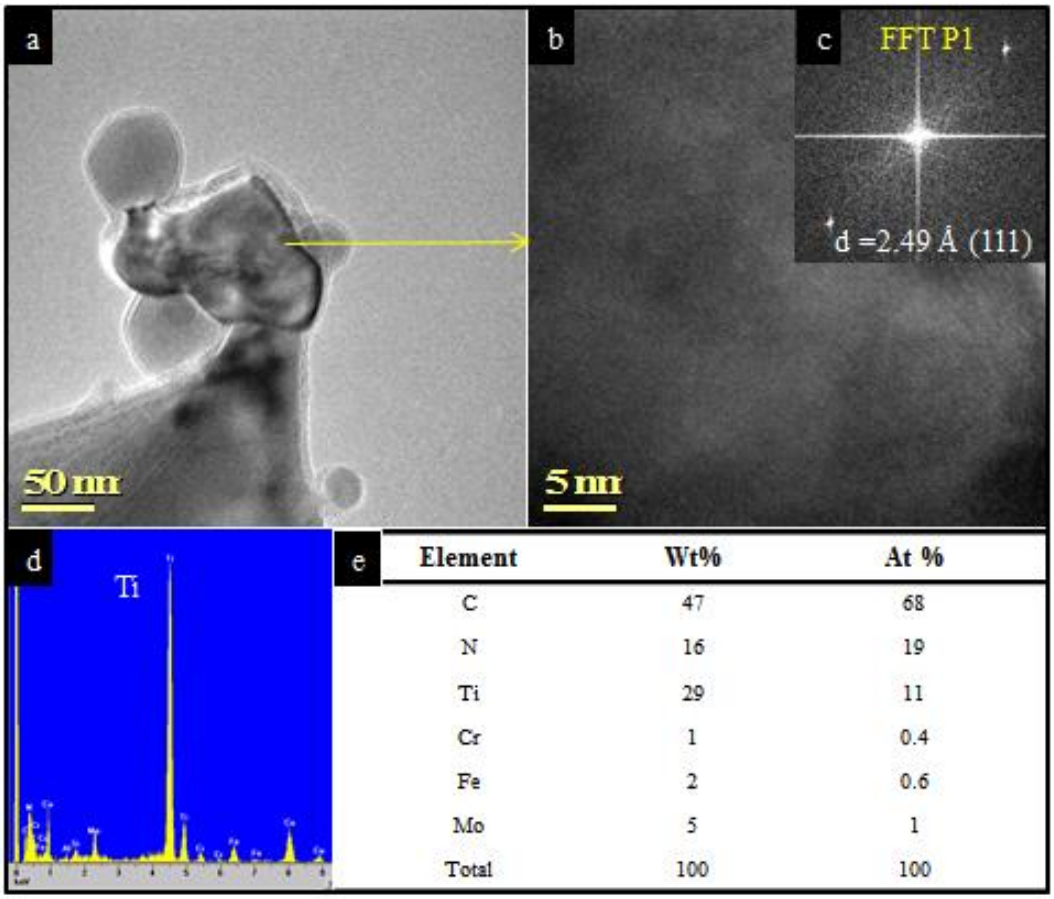

e

Element	Wt%	At %
C	47	68
N	16	19
Ti	29	11
Cr	1	0.4
Fe	2	0.6
Mo	5	1
Total	100	100

***Figure 7.21a**) Bright field TEM image of an agglomerated particle, b) a HRTEM image of the central part of the particle, c) FFT of the HRTEM image with a pair of diffraction spots which correspond to a d spacing of 2.49Å consistent with a TiCN type particle. EDX analysis d) and quantitative data e) confirm the presence of Ti along with C and N.*

In addition to the presence of particles rich in Ti, several particles were observed that were rich in Zr, Ta and Hf. These are compositional elements from APMT. One such cluster of particles is presented in Figure 7.22. The bright field TEM image (Figure 7.22a) shows a cluster of particles named P1, P2 and P3. EDX analysis of P1 (Figure 7.23a) indicates a Ti rich particle with P2 and P3 being Hf, Ta and Zr rich particles as indicated in the EDX spectra in Figure 7.22d and 7.23b. A CBED pattern was obtained for P2 (Figure 7.22b) and it was indexed as a carbide type particle with a possible composition of any combination of Hf, Zr and Ta, which are all strong carbide formers, with a zone axis of [0, 1, $\bar{3}$] although the exact composition is not known. Particles of this type were observed on the APMT side of the boundary.

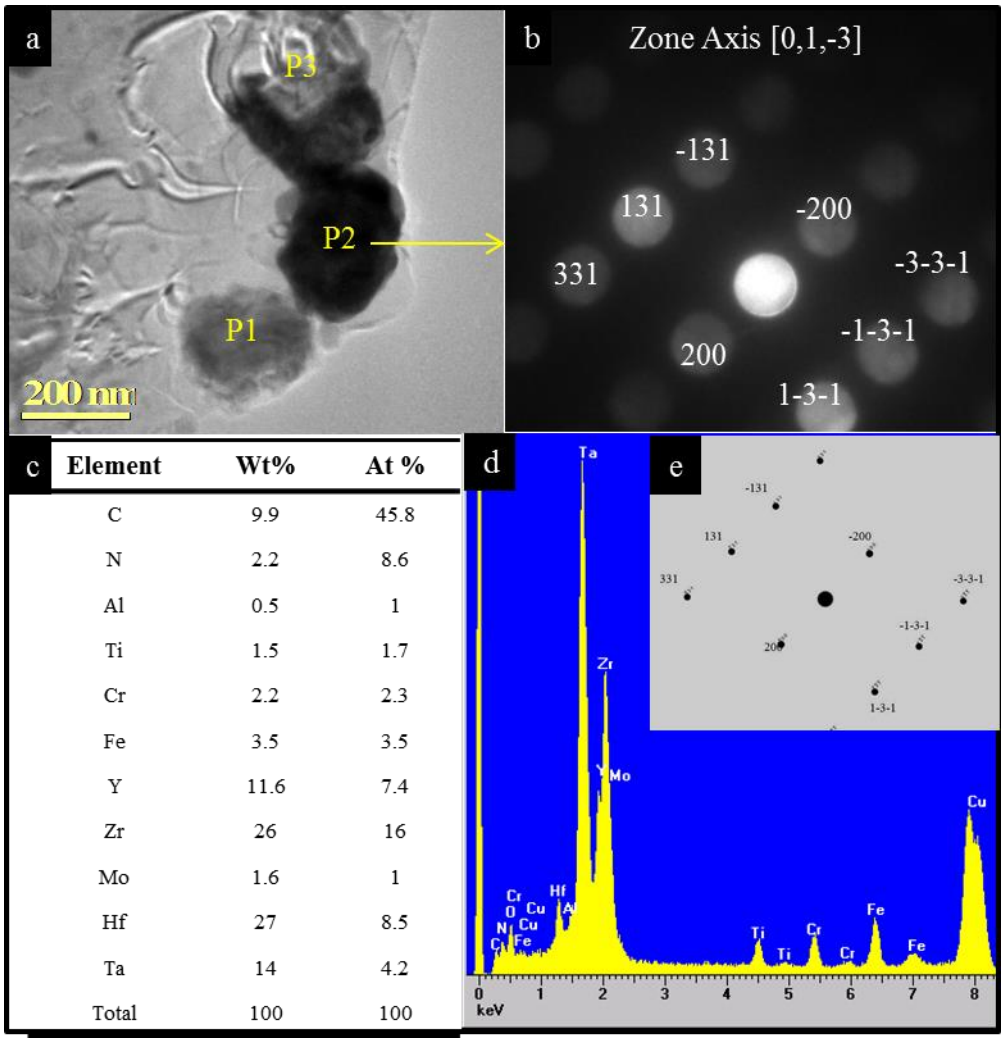

Element	Wt%	At %
C	9.9	45.8
N	2.2	8.6
Al	0.5	1
Ti	1.5	1.7
Cr	2.2	2.3
Fe	3.5	3.5
Y	11.6	7.4
Zr	26	16
Mo	1.6	1
Hf	27	8.5
Ta	14	4.2
Total	100	100

Figure7.22 *a) Bright field TEM image of a cluster of 3 particles marked P1, P2 and P3, b) indexed CBED pattern of P2 with a zone axis of [0,1,-3], c) quantitative analysis of P2 indicating the presence of Hf, Zr, C, and N amongst other elements. and d) EDX spectrum of P2.*

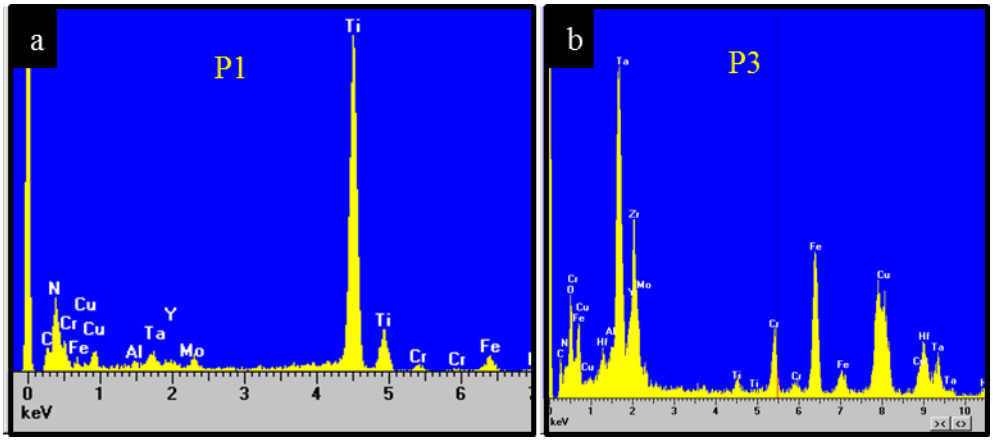

Figure 7.23 *EDX spectra of particles P1 and P3 as indicated in Figure 7.22*

7.7 Recrystallisation of PM2000

The W35 sample with 10 minutes of PWHT has been useful in that on the retreating side of the weld, the parent PM2000 has only partially recrystallised giving some clues about the process occurring during recrystallisation.

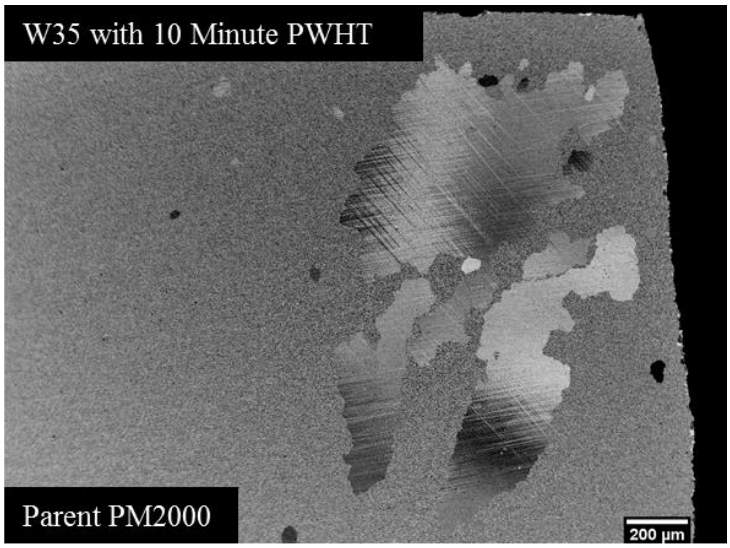

Figure 7.24 *Channelling contrast image of W35 retreating sidePM2000 parent region showing a number of recrystallised grains amongst the sub-micron grain structure.*

In Figure 7.24 a channelling contrast image of the retreating side of the parent PM2000 region is presented. The scale bar indicates a 200 micron scale. Assuming that the fine grain structure of the parent PM2000 is made up of 1micron square grains then the approximate number of fine grains in the image is in the region of 4,000,000 grains. The number of grains that have recrystallised with a large grain size is about 20. This confirms that the frequency of grains with the potential to grow and consume the rest of the grains is 1: 500,000. This is broadly in agreement with literature where the number of grains with potential to grow was estimated at 1:1,000,000 [30].

7.8 Summary and Conclusions

The dissimilar metal FSW between APMT and PM2000 was examined using optical microscopy, hardness tests, electron microscopy and EDX mapping.

7.8.1 General Observations

The surface quality of W35 was poor in comparison with W34 and the APMT welds W29, W30 and W31. The transverse speed used was 140mm/m which was the same speed chosen for the W34 weld in Chapter 5 and for W31 weld in Chapter 6. Both these welds were of good quality. The difference in the down force could be the reason for the difference in surface quality. With W34 the downforce of 40kN was used and for W31 a downforce of 25kN was used. With W35 the downforce used was nearly 25kN. The downforce used might not have been enough to obtain a good surface quality. Once again voids were observed in W35 as with previous welds. Despite the presence of voids, a good join was achieved.

7.8.2 Parent Material

The advancing side parent APMT displayed the elongated microstructure as the weld line was along the transverse direction. With the application of PWHT large grains were observed. Smaller grains were observed from the APMT advancing side into

the TMAZ as the boundary was well defined. The retreating side parent PM2000 on the application of PWHT has undergone full recrystallisation to form a large grain size recrystallisation as seen with W34 weld with the parent material grains forming across the parent material and the TMAZ boundary which is the desired outcome.

7.8.3 TMAZ

The TMAZ of the as welded W35 has undergone dynamic recrystallisation with the grain size that corresponded to the relevant alloy. Regions of PM2000 with fine dynamically recrystallised grains of several microns contrasted with the surrounding APMT regions with a dynamically recrystallised grain size of 10 to 15 microns in size. The TMAZ has also undergone recrystallisation despite the fact that in the W34 weld regions of PM2000 in the TMAZ had not. Large grains were observed right across the APMT/PM2000 regions in the TMAZ. This was a desirable result as the large grain structure improves the high temperature creep resistance.

7.8.4 APMT/PM2000 Boundary in the TMAZ

One of the surprising finds of this research was the EDX mapping of the APMT PM2000 boundary in the TMAZ. This had revealed the diffusion across the boundary of several elements due to concentration differences between the two alloys. The exception was Ti. Due to the very low concentration of carbon and nitrogen in PM2000 and the low concentration of Ti in APMT, the application of PWHT had resulted in the diffusion of C and N from APMT towards the PM2000 region and conversely the diffusion of Ti from PM2000 towards the APMT regions of the TMAZ. The EDX mapping had revealed that the Ti was attached to particles at the boundary. Given the high affinity of Ti to N and C, carbides and or nitrides and or carbonitrides were observed at the boundary region of the TMAZ between APMT and PM2000.

7.8.5 Recrystallisation Behaviour of PM2000

The investigation of the W35 with 10 minutes of PWHT has given an insight into the recrystallisation behaviour of PM2000. At the retreating side of the parent PM2000 the submicron microstructure was visible with the notable exception of several very large recrystallised grains. This confirms the process were by a few recrystallisation nucleation sites are involved which then consume all the fine grain microstructure to form the desirable large grain recrystallised microstructure.

7.8.6 Consolidation of the Agglomerated Particles.

Partially consolidated particles were observed in the TMAZ of W35 with the application of 10 minutes of PWHT. The HRTEM image in Figure 7.18 clearly shows the lattice arrangement of a particle but the edges of the particle do not seem to be in equilibrium. Many particles were observed in the course of this study and no other similar particles were observed from other samples examined.

Necking of material from a smaller particle into a larger particle was also observed where the particles were of a different lattice arrangement. This confirms the findings of the W34 welds in Chapter 5 where a high number of agglomerated particles were observed in the TMAZ before the application of PWHT and the mainly single phase particles observed after the application of PWHT.

CHAPTER 8

Discussion

8.1 Introduction

Four different welds made by the solid state joining process FSW were analysed in order to investigate the suitability of FSW as a joining technique for ODS steels.

The four FSW studied were as follows:

1. Chapter 4 BOP FSW of rolled PM2000
2. Chapter 5 Butt FSW of as extruded PM2000
3. Chapter 6 BOP and Butt FSW of APMT
4. Chapter 7 Dissimilar metal Butt FSW between APMT and as extruded PM2000

The main requirements of joining ODS steels is a defect free join with the retention of the dispersion of oxide particles in the weld, that provides the additional creep strength at high temperatures. Alternative welding techniques with a melt pool cause the oxide particles to agglomerate and slag off to the surface.

The welds were investigated using a variety of analytical techniques including optical microscopy, hardness tests, Charpy impact v-notch tests, SEM imaging using both secondary electrons and backscatter electrons, both with EDX analysis; and TEM analysis with HRTEM imaging and EDX analysis.

8.2 Microstructure

As Received Microstructure

The first welds analysed were the BOP welds using 4mm thick PM2000 rolled plates. The grain structure of the rolled PM2000 is of a sub-micron grain size, elongated along the rolling direction. HT had increased the grain size to a flattened cigar shaped 10µm by 30µm by 100µm grain size which gives an aspect ratio of about 3.

As extruded PM2000 had a slightly larger grain size of 1.2micron with again an elongated grain structure along the extrusion direction but with a lower aspect ratio than the as rolled PM2000. Stringers of particles were found to be aligned with the extrusion direction. Recrystallisation that formed large grains had taken place with the application of HT with very large grains of several cm in size. Pockets of small grains did not undergo recrystallisation.

The microstructure of APMT plate is one of high aspect ratio grains of about 50µm by about 500µm elongated along the rolling direction. The grain structure near the top and bottom of the plate is one of equiaxed grains with a size that varies from between 20µm to 50µm down to several microns as you approach the surface. It seems that the rolling process has induced an element of dynamic recrystallisation near the surface of the APMT plate. The application of HT resulted in a recrystallised grain structure with a somewhat larger grain size.

As Welded Microstructure

The FSW process altered the microstructure in the TMAZ from the parent alloy. The process is one of dynamic recrystallisation which is defined as recrystallisation under deformation and elevated temperatures [24]. There is a large amount of plastic strain, with high temperature due to the friction introduced by the FSW process [79]. The TMAZ grain structure is an equiaxed grain structure with a grain size in the region of several microns for PM2000. Similar grain size refinement of the TMAZ has been observed by Dawson et al. [101] with the FSW of PM2000 and by Baker et al. [121] and Brewer [110], with the FSW of MA956 which is a similar alloy to PM2000.

The microstructure of the APMT TMAZ has altered as well. Starting from a large elongated grain structure, the TMAZ was refined to an equiaxed grain size of about 10 µm. To date no work has been published with regards to the FSW of APMT. The larger grain structure of the TMAZ of APMT can be attributed to the low particle number density of APMT which is in the order of 10^{18} particles per m^3 [118] compared to the number density of particles of PM2000 which is in the order of 10^{21} particles per m^3 [122]. That equates to 3 orders of magnitude difference between the two alloys. Particles pin down grain boundaries which limit the grain size.[123].

With PWHT Microstructure

The TMAZ of the BOP 7, the FSW of rolled PM2000 with PWHT in Chapter 4 has undergone recrystallisation to form a large grain size but the parent region has failed to do so. In Chapter 5, the parent material of the FSW of as extruded PM2000, W34 with PWHT has undergone recrystallisation from limited nucleation sites producing a large grain size along with most of the TMAZ apart from a region across the middle of the TMAZ. A large recrystallised grain structure in the TMAZ of PM2000 is reported in Dawson et al. [101]

A small recrystallised grain size in the TMAZ in AMPT BOP FSW, W26 and W27 in Chapter 6 was observed which was linked to the lower heat input of the FSW process. With the APMT butt FSW W29, W30 and W31, all the TMAZ regions secondary recrystallised to form a large grain size as expected but the parent regions in the AMPT did not. A small recrystallised grain structure in the TMAZ, after the application of PWHT is reported in Chen et al. [115] in PM2000 but no details were available with regards to the welding parameters.

The dissimilar APMT/PM2000 butt FSW, W35 was interesting because all of the TMAZ regions recrystallised with a large grain size, even the region of PM2000 at the advancing side that, in the equivalent PM2000 as extruded FSW W34, did not. The 10 minute PWHT of W35 has revealed that APMT recrystallises first in the TMAZ. The same amount of deformation was introduced by the FSW process but PM2000 did not form a large grain structure. The pinning effect of the finer particle distribution and the smaller TMAZ grain structure of PM2000 are obstacles to the driving force for secondary recrystallisation [24] and that is why these alloys are very unlikely ever to undergo secondary recrystallisation. Only a few studies have been reported on dissimilar metal FSW with at least one of the components of the weld being ODS steel [124-127].

Another interesting region is the HAZ which is an area next to the TMAZ which has not been mechanically stirred. In the BOP welds of the as rolled PM2000, an elongated grain structure was observed in the HAZ which was decreasing in size as you moved further away from the TMAZ. The rolling process increases the stored energy in the form of additional dislocations and grain boundaries in the plate. Due

to the proximity of the region to the TMAZ a temperature increase was experienced which resulted in partial recovery in the HAZ and after the application of PWHT recrystallisation of the immediate grain structure next to the TMAZ [24]. It is easily observed that the grain size of the HAZ is dependent on the distance away from the TMAZ to a point that no difference can be observed. The elongated grain structure did not alter. The changed microstructure of the HAZ was only observed with the as rolled PM2000 BOP welds.

8.3 Hardness Profiles

Hardness tests such as Vickers Hardness is a measure of the resistance of a material to plastic deformation and it is a measure of the tensile strength of a material [25]. The as-rolled PM2000 had the highest average hardness value of 380HV. The hardness value for the as-extruded PM2000 was 310HVand the as-received APMT hardness value was in the region of 250HV. Therefore when as extruded PM2000 is deformed by the rolling process the increase in dislocation density results in an increase in the HV number of the material compared to the as extruded PM2000. The rolling process work hardened the as-extruded PM2000 increasing the tensile strength. The increase in the tensile strength is directly linked to the amount of work hardening which was performed.

The hardness value of the as extruded PM2000 was higher than the as received APMT plate. The particle distribution contribution to the tensile strength of PM2000 is much higher than of APMT and the smaller grain size of PM2000 compared to APMT means that, due to the Hall-Petch relationship, results in a higher hardness number for the as-extruded PM2000.

8.4 Contributions to Hardness of Parent Material

There are several contributions to the tensile and yield strength of any alloy composition as mentioned in the literature review in Chapter 2.

1. Solution Strengthening

2. Grain Boundary Strengthening
3. Orowan Strengthening
4. Dislocation Strengthening (Strain Hardening)

Kang et al. [128] investigated the contributions to the yield strength from the various strengthening mechanisms in MA956, a similar alloy to PM2000. Using some of the parameters in Kang et al. and from the compositions of PM2000 and APMT the various contributions to the yield strength and tensile strength were calculated. In order to equate the yield strength and the tensile strength to the HV hardness number, a correction factor was used, which was taken from the work of Pavlina et al. [129].

Solute Strengthening

The addition of solute atoms creates a misfit in the matrix which hinders dislocation movement. The addition of Cr has a strengthening contribution of 8.5 MPa per %Wt of composition [128, 130]. The strengthening contribution of Ti to the matrix is in fact negative because it combines with interstitial atoms such as C and N by forming carbides, which reduces the tensile strength. The effect of Ti is to reduce the tensile strength by 107MPa per Wt%. Al has little effect on the tensile strength of the matrix [128]. If the minor additions are ignored, by knowing the composition of the alloys the contribution to solute strengthening was calculated and listed in Table 8.1.

Grain Boundary Strengthening

The Hall Petch relationship describes the grain boundaries contribution, which depends on the grain size, to the tensile strength. Grain boundaries are obstacles to dislocation movement. The smaller the grain size the bigger the strengthening effect. The contribution to the yield strength from grain boundary energy is given by the Hall-Petch equation:

$$\sigma_{GB} = k{d_G}^{-1/2} \qquad \textit{(Equation 8.1)}$$

where k is the Hall-Petch constant and d_G is the average grain diameter. For ferritic steels the value of 15.9MPa/mm^2 for the constant k was used [130]. Grain size of 1 μm was used for as rolled PM2000 and a grain diameter of 1.2 μm was used and for the as extruded PM2000. For the APMT due to the elongated grain structure a grain

size of 50µm was used. This was calculated from the cube root of the volume of a grain with dimensions of 35µm x 35µm x 100µm.

Orowan Particle Strengthening

The pinning effect of second phase particles on dislocations increases the yield strength of the alloy. The equation used, is from the work of Brown et al. [131], and given by the equation:

$$\sigma_{oro} = M \frac{0.4}{\pi} \frac{Gb}{\sqrt{1-v}} \frac{\ln(\frac{2r}{b})}{\lambda_p} \qquad \textit{(Equation 8.2)}$$

Where M is the Taylor factor which for a bcc structure is taken as 2.7 [132] G is the shear modulus which was taken from the work of Wasilskowska et al. [122] and the figure of 60 GPa was used, b is the Burgers vector and v is Poisson's ratio. The inter-particle spacing λ_p was calculated using the particle number density N_v of PM2000 from [122], and of APMT [118] using the equation for the Wigner–Seitz radius [122]:

$$\lambda_p = 2 \times (\frac{3}{4\pi N_v})^{1/3} \qquad \textit{(Equation 8.3)}$$

For PM2000 the mean interparticle distance using Equation 8.3 was calculated to be 126nm. This was in good agreement with the work of Wasilkowska et al. [122] where the interparticle distance was calculated to be 137nm. The interparticle spacing for APMT was calculated to be 550nm. Although there is no figure available from literature, the bright field TEM images of the APMT matrix in the work of Jönsson et al. [118] seem to be in good agreement with the calculations.

Strain Hardening and Cold Working

The tensile strength of metals can be increased by strain hardening. This is a mechanism where dislocations are introduced by deformation [25]. It is also termed cold working because the temperature of deformation is below the absolute melting temperature of the metal. The amount of deformation is sometimes referred to as %CW which refers to the amount or cross sectional area reduction after the deformation.

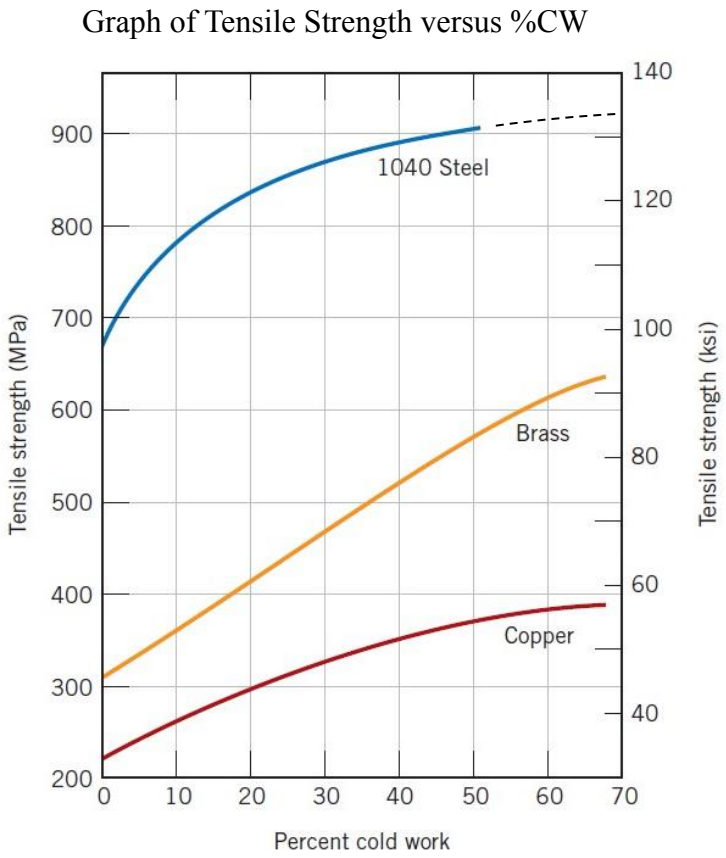

Figure 8.1 *Graph of tensile strength versus % cold work with the dashed line extrapolating results to 70% CW for the 1040 Steel [25].*

In a rolling setup the width of the cross section is kept the same and only the thickness of a plate is reduced. Figure 8.1 shows the increase in the tensile strength with the amount of cold working. Typical cold worked steels are reduced by 50% but usually the % CW is specified in data sheets.

The as rolled PM2000 was cut from the as extruded plates and then cold rolled to a total reduction of 67%. The increase in the tensile strength used for the calculations was 250MPa. This was estimated by extrapolating the %CW from the graph in Figure 8.1

The strength of the low carbon steel was used as the strength of the base metal without any of the strengthening mechanisms. The data was taken from Ref [133]

data book for the tensile strength of low carbon low alloy steel annealed at 925°C. This steel is relatively soft as there are no strengthening mechanisms in place to increase tensile strength.

The HV numbers are for illustration purposes only as they cannot be determined accurately just by tensile or yield strength data but it serves as an illustration as to the various processes in manufacture of alloys and their effect on the material properties of the alloy.

Table 8.1 *Contributions to HV hardness from the different strengthening mechanisms.*

Contributions to Yield Strength	PM2000 As Rolled	PM2000 As Extruded	APMT
Solute Strengthening MPa	107	107	185
Grain Size (Hall-Petch) MPa	16	7	15
Orowan Particle Strengthening MPa	214	214	65
Total contribution to Yield Strength MPa	337	328	265
YS to HV conversion HV = (YS+90.7)/2.876	149	146	124
Contributions to Tensile Strength			
60% CW Strain Hardening MPa	250	0	0
Strength of Low carbon Steel Ref [113] MPa	295	295	295
Total contribution to Tensile Strength	545	295	295
TS to HV Conversion HV = (TS+99.8)/2.876	224	137	137
Total HV Calculated	373	283	261
Actual HV	380	310	250

The actual HV numbers are roughly in agreement with the calculated numbers for as rolled PM2000, the as extruded PM2000 and for the APMT. Whereas the thermomechanical history of the PM2000 alloys was well documented, with the APMT plate vague details were available. The latter stages of the process were hot processing and cold processing. Any cold work reduction by rolling and any

subsequent heat treatment would have an effect on the tensile strength and therefore the HV number.

8.5 Hardness of the TMAZ

The HV value in the TMAZ of the as rolled PM2000 has reduced from about 350Hv just as you enter the TMAZ on the advancing side and it gradually recovered as you moved from the advancing side to the retreating side of the TMAZ. This anisotropy in the hardness is in agreement with both Dawson et al. [101] and Legendre et al. [99] with their work on FSW of PM2000.

With the as rolled PM2000 a gradual reduction in the hardness number was observed in the HAZ prior to the TMAZ region before the application of PWHT. The hardness was homogenised after the application of PWHT in both the as rolled PM2000 and the as-extruded PM2000

Mathon et al. [48] studied the residual stresses across a lap FSW of PM2000 and found that there is a decrease in the residual stresses just inside the TMAZ on the advancing side of the weld and again at the retreating in a characteristic M shape graph as illustrated in the conclusions of Chapter 5. Although the hardness profile does not follow the same characteristic M line, it does show a sharp drop just on the inside of the TMAZ at the advancing side.

The hardness profile of the as extruded PM2000 follows the same outline as the as rolled PM2000 but with a lower hardness number scale. With both PM2000 welds there is a small but measureable difference in the hardness number between the 3 depths of measurements taken suggesting that there is a variation of hardness with depth of the TMAZ region of the weld. The higher temperature at the top of the weld along with the higher material shear due to the rotation of the tool compared to the base of the weld means that as the tool moves away there is more time for the stresses to even out. Due to the lower temperature deeper in to the weld, as soon as the tool moves on any stresses in the region have not had as much time to resolve. Noh et al. [100] performed hardness tests on the top middle and bottom of a FSW on

a Fe14Cr4Al ODS alloy and found very similar results with the lower HV numbers at the top of the weld and higher HV number deeper into the weld.

With the APMT FSW the hardness profile was fairly uniform across the TMAZ. Any subsequent PWHT had little or no effect on the hardness. The grain refinement in the TMAZ had little impact on the hardness despite the fact that the parent region had an elongated large grain microstructure to begin with.

8.6 Mechanical Tests

Only very small end sections of weld material was available with the as rolled PM2000 BOP welds so no mechanical testing was possible. With the as extruded PM2000 W34 and the dissimilar metal W35 welds, a section of each weld was retained for future tensile testing to be carried out at Oak Ridge National Laboratory in the USA. Not enough material was available from these two welds to carry out any additional testing such as Charpy v-notch impact testing.

Tensile Testing

A limited amount of mechanical testing was carried out on the as received APMT and APMT FSW W31. Tensile tests at Oak Ridge National Laboratory have shown the FSW process increases the ductility of the TMAZ compared to the parent region with only a small reduction in the tensile strength and the yield strength. No previous work on mechanical testing was available in the literature for comparison for APMT but Wang et al. [112] saw an increase in the ductility with little loss in the tensile strength of FSW of MA754, a nickel based ODS steel. The application of PWHT had decreased the tensile strength from nearly 1GPa to 850MPa. Wang et al study of the FSW of MA 956 [134], an ODS steel similar to PM2000 steel, but with a coarse grain structure has reported an increase of 150MPa in the tensile strength of the TMAZ compared to the as received material. This was attributed to the refinement of the grain structure in the TMAZ

Fractography

Fractographs of the TMAZ of W31 confirmed observations made from the tensile test results that the increase in ductility was evidenced by an increase in the ductile regions seen in the TMAZ region compared to the parent region. Brittle fracture regions were surrounded by larger areas of ductile fracture regions in the TMAZ. This is in agreement with Baker et al. [121] who performed tensile tests on base metal MA956 and on FSW TMAZ of MA956. An increase in ductile fracture regions were observed in the TMAZ compared to the brittle fracture regions of the base metal at room temperature.

Fractographs of W31 have also revealed the presence of cracks that have originated from the voids that were present in the TMAZ.

8.7 Recrystallisation Behaviour

A large grain structure is desirable in high temperature applications to maximise creep resistance. A set of conditions have to be satisfied in order to minimise nucleation sites that results in a large grain structure. As discussed in the literature review in Chapter 2, Sections 2.4 and 2.5, the driving force for recrystallisation is the stored energy in the form of dislocations and the driving force for grain growth is the reduction of the grain boundary energy The limiting grain size is reached when the pining force of the particle distribution is compatible with the driving force for recrystallisation. [24].

Parent Material

The recrystallisation behaviour of the parent regions of the welds depended on the processing route of the material. Both as rolled PM2000 and APMT parent regions have recrystallised with a fine grain structure after the application of PWHT. The as extruded PM2000 has recrystallised with a much larger grain structure.

In a deformed metal that has been cold rolled, both the stored energy due to the increase in dislocation density and the grain boundary energy due to the formation of additional grain boundaries to accommodate the deformation. The increase in the

deformation also increases nucleation sites for recrystallisation thereby limiting the size of the recrystallised grains. These sites are high angle orientated structures within grains such as deformation bands [24]. The application of PWHT has resulted in recrystallisation that has caused some increase in grain size in the parent material in both the as rolled PM2000 and the APMT. The as extruded PM2000 parent material has undergone recrystallisation with a large grain structure. The extrusion process results in a less deformed structure than cold rolling. Nucleation sites for recrystallisation are reduced, which results in a large recrystallised grain structure.

Dawson et al. [101] and Chen et al. [115] both reported recrystallisation with grain growth of the parent PM2000. In both cases the parent material had the rolled microstructure. There are no reports of the parent regions with a small grain microstructure that have undergone recrystallisation after the application of PWHT which resulted in the formation of large grains.

TMAZ Regions

The stirring of material by the tool in the FSW process is the source of deformation that provides the driving force for recrystallisation.

As observed in the FSW of APMT in Chapter 6, W26 and W27 had the lower heat input from the FSW process, compared to the rest of the APMT welds. After the application of PWHT, the TMAZ failed to undergo recrystallisation to form a large grain structure. The lower heat input resulted in an increase in deformation due to higher thermal stresses which was due to the lower temperatures reached during the welding process. This resulted in an increase in the nucleation sites. All other welds had successfully recrystallised with a large grain structure in the TMAZ apart from the as extruded W34 FSW in Chapter 5 where a small band of material across the middle of the weld recrystallised forming a fine grain structure. This can be explained in terms of a variation in the internal stresses with regards to the depth of the weld.

A large recrystallised grain structure in the PM2000 TMAZ was reported by Dawson et al. [101]. Chen et al. [85] had reported a fine recrystallised grain structure in the TMAZ of PM2000 with PWHT similar to W26 and W27. The welding parameters

were not available but the finer grain structure could be the result of excessive deformation caused by the friction stir weld process which would increase the number of nucleation sites giving a finer recrystallised grain size.

8.8 Second Phase Particle Distribution

There is a big difference in second phase particle distribution between PM2000 and APMT. In PM2000 the particles consist of mainly Y Al O particles and a number of Al_2O_3 and Y_2O_3 particles. The Y Al O and the Y_2O_3 particles tend to be smaller in diameter with an average size of 11nm, with a few of the Al_2O_3 particles over 100nm in size. In APMT large Al_2O_3 particles were also observed along with some smaller Y Al O and Y_2O_3 particles as well. In addition oxides of Zr and Hf were observed along with carbide type particles rich in both Zr and Hf.

The average size of the particle distribution in the as received rolled plate PM2000 and APMT are compared in the bar chart in Figure 8.1. With the PM2000 data the average size of the particles from the three regions (top, middle and bottom) within the TMAZ were used for the chart.

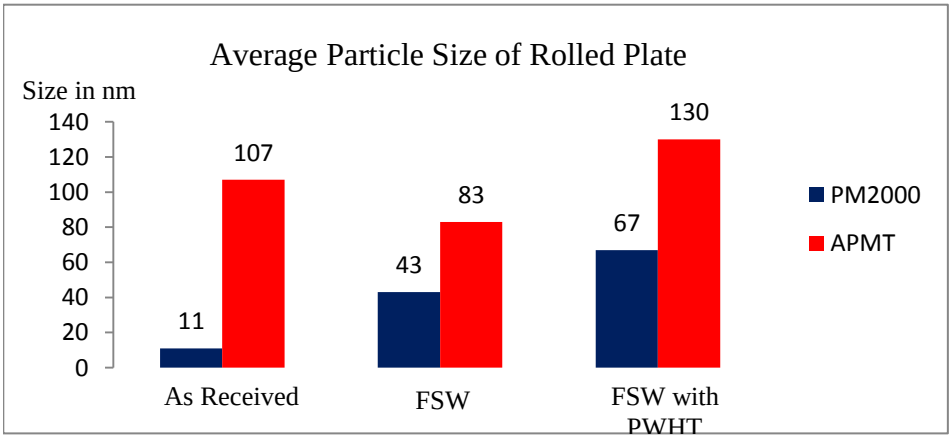

Figure 8.1 *Bar chart of average particle size of as received rolled PM2000 and APMT, after FSW and after FSW with PWHT*

With PM2000 the average particle size increases with the FSW process and even more with the application of PWHT. With APMT there seems to be a reduction in

the average size of the particle distribution after FSW but after PWHT an overall increase is observed. Further analysis on the changes in the particle size distributions are discussed separately for each alloy system below.

APMT

In APMT the average size of the particle distribution was 107nm and some of the particles measured were nearly 260nm. The second phase particles in APMT consist of a variety of particles which include Y Al O, Y_2O_3, Al_2O_3, oxides of Hf and Zr, and carbides, carbonitrides and nitrides.

The particle size analysis on APMT shows a reduction in the average size after the FSW process from 103 nm to 83 nm. There are 3 possible explanations for the reduction in the average size:

1. A big variation in the data from sample to sample as in the literature the reported average size is 75nm.

2. The FSW process dissolves some of the larger particles through a process akin to mechanical alloying therefore reducing the average size.

3. Dissolution of some of the carbides due to the large temperatures (up to 1200°C) of the FSW process and the re-precipitation of smaller carbides post FSW.

Several investigations on the particle size analysis on the APMT butt FSW did produce a wide range of values for the average size but all showed a reduction after the application of the FSW process and a subsequent increase in the average particle size after the application of PWHT. That would suggest that the FSW process does in effect either break up some of the larger particles or results in the dissolution of some of the carbides.

The FSW process did not reduce the average size of the much smaller particles in PM2000 but increased the average size due to agglomeration. If the FSW process reduces the average size of the particles in APMT then it must be that it affects the

larger particles rather than the smaller ones. Friction stir processing of aluminium, which is a process similar to FSW, but is used to alter the microstructure of the surface instead of welding, has been found to cause the dissolution of $CuAl_2$ inter metallic particles in aluminium [135]. Dawson et al. [101] observed precipitation of particles coherent with the matrix. One possible explanation offered was that an amount of mechanical alloying has taken place during the FSW process with particles re-precipitating once the tool has passed on.

In addition, peak temperatures in FSW process can reach nearly 1200°C [136]. In Figure 8.2 the ternary phase diagram of Fe-Cr-C at 1200°C is shown [137]. Due to the very low carbon content PM2000 remains in the ferritic phase. APMT with a slightly higher Cr content and the higher carbon content is in the mixed phase region. Some of the carbides could dissolve due to the partial austenitic (γ) phase regions at the FSW temperatures. This momentary elevated temperature could be enough to dissolve some of the carbides, which could re-precipitate as smaller particles with the net effect that the average particle size is reduced.

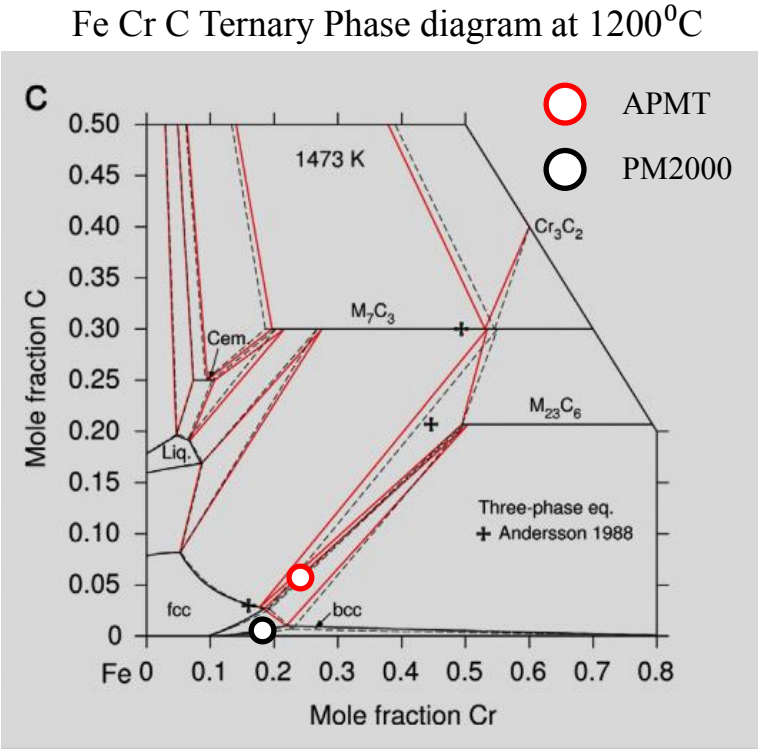

Figure 8.1 *The ternary phase diagram of Fe Cr C, at 1200C. Taken from [137].*

In reality the reduction of the average size of the particle distribution could be a combination of both factors discussed.

PM2000

The FSW process had coarsened the particle distribution by the agglomeration of the Y Al O particles. This was more noticeable in the top part of the welds. In Chapter 4 a mechanism was proposed where the higher rate of flow of material on or near the surface due to the tool geometry resulted in more encounters with other nearby particles to explain the different average particle size near the top of the weld compared to the average particle size in the middle and at the base of the weld. In Chapter 5 TEM images of the TMAZ has indicated the extent of the agglomeration where several particles were attached. Particle agglomeration has been reported in the literature. Wang et al. [112] and Kang et al. [113] have reported agglomeration of particles in the TMAZ in MA754 and MA 956 ODS alloys respectively. Wang et al. reported necking between two particles and both report a number of smaller particles agglomerating on a large particle such as Al_2O_3 or Ti (C, N) particles. Kang et al. has proposed a mechanism where the agglomerated smaller Al Y O particles attached to a larger particle as mentioned in the conclusions in Chapter 6. TEM analysis in Chapter 7, of the dissimilar FSW between APMT and as extruded PM2000 sample with only 10 minutes PWHT has given an insight of a possible particle consolidation after the agglomeration due to the FSW process. In Figure 7.18 the HRTEM image of a near fully consolidated particle is presented with an irregular outline. In Figure 7.19 the bright field TEM image shows two particles close together with possibly material from the smaller particle diffusing away to a nearby larger particle which is a classic case of Oswald ripening process.

8.9 Tool Fragments and Voids in the TMAZ

Tool Fragments

The FSW of steels is a recent development as the tools required to FSW steels were not sufficiently strong enough to withstand the thermal stresses and strains until the development of the PCBN tool. The high cost of the tool means that the length of

weld available from the tool needs to be maximised to reduce the cost base of FSW process. Tool wear is an important factor in the consideration of the FSW process for more industrial applications.

The tool used for the FSW process is a Q70 type tool. This specifies that the PCBN content is 70% with a Re/W binder. This combination gives a longer lifespan for the tool compared to tools with higher concentrations of PCBN for machining tool steels [138]. In a review of wear mechanisms of PCBN tools for hard turning applications by Lahiff [139] several wear mechanisms are discussed. The 4 main modes of wear are abrasion, adhesion, diffusion and chemical wear. The most relevant modes in FSW are the abrasion and diffusion mechanisms. In abrasion the binder is worn away releasing some of the PCBN fragments that in turn increase the abrasion wear of the tool [138].

Diffusion of B was observed for PCBN tool with a ceramic binder using a carbon steel workpiece. The depletion of B away from the tool surface was detected to 50μm depth of the tool and the grain boundaries regions of the PCBN were thought to be the most likely source rather than from the bulk of the grains.

The combination of abrasion of the binder which then exposes PCBN fragments to break off the tool and the diffusion of B into the material being FSW due to the high temperatures involved are the most likely wear mechanisms observed in the FSW of as rolled PM2000.

Fragments from the PCBN tool have been observed in the BOP welds of the as rolled PM2000. No tool fragments were observed in any of the other welds. The most likely location of the fragments was near the surface of the weld and along the advancing side boundary between the TMAZ and the parent material. The high hardness value of the as rolled PM2000 plate compared to the rest of the samples must be the main reason that it was observed only in the as rolled BOP welds. Although the fragments were stable in the as welded condition, it was found that during the PWHT process the fragments broke down to form TiN grains at the fragment location. Further analysis of the particles has determined that at a temperature between 900°C and 1100°C the PCBN tool fragment starts to breakdown. The phase diagram of BN shows a phase transformation from a dense cubic structure to a hexagonal structure

which results in an increase in the volume of 53% of the original volume. This volume change initiates the breakdown of the fragments. The affinity of Ti present in PM2000 to N from the breakdown of the fragment had resulted in a Ti rich region around the fragment. There is no literature on the transformation of the PCBN tool fragments in ODS steels after the application of PWHT.

The BN fragments were observed at the top of the BOP welds and at the advancing side of the TMAZ boundary. In a stressed environment the lining of BN fragments along the advancing side could prove detrimental to the integrity of the weld especially after the application of PWHT as a 'fault line' of hard brittle particles could weaken the weld.

Voids

Voids were observed in all of the FSW samples examined. The fractographs in Chapter 6 of the FSW sample W31 with and without PWHT, Charpy v-notch impact tests were performed and several cracks were observed to originate from the void region. Void formation was attributed to an area close to the bottom of the tool, possibly a feature such as a groove that causes the voids to form in a spiral pattern as viewed from the plan direction of the sample. Nandan et al. [136] in an overview of several studies breaks down the material flow from the FSW process into three different types. The first is a slug of plasticised material that rotates near the tool. The second type of flow is the downward material flow due to threaded pin geometry which must also cause some upward flow somewhere else in the TMAZ. This flow characteristic is also responsible for the elongation of grains at the advancing side of the weld. The third is the flow of material from the retreating side of the tool that forms the join as the tool moves forward in the direction of the weld line. Modelling of the flow characteristics in FSW of aluminium by Crawford et al. [82] has indicated a region near the base of the advancing side of the welds where voids are caused due to insufficient flow of material towards the bottom of the weld. These voids tend to form at or near the boundary of the TMAZ and the parent region. The size of the voids has been linked to increasing transverse speed compared to the rotational speed i.e. the Heat Index. There is no mention in literature about the regular nature of the voids along the weld line that is due to the tool itself or any particular features on the tool.

From the results obtained in Chapter 6 and from literature one can conclude that there are two types of voids that can be observed. The first is dependent on the flow characteristics of the weld parameters and will depend on the heat index. If the transverse speed is too high compared to the rotational speed the material will not flow fast enough behind the tool to fill the void of the material displaced by the tool at the advancing side of the weld. This is the type of void that is mentioned in the literature. The second type of void was observed in Chapter 6 and is purely dependant on the tool geometry. Grooves in the tool that assist in the flow characteristics of the weld as mentioned in Chapter 6 producing spiral voids that partly are filled in at the retreating side but stay as voids in the advancing side of the weld.

8.10 Diffusion and the Formation of Ti (C, N) Particles

The investigation of the dissimilar metal FSW between APMT and as-extruded PM2000 W35 in Chapter 7 has revealed the formation of Ti(C, N) particles in the TMAZ, after the application of PWHT, at the boundary area between the two alloys. This is the region of interest at the advancing side of the TMAZ where a region of PM2000 is surrounded above and below by APMT. EDX mapping of the region in Chapter7 Figure 7.12 has confirmed the diffusion, due to a concentration differential, across the boundary of Fe, Cr, Mo and Ti.

Table 8.2 *Composition %Wt of PM2000 and APMT*

	Fe	Cr	Al	Mo	Si	Mn	C	Y	Zr	Hf	Ti	Mg	S	N
PM2000	bal	19	5.5	-	-	-	-	.5(Y_2O_3)	-	-	0.5	-	-	-
APMT	bal	22	5	3	0.7	0.4	.05	0.1	.05	.1	.02	.01	.002	.05

From the composition %Wt of PM2000 and APMT listed in Table 8.2, Fe concentration in APMT is 68.5%Wt and in PM2000 is 74.5%Wt. This concentration differential is the driving force for the diffusion of Fe from PM2000 to APMT. The EDX mapping of Fe indicates that after 10 minutes, diffusion is observed and after the full hour of PWHT the concentration differential is hardly visible.

The diffusion of Cr was observed, from the EDX mapping, from APMT to PM2000. The concentration of Cr in APMT is 22%Wt and in PM2000 the concentration is 19%Wt. Once again partial diffusion is observed after 10 minutes but after 1 hour the difference in concentrations between the two regions from the EDX map is hardly visible.

Diffusion of Mo was observed from APMT to PM2000. The Mo concentration of APMT is 3%Wt. There is no Mo present in PM2000. Once again progressive diffusion is seen at 10 minutes and after 1 hour of PWHT.

In the case of diffusion of Fe from PM2000 to APMT, it may be more appropriate to use the equation for diffusion from a slab of material as the PM2000 region is surrounded by two regions of APMT either side. The equation for diffusion from a slab is given by Shewmon et al. [140]:

$$C(x,t) = \frac{4C_0}{\pi}\sum_{j=0}^{\infty}\frac{1}{2j+1}\sin\frac{(2j+1)\pi x}{h}\exp[-(\frac{(2j+1)\pi}{h})^2 Dt] \qquad \textit{(Equation 8.1)}$$

with the boundary conditions $c = c_0$ for $0 < x < h$ at $t = 0$

and $c = 0$ for $x = h$ and $x = h$ $t > 0$

where h is the thickness of the slab.

The terms of the above equation are exponentially reducing and as an approximation only the first term needs to be calculated.

The self-diffusion coefficient of Fe can be calculated using Equation 2.21:

$$D = D_o\exp[\frac{-Q}{RT}]$$

Using the PWHT temperature of 1653°K, D_o=2.810x10^{-4}m^{2}s^{-1}, Q=251x10^{3}J/mole and R =8.31J/mole-K [25] then the coefficient of diffusion for Fe in αFe is calculated as

D=3.28x10^{-12}m^2/s

If the equation for diffusion out of a slab (Equation 8.1) is approximated to the first term only the error is calculated at less than 1% if the following condition is met [140]:

$$t \geq \frac{h^2}{16D}$$

Since h and D are known this equates to a time of approximately 16 minutes. In order to simplify the calculations, the time required for the concentration of the middle of the slab to reduce by 50% was calculated. For the section of PM2000 in between the two regions of APMT the image in Figure 7.13 was used. The thickness of the slab was 230μm and the concentration at the middle of the slab was calculated using the following conditions: $x = h/2,$ and $c = \frac{C_0}{2}$

The time required for the concentration of Fe from the middle of the slab to fall by 50% was calculated at t =25.5 minutes. This time is above the 1% error threshold for using the first term of *Equation 8.1*.

If $t = 1\ hour$ the ration c/c_0=0.061 and so there is little difference of concentration across the slab. This is in agreement with the EDX map for Fe where the 1 hour PWHT sample looks uniform across the slab region.

The Diffusion of Ti, C and N

The diffusion of Ti was different to the rest of the elements observed. The concentration of Ti in APMT is 0.02%Wt and in PM2000 it is 0.5%Wt. This is a concentration difference of 25 times greater in PM2000 than in APMT. After the 10 minute PWHT one can observe that there is a concentration of Ti near the boundary regions between APMT and PM2000. A line scan has confirmed that indeed Ti is concentrated at each of the boundaries with a peak in the signal of TiKa1. The Ti is not concentrated in the matrix but what seems to be happening is that Ti is being captured in particles lining the boundary. A magnified image of the boundary region was analysed using EDX mapping shown in Figure 7.15 where large particles are concentrated at this region showing a strong Ti signal. Taking into account that there

is also a concentration difference of N and C which are diffusing into the PM2000 regions then one can assume that the process is as follows.

At the PWHT temperature of 1380°C, N and C are diffusing into the PM2000 region at a faster rate than Ti is diffusing into APMT. The diffusion coefficient of C and of N in αFe at 1380°C is $1.8x10^{-8}m^2s^{-1}$ and $1.17x10^{-9}m^2s^{-1}$ respectively. The diffusion coefficient of Ti in αFe is $1.16x10^{-10}m^{-2}s^{-1}$ [141]. Due to the high affinity of both C and N, to Ti, particles are formed, mainly near the boundaries but also throughout the PM2000 region consisting of Ti (C,N).

Although several successful dissimilar FSW were studied by other authors, [124-127] the formation of such particles has not been reported.

CHAPTER 9

Conclusions and Future Work

9.1 Introduction

Four types of FSW each with a different combination of two types of ODS steels were investigated in this study. The main aims of the study was to investigate the effectiveness of the FSW process and how it affects the microstructure of the ODS steels, their particle distribution and their mechanical properties. The two types of ODS steels were PM2000 and APMT.

PM2000 is produced via the MA process which is an expensive, time consuming process but results in an alloy with a fine distribution of particles. This imparts excellent high temperature creep properties for applications such as heat exchangers and power generation. PM2000 is no longer in production and material for FSW was limited.

APMT is produced via the RSP process which is more cost effective than MA. The particle distribution is inferior to PM2000 but has excellent oxidation and corrosion properties at high temperatures.

The four FSW studied were as follows:

1. Chapter 4 BOP FSW of rolled PM2000
2. Chapter 5 Butt FSW of as extruded PM2000
3. Chapter 6 BOP and Butt FSW of APMT
4. Chapter 7 Dissimilar metal Butt FSW between APMT and as extruded PM2000

The welds were investigated using a variety of analytical techniques including optical microscopy, hardness tests, Charpy impact v-notch tests, SEM imaging using both secondary electrons and backscatter electrons, both with EDX analysis, and TEM with HRTEM imaging and EDX analysis.

The ultimate goal of the research was to produce defect free welds with a fine particle size distribution and with the application of PWHT a large microstructure that provides the maximum amount of creep resistance at the high temperature applications that the ODS steels are designed for.

9.2 Conclusions

The main conclusion from this research is that the FSW of ODS steel has been shown to be a feasible joining technique. Fine tuning of the parameters is required for each different type of ODS steel as properties such as hardness and thickness of the plate to be welded can affect the quality of the weld. The main conclusions from each of the four types of welds are summarised below.

FSW of As-Rolled PM2000

The FSW of the as-rolled PM2000 has enabled the parameters to be adjusted for subsequent welds and so it was an important first attempt to weld ODS steels. These welds were BOP configuration. The as-rolled PM2000 plate used had the highest hardness number and was probably the reason for the observation of PCBN tool fragments near the surface of the weld and at the advancing side of the TMAZ boundary with the parent material. On the application of PWHT these fragments broke down due to a phase change from cubic structure to a hexagonal structure. The matrix surrounding the tool fragment was found to be rich in Ti. This was attributed to the high affinity of Ti to N. Grains of TiN were observed on the outer parts of the fragments. No trace of B could be detected from EDX analysis. Tool fragments were not observed in any of the other welds.

The particle size distribution had coarsened slightly overall with the largest amount of coarsening observed at the top part of the weld. The stirring of the material due to the shoulder of the tool creates more encounters between particles which then agglomerate. These then consolidate to form much larger particles after the application of PWHT.

The parent region of the BOP welds retained a fine grained structure while the TMAZ recrystallised to form a large grain structure, the large rains forming because

there were a reduced number of nucleation sites from which the recrystallisation process could start.

As-Extruded PM2000

As-extruded plates were used for the FSW of PM2000 mainly because the as-rolled PM2000 parent region did not form a large grain size. A test sample of as-rolled PM2000 was heat treated and a large grain structure was observed. The expectation was that the whole sample would recrystallise with large grains across the TMAZ boundary.

The result was surprising in that although the parent region had formed a large grained recrystallised structure after the application of PWHT, a large region of the TMAZ did not. Large grains did form across the boundary with the TMAZ.

The agglomeration of particles was investigated further with the particle size analysis confirming the results from the as-rolled BOP welds. Large agglomerated particles were observed in the TEM. The particles had several different lattice arrangements that made identification difficult. After the application of PWHT very few agglomerated particles were observed. It seems that the agglomerated particles had consolidated and a larger particle size distribution was observed.

APMT

Two BOP welds and three butt FSW of APMT plate were examined. The TMAZ formed a large rained recrystallised structure after the application of PWHT but with a variation in the grain size between the different welds. The two BOP welds, W26 and W27 had a smaller recrystallised grain structure than the butt welds W29 W30 and W31. The Heat Input for W26 and W27 was lower than the rest of the APMT welds.

The particle size distribution of APMT is one of much larger particles with a lower number density.

Voids were investigated by looking at the longitudinal cross section of the W30 weld near the advancing side. The regularity of the voids observed was linked to the

rotation of the tool. Further analysis had identified a region next to the lower part of the tool as the source of the voids.

Tensile tests were carried out on as-received APMT and as-welded W31. An increase in ductility without a significant loss in tensile strength was observed in the tensile tests. Charpy impact tests were carried out on as-received APMT and W31 with and without PWHT. Charpy v-notch impact test had confirmed the increase in ductility which was observed by the increase in ductile fracture regions in the fractographs. Cracks were seen to originate from some void regions.

The particle distribution in APMT is made up of carbides and nitrides of Hf, Ta and Zr as well as oxides of Y and Y Al.

Dissimilar Metal FSW between APMT and As-Extruded PM2000

The interesting feature of this weld was the region in the TMAZ at the advancing side of the weld where a region of PM2000 was surrounded by APMT above and below. On the application of PWHT for 10 minutes the APMT region recrystallised first which created a boundary of grains when PWHT was applied for the full hour. Large recrystallised grains grew across the APMT/PM2000/APMT.

EDX mapping on the as welded sample, with 10minutes PWHT and 1Hour PWHT revealed the diffusion of Fe from PM2000 to APMT in the PWHT samples. The diffusion of Mo and Cr was also observed in the PWHT samples but from APMT into the PM2000 region. The diffusion of Ti after the application of PWHT was different in that the formation of carbides and nitrides of Ti were observed at the prior boundary between APMT and PM2000. The relatively rapid diffusion of carbon and nitrogen from the APMT to PM2000 region had the effect of capturing the Ti and formed carbides and nitrides which were concentrated at the prior boundary of APMT and PM2000.

TEM analysis on a sample with 10 minutes of PWHT had revealed the presence of necking between particles. Also observed were particles with edges that were not fully in equilibrium.

9.3 Future Work

Residual Stress

The most surprising aspect of the study was the band of unrecrystallised PM2000 in W34 as reported in Chapter 5. Further investigation on this region of the weld is necessary to gain understanding as to why this region did not undergo recrystallisation. At the Euromat 2015 conference in Poland, while presenting a poster on the dissimilar metal FSW between APMT and PM2000, a fellow researcher was presenting his work on the non-destructive energy resolved neutron imaging technique on dissimilar metal welds.[142] . An offer of collaboration was made to use this non-destructive technique to analyse the cross section of the welds. A stress map could be produced that could provide some answers as to why this region did not recrystallise. This would be ideal as the non-destructive nature of the analysis means that even with limited material a residual stress map of the weld can be produced.

Particle Agglomeration

The particle agglomeration seen in the TMAZ of W34 in Chapter5 and the partial consolidation of some particles in the TMAZ of W35 with 10 minutes of PWHT have given some clues as to the interactions between particles after FSW and after PWHT. Further analysis could be undertaken with several TMAZ samples that are PWHT for different times to see the progress in the consolidation process.

Voids

The voids observed in the TMAZ of the welds have been attributed to the design of the tool or a feature on the tool surface near the base of the tool. Tool design refinement would be interesting to see whether the voids seen can be eradicated by a slight change in the design of the tool.

PCBN Tool Fragments

Fragments of the tool have been observed only with the as rolled PM2000 BOP welds. The high Vickers hardness number of the as rolled PM2000 compared to the as extruded PM2000 has increased the stress and the amount of abrasion that the

FSW tool had experienced during the FSW process. Further work is needed to investigate further design changes with regards to the composition of the tool to avoid the fragments embedded in the TMAZ that subsequently breakdown after the application of PWHT.

REFERENCES

[1] J. S. Benjamin, "Mechanical alloying," *Scientific American,* vol. 234, pp. 40-48, 1976.

[2] J. S. Benjamin, "Dispersion strengthened superalloys by mechanical alloying," *Metallurgical and Materials Transactions B,* vol. 1, pp. 2943-2951, 1970.

[3] B. Jönsson, Q. Lu, D. Chandrasekaran, R. Berglund, and F. Rave, "Oxidation and Creep Limited Lifetime of Kanthal APMT®, a Dispersion Strengthened FeCrAlMo Alloy Designed for Strength and Oxidation Resistance at High Temperatures," *Oxidation of Metals,* vol. 79, pp. 29-39, 2013.

[4] C. Capdevila, "Oxide coarsening and its influence on recrystallization in a mechanically alloyed Fe-base oxide-dispersion-strengthened alloy," *Metallurgical and Materials Transactions A,* vol. 36, pp. 1547-1555, 2005.

[5] B. A. Pint and I. G. Wright, "Long-term high temperature oxidation behavior of ODS ferritics," *Journal of Nuclear Materials,* vol. 307, pp. 763-768, 2002.

[6] D. P. Whittle and J. Stringer, "Improvements in high temperature oxidation resistance by additions of reactive elements or oxide dispersions," *Philosophical Transactions of the Royal Society of London.Series A, Mathematical and Physical Sciences,* vol. 295, pp. 309-329, 1980.

[7] J. Armitt, D. R. Holmes, I. Manning, D. B. Meadowcroft, and E. Metcalfe, "EPRI Report FP 686," 1978.

[8] J. Stringer, "Stress generation and relief in growingoxide films," *Corrosion Science,* vol. 10, pp. 513-543, 1970.

[9] L. B. Pfeil and W. T. Griffiths, "Improvement in heat-resisting alloys," *UK patent,* vol. 459848, 1937.

[10] D. R. Sigler, "The influence of sulfur on adherence of Al2O3 grown on Fe-Cr-Al alloys," *Oxidation of Metals,* vol. 29, pp. 23-43, 1988.

[11] A. W. Funkenbusch, J. G. Smeggil, and N. S. Bornstein, "Reactive element-sulfur interaction and oxide scale adherence," *Metallurgical Transactions A,* vol. 16, pp. 1164-1166, 1985.

[12] W. J. Quadakkers, H. Holzbrecher, K. G. Briefs, and H. Beske, "Differences in growth mechanisms of oxide scales formed on ODS and conventional wrought alloys," *Oxidation of Metals,* vol. 32, p. 67, Jan-1 1989.

[13] B. A. Pint, "Experimental observations in support of the dynamic-segregation theory to explain the reactive-element effect," *Oxidation of Metals*, vol. 45, pp. 1-37, 1996.

[14] C. Suryanarayana, "Mechanical alloying and milling," *Progress in materials science*, vol. 46, pp. 1-184, 2001.

[15] W. D. Coolidge, "Ductile tungsten," *Transactions of the American Institute of Electrical Engineers*, vol. 29, pp. 961-965, 1910.

[16] "Japan Atomic Energy Agency. Access online at http://www.jaea.go.jp/english/news/p06101302/," Access Date 01/09/2016.

[17] A. Hishinuma, A. Kohyama, R. L. Klueh, D. S. Gelles, W. Dietz, and K. Ehrlich, "Current status and future R&D for reduced-activation ferritic/martensitic steels," *Journal of Nuclear Materials*, vol. 258, pp. 193-204, 1998.

[18] L. Dai, Y. Liu, and Z. Dong, "Size and structure evolution of yttria in ODS ferritic alloy powder during mechanical milling and subsequent annealing," *Powder Technology*, vol. 217, pp. 281-287, 2012.

[19] P. Dou, A. Kimura, T. Okuda, M. Inoue, S. Ukai, S. Ohnuki, *et al.*, "Effects of extrusion temperature on the nano-mesoscopic structure and mechanical properties of an Al-alloyed high-Cr ODS ferritic steel," *Proceedings of ICFRM-14*, vol. 417, pp. 166-170, 2011.

[20] D. T. Hoelzer, J. Bentley, M. A. Sokolov, M. K. Miller, G. R. Odette, and M. J. Alinger, "Influence of particle dispersions on the high-temperature strength of ferritic alloys," *Journal of Nuclear Materials*, vol. 367, pp. 166-172, 2007.

[21] M. J. Alinger, G. R. Odette, and D. T. Hoelzer, "On the role of alloy composition and processing parameters in nanocluster formation and dispersion strengthening in nanostuctured ferritic alloys," *Acta Materialia*, vol. 57, pp. 392-406, 2009.

[22] "Material Technology Innovations Co Ltd. Access online at http://www.mt-innov.com/index.php?ac=article&at=list&tid=14," Access Date 01/09/2016.

[23] R. Berglund, B. Jonsson, and J. Magnusson, "Method of making a FeCrAl material and such material," *Patent WO 2001049441 A1*, 2001.

[24] F. J. H. M. Humphreys, *Recrystallization and Related Annealing Phenomena*. UK: Elsevier, 2004.

[25] W. D. Callister and D. G. Rethwisch, *Materials science and engineering: an introduction* vol. 7: Wiley New York, 2007.

[26] N. D. T. R. Centre, "Available online at www.nde-ed.org/EducationResources/CommunityCollege/Materials/Structure/linear_defects.htm," Access Date 2016.

[27] H. Lawrence and V. Vlack, "Elements of materials science and engineering," 1989.

[28] C. R. Weinberger, B. L. Boyce, and C. C. Battaile, "Slip planes in bcc transition metals," *International Materials Reviews*, vol. 58, pp. 296-314, 2013.

[29] D. Kuhlmann-Wilsdorf and N. Hansen, "Geometrically necessary, incidental and subgrain boundaries," *Scripta metallurgica et materialia*, vol. 25, pp. 1557-1562, 1991.

[30] R. D. Doherty, D. A. Hughes, F. J. Humphreys, J. J. Jonas, D. J. Jensen, M. E. Kassner, *et al.*, "Current issues in recrystallization: a review," *Materials Science and Engineering: A*, vol. 238, pp. 219-274, 1997.

[31] "Online Access at http://engineering.dartmouth.edu/defmech/chapter_2.htm," Access Date 01/09/2016.

[32] A. Najafizadeh and J. J. Jonas, "Predicting the critical stress for initiation of dynamic recrystallization," *ISIJ International*, vol. 46, pp. 1679-1684, 2006.

[33] G. Pimentel, J. Chao, and C. Capdevila, "Recrystallization Process in Fe-Cr-Al Oxide Dispersion-Strengthened Alloy: Microstructural Evolution and Recrystallization Mechanism," *JOM*, vol. 66, p. 780, Jan-1.

[34] I. M. Lifshitz and V. V. Slyozov, "The kinetics of precipitation from supersaturated solid solutions," *Journal of physics and chemistry of solids*, vol. 19, pp. 35-50, Jan-1 1961.

[35] C. Wagner, "Theorie der alterung von niederschlägen durch umlösen (Ostwald-reifung)," *Zeitschrift für Elektrochemie, Berichte der Bunsengesellschaft für physikalische Chemie*, vol. 65, pp. 581-591, 1961.

[36] C. V. Thompson, H. J. Frost, and F. Spaepen, "The relative rates of secondary and normal grain growth," *Acta Metallurgica*, vol. 35, pp. 887-890, 1987.

[37] R. D. Doherty, "Recrystallization of Metallic Materials," *Ed.By Frank Haessner.Dr.Riederer Verlag GmbH, Stuttgart*, 1978.

[38] R. W. Cahn, "A new theory of recrystallization nuclei," *Proceedings of the Physical Society.Section A*, vol. 63, p. 323, 1950.

[39] W. Sha and H. Bhadeshia, "Modelling of recrystallisation in mechanically alloyed materials," *Materials Science and Engineering: A*, vol. 223, pp. 91-98, 1997.

[40] C. Capdevila, Y. L. Chen, A. R. Jones, and H. Bhadeshia, "Grain boundary mobility in Fe-base oxide dispersion strengthened PM2000 alloy," *ISIJ International*, vol. 43, pp. 777-783, 2003.

[41] C. Capdevila and H. K. D. H. Bhadeshia, "Manufacturing and microstructural evolution of mechanuically alloyed oxide dispersion strengthened superalloys," *Advanced Engineering Materials,* vol. 3, pp. 647-656, 2001.

[42] G. Pimentel, I. Toda-Caraballo, J. Chao, and C. Capdevila, "Role of strain heterogeneity on recrystallisation of oxide dispersion strengthened Feâ€“Crâ€“Al alloys for high-temperature applications," *Journal of Materials Science,* pp. 1-12.

[43] C. Capdevila, Y. Z. Chen, N. C. K. Lassen, A. R. Jones, and H. K. D. H. and Bhadeshia, "Heterogeneous deformation and recrystallisation of iron base oxide dispersion strengthened PM2000 alloy," *Materials Science and Technology,* vol. 17, pp. 693-694 695 696 697 698 699, 2001.

[44] C. Capdevila Montes and H. K. D. H. Bhadeshia, "Influence of Deformation on Recrystallization of an Yttrium Oxide Dispersion-Strengthened Iron Alloy (PM2000)," *Advanced Engineering Materials,* vol. 5, pp. 232-237, 2003.

[45] C. Capdevila and H. K. D. H. Bhadeshia, "Manufacturing and Microstructural Evolution of Mechanuically Alloyed Oxide Dispersion Strengthened Superalloys," *Advanced Engineering Materials,* vol. 3, p. 647, Jan-1 2001.

[46] H. Regle and A. Alamo, "Secondary recrystallization of oxide dispersion strengthened ferritic alloys," *Le Journal de Physique IV,* vol. 3, pp. C7-727-C7-730, 1993.

[47] H. K. D. H. Bhadeshia, "Recrystallisation of practical mechanically alloyed iron-base and nickel-base superalloys," *Seminars on the Modelling of Atomic and Microstructures in Metals and Alloys,* vol. 223, pp. 64-77, 2/28 1997.

[48] M. H. Mathon, V. Klosek, Y. de Carlan, and L. Forest, "Study of PM2000 microstructure evolution following FSW process," *Journal of Nuclear Materials,* vol. 386-388, pp. 475-478, 2009.

[49] F. J. H. M. Humphreys, *Recrystallization and Related Annealing Phenomena* vol. Second. UK: Elsevier, 2004.

[50] R. L. Miller, "Ultrafine-grained microstructures and mechanical properties of alloy steels," *Metallurgical Transactions,* vol. 3, pp. 905-912, 1972.

[51] E. O. Hall, "The deformation and ageing of mild steel: III discussion of results," *Proceedings of the Physical Society.Section B,* vol. 64, p. 747, 1951.

[52] T. Okuda and M. Fujiwara, "Dispersion behaviour of oxide particles in mechanically alloyed ODS steel," *Journal of Materials Science Letters,* vol. 14, p. 1600, Jan-1 1995.

[53] E. Nes, N. Ryum, and O. Hunderi, "On the Zener drag," *Acta Metallurgica,* vol. 33, pp. 11-22, 1985.

[54] C. S. Smith, "Zener pinning," *Met. Technol. Trans. Metall. Soc.*, pp. 15-51, 1948.

[55] R. D. Doherty and J. W. Martin, "Stability of microstructure in metallic systems," *Metal Science*, vol. 16, 1982.

[56] D. A. Porter, K. E. Easterling, and M. Sherif, *Phase Transformations in Metals and Alloys, (Revised Reprint)*: CRC press, 2009.

[57] "Image taken from https://www.slideshare.net/RakeshSingh125/f-precipitation-hardening," ed.

[58] M. Klimiankou, R. Lindau, A. Moslang, J. Schroder, Klimiankou, Lindau, *et al.*, "TEM study of PM 2000 steel," *Powder Metallurgy*, vol. 48, p. 277, Sep-1 2005.

[59] A. Czyrska-Filemonowicz, K. Szot, A. Wasilkowska, A. Gil, and W. J. Quadakkers, "Microscopy (AFM, TEM, SEM) studies of oxide scale formation on FeCrAl based ODS alloys," *Solid State Ionics*, vol. 117, pp. 13-20, 2/1 1999.

[60] "Inorganic Crystal Structure Database – ICSD https://www.fiz-karlsruhe.de/de/leistungen/kristallographie/icsd.html " Access Date 2016.

[61] C. Capdevila, G. Pimentel, M. M. Aranda, R. Rementeria, K. Dawson, E. Urones-Garrote, *et al.*, "Role of Y-Al oxides during extended recovery process of a Ferritic ODS alloy," *JOM*, vol. 67, pp. 2208-2215, 2015.

[62] Y. Z. Shen, T. T. Zou, S. Zhang, and L. Z. Sheng, "Identification of Oxide Phases in Oxide Dispersion Strengthened PM2000 Steel," *ISIJ International*, vol. 53, pp. 304-310, 2013.

[63] J. C. Anderson, K. D. Leaver, R. D. Rawlings, and P. S. Leevers, *Materials science for engineers*: CRC Press, 2004.

[64] R. E. Smallman and R. E. Smallman, *Modern physical metallurgy*: Butterworths London, 1985.

[65] "Image taken from: http://m.blog.naver.com/cosmoscent/150173506706," Access Date 2016.

[66] S. J. Zinkle and G. E. Lucas, "Deformation and fracture mechanisms in irradiated FCC and BCC metals," *Fusion Materials Semi-annual Progress Report for Period ending June*, vol. 30, p. 101, 2003.

[67] Z. Feng, X. Yu, W. Tang, D. Hoelzer, and L. T. Tan, "2.5 FRICTION STIR WELDING OF ODS STEELS AND ADVANCED FERRITIC STRUCTURAL STEELS."

[68] P. A. Molian, Y. M. Yang, and P. C. Patnaik, "Laser welding of oxide dispersion-strengthened alloy MA754," *Journal of Materials Science*, vol. 27, pp. 2687-2694, 1992.

[69] G. J. Tatlock, E. G. Dyadko, S. N. Dryepondt, and I. G. Wright, "Pulsed Plasma-Assisted Diffusion Bonding of Oxide Dispersion-Strengthenedâ€“FeCrAl Alloys," *Metallurgical and Materials Transactions A*, vol. 38, pp. 1663-1665, 2007.

[70] V. G. Krishnardula, N. I. Sofyan, W. F. Gale, and J. W. Fergus, "Joining of ferritic oxide dispersion strengthened alloys," *Transactions of the Indian Institute of Metals*, vol. 59, pp. 199-203, 2006.

[71] W. Sittel, W. W. Basuki, and J. Aktaa, "Diffusion bonding of the oxide dispersion strengthened steel PM2000," *Journal of Nuclear Materials*, vol. 443, pp. 78-83, 2013.

[72] W. M. Thomas, E. D. Nicholas, J. C. Needham, M. G. Murch, P. Templesmith, and C. J. Dawes, "Friction stir welding," *International patent application no.PCT/GB92102203 and Great Britain patent application*, 1991.

[73] H. Bhadeshia and T. DebRoy, "Critical assessment: friction stir welding of steels," *Science and Technology of Welding & Joining*, vol. 14, pp. 193-196, 2009.

[74] S. R. Cater, A. M. Galloway, N. A. McPherson, R. Steel, G. J. Tatlock, and K. Dawson, "Friction Stir Welding of Steel : A Process Update," *Welding & Cutting;2013, Issue 4, p268*, p. p268, 2013.

[75] "MegaStir website http://www.slb.com/services/megastir/friction-stir-welding/fsw-tool.aspx " Date of Access 2016.

[76] S. H. C. Park, Y. S. Sato, H. Kokawa, K. Okamoto, S. Hirano, and M. Inagaki, "Boride formation induced by pcBN tool wear in friction-stir-welded stainless steels," *Metallurgical and Materials Transactions A*, vol. 40, pp. 625-636, 2009.

[77] R. Rai, A. De, H. Bhadeshia, and T. DebRoy, "Review: friction stir welding tools," *Science and Technology of Welding & Joining*, vol. 16, pp. 325-342.

[78] R. Nandan, T. DebRoy, and H. Bhadeshia, "Recent advances in friction-stir weldingâ€“Process, weldment structure and properties," *Progress in Materials Science*, vol. 53, pp. 980-1023, 2008.

[79] R. S. Mishra and Z. Y. Ma, "Friction stir welding and processing," *Materials Science and Engineering: R: Reports*, vol. 50, pp. 1-78, 2005.

[80] Ø. Frigaard, Ø. Grong, and O. T. Midling, "A process model for friction stir welding of age hardening aluminum alloys," *Metallurgical and materials transactions A*, vol. 32, pp. 1189-1200, 2001.

[81] H. Schmidt, J. Hattel, and J. Wert, "An analytical model for the heat generation in friction stir welding," *Modelling and Simulation in Materials Science and Engineering*, vol. 12, pp. 143-157, 2004.

[82] R. Crawford, G. E. Cook, A. M. Strauss, D. A. Hartman, M. A. Stremler, R. Crawford, *et al.*, "Experimental defect analysis and force prediction simulation of high weld pitch friction stir welding," *Science and Technology of Welding and Joining*, vol. 11, pp. 657-665, 2006.

[83] M. S. Bennett, "Characterization of residual stress as a function of friction stir welding parameters in ODS steel MA956," 2013.

[84] "Image taken from http://www.rpip.tohoku.ac.jp/seeds/profile/125/lang:en/," Date of Access 2016.

[85] C. L. Chen, G. J. Tatlock, and A. R. Jones, "Microstructural evolution in friction stir welding of nanostructured ODS alloys," *Journal of Alloys and Compounds*, vol. 504, pp. S460-S466.

[86] "Image taken from http://www.capcoat.be/auger-electron-spectroscopy-aes," Date of Access 2016.

[87] D. B. Williams and C. B. Carter, *Transmission Electron Microscopy : A Textbook for Materials Science*. Boston, MA: Springer US, 2009.

[88] D. Tomus and H. P. Ng, "In situ lift-out dedicated techniques using FIB–SEM system for TEM specimen preparation," *Micron*, vol. 44, pp. 115-119, 2013.

[89] L. A. Giannuzzi, J. L. Drown, S. R. Brown, R. B. Irwin, and F. A. Stevie, "Applications of the FIB lift-out technique for TEM specimen preparation," *Microscopy research and technique*, vol. 41, pp. 285-290, 1998.

[90] "JOEL UK Webite http://www.jeoluk.com/Resources/DocumentsDownloads.aspx," Access Date 2016.

[91] " Image taken from www.globalsino.com/EM," Date of Access 2016.

[92] "Image Adapted from http://hyperphysics.phy-astr.gsu.edu/hbase/quantum/bragg.html," Date of Access 2016.

[93] S. Mondini, A. M. Ferretti, A. Puglisi, and A. Ponti, "PEBBLES and PEBBLEJUGGLER: software for accurate, unbiased, and fast measurement and analysis of nanoparticle morphology from transmission electron microscopy (TEM) micrographs," *Nanoscale*, vol. 4, pp. 5356-5372, 2012.

[94] T. S. Chou and H. Bhadeshia, "Grain control in mechanically alloyed oxide dispersion strengthened MA 957 steel," *Materials science and technology*, vol. 9, pp. 890-898, 1993.

[95] X. Mao, T. K. Kim, S. S. Kim, K. H. Oh, and J. Jang, "Thermal stability of oxide particles in 12Cr ODS steel," *Journal of Nuclear Materials,* vol. 428, pp. 82-89, 9/ 2012.

[96] S. Swaminathan, K. Oh-Ishi, A. P. Zhilyaev, C. B. Fuller, B. London, M. W. Mahoney, *et al.*, "Peak Stir Zone Temperatures during Friction Stir Processing," *Metallurgical and Materials Transactions A,* vol. 41, p. 631, 2010.

[97] H. W. Jeong, S. M. Seo, H. U. Hong, and Y. S. Yoo, "Characterization of the parameters relating adjacent grains using transmission electron microscopy," *Journal of Applied Crystallography,* vol. 43, pp. 1495-1501, Jan-1, 2010.

[98] S.-C. Wang and P.-W. Kao, "The effect of alloying elements on the structure and mechanical properties of ultra low carbon bainitic steels," *Journal of Materials Science,* vol. 28, pp. 5169-5175, 1993.

[99] F. Legendre, S. Poissonnet, P. Bonnaillie, L. Boulanger, and L. Forest, "Some microstructural characterisations in a friction stir welded oxide dispersion strengthened ferritic steel alloy," *Journal of Nuclear Materials,* vol. 386, pp. 537-539, 2009.

[100] S. Noh, R. Kasada, A. Kimura, S. H. C. Park, and S. Hirano, "Microstructure and mechanical properties of friction stir processed ODS ferritic steels," *Proceedings of ICFRM-14,* vol. 417, pp. 245-248, 10/1.

[101] K. Dawson, S. Cater, G. J. Tatlock, and C. Stanhope, "Friction stir welding of PM2000 ODS alloy," *Materials Science and Technology : MST : A Publication of the Institute of Metals,* vol. 30, pp. 1685-1690, Jan-1, 2014.

[102] I. Mejía, A. Bedolla-Jacuinde, C. Maldonado, and J. M. Cabrera, "Hot ductility behavior of a low carbon advanced high strength steel (AHSS) microalloyed with boron," *Materials Science and Engineering: A,* vol. 528, pp. 4468-4474, 2011.

[103] G. Kern, G. Kresse, and J. Hafner, "Ab initio calculation of the lattice dynamics and phase diagram of boron nitride," *Physical Review B,* vol. 59, p. 8551, 1999.

[104] M. Eremets, K. Takemura, H. Yusa, D. Golberg, Y. Bando, V. Blank, *et al.*, "Disordered state in first-order phase transitions: Hexagonal-to-cubic and cubic-to-hexagonal transitions in boron nitride," *Physical review.B, condensed matter and materials physics,* vol. 57, p. 5655, Jan-1 1998.

[105] M. W. Chase, Jr., C. A. Davies, J. R. Downey, Jr., D. J. Frurip, R. A. McDonald, and A. N. Syverud, *Â JANAF Thermochemical Tables (Third Edition),Â J. Phys. Chem. Ref. Data,Suppl. 1, 1985, 14, 1. [all data]*: J. Phys. Chem. Ref. Data,Suppl. 1, 1985.

[106] S. N. Ghali, H. S. El-Faramawy, and M. M. Eissa, "Influence of Boron Additions on Mechanical Properties of Carbon Steel," *Journal of Minerals and Materials Characterization and Engineering,* vol. 11, p. 995, 2012.

[107] Z. Foxman, O. Sobol, M. Pinkas, A. Landau, P. HÃ¤hner, V. Krsjak, *et al.*, "Microstructural Evolution of Cr-Rich ODS Steels as a Function of Heat Treatment at 475°C," *Metallography, Microstructure, and Analysis,* pp. 1-7.

[108] T. Boegelein, *Selective laser melting of a ferritic oxide dispersion strengthened steel,* 2014.

[109] Y. Kimura, S. Takaki, S. Suejima, R. Uemori, and H. Tamehiro, "Ultra grain refining and decomposition of oxide during super-heavy deformation in oxide dispersion ferritic stainless steel powder," *ISIJ International,* vol. 39, pp. 176-182, 1999.

[110] L. N. Brewer, M. S. Bennett, B. W. Baker, E. A. Payzant, L. M. Sochalski-Kolbus, L. N. Brewer, *et al.*, "Characterization of residual stress as a function of friction stir welding parameters in oxide dispersion strengthened (ODS) steel MA956," *Materials Science and Engineering: A,* vol. 647, p. 313, 2015.

[111] M. Peel, A. Steuwer, M. Preuss, and P. J. Withers, "Microstructure, mechanical properties and residual stresses as a function of welding speed in aluminium AA5083 friction stir welds," *Acta Materialia,* vol. 51, pp. 4791-4801, 2003.

[112] J. Wang, W. Yuan, R. S. Mishra, and I. Charit, "Microstructural evolution and mechanical properties of friction stir welded ODS alloy MA754," *Journal of Nuclear Materials,* vol. 442, pp. 1-6, Jan-1.

[113] C. Y. Kang, T. H. North, and D. D. Perovic, "Microstructural features of friction welded MA 956 superalloy material," *Metallurgical and Materials Transactions A,* vol. 27, pp. 4019-4029, 1996.

[114] M. M. Kuklja and M. M. Kuklja, "Defects in yttrium aluminium perovskite and garnet crystals: atomistic study," *Journal of Physics: Condensed Matter,* vol. 12, p. 2953, 2000.

[115] C. L. Chen, P. Wang, and G. J. Tatlock, "Phase transformations in yttrium-aluminium oxides in friction stir welded and recrystallised PM2000 alloys," *Materials at High Temperatures,* vol. 26, pp. 299-303, 2009.

[116] C. L. Chen, A. Richter, and R. Kögler, "The effect of dual Fe /He ion beam irradiation on microstructural changes in FeCrAl ODS alloys," *Journal of Alloys and Compounds,* vol. 586, pp. S173-S179, Jan-1, 2014.

[117] W. Han, S. Ukai, F. Wan, Y. Sato, B. Leng, H. Numata, *et al.*, "Hardness and micro-texture in friction stir welds of a nanostructured oxide dispersion strengthened ferritic steel," *Materials Transactions,* vol. 53, pp. 390-394, 2012.

[118] B. Jönsson, P. Henning, R. Berglund, J. Magnusson, and M. Hättestrand, "High temperature properties of a new powder metallurgical FeCrAl alloy," in *Materials Science Forum*, pp. 455-462.

[119] J. Perrett, J. Martin, J. Peterson, R. Steel, and S. Packer, "Friction stir welding of industrial steels," *Friction Stir Welding and Processing VI, New Jersey: Wiley*, pp. 65-72, 2011.

[120] P. Hugh, "Handbook of refractory carbides and nitrides," *New Jersy*, pp. 100-117, 1996.

[121] B. W. Baker, T. R. McNelley, L. N. Brewer, B. W. Baker, T. R. McNelley, and L. N. Brewer, "Grain size and particle dispersion effects on the tensile behavior of friction stir welded MA956 oxide dispersion strengthened steel from low to elevated temperatures," *Materials Science and Engineering: A*, vol. 589, pp. 217-227, 2014.

[122] A. Wasilkowska, M. Bartsch, U. Messerschmidt, R. Herzog, and A. Czyrska-Filemonowicz, "Creep mechanisms of ferritic oxide dispersion strengthened alloys," *7th International Scientific Conference: Achievements in Mechanical & Materials Engineering*, vol. 133, pp. 218-224, 2/1 2003.

[123] M. Hillert, "Inhibition of grain growth by second-phase particles," *Acta Metallurgica*, vol. 36, pp. 3177-3181, 1988.

[124] S. H. Kang, J. Jang, S. Noh, and T. K. Kim, "Friction Stir Joining of Dissimilar Ferritic ODS Steels," 2012.

[125] V. Widak, B. Dafferner, S. Heger, M. Rieth, V. Widak, B. Dafferner, *et al.*, "Investigations of dissimilar welds of the high temperature steels P91 and PM2000," *Fusion Engineering and Design*, vol. 88, pp. 2539-2542, 2013.

[126] C.-L. Chen, A. Richter, L.-T. Wu, and Y.-M. Dong, "Microstructural evolution and hardness of dissimilar lap joints of ODS/stainless steel by friction stir welding," *Materials Transactions*, vol. 54, pp. 215-221, 2013.

[127] D. T. Hoelzer, K. A. Unocic, M. A. Sokolov, and Z. Feng, "Joining of 14YWT and F82H by Friction Stir Welding," *Journal of Nuclear Materials*.

[128] J. Wang, W. Yuan, R. S. Mishra, and I. Charit, "Microstructure and mechanical properties of friction stir welded oxide dispersion strengthened alloy," vol. 432, pp. 274-280.

[129] E. J. Pavlina and C. J. Tyne, "Correlation of Yield Strength and Tensile Strength with Hardness for Steels," *Journal of Materials Engineering & Performance*, vol. 17, pp. 888-893, 2008.

[130] D. B. Lewis and F. B. Pickering, "Development of recrystallization textures in ferritic stainless steels and their relationship to formability," *Metals Technology*, 2013.

[131] L. M. Brown and R. K. Ham, "Dislocation-particle interactions," *Strengthening methods in crystals,* pp. 9-135, 1971.

[132] J. M. Rosenberg and H. R. Piehler, "Calculation of the Taylor factor and lattice rotations for bcc metals deforming by pencil glide," *Metallurgical Transactions,* vol. 2, pp. 257-259, 1971.

[133] B. L. Bramfitt, "Materials Selection and Design, Volume 20, ASM Handbook, 1997, pages 357-382," in *Metals Handbook Desk Edition, Second Edition,* J. R. Davis, Ed., ed, 1997, pp. 357-382.

[134] J. Wang, W. Yuan, R. S. Mishra, and I. Charit, "Microstructure and mechanical properties of friction stir welded oxide dispersion strengthened alloy," vol. 432, pp. 274-280, 2012.

[135] K. Surekha, B. S. Murty, and K. Prasad Rao, "Effect of processing parameters on the corrosion behaviour of friction stir processed AA 2219 aluminum alloy," *Solid State Sciences,* vol. 11, pp. 907-917, 2009.

[136] R. Nandan, G. G. Roy, T. J. Lienert, and T. Debroy, "Three-dimensional heat and material flow during friction stir welding of mild steel," *Acta Materialia,* vol. 55, pp. 883-895, 2 2007.

[137] A. V. Khvan, B. Hallstedt, and C. Broeckmann, "A thermodynamic evaluation of the Fe–Cr–C system," *Calphad,* vol. 46, pp. 24-33, 2014.

[138] N. Narutaki, Y. Yamane, and K. Okushima, "Tool wear and cutting temperature of CBN tools in machining of hardened steels," *Ann.CIRP,* vol. 28, pp. 23-28, 1979.

[139] C. Lahiff, S. Gordon, and P. Phelan, "PCBN tool wear modes and mechanisms in finish hard turning," *Robotics and Computer-Integrated Manufacturing,* vol. 23, pp. 638-644, 2007.

[140] P. Shewmon, "Diffusion in Solids," *The Minerals, Metals & Materials Society, Diffusion in Solids. Second Edition. (RetroactiveCoverage) (United States), 1989,* 1989.

[141] W. F. Gale and T. C. Totemeier, *Smithells metals reference book*: Butterworth-Heinemann, 2003.

[142] A. S. Tremsin, S. Ganguly, S. M. Meco, G. R. Pardal, T. Shinohara, and W. B. Feller, "Investigation of dissimilar metal welds by energy-resolved neutron imaging," *Journal of Applied Crystallography,* vol. 49, 2016.